DISSERTATION

submitted
to the
Combined Faculty for the Natural Sciences and Mathematics
of
Heidelberg University, Germany
for the degree of
Doctor of Natural Sciences

Put forward by

Diplom-Informatiker Maurice Debatin
Born in Karlsruhe, Germany

Accurate Low-Dose Iterative CT Reconstruction from Few Projections using Sparse and Non-Local Regularization Functions

Advisor:
Prof. Dr. Jürgen Hesser

"Essentially, all models are wrong, but some are useful."
George E. P. Box

Abstract

THIS dissertation aims at reducing the dose and the acquisition time in medical and in industrial **C**omputed **T**omography (CT). Since X-rays carry enough energy to free electrons from atoms, they are extremely harmful to human cells and therefore the dose in X-ray CT should be as low as possible. For industrial CT, short acquisition and reconstruction times decrease the availability time of the X-ray machine and therefore increase the sales, due to a higher throughput. As a matter of principle, there are three strategies to reduce the dose, defined as the product of the tube current and the pulse length of the CT system: (1) Lowering the X-ray exposure by reducing the X-ray tube current; (2) lowering the pulse length of the industrial CT system which allows for a shorter acquisition process as well and (3) acquiring less projection views per full rotation of the source around the object, which enables both, a faster acquisition and reconstruction. However, all of these strategies have a strong negative impact on the resulting image quality, especially when they are combined. (1) and (2) introduce additional noise and (3) leads to streaking artifacts in the reconstructed images. Therefore, efficient reconstruction algorithms have to be found which can compensate the resulting image quality degradation.

The X-ray model can be solved analytically by **F**iltered **B**ack**p**rojection (FBP) or iteratively by solving (regularized) objective functions. Up to now, commercial scanners still employ analytical FBP due to its fast execution times. However, the aforementioned strategies of dose reduction are not suitable for this method: The images are heavily corrupted by noise and artifacts and are therefore not suitable for medical inspection or industrial CT quality control. **T**otal **V**ariation (TV) is the current state of the art method for the regularization term of iterative algorithms in X-ray CT. It can remove the noise and the streaks in the images at the cost of over-smoothing of small-scaled image features and those of small intensity. Furthermore, the images suffer from a loss of contrast and spatial resolution and "stair-casing" artifacts are introduced in image regions which should be homogeneous.

This dissertation presents three new regularization functions for low-dose, under-sampled, iterative CT which successively improve the reconstruction results of the current state of the art techniques: FBP and Total Variation.

The first method is called the **A**nisotropic **T**otal **V**ariation (ATV). We propose a gradient re-definition so as to overcome TV's problem of over-smoothing fine structures. The re-definition is accomplished by multiplying the gradient in the definition of TV by an exponential function. We include a parameter in this function and this parameter acts like a threshold of the noise and controls which structures (noise and prominent edges) to penalize during the reconstruction.

The second method focuses on the main drawbacks of TV: The production of stair-casing artifacts in regions which should be homogeneous and the over-smoothing of fine structures. To reduce the stair-casing effect of TV and at the same time to reconstruct high resolution images, we combine first and second order derivatives and we create a new regularization function. The first order Anisotropic Total Variation can separate noise and prominent edges up to a certain noise magnitude and the second order Total Variation better penalizes undesired edges than first order TV. The resulting method is called **ATV+TV**^{2}.

The third method discusses a novel generalization of TV. It is called **G**eneralized **A**nisotropic **T**otal **V**ariation (GATV). GATV uses a priori information about the **G**radient **M**agnitude **D**istribution (GMD) of the underlying object for the reconstruction. By efficient parametrization, this method can separate noise and prominent image features and it can therefore overcome the problems of TV and reconstruct high quality CT images.

We reconstruct real patient data and digitally simulated phantom data. We evaluate the efficiency of our proposed regularization methods based on a large experiment with 560 measurements where different numbers of projections, noise levels and 10 different realizations of the noise random variable were selected. We judge the results from a qualitative point of view by analyzing the reconstructed images in terms of edge sharpness and accuracy, image homogeneity and image details, like small structures and features. Furthermore, we apply quantitative measures to assess the image quality: The **R**elative **R**oot **M**ean **S**quared **E**rror (RRMSE), the **C**ontrast to **N**oise **R**atio (CNR), the Kullback-Leibler distance and a measure to rate the spatial resolution and the homogeneity of the image.

The main findings of this dissertation indicate that all of the three methods successively improve the visual impression of the reconstruction results in terms of preservation of small-scaled image features and features of small intensity. Furthermore, they can improve the edge sharpness and accuracy, spatial resolution, image contrast and homogeneity and each method, ATV, ATV+TV^2 and GATV, thereby improves the reconstruction results of its preceding method.

In case of noise-free projections, GATV can **accurately** reconstruct digitally simulated data from **20** projections and it can achieve a RRMSE which is up to **1770** times smaller than the RRMSE of TV. In case of noisy projections, all of the three methods can achieve an extreme dose reduction factor of approximately **16** compared to the results of TV. Furthermore, at this reduction factor, ATV, ATV+TV^2 and GATV can still lower the RRMSE by approximately **11**%, **20**% and **33**% compared to the results of TV, obtained from a high dose and many view setting.

From previous publications [165] we know that a 72 times dose reduction can be achieved for a TV regularized iterative reconstruction compared to FBP. Combining this information with the dose reduction potential of the proposed methods, ATV, ATV+TV^2 and GATV, reveals the potential to decrease the dose and acquisition time in CT by a factor of approximately **three orders of magnitude** (1000), compared to conventional FBP.

Zusammenfassung

Ziel dieser Dissertation ist es, die Dosis und die Aufnahmezeit bei der medizinischen und industriellen Computertomographie zu verringern. Weil Röntgenstrahlen genug Energie transportieren um Elektronen von Atomen zu lösen, sind sie extrem schädlich für menschliche Zellen. Deshalb sollte die Dosis der CT-Aufnahme so gering wie möglich sein. Bei industriellem CT verringern kurze Aufnahme- und Rekonstruktionszeiten die Bereitschaftszeit der Röntgenmaschine, was bedingt durch den erhöhten Durchsatz den Umsatz steigert. Grundsätzlich gibt es drei Strategien, die Dosis – definiert als Produkt aus dem Anodenstrom und der Pulslänge des CT Systems – zu reduzieren: (1) Reduktion des Strahlenbelastung durch Senkung des Anodenstroms; (2) Verringerung der Pulslänge des industriellen CT-Systems, welche auch einen kürzeren Aufnahmeprozess erlaubt und (3) Erfassung von wenigen Projektionen, wobei die Quelle komplett um das Objekt rotiert, was eine schnellere Aufnahme und Rekonstruktion ermöglicht. Jedoch haben alle diese Strategien einen starken negativen Einfluss auf die resultierende Bildqualität, besonders wenn sie kombiniert werden. (1) und (2) führen zu zusätzlichem Rauschen und (3) zu Streifenartefakten in den rekonstruierten Bildern. Deshalb müssen effiziente Rekonstruktionsalgorithmen gefunden werden, die die resultierende Verschlechterung der Bildqualität kompensieren können.
Das Röntgen-Modell kann analytisch durch Filtered Backprojection oder iterativ durch die Lösung von (regularisierten) Zielfunktionen gelöst werden. Aufgrund der schnellen Ausführungszeiten wenden kommerzielle Scanner heute immer noch FBP an. Jedoch sind die zuvor genannten Strategien zur Dosisreduktion nicht geeignet für diese Methode: Die Bilder weisen starkes Rauschen und Artefakte auf und sind daher nicht für die medizinische Untersuchung oder die Qualitätskontrolle bei industriellem CT geeignet. Die Methode Total Variation ist der aktuelle Stand der Technik für den Regularisierungsterm iterativer Algorithmen in Röntgen-CT. Sie kann das Rauschen und die Artefakte in den Bildern entfernen, führt jedoch zu einer Homogenisierung klein-skalierter Bildmerkmale sowie jener von niedriger Intensität. Ein weiterer Nachteil der Methode ist der Verlust von Kontrast und räumlicher Auflösung. Außerdem erscheinen treppenstufenförmige Artefakte in Bildregionen die homogen sein sollten.
In dieser Dissertation haben wir drei neue Regularisierungsfunktionen für die niedrigdosierte, unterabgetastete iterative CT entwickelt, die sukzessive die Rekonstruktionsergebnisse des aktuellen Stands der Technik, FBP und Total Variation, verbessern.
Bei der ersten Methode handelt es sich um „Anisotropic Total Variation". Wir schlagen eine Gradienten-Neu-Definition vor, um das Problem von TV, die Homogenisierung von kleinen Strukturen, zu bewältigen. Jene wird durch die Multiplikation des Gradienten in der Definition von TV mit einer Exponentialfunktion erreicht. Hierzu wird ein Parameter in diese Funktion mit einbezogen, der einen Schwellwert für das Rauschen darstellt und kontrolliert, welche Strukturen (Rauschen und markante Kanten) während der Rekonstruktion zu entfernen sind.
Die zweite Methode konzentriert sich auf die Hauptnachteile von TV: Die Erzeugung treppenstufenförmiger Artefakte in Regionen, die homogen sein sollten und die Homogenisierung feiner Strukturen. Um den durch TV ausgelösten „Treppenstufen-Effekt" zu verringern und gleichzeitig hochauflösende Bilder zu rekonstruieren, kombinieren wir Ableitungen 1. und 2. Ordnung und erzeugen eine neue Regularisierungsfunktion. Die Anisotropic Total Variation 1. Ordnung kann bis

zu einem gewissen Rauschlevel Rauschen von markanten Kanten trennen und die Total Variation 2. Ordnung bestraft ungewünschte Kanten stärker als TV 1. Ordnung. Die sich daraus ergebende Methode heißt „ATV+TV^2".
Die dritte Methode diskutiert eine neue Generalisierung von TV. Sie heißt „Generalized Anisotropic Total Variation". GATV nutzt für die Rekonstruktion das Vorwissen über die Verteilung der Gradientenmagnituden des zugrundeliegenden Objekts. Durch effiziente Parametrisierung kann diese Methode Rauschen und markante Kanten trennen und überwindet somit jene mit der TV-Methode verbundenen Probleme. Somit können qualitativ hochwertige CT Bilder rekonstruiert werden.
Wir rekonstruieren sowohl echte Patientendaten als auch digital simulierte Phantomdaten. Die Effizienz von unseren vorgeschlagenen Regularisierungsfunktionen wird auf der Basis eines großen Experiments mit 560 Messungen evaluiert, bei dem eine unterschiedliche Anzahl von Projektionen, Rauschleveln und 10 verschiedenen Realisierungen der Rauschzufallsvariable ausgewählt wurden. Daraufhin folgt eine qualitative Beurteilung der Resultate durch die Analyse der rekonstruierten Bilder in Bezug auf die Kantenschärfe und -genauigkeit, Bildhomogenität und Bilddetails, wie kleine Strukturen und Besonderheiten. Des Weiteren wenden wir quantitative Maße zur Bewertung der Bildqualität an: den *Relative Root Mean Squared Error*, das *Contrast to Noise Ratio*, die *Kullback-Leibler distance* und ein Maß zur Bewertung der räumlichen Auflösung und Homogenität des Bildes.
Die wesentlichen Erkenntnisse dieser Dissertation sind, dass alle drei Methoden sukzessive den visuellen Eindruck der Rekonstruktionsergebnisse verbessern. Dies gilt für die Erhaltung kleinskalierter Kanten sowie jener von niedriger Intensität, die Kantenschärfe und -genauigkeit, die räumliche Auflösung, den Bildkontrast und die Homogenität des Bildes. Die drei nacheinander vorgestellten Methoden, ATV, ATV+TV^2 und GATV, verbessern jeweils die Rekonstruktionsergebnisse der vorherigen Methode.
Im Fall von rauschfreien Projektionen kann GATV digital simulierte Daten von **20** Projektionen akkurat rekonstruieren und so einen RRMSE erreichen, der bis zu **1770** Mal kleiner ist als der RRMSE der Resultate von TV. Im Fall von verrauschten Projektionen ermöglichen alle drei Methoden im Gegensatz zu TV eine extreme Reduktion der Dosis um einen Faktor von ungefähr **16**. Des Weiteren können bei diesem Faktor der Dosisreduktion, ATV, ATV+TV^2 und GATV den RRMSE im Vergleich zu dem Ergebnis von TV (das von vielen Projektionen und einer hohen Dosis gewonnen wurde) um ungefähr **11**%, **20**% und **33**% weiter verringern.
Von vorherigen Publikationen [165] wissen wir, dass im Vergleich zu FBP mit der TV-regularisierten iterativen Rekonstruktion eine 72-fache Dosisreduktion erreicht werden kann. Kombiniert man diese Information mit der Schlussfolgerung dieser Dissertation, ergibt sich im Vergleich zu konventionellen FBP eine mögliche Reduktion der Dosis und Aufnahmezeit in CT von einem Faktor von **drei Größenordnungen** (1000), wenn ATV, ATV+TV^2 und GATV genutzt werden.

For Ines ♡

Acknowledgments

This dissertation originated during my work at the Department of Radiation Oncology, University of Heidelberg, Mannheim, in the period 11/2011 to 10/2015.
First and foremost I would like to thank my doctoral advisor, Prof. Dr. Jürgen Hesser, for his ongoing support during the last years. I entered the department of Experimental Radiation Oncology of the University Medical Center Mannheim as a student of Computer Science in 2010 and since then, Mr. Hesser has accompanied me on my educational way, supervising both, the diploma thesis and this dissertation project. I want to thank him for giving me the opportunity to work on interesting topics and for always being available for scientific discussions, advices, critical proof-reading of publications and for teaching me the basic foundations of scientific research and the importance of loyalty and correctness in science. I want to thank him for providing the financial support through the various interesting third-party funded projects, where I learned a lot apart from my PhD topic.
I would like to express my gratitude to the Faculty of Mathematics and Computer Science of the University of Heidelberg for providing the foundation for my research as a PhD-Student, making this dissertation possible.
I also want to thank my colleagues at the department for their practical help and for theoretical discussions. Especially I want to thank Stanislav Pyatykh for supporting me with the mathematics and for proofreading the thesis, Dzmitry Stsepankou for providing some useful implementations and many discussions on the topic of CT and Manuel Blessing for proofreading the thesis, enriching discussions and for being there as a colleague and as a friend.
I want to thank my parents for their continuous support throughout my lifetime, both in word and deed.
Most of all I want to thank my beloved wife, Ines, for always being there when I needed her and for her support and understanding in every circumstance. I dedicate this dissertation to you.

Maurice Debatin

Mannheim, 01/23/2016

Contents

Notation

The following notation and abbreviations are used in this thesis:

THE NOTATION OF THIS THESIS

Scalars, vectors and matrices

n	iteration number
N	overall number of iterations
$h \in \mathbb{N}$	step size
i	projection subscript
j	pixel subscript in vector representation
x	cartesian column coordinate subscript in matrix representation
y	cartesian row coordinate subscript in matrix representation
z	x or y
o	cartesian row coordinate of the GLCM
p	cartesian column coordinate of the GLCM
t	specific ROI_t, where $t \in T$
T	the number of ROIs
I_i	set of pixels contributing to projection i
J_j	set of projections contributing to pixel j
Y_i	detected number of photons for projection i (not log-converted)
y_i	detected number of photons for projection i (log-converted)
l_{ij}	length of projection line i that intersects pixel j
d_0	number of photons leaving the source
μ	vector of attenuation coefficients
μ_j	linear attenuation coefficient of pixel j in vector notation
$\mu_{x,y}$	linear attenuation coefficient of pixel (x, y) in matrix notation
μ_j^{ref}	linear attenuation coefficient of the reference phantom

Abbreviations

ABOCS	Accelerated Barrier Optimization Compressed Sensing
ASD - POCS	Adaptive Steepest Descent - Projection Onto Convex Sets
ASiR	Adaptive Statistical Iterative Reconstruction
ASSR	Advanced Single Slice Rebinning
ATV	Anisotropic Total Variation
ATV+TV^2	Anisotropic Total Variation + 2^{nd} order Total Variation
AwTV	Adaptive weighted Total Variation regularization ([218])
b	binned GMs in the GMD
BB	Barzilai-Borwein
bg	background
CBCT	Cone-Beam Computed Tomography
CNR	Contrast to Noise Ratio
CS	Compressed Sensing
CT	Computed Tomography
DART	Discrete Algebraic Reconstruction Technique
DBT	Digital Breast Tomography
DRR	Digitally Reconstructed Radiograph
eb	engine block
EM	Expectation Maximization
EPTV	Edge Preserving Total Variation
FBP	Filtered Backprojection

Abbreviations	
FT	Fourier Transform
GATV	Generalized Anisotropic Total Variation
GLCM	Gray Level Co-Occurrence Matrix
GM	Gradient Magnitude
GMD	Gradient Magnitude Distribution
GMT	Gradient Magnitude Transform
GPU	Graphics Processing Unit
H	the degree of homogeneity
HU	Hounsfield Unit
IGRT	Image Guided Radiation Therapy
IRIS	Iterative Reconstruction in Image Space
KLD	Kullback-Leibler Distance
LAC	Linear Attenuation Coefficient
LFV	Limited Field of View
lp	line pair
MAC	Mass Attenuation Coefficient
MAP	Maximum A Posteriori
ML	Maximum Likelihood
ML-EM	Maximum Likelihood Expectation Maximization
MSE	Mean Squared Error
MTF	Modulation Transfer Function
na	not applicable
NUEI	Non Uniformity Error Index
OSC	Ordered Subsets algorithm for Transmission CT ([15])
OSL	One Step Late
PET	Positron Emission Tomography
PICCS	Prior Image Constrained Compressed Sensing
PVM	Pixel Variance Map
PWLS	Penalized Weighted Least Squares
Ram-Lak	Ramachandran-Lakshminarayanan
rgb	red-green-blue
RIP	Restricted Isometry property
ROI	Region of Interest
RRE	Relative Reconstruction Error
RRMSE	Relative Root Mean Squared Error
SD	Standard Deviation
SNR	Signal to Noise Ratio
SPECT	Single Photon Emission Computed Tomography
SVD	Single Value Decomposition
TF	Tight Frame
TGV	Total Generalized Variation
TV	Rudin-Osher-Fatemi Total Variation regularization ([294])
UPN	Unknown Parameter Nesterov
XVI	X-ray volume imaging
Parameter definitions	
$\beta \geq 0$	regularization parameter
$0 < \varepsilon \ll 1$	a very small parameter of TV to enable differentiability
$0 < \zeta < 1$	relaxation parameter controlling the convergence speed of OSC
$\delta \geq 0$	a parameter of AwTV
$\tau > 0$	a parameter of GATV controlling the penalization of GMs
$\sigma > 0$	a parameter of ATV controlling the threshold of the noise
$1 < \lambda < 1$	a parameter of ATV + TV^2 controlling the penalization of GMs
$\kappa \geq 0$	a parameter of GATV controlling the cooling scheme of GATV
	a bounded domain of $\mathbb{R}$
Operators	
∇_x, ∇_y	the gradient in x and y direction
$\max(\cdot), \min(\cdot)$	the maximum or the minimum value of a vector or matrix

Table 1: The notation we use throughout this thesis.

Chapter 1

Preamble

1.1 Introduction

COMPUTED Tomography is treated as a mathematical process in which projection images, acquired from different viewing angles around the object, are reconstructed so as to obtain the inner structures or cross-sections of the object. X-rays are extremely harmful to human cells since they produce ionizing radiation (radiation that carries enough energy to free electrons from atoms) and therefore the dose is an important factor for medical CT. Reducing the anode current or acquiring less projection views are promising strategies to decrease the dose. Unfortunately, these operations introduce noise and artifacts in the reconstructed images. Therefore, algorithms have to be found which can remove the noise and artifacts and maintain the same image quality, accuracy and spatial resolution as if the reconstructions were performed from a high dose - many projection view setting.
There are two major categories of methods: Iterative reconstruction and analytical approaches. The latter use Filtered Backprojection [93] which has extremely fast execution times. Since the invention of CT it is therefore mostly applied as the standard reconstruction method for clinical systems [264]. However, in case of few projection views and a low-dose setting, this method produces results which are not usable for clinical diagnostics or industrial quality control since the images are heavily corrupted by noise and streaking artifacts.
In addition to the analytical approach, quasi-iterative methods exist, which directly operate on the image or the projection data. Hereby, a priori or a posteriori denoising plays an important role. For some scenarios these methods perform quite well. However, the risk of loosing structures is quite high.
Iterative algorithms are promising since they allow for an accurate physical model, like a noise model for the acquired projections, different detector and scanning geometries, photon statistics, X-ray beam spectrum, scattering and so on. Modeling these effects can reduce the noise and artifacts in the reconstruction. Compared to Filtered Backprojection, iterative algorithms yield images with lower noise and higher resolution. However, there is still a trade-off between spatial resolution and noise left in the image which has to be balanced. A promising strategy to reduce the artifacts and noise in an under-sampled and low-dose scenario is to introduce a regularization term into the objective function of iterative CT. This term incorporates a priori knowledge about the object being scanned into the reconstruction and can therefore remove noise and artifacts.
In this dissertation, we have developed three new regularization functions for low-dose, under-sampled, iterative CT reconstruction which successively improve the reconstruction results of the current state of the art techniques, both, for analytical and iterative CT.

1.2 Purpose of this thesis

The purpose of this thesis is to provide (regularization) methods which enable a reduction of the dose in medical CT and lower the acquisition in industrial CT. Under-sampling reduces the acquisition and reconstruction time of iterative CT, since less data has to be processed then. At the

same time, the new methods should produce a better image quality than the common state of the art techniques, which is to be analyzed quantitatively by applying quality metrics and qualitatively by visually analyzing the reconstruction results.
In general, there are two strategies to decrease the dose for medical CT: The first one is a hardware based optimal data acquisition protocol [180, 321, 236]. The second possibility is based on software solutions, such as regularized, iterative algorithms for X-ray CT, which we concentrate on in this dissertation. This solution is cheap and easy to realize with the available hardware. As a matter of principle, the dose in medical CT can be reduced by:

- lowering the X-ray exposure by reducing the X-ray tube current (as measured by the **mA**s).
- acquiring less projection views per full rotation of the scanner around the object.

For industrial CT, short acquisition and reconstruction times are of high importance since they decrease the availability time of the X-ray machine and therefore increase the sales. This can be achieved by:

- lowering the pulse length of the industrial CT system for a shorter acquisition process (as measured by the mA**s**).
- acquiring less projection views, which enables a faster acquisition and reconstruction.

The reduction of the tube current and under-sampling the target are strategies used to notably reduce the dose in medical imaging. Decreasing the pulse length of an industrial CT system allows for a faster acquisition process and a sparse scanning protocol enables fast reconstruction and less radiation exposure. We therefore apply these strategies to design new reconstruction methods in this thesis.

1.3 Scientific contribution

The scientific contribution of this dissertation is as follows:

- Maurice Debatin, *GPU-Accelerated Iterative Stochastic Limited-Angle Tomography with Non-Linear Regularization and A Priori Information*, Diploma Thesis, University of Mannheim, pages 1–179, 2011.
- Maurice Debatin, Piotr Zygmanski, Dzmitry Stsepankou, and Jürgen Hesser, *CT Reconstruction from Few-Views by Anisotropic Total Variation Minimization*, Nuclear Science Symposium and Medical Imaging Conference (NSS/MIC), IEEE, pages 2295–2296, 2012.
- Maurice Debatin, Dzmitry Stsepankou, and Jürgen Hesser, *CT Reconstruction from Few-Views by Higher Order Adaptive Weighted Total Variation Minimization*, Fully 3D, pages 134–137, 2013.
- Maurice Debatin and Jürgen Hesser, *Accurate Low-Dose Iterative CT Reconstruction from Few Projections by Generalized Anisotropic Total Variation Minimization for Industrial CT*, IOS Journal Of X-Ray Science and Technology, issue 23(6), pages 701–726, 2015.

As a consequence, some parts, formulations, expressions and results in this thesis are based on these contributions and have been adopted, copied, changed or extended without a direct quotation or citation of the respective publication.

1.4 Structure

In chapter 2, we present the current state of the art in Computed Tomography. We provide a general introduction and then we walk through the essential topics of iterative and analytical image reconstruction, presenting the most important scientific contributions of the last 59 years. Furthermore, we define, declare and describe all operations and methods necessary for the next chapters. Chapters 3, 4 and 5 are the core of this dissertation: We present three new regularization

functions for low-dose, under-sampled iterative CT reconstruction which successively improve the reconstruction results of the current state of the art techniques. Since these methods were evaluated at different reconstruction settings and different reconstruction algorithms were used as well, we evaluate all three methods in a common framework so as to enable an overall conclusion of this dissertation concerning the performance of the methods, see chapter 6. In chapter 7 we provide a general discussion and conclusion.

1.5 A note to the reader

If you read this dissertation on a PC using Adobe's Acrobat Reader it is extremely useful to know that you can jump back to the original position in the text using the key-combinations „ALT + ←" after you have followed a hyperlink.

Chapter 2

State of the Art in X-Ray Computed Tomography

2.1 Introduction

The history of Computed Tomography goes back to the pioneering work of Cormack [55] and Hounsfield [145] in the last century and is based on the findings of Röntgen in the beginning of the 19$^{\text{th}}$ century [293]. The concept of iterative CT reconstruction was established for **S**ingle **P**hoton **E**mission CT (SPECT) in the 1960's [33]. X-ray CT is the first imaging modality for non-destructive image reconstruction of the interior parts of an object from a sufficient number of X-ray projections. It is nowadays found in every modern radiology department, where it is used e.g. for screening, pediatric imaging and image-guided intervention [85].

Image Guided Radiation Therapy

In **I**mage **G**uided **R**adiation **T**herapy (IGRT), daily **C**one-**B**eam CT (CBCT) scans are acquired and hereby patients are exposed to harmful X-radiation [328]. Three-dimensional CBCT images contain anatomic and geometric information [269, 327] and CT numbers [103] (the CT number is a quantitative scale for describing radiodensity). The information is then used for dose-calculations and treatment plan re-optimizations [379, 136]. For each CBCT scan, the error of the patient setup can be up to 10mm in translation and 2 ° in rotation [340, 344]. These uncertainties can lead to an under-dose of the tumor or over-dose of the normal tissue. This risk is minimized by IGRT because CBCT enables a precise on-line positioning of patients [159, 160], since it aids the patient setup [315, 361, 245].
The main problem of IGRT is that patients are exposed to a considerable amount of excessive radiation dose in case of daily use of CBCT imaging [155, 59, 78]. There is a strong need to lower this dose, since especially younger patients are very sensitive to radiation [189]. High radiation doses result in a life-time cancer risk [322]. Furthermore, the risk caused by radiation dose yet increases when it is repeatedly used [32, 85]. For each scan, the approximate imaging dose prescribed to a patient is 5cGy at the skin and 10cGy at an organ [155]. While the dose of a single scan is negligible [272], in case of daily use of CBCT in IGRT over a treatment plan of usually 6 weeks (and 30–35 scans), the dose accumulates and therefore represents a potential risk.

Industrial CT

In the field of **N**on **D**estructive **T**esting (NDT), CT scans aid to investigate the objects for internal inspection of components. It is used for airport security, non-intrusive cargo scanning and especially for void crack and defect detection in industrial radiography.

The task of reconstructing projection images obtained by an X-ray Computed Tomography system can be accomplished by two conventional ways:

- The analytical approach, Filtered Backprojection [93], is the standard method in the field due to its fast execution time. The method will be described in section 2.3, where we will present common methods related to FBP as well.
- The iterative approach, presented in section 2.2. Iterative reconstruction can be accomplished non-statistically by algebraic models in section 2.2.3 or statistically, where a noise model for the raw measurements is the basis for the design of an iterative algorithm, see section 2.2.4.

2.2 Iterative reconstruction

The goal of iterative CT is to reconstruct a continuous object, such as parts of the human body or an industrial machine, from a finite set of measurements so as to obtain the inner structure, i.e. the **L**inear **A**ttenuation **C**oefficients (LAC)s of the cross-sections. The algorithms of iterative reconstruction are based on a discrete-to-discrete model. This means that both, the object and the reconstruction, are discretized. This is contrary to the analytical methods which are based on a linear continuous-to-continuous model. Iterative algorithms have many advantages over analytical ones: Arbitrary scan protocols such as helical or spiral trajectory paths and non-standard geometries of the CT scanner can be applied. Iterative algorithms enable a constricted reconstruction: A non-negativity constraint, for example, can be introduced in the objective function. The CT scanner only counts positive events. Ignoring the detector noise, a projection therefore cannot have negative LACs. Consequently, such a constraint improves the reconstruction in case of incomplete and noisy data [129]. Furthermore, for iterative algorithms, noise and other acquisition related effects which modify the projection values compared to an ideal measurement can be modeled and this further improves the reconstruction quality, compared to FBP. Unfortunately, the models of iterative CT can be very complex and many iterative algorithms are not yet fast enough for clinical or industrial applications. The computational burden of iterative CT is the main problem why commercial CTs still employ the classical analytical approach [264], namely Filtered Backprojection.
Iterative reconstruction can be classified into five categories. In each category, we want to provide all necessary definitions, functions and operations for the following chapters of the thesis. Furthermore, we want to present the common state of the art publications for each of the categories.
Iterative CT can be classified by these categories:

1. Object model in section 2.2.1: From the unknown continuous-space data that is to be reconstructed, a finite series of unknown coefficients has to be estimated from the data. This step involves object parametrization by a suitable choice of a (linear) basis function, yielding a discrete set of points. Common methods are presented in section 2.2.1.1. After a suitable image representation for the object has been found, digitally simulated phantoms (section 2.2.1.3), real patient data and physical phantoms (section 2.2.1.4) can be defined, based on their LACs (section 2.2.1.2).

2. System physical model in section 2.2.2: The system physical model mathematically describes the acquisition process of iterative CT. In other words: It relates the "ideal" (noise-free) measurements to the unknown object. It includes the data acquisition and the scan geometry of an X-ray CT system (section 2.2.2.1), different scan trajectories (section 2.2.2.2), the definition of the forward- and backprojection (section 2.2.2.3) and other system-specific parameters (section 2.2.2.4).

3. Non-statistical model in section 2.2.3: Based on the object and the system model, the unknown data can be reconstructed directly using non-statistical, algebraic models. Those methods are iterative but they do not model any physical effects, like projection noise or scatter.

4. Statistical model in section 2.2.4: The measurements acquired by the CT system vary around their ideal values due to physical effects, i.e. projection noise. Usually Poisson noise or

Gaussian noise is assumed since this is the main source for the discrepancy to the ideal measurements, see section 2.2.4.1. Statistical, iterative methods, try to accurately model the physics in X-ray CT e.g. projection noise, X-ray spectrum, scatter, detector blurring, transmission source extent or the focal spot size. Accurate physical modeling improves the image quality of the reconstruction a lot. Appropriate statistical models lower the image noise in the reconstruction and can remove streaking artifacts caused by under-sampling the object. Iterative reconstruction techniques therefore yield images of improved quality from low-dose scans, compared to the traditional analytical approach.

5. Objective function in section 2.2.4.1: Based on the statistical model, an objective function can be established. The objective function consists of a data-mismatch term providing for data accuracy. A regularization term can be included into the cost function. The regularization term is designed by including a priori information about the object (e.g. piece-wise smoothness of the noise-free data) and it constricts the data-mismatch term (for example to smooth solutions). All of them incorporate a priori knowledge about the scanned object into the reconstruction and are capable to remove noise and artifacts. Efficient balancing of the data and the regularization term is a difficult task.

6. Reconstruction algorithm in section 2.2.4.2: The cost function has to be either minimized or maximized (depending on the task) so as to estimate the image coefficient vector. The reconstruction algorithm includes an initial estimate, an update scheme and a stopping criterion for terminating the iterations when the final reconstructed image has been obtained or the algorithm has converged. The regularization term is included in the reconstruction algorithm. Publications for different types of regularization terms are presented in section 2.2.4.3.

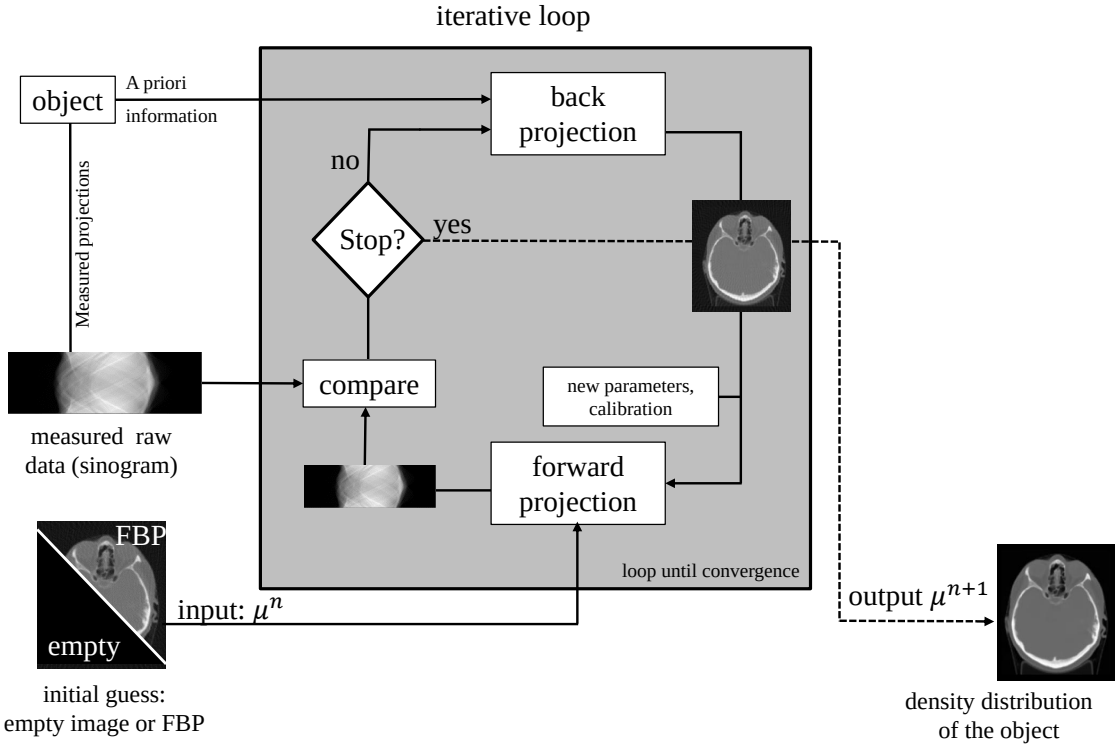

Figure 2.1: A schematic overview of the iterative reconstruction process according to [17]. In each iteration, a forward-projection (e.g. equation 2.9) is performed and compared to the measured data. If the current forward-projection agrees with the measured raw data, up to a certain degree, the iteration is stopped and the final result is obtained.

The process of iterative reconstruction is visualized in figure 2.1. The goal of iterative CT is to obtain the cross-sections of the object, i.e. the LACs of the data, based on the measurement projections. For this purpose, iterative algorithms usually try to (perfectly) match simulated projections with the available projection data by taking the physical model, the statistical model and the prior information into account. Simulated projections are obtained by the process of the forward-projection[1] (of the current image vector) in every iteration. In figure 2.1, one can see that iterative reconstruction is a three-step process which is repeated until the method has converged or a stopping criterion is met. Usually, one starts with an empty image or a result obtained by standard Filtered Backprojection. Depending on the reconstruction algorithm, the start image is initialized with zeros: $\mu_j = 0 \ \forall \ j \in I_i$, or very small numbers $\mu_j = 10^{-6} \ \forall \ j \in I_i$, see table 1 for the notation. In every iteration, artificial projection data is created by a forward-projection and this data is then compared with the measured projection data. Then, the update is computed and new parameters for the correction term are applied: The current sinogram is back-projected into the image domain to obtain the image estimate for the next iteration. If the algorithm has converged or the stopping criterion is fulfilled, the iteration stops and the final result is obtained.

2.2.1 Object parameterization

From the unknown continuous-space data that is to be reconstructed, a finite series of unknown coefficients has to be estimated from the data. This step involves object parametrization by a suitable choice of a (linear) basis function, yielding a discrete set of points. Common methods are presented in section 2.2.1.1. After a suitable image representation for the object has been found, digitally simulated phantoms (section 2.2.1.3), real patient data and physical phantoms (section 2.2.1.4) can be defined, based on their LACs (section 2.2.1.2).

2.2.1.1 Image representation

In iterative X-ray Computed Tomography the continuous object has to be transformed to the discrete data space and this step involves a discretization process and an image representation routine. The most intuitive image representation is probably a weighted sum of a finite set of spatial basis functions with a squared grid of cubic, uniform, non-overlapping pixels which cover the field of view: This is commonly referred to as the "natural pixel representation" [249, 36, 150], see figure 2.2.

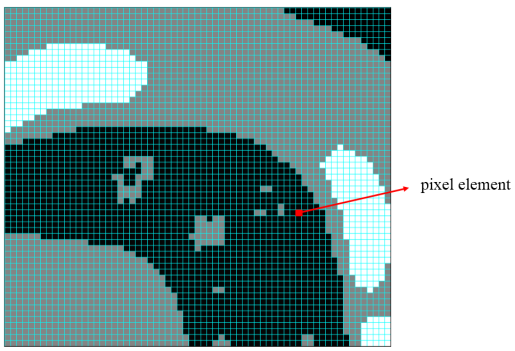

Figure 2.2: In this thesis we chose a natural square pixel image representation. This applies to images and volumes as well. Squared pixels or voxels are perfectly matched to the digital display.

Once the image representation is defined, we have a basis for the interpretation of the continuous object data. Then, the simulated phantoms and real data can be digitally represented. Another possibility is to approximate the continuous object by a linear combination of basis functions, where pixels are either represented by symmetric Kaiser-Bessel functions called blobs [354, 404, 210, 233] or B-splines [144, 131, 75].

[1]The forward- and backprojection operators will be later defined in section 2.2.2.3: These operators transform the image to the projection domain (forward-projection) and the projections to the image domain (back-projection).

Although these types of basis functions increase the computation cost, they are attractive since they can overcome the general problems of classical pixel-representations, like dampened high frequencies or the introduction of aliasing artifacts, because they provide a smoother image representation. It is known that the introduction of edge and aliasing artifacts for a natural pixel representation depends on the fineness of the grid [392]. Mollified pixel representations for iterative reconstruction are as smooth as blobs or B-splines but have a smaller support [255].
Furthermore, other basis functions have been under investigation, like Fourier series [9], circular harmonics [127, 296, 55], wavelets [191], square voxels [339], Dirac impulses or Gaussian functions [326, 125], organ-based basis functions [323, 44, 43, 101], polygons [51], polar grids [138] and tetrahedral meshes [320]. In this thesis, we use the square pixel (or voxel) basis representation illustrated in figure 2.2 since it is simple, perfectly matched to digital displays and leads to a maximally sparse system matrix[2].

2.2.1.2 Linear Attenuation Coefficients and CT numbers

The Linear Attenuation Coefficient, μ, is the signal of interest in Computed Tomography. It depends on the energy of the X-ray anode and the material. Based on the **M**ass **A**ttenuation **C**oefficients (MAC) which were taken from [152] and the density of the material, different LACs can be defined (by multiplying the MAC with the density of the material), see table 2.1. We use these values to carefully simulate realistic digital phantom data.

LINEAR ATTENUATION COEFFICIENTS OF DIFFERENT MATERIALS

energy (MeV)	material	Mass Attenuation Coefficient $\left(\frac{m^2}{kg}\right)$	density $\left(\frac{kg}{m^3}\right)$	Linear Attenuation Coefficinet, μ $\left(\frac{1}{mm}\right)$
2	iron	$4.2650 \cdot 10^{-3}$	7723	$3.294 \cdot 10^{-2}$
2	aluminum	$4.1800 \cdot 10^{-3}$	4500	$1.881 \cdot 10^{-2}$
2	air	$4.4470 \cdot 10^{-3}$	1.205	$5.360 \cdot 10^{-6}$
0.08	bone	$0.0178 \cdot 10^{-2}$	1850	$3.294 \cdot 10^{-2}$
0.08	fat	$1.8050 \cdot 10^{-2}$	920	$1.660 \cdot 10^{-2}$
0.08	muscle	$1.8220 \cdot 10^{-2}$	1040	$1.890 \cdot 10^{-2}$
0.08	water	$1.8350 \cdot 10^{-2}$	1000	$1.835 \cdot 10^{-2}$
0.08	air	$1.6610 \cdot 10^{-2}$	1.205	$2.000 \cdot 10^{-5}$

Table 2.1: Mass attenuation coefficients, the corresponding densities and Linear Attenuation Coefficients for different materials at energies of 80keV and 2MeV.

The Linear Attenuation Coefficient can be transformed to the corresponding **H**ounsfield **U**nit (HU) scale by the following formula:

$$\text{CT-number in HU} = 1000 \left(\frac{\mu - \mu_{\text{water}}}{\mu_{\text{water}} - \mu_{\text{air}}} \right) \tag{2.1}$$

The Hounsfield Unit (or CT-number) quantitatively measures the radiodensity [103] and this measure is suited to the CT scan of human anatomy, see table 2.2. It is defined for CT scanners that are calibrated with reference to water. A change of 1 HU represents a change of 0.1% of the LAC of water. Generalized models for accurate conversion from CT numbers to LACs for different densities and voltages of the CT scanner exist [7].

[2]The system matrix will be defined in section 2.2.2.3. It is a non-square matrix which holds the intersection lengths of the projection lines with the object.

CT NUMBERS OF COMMON SCALE

Substance	Hounsfield Unit
bone	+700 (cancellous bone) to +3000 (dense bone)
fat	-100 to -50
muscle	10 to 40
water	0
air	-1000

Table 2.2: The Hounsfield Unit for different substances.

Since the dynamic range of a medical image is typically too high to be perceived for a single image, contrast and image brightness have to be adapted so as to visualize different image features, e.g. the structures of the lung or soft tissue in figure 2.3. Let us assume the display interval is $[\mathrm{CT}_{\min}, \mathrm{CT}_{\max}]$. Then, the level is defined as the center of this interval: Level= $(\mathrm{CT}_{\min} + \mathrm{CT}_{\max})/2$ and the window is defined as the total span of this interval: Window = $(\mathrm{CT}_{\max} - \mathrm{CT}_{\min})$ (description taken from [62]). The window/level or "display range" can equivalently be expressed by the LAC intensities, as it is done in this thesis. Then, the display interval covers the range $[\mathrm{LAC}_{\min}, \mathrm{LAC}_{\max}]$.

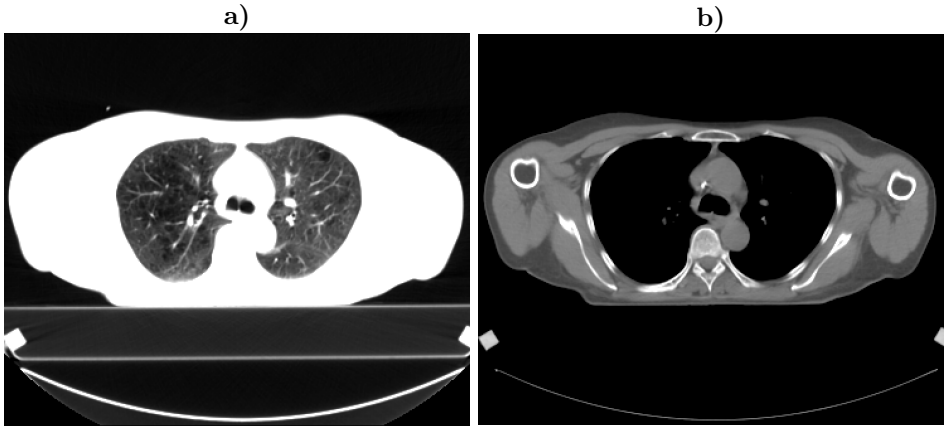

Figure 2.3: A human chest at different window/level settings (in CT numbers): a) lung (window: 692, level: -678), b) soft tissue (window: 693, level: 50).

2.2.1.3 Digitally simulated phantom data

Based on the Linear Attenuation Coefficient, realistic digitally simulated phantom data can be designed. The digitally simulated lung phantom in figure 2.4 a) and b) shows a cross section through the human chest, modeled at 80keV. The corresponding LACs are directly printed on the phantom. The phantom consists of 256×256 pixels and contains small bronchi. Some of them have a width of only a single pixel. Realistic human anatomy is modeled by introducing ribs or fat and muscle tissue.
We obtained the industrial CT engine data in figure 2.4 c) from the Volume library [2] and thresholded it such that the resulting LACs correspond to the given materials at 2MeV. This process also removes undesired noise and under-sampling artifacts. We simulated cracks and porosities of different sizes. The phantoms are labeled with the corresponding LAC values and the crack/porosity dimensions in pixels (width×height).
The Forbild head phantom in figure 2.4 e), f) and g) was designed as described in [387]. An energy of 80keV was selected and the phantom was normalized to the LAC of water at that energy (by multiplying each LAC by $\frac{0.01835}{\mathrm{mm}}$). The phantom is well-suited to evaluate the quality of the results at extreme low-contrast regions since it contains structures where the LAC intensity of an object compared to its background differs only by 0.026% (e.g. region 5). It also contains some high-contrast structures, like the left "ear" which are challenging to reconstruct, since it has dimensions of only a single pixel width.

For all phantoms we ignored the partial volume effect during acquisition and assumed that the objects' edges have a high acutance: They are discrete and have steep descents (abrupt changes of LACs). All phantoms are piece-wise constant.

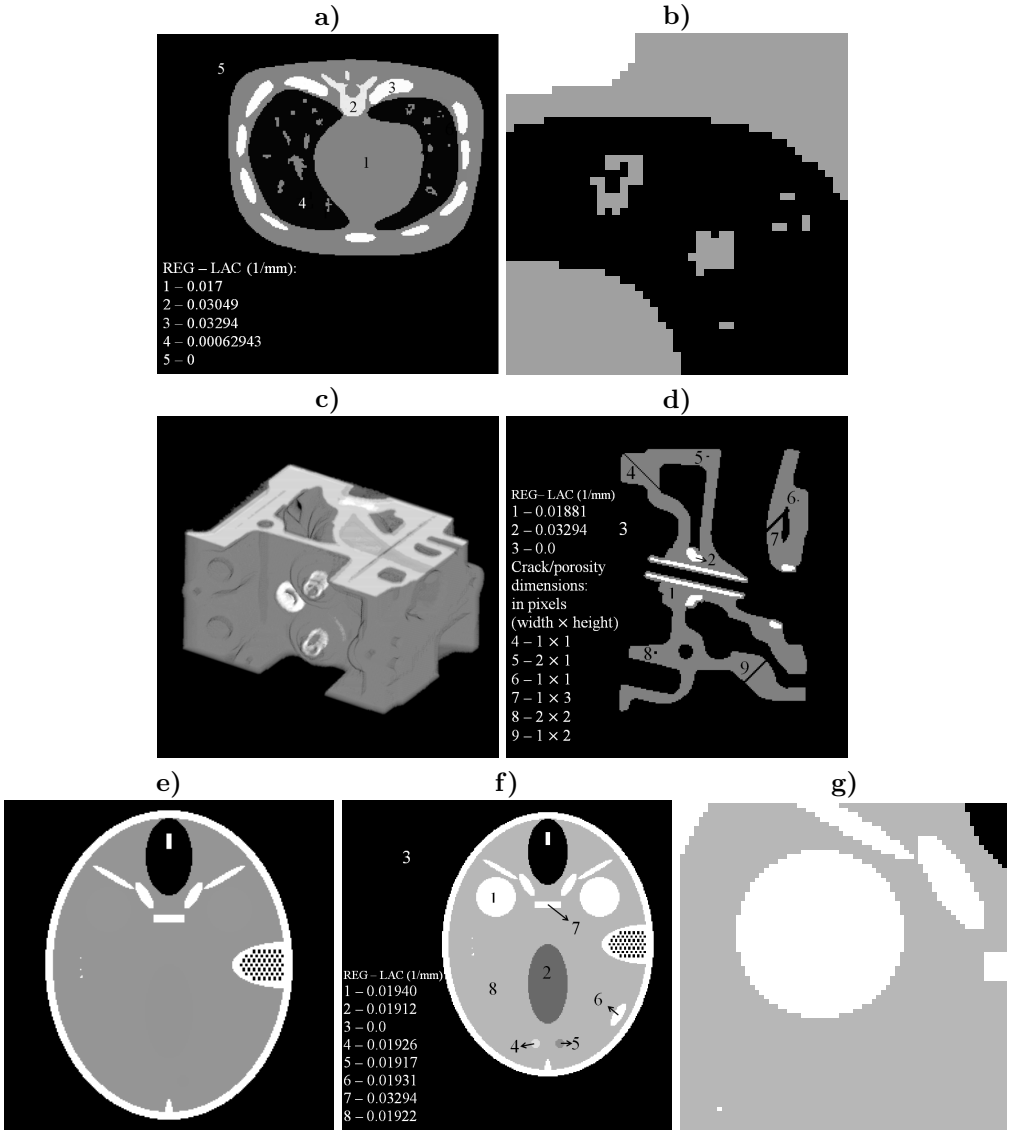

Figure 2.4: a) and b) A digitally simulated lung phantom with small bronchi (display range (in LAC intensities): $[0, 0.0329]$). c), d) A three-dimensional surface reconstruction of an industrial CT engine and a reconstructed slice of it with simulated cracks and porosities (display range: $[0, 0.0329]$). e) - g) The Forbild phantom, the phantom displayed at a different window/level (display range: [0.0190,0.0193]) and a cropped region of the phantom.

2.2.1.4 Patient data and physical phantoms

We reconstruct patient data acquired by an Elekta **X**-ray **V**olume **I**maging (XVI) CBCT, located at the University Medical Center in Mannheim. This makes it possible to evaluate the quality of the reconstruction algorithms in a real clinical environment. Figures 2.5 a) and b) show a reconstruction of a human head. The Catphan phantom in figure 2.5 c) is a real physical phantom and it is used for quality control in CT. It contains several modules, for example the resolution module with 21 **l**ine-**p**airs (lp), which can be used to measure the spatial resolution of the reconstruction result. The gauge accuracy is ± 0.5 line-pairs and is cast into epoxy and cut from 2mm thick aluminum sheets.

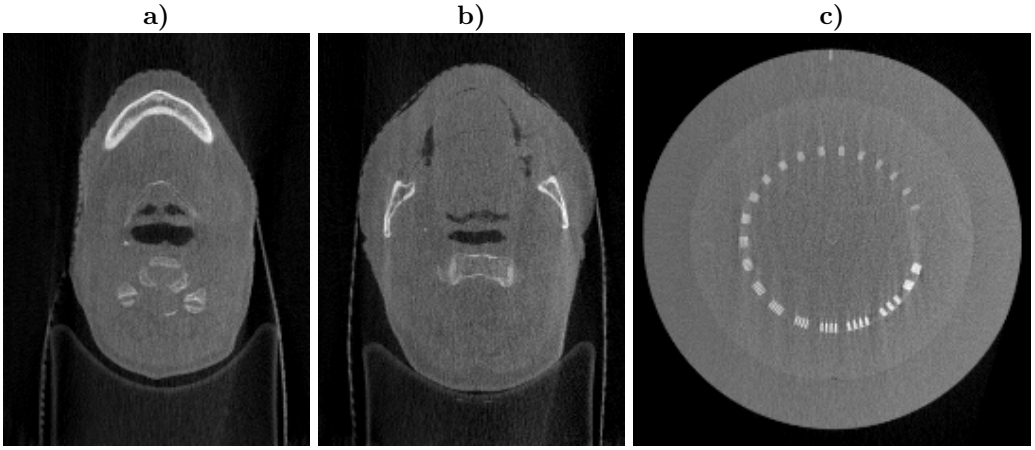

Figure 2.5: a) and b) A reconstruction of a human head from 360 projections. c) A reconstruction of the Catphan phantom from 360 projections.

In the last sections, we have parametrized the object by defining a well-suited image representation. We set up the pixel intensities by defining the LACs or CT-numbers in Hounsfield units and we defined digitally simulated phantoms and real data obtained from an Elekta XVI CBCT. Next, the system physical model for CT can be described.

2.2.2 System physical model

The system physical model mathematically describes the acquisition process of iterative CT. In other words: It relates the "ideal" (noise-free) measurements to the unknown object. It includes the data acquisition and the scan geometry of an X-ray CT system (section 2.2.2.1), different scanning trajectories (section 2.2.2.2), the definition of the forward- and back-projection (section 2.2.2.3) and other system-specific parameters (section 2.2.2.4).

2.2.2.1 Data acquisition and scan geometry

Since the invention of CT in the early 1970's, the principle of data acquisition has changed from parallel-beam and single detector over parallel-ray and multiple detector to partial fan-beam detectors with a small fan angle at about 10 degrees and then to fan-beam detectors with a fan angle of 40 to 60 degrees and longer detector arrays, covering the whole measuring field at once. The latest generation of CT scanners contains about 5000 detectors and has a stationary detector ring. Figure 2.6 a) shows a parallel-beam and b) shows a fan-beam scan geometry and the process of data acquisition in CT. The X-ray source travels on a circular orbit. The emitted x-ray photons, I_i, are attenuated as they travel through the discretized object $\mu_{x,y}$. Y_i are the detected number of photons on each detector cell for projection i, obtained at angle θ. A new coordinate system, (r, s), is obtained by rotating (x, y) by angle θ. The source-to-isocenter distance represents the distance to the origin of the x, y-cartesian grid. The source-to-detector distance is the space between the X-ray source and the detector. The signal of interest is the spatial distribution and intensity distribution of the attenuation values $\mu_{x,y}$.

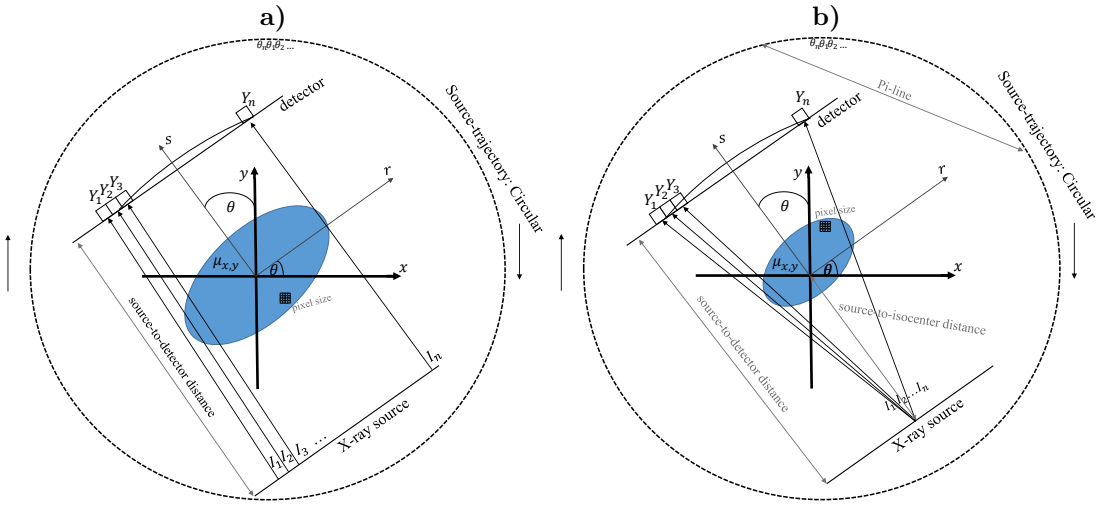

Figure 2.6: a) A two-dimensional parallel beam setup, as it is used in chapters 5 and 6. b) A two-dimensional fan-beam CT configuration. The corresponding three-dimensional version is straightforward to derive.

The parallel ray geometry presented in figure 2.6 a) is used in chapters 5 and 6. The fan beam geometry (two-dimensional case) of figure 2.6 b) can directly be translated to a cone-beam geometry (three-dimensional case), which is used in chapters 3 and 4. The interested reader is referred to section 2.4 to obtain more details about other CT scanning configurations.

2.2.2.2 Scan trajectories

In case of a circular arc trajectory of the CT scanner, the "Tuy condition" is violated. The Tuy condition requires that every plane which intersects the object must intersect the focal trajectory as well [347] and this is not the case for a circular orbit. As a consequence, (cone-beam) artifacts are introduced in the reconstruction results as it is shown in [243, 386]. [403] propose to use a trajectory that consists of two concentric arcs, where each arc is shaped like a "C". The system is called C-arm. The authors provide a mathematically exact cone-beam CT reconstruction algorithm. This trajectory satisfies Tuy's sufficiency condition but is not well populated with PI-lines (a PI-line is the line connecting two source points on the trajectory path, see figure 2.6 b). Therefore, [389] provide a non-PI-line based reconstruction method. As an alternative, helical or spiral trajectories have been proposed for exact reconstructions [184, 185, 405].
In case of a circular trajectory, at least a region-of-interest in the object can be exactly and stably reconstructed: [254] use short scan arcs of different angular directions, e.g. 80 views at $\theta = 0°$, $45°$ and $90°$ for the acquisition. They show that exact reconstruction is possible if a least every line passing through the **R**egion **O**f **I**nterest (ROI) intersects the vertex path in a non-tangential way [254].

2.2.2.3 Forward- and Backprojection

Before we define the forward- and back-projection operators, we give a short introduction to the essential physics for Computed Tomography. Hereby, X-rays and their interaction with matter play the most important role.

X-rays and their interaction with matter

X-rays are electromagnetic waves and they have a wavelength of 0.01 to 10nm, frequencies in the range of $3{\cdot}10^{16}$Hz to $3 \cdot 10^{19}$Hz and energies in the range of 100eV to several MeV. Electromagnetic radiation consists of photons and their energy is proportional to their wavelength:

$$E = \frac{h \cdot c}{\lambda} = h \cdot v, \tag{2.2}$$

where $c = 3 \cdot 10^8 m/s$ is the speed of light, $h = 6.6261 \cdot 10^{-20}$Js is Planck's constant and v is the wave frequency.
X-rays cause ionizing radiation (radiation that carries enough energy to free electrons from atoms), which is extreme harmful to human cells. The interaction with matter is a statistical process, which can happen in three different ways: Through photo absorption (dominant interaction mechanism), Compton scattering and Rayleigh scattering. The attenuation length of the rays depends on the energy, as shown in figure 2.7.

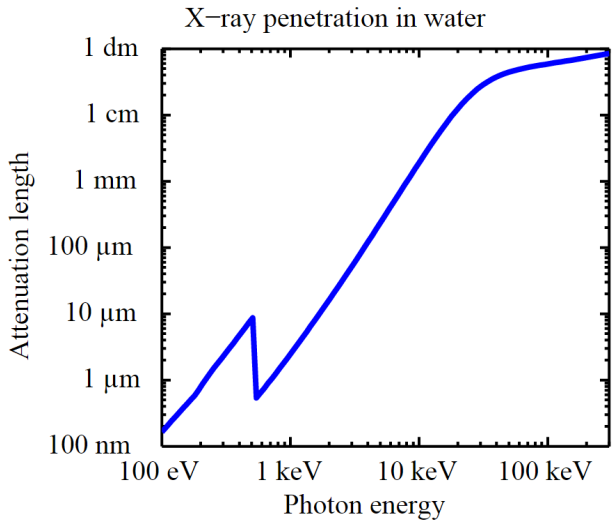

Figure 2.7: Attenuation length of X-rays in water as a function of the photon energy. One can clearly see the oxygen absorption edge at 540eV.

Let us imagine the X-ray beam travels through an infinitesimally thin object μ of thickness ds. The intensity of the ray of a constant photon energy before it enters the object is I and the intensity of the outgoing ray is $I + dI$. The intensity is defined as the energy per time unit and the energy is proportional to the number of emitted photons. The Linear Attenuation Coefficient is therefore defined as:

$$\mu = -\frac{\frac{dI}{ds}}{I} \tag{2.3}$$

Integration of equation 2.3 over the thickness s of the object leads to:

$$I_s = d_0 e^{-\left(\int_0^s \mu(s')\right)}, \tag{2.4}$$

where d_0 are the number of photons leaving the X-ray source. Equation 2.4 is the basic formula of CT. Next we want to further specify this formula, i.e. we want to find a representation for the LACs, $\mu(s')$, in equation 2.4.

Forward projection

From figure 2.6 a) the following general formulas can be derived:

$$\begin{bmatrix} x \\ y \end{bmatrix} = \begin{bmatrix} \cos(\theta) & -\sin(\theta) \\ \sin(\theta) & \cos(\theta) \end{bmatrix} = \begin{bmatrix} r \\ s \end{bmatrix} \tag{2.5}$$

and

$$\begin{bmatrix} r \\ s \end{bmatrix} = \begin{bmatrix} \cos(\theta) & \sin(\theta) \\ -\sin(\theta) & \cos(\theta) \end{bmatrix} = \begin{bmatrix} x \\ y \end{bmatrix} \tag{2.6}$$

Based on equation 2.4, for a fixed angle θ and a constant photon energy, the measured intensity profile is given by:

$$I_\theta(r) = d_0 e^{-\left(\int_{L_{r,\theta}} \mu(r\cdot\cos(\theta)-s\sin(\theta), r\sin(\theta)+s\cos(\theta))\ ds\right)}, \tag{2.7}$$

where d_0 are the number of photons leaving the source and $L_{r,\theta}$ is the line that creates an angle, θ, with the y-axis at distance r from the origin, see figure 2.6 a). Vector r basically represents the detector coordinate. The notation is taken from [65].
Each intensity profile for the different angles is then converted into a logarithm-transformed attenuation profile by the Radon transform:

$$p_\theta(r) = \Re(\mu(x,y),\theta) = -\frac{ln(I_\theta(r))}{d_0} = \int_{-\infty}^{\infty} \mu(r\cos(\theta) - s\sin(\theta), r\sin(\theta) + s\cos(\theta))\ ds \tag{2.8}$$

$p_\theta(r)$ is the projection of the Linear Attenuation Coefficient, $\mu(x,y)$, along a fixed angle θ for the rotated coordinate system (r,s). By stacking together all projections, $p_\theta(r)$, for a varying angle θ, e.g. from 0 to 2π, we obtain the sinogram: $p(r,\theta)$. The Radon transform, $\Re(\cdot)$, is periodic in θ with period 2π and symmetric in θ with period π. The Radon transform is the simplest mathematical formulation to obtain parallel-beam projections from an object since it does not consider any physical properties of the acquisition geometry like the pixel size of the discretized object or the detector bin scale. Furthermore, the Radon transform is very imprecise and cannot yield an accurate forward model. To consider these and other physical properties of the acquisition process, let us reformulate equation 2.7 and provide its discrete counterpart:

$$Y_i = d_0 \cdot e^{-\left(\sum_{j\in I_i} l_{ij}\mu_j\right)} \tag{2.9}$$

where Y_i are the detected number of photons for projection i. l_{ij} is a matrix containing the intersection lengths of the projection line, i, at a given angle θ, with the LACs of the object, μ_j. μ_j is the signal of interest, where j is the pixel position (here denoted in vector form). Y_i is called the **sinogram** and l_{ij} the **system matrix**. The log converted sinogram reads as follows:

$$y_i = -\frac{ln(Y_i)}{d_0} = \sum_{j\in I_i} l_{ij}\mu_j \tag{2.10}$$

Equations 2.9 and 2.10 are called the **forward projection**: Hereby, the discretized object is transformed to the projection domain. This is visualized in figure 2.8 which shows the forward projection of a phantom containing a simple 2×2 pixel wide square and a human head. The top right image explains why the projections are called "sinogram": It has a sinusoidal shape. The complete sinogram can be obtained by stacking together all one-dimensional projection images from the different viewing angles. In this case, 400 uniformly distributed projections were acquired in the interval $[0,\pi]$.

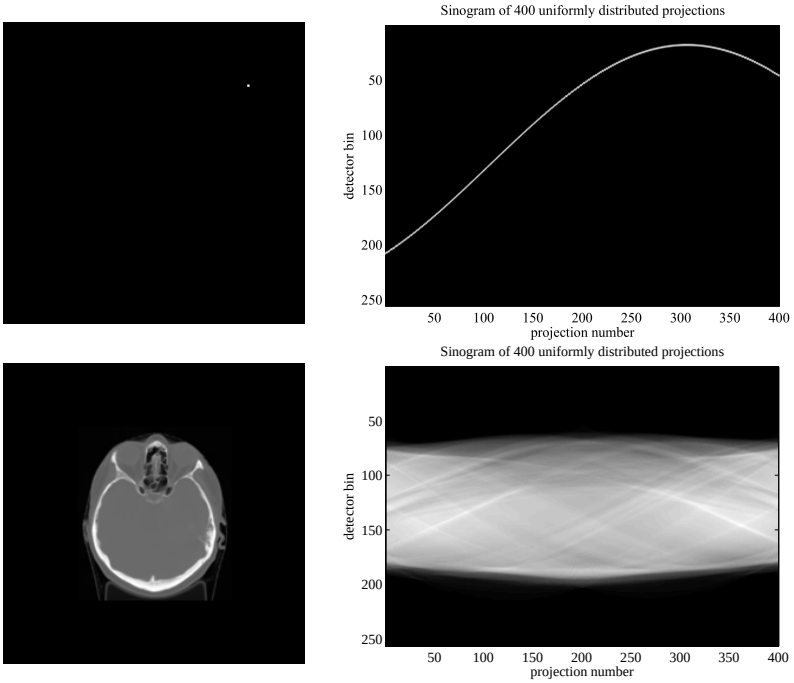

Figure 2.8: Sinograms obtained through the forward projection in equation 2.10. 400 uniformly distributed projection views were used.

As a matter of principle, there are two ways to obtain the parameters for the system matrix: One could pre-calculate the expected system parameters prior to the iterative reconstruction, as it is done in chapters 5 and 6 in this thesis. This strategy is highly accurate but it consumes a lot of memory and can therefore be performed solely for two-dimensional scenarios. "On-the-fly" computation, as it is done in chapters 3 and 4 in this thesis, constitutes an alternative which is not that time consuming, since the parameters are calculated in each iteration at the time when they are needed. This mechanism suits to the three-dimensional case. However, in this case the accuracy is inversely proportional to the execution speed.
For iterative CT reconstruction, an accurate model for the measurement system improves the reconstruction due to a better match of the artificial sinogram (obtained through the forward projection in each iteration) and the acquired raw data. As a consequence, better correction terms for the next update can be obtained. However, the X-ray CT setup leads to huge number of parameters to estimate. For example, in a three-dimensional cone-beam configuration, the system matrix can have a size of several Petabytes. This is intuitively clear, since the matrix stores all intersection lengths for each source angle, θ, and detector bin Y_i. If we assume a 32-bit data accuracy, a two-dimensional detector containing 512×512 detector bins, a three-dimensional discretized volume of dimensions 512×512×512 voxels and $\theta = 512$ projection angles, the matrix would have a size of 64 Petabytes. This matrix is far too large to store. Thus this matrix has to be computed "on-the-fly" for each projection angle separately. If the projection angles and the image size are reduced, the matrix fits into the memory. For example, for the two-dimensional case where the discretized object has dimensions of 256×256 pixels and the detector consists of 256 bins, 32bit data accuracy is assumed and 40 projections are acquired, the system matrix would have a size of only 2560 Megabytes. This easily fits into the memory of modern **G**raphics **P**rocessing **U**nits (GPU)s. For a parallel-ray geometry the projection views can be processed individually and therefore the reconstruction can be parallelized easily but for a cone-beam geometry the system-matrix cannot be partitioned since the slices depend on each other. **A**dvanced **S**ingle-**S**lice **R**ebinning (ASSR) [173] is a method which transforms the projections from a cone-beam to a parallel beam geometry and then the slices can be processed in parallel. An alternative is to group the projections into subsets and then parallelize the reconstruction [153]; this is called the **O**rdered **S**ubsets (OS) approach. Unfortunately, the algorithm does not converge to a unique solution, but to different local optima which are related to each subset.

The system matrix can consider the physical properties of the geometry and acquisition process. This includes the detector bin scale, the pixel size of the object and different acquisition geometries like fan and cone-beam and source trajectories like circular, spiral or helical paths. Precise modeling is important since each parameter influences the accuracy and the spatial resolution of the final result. For example increasing the pixel size decreases the noise, but also leads to a reduced spatial resolution of the resulting image.
Up to now, many solutions have been proposed to accurately compute the intersection lengths l_{ij} of equation 2.10. There are forward projection methods for parallel-beam geometry [27, 302, 302, 27, 300, 234, 143] and cone-beam geometry [24, 63, 404, 233, 105, 289, 10]. All methods balance between computational complexity and accuracy.
There are **source-driven** methods based on ray-tracing approaches [310, 170, 157] and methods which derive the intersection lengths from measurements based on point-source acquisitions [266, 345] or simulations [4]: The authors use the system response function to model the spatially variant component of the intersection length. Source-driven approaches do not suffer from introduction of additional noise if the size of the voxels is too large and the sampling thereby too coarse. The disadvantage is that they are computationally expensive.
Distance-driven approaches are more accurate than source-driven methods [63]. They map the horizontal and vertical boundaries of the image voxels and detector cells onto a common plane and then approximate their shapes by rectangles: **S**eparable **F**ootprint (SF) approaches like SF-TR use **T**rapezoid and **R**ectangle functions and approximate the voxel footprint as two-dimensional seperable functions with trapezoid and rectangle functions in the transaxial and axial directions, respectively. In case the voxel footprint is approximated as two-dimensional seperable functions with trapezoid functions in both directions, transaxial and axial, the method is called SF- **T**rapezoid **T**rapezoid (SF-TT). SF-TT projectors provide the most accurate solution for the forward projection up to now [219].
The system response can be modeled by Monte Carlo simulation as well and this can be established by directly incorporating all physical effects into the system matrix [349, 282].
To test the algorithm efficiency it is practicable to apply an inverse-crime study, as discussed in [53, 177]. Hereby, the same forward projector (and system matrix) is used to generate the projections from the given discrete data and the same projector is used to reconstruct them. This is done in this dissertation.

Back projection

The objective of CT is to reconstruct the LAC-distribution and LAC-intensity based on the acquired sinogram. An intuitive way to obtain μ would be to invert equation 2.10 and back-project the image from the projection domain to the image domain. However, the inverse of l_{ij} does not exist: In Computed Tomography, the number of projection views does typically not equal the number of detector bins and therefore the system matrix is non-square. If it was a square matrix (in case the detector bins equals the number of projections), the matrix would not be invertible, since it does not have a full rank.
A possible solution to this problem is to compute the pseudo-inverse:

$$\mu_j = \sum_{j \in I_i} \left(l_{ji} l_{ij}\right)^{-1} l_{ji} y_i \tag{2.11}$$

$\left(l_{ji} l_{ij}\right)^{-1} l_{ji}$ is the Moore-Penrose pseudo-inverse [276], where l_{ji} is the adjoint of the system matrix, $(l_{ji} l_{ij})$ represents the Backprojection and $\left(l_{ji} l_{ij}\right)^{-1}$ represents a deblurring (ramp) filter. The problem with the pseudo-inverse is that the pre-computation of the required **S**ingle **V**alue **D**ecompositions (SVD)s is hard since they depend on the object (and different attenuation coefficients therein). Thus, for realistic models, pseudo-inverse methods are impractical.
To obtain μ_j in equation 2.10, one therefore has the following possibilities:

- Simple Back-projection: Intuitively one can obtain the LACs by the following procedure: For a particular line (r,θ) in equation 2.8, assign the value of the sinogram, $p(r, \theta)$, to all its corresponding points (x, y) along that line. Then repeat this for different angles in the interval $[0, \pi]$.

  $$b(x, y) = B\left(p(r, \theta)\right) = \int_0^{\pi} p(x \cos(\theta) + y \sin(\theta), \theta)\ d\theta \tag{2.12}$$

  We obtain the back-projected image, see figure 2.9 for an example. The back-projection is blurred. This can be seen in the reconstructions of the dot and the human head. This straightforward way is therefore not a good solution to obtain the desired LACs.

- Filtered Backprojection or the inverse Radon transform: Apply an analytical Filtered Backprojection in the Fourier domain as described in section 2.3. The problem with filtered Backprojection is that it introduces artifacts in case of few projection data and the noise removing capabilities of FBP are rather weak.

- The approximate inverse maps the measurement data to a regularized version of equation 2.10 of the first kind [221]. In this way a reconstruction kernel can be pre-computed from an auxiliary problem which can then be used to compute the approximate solution of the inverse problem. The particular thing about this method is that the solution is independent of the data. For the regularization, mollified versions of the minimum norm solution are computed. It is a general version of the Tikhonov-Phillips regularization [343]. The method was later improved to reduce the computation effort and extended to three-dimensional cone-beam CT [222].

- Algebraic reconstruction methods presented in section 2.2.3 neglect the physical effects of the acquisition (like a noise model for the projections) and analytically solve the huge system of linear equations so as to obtain the LACs.

- Iterative reconstruction algorithms are based on a statistical noise model and an objective function (section 2.2.4.1), a reconstruction algorithm (section 2.2.4.2) which can be regularized (section 2.2.4.3). These methods are up to now most promising and they can produce the best image quality among the other possible methods.

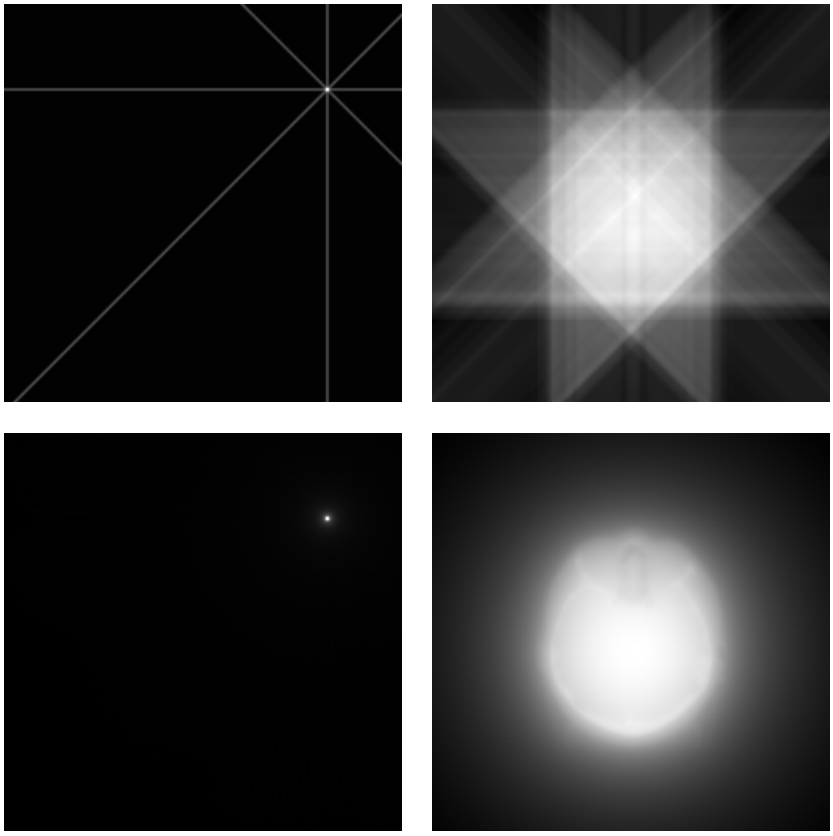

Figure 2.9: Simple back-projection (equation 2.12) of a dot and a human head in case of 4 (top) and 400 (bottom) uniformly distributed projection angles for a 2×2 pixel wide square (left) and a head (right).

2.2.2.4 Other system-specific parameters

Accurately modeling the physics in iterative reconstruction [256] further improves the reconstruction results. The finite detector and X-ray focal spot size influence the spatial resolution. Footprint approaches, such as the distance driven projector (SF-TR or SF-TT), depend on the voxel basis function. As a consequence, they already take into account the geometry of the beam and they model the finite detector size (and the ray-induced blurring on the detector) in contrast to ray-driven approaches which introduce Moiré patterns [63]. The focal spot of the X-ray tube has, of course, only a finite size and this has to be modeled, see for example [216] for details.
Detector crosstalk and afterglow leads to blurring and this blurring also spreads out to other views. [339] convolve the sinogram with a kernel and enlarge the detectors into overlapping virtual detectors in the forward model so as to simulate detector crosstalk and after glowing [396]. This results in reconstructions with a higher spatial resolution.
Adaptive bowtie filters are used to shape the X-ray beam. They allow for a uniform distribution of photon flux and they remove lower energy photons which would else lead to a higher dose, as they do not reach the detector cells. As a result, the X-ray photon energy is different for each ray and this fact can be included in the model [346].
In [256], it is stated that X-ray sources produce a polychromatic spectrum. However, most of the methods assume a monochromatic spectrum for simplicity. If the spectrum is not modeled correctly, this leads to beam hardening effects (hereby low-energy photons are removed from the beam) and image artifacts such as cupping and shadows are introduced in the result [237]. Algorithms which consider a polychromatic spectrum of the X-rays are for example [65, 86, 87]. These methods divide the spectrum into a number of energy bins and then they compute each interaction within a voxel for each bin [3]. As a result, these methods can suppress beam hardening artifacts while providing low noise in the reconstructed images.
Without a scatter correction, the image quality worsens due to the detection of "undesired" X-rays

which are not directly related to the current intersection path of the ray with the object. Up to now, only few papers include a scatter estimation term in the iterative reconstruction [89, 167, 359]. With increasing detector size, modeling the scatter contribution is more and more important. One potential way to measure the scatter contribution part is to estimate it from the projection data and then remove it by deconvolution [303] or to estimate it using accurate Monte Carlo simulation techniques [393].

2.2.3 Non-statistical, algebraic models

The **A**lgebraic **R**econstruction **T**echnique (ART) [116], also referred to as the Kaczmarz method [175], is the simplest form of iterative reconstruction and it assumes that the cross-sections of the object can be expressed by a linear array of unknowns. Therefore, the reconstruction problem is defined as a system on linear equations as well. After setting up an appropriate object parametrization and defining the system physical model, these equations can be solved. Intuitively, the system of equations is huge and therefore ART methods are computationally demanding: For a 512^3 volume, scanned at 512 angles with a two-dimensional detector consisting of 512×512 elements, 512^5 equations would have to be solved to obtain the reconstructed image. As a matter of principle, ART methods are not based on a statistical model and they theoretically require only about half the number of projections for an accurate reconstruction, compared to the FBP methods [123]. Since ART methods are computationally demanding, methods were proposed to overcome this problem: [141] showed that ART can be made computationally efficient. The **S**imultaneous **ART** [5, 112] (SART) processes the complete sinogram at once and can provide a reasonable reconstruction result in only one iteration. The method has a faster convergence rate than standard ART and is controlled by a relaxation parameter. [244] provides a fast implementation of SART where the objective function is minimized using a steepest descent method [279] with an adaptive step size. The **O**rdered **S**ubset **SART** (OS-SART) [353] uses the principle of ordered subsets, which was previously introduced for the Maximum Likelihood algorithm [153] to further speed up the computation of SART. Ordered subsets methods group projection data into an ordered sequence of subsets and then process these subsets in parallel.
There are many different modifications of ART. Block-iterative projection methods are familiar with ART [45, 84] and have been proposed to solve a large system of equations. Coordinate-descent methods such as the Gauss-Seidel algorithm update sequentially individual image voxels [339].

2.2.4 Statistical models

Statistical iterative methods try to accurately model the physics in X-ray CT, e.g. projection noise, X-ray spectrum, scatter, detector blurring, transmission source extent or the (finite) focal spot size [100, 260, 14, 280, 13, 390]. Appropriate statistical models can lower the image noise in the reconstruction. They can improve the quantitative accuracy, spatial resolution, contrast and the **S**ignal to **N**oise **R**atio (SNR) and they can remove streaking artifacts caused by under-sampling the object. Iterative reconstruction techniques therefore yield images of improved quality from low-dose scans, compared to the traditional analytical approach [339, 133, 316, 318, 319, 208, 278, 110, 181, 385, 67, 242, 147].
Unfortunately the CT measurement statistics are very complicated, particularly at low doses. For example there are variations in the incident photon flux, X-ray absorption or scattering, energy-dependent light production in the scintillator, shot noise in the photo diodes and electronic noise in the readout electronics [358, 362, 204]. To model these effects requires additional computation due to the higher algorithm complexity. Based on a statistical noise model, a cost function can be set up, see section 2.2.4.1. The cost function consists of a data term, which cares for the data accuracy, or data fit: It constrains the estimation of the Linear Attenuation Coefficients to solutions that fit the measured data. Either the distance between the simulated projections and the measured projections is minimized (as measured by the **M**ean **S**quared **E**rror (MSE) of the minimum ℓ_2 least-squares norm), or the probability that the simulated projections match the measured projections up to a certain value is maximized, as measured by the likelihood. Prior knowledge of the scanned object (e.g. piece-wise homogeneity of the noise-free data) can be included in the cost function by a regularization function. This function typically cares for the non-idealities of the scanner

(e.g. noise) or the acquisition process (e.g. under-sampling artifacts due to under-sampling of the object) and tries to remove them during the optimization. The reconstruction algorithm is deduced from the derivative of the cost function and it tries to find a unique solution to the problem to be solved. The algorithms are sometimes manually modified (by changing the numerics) to fit to the particular issues.

2.2.4.1 Noise models and their corresponding cost functions

As we have discussed before, including statistics about the acquisition process into the reconstruction notably improves the resulting image quality. Many statistical properties can be considered. Among them, a suitable noise model for the raw measurements is the most important one.

The noise model

The forward projection in equation 2.9 can be extended so as to include the physical aspects of the acquisition process and the physics of the CT system. The most important part is an appropriate noise model. For transmission CT, it is realistic to assume the following statistical model for the raw measurements, which are obtained by the Lambert-Beer law. For a mono-energetic X-ray source we define:

$$Y_i = d_0 e^{-\left(\sum\limits_{j \in I_i} l_{ij}\mu_j\right)} + s_i + n_i, \tag{2.13}$$

where Y_i is the projection data with projection subscript i. l_{ij} is the length of the projection line that intersects pixel j and μ_j are the linear attenuation coefficients. d_0 is the number of initial photons, which was found in the range of 10^5 to 10^7 for clinical scanners [355, 74, 204, 261]. s_i respresents possible additive contributions, such as Compton scatter and n_i is the probability distribution of the noise. Recall, since the logarithm is monotonic, it can be applied to equation 2.13 leading to a simpler, linear model. Ignoring the scatter term, s_i, we write:

$$y_i = -ln\left(\frac{Y_i}{d_0}\right) = \sum_{j \in I_i} l_{ij}\mu_j + n_i' \tag{2.14}$$

The logarithm changes the noise contribution n_i to n_i' [256]. This operation, however, does not change the noise characteristics quite much. This was shown on repeated phantom experiments, for example for low-dose calibrated CT.
The projection data after the transformation into the log-domain is found to follow approximately a Gaussian distribution with a non-linear dependence between the sample mean and sample variance, i.e., the noise is signal-dependent [223]. We can therefore assume that $n_i' \approx n_i$ [256]:

$$n_i' \approx n_i \sim N(0, \sigma_i^2) \tag{2.15}$$

where $N(\cdot)$ is the normal distribution with 0 mean and a standard deviation of σ_i. According to the Central Limit Theorem, the normal distribution is an excellent approximation to the Poisson distribution in case of $d_0 \geq 1000$, as empirical experiments have shown [287].
Alternatively to additive Gaussian noise, we can therefore apply the Poisson noise directly to the log-converted data and define:

$$y_i = POISSON\left(\sum_{j \in I_i} l_{ij}\mu_j\right), \tag{2.16}$$

where $POISSON(\cdot)$ denotes the Poisson distribution.
Accurate noise modeling can be achieved by not converting the projection data into the logarithm domain. Then, the Poisson noise corrupted sinogram is defined as:

$$Y_i = POISSON\left(d_0 e^{-\left(\sum\limits_{j \in I_i} l_{ij}\mu_j\right)}\right), \tag{2.17}$$

Let us now assume we have a scan without an object by setting $\mu_j = 0,\ \forall\ j \in I_i$. Equation 2.17 then reads as: $Y_i = POISSON\,(d_0)$. Since the variance of a Poisson Distribution equals its mean, the standard deviation of the Poisson distribution is equal to the square root of the average number of events and therefore a relation of the Signal to Noise Ratio of the projection data (where no object was measured) to the number of incident photon counts, d_0, exists:

$$SNR = \frac{d_0}{\sqrt{d_0}} \sim \sqrt{d_0} \tag{2.18}$$

The measurements presented in [332] and summarized in table 2.3 show the relation of the SNR to the tube current for an Elekta XVI CBCT and a water phantom experiment. In case of air, the dose is significantly higher for each SNR.

SNR AND SOURCE CURRENT OF AN ELEKTA XVI CBCT

SNR	d_0	approx. dose per view of an Elekta CT [mAs]
2236	$5.0 \cdot 10^6$	1.0
1000	$1.0 \cdot 10^6$	0.7
707	$5.0 \cdot 10^5$	0.5
316	$1.0 \cdot 10^5$	0.25
223	$5.0 \cdot 10^4$	0.2
158	$2.5 \cdot 10^4$	0.15
100	$1.0 \cdot 10^4$	0.1

Table 2.3: SNR and source current of an Elekta XVI CBCT. The table was taken from [332].

Let us further specify equation 2.16. Due to the interaction of ionizing radiation with matter, the detected number of photons, y_i, obey Poisson statistics. Thus, the detected number of photons represent a Poisson-distributed random variable and the expected value:

$$y_i' = \sum_{j \in I_i} l_{ij}\mu_j' \tag{2.19}$$

is again Poisson distributed and statistically independent. μ_j' represents the expected value of the LACs, μ_j. Therefore, the probability of detecting y_i photons, given the expected value y_i' is obtained through the multiplication of all single probabilities over all projection views:

$$POISSON(y_i|y_i') = P(y_i|y_i') = \prod_{i \in J_j} \frac{\left(\sum\limits_{j \in I_i} l_{ij}\mu_j'\right)^{y_i}}{y_i!} e^{\left(-\sum\limits_{j \in I_i} l_{ij}\mu_j'\right)} = P(y_i|\mu_j') \tag{2.20}$$

Equation 2.20 is the Poisson distribution for the measured log-converted projection data or the likelihood of obtaining y_i, given y_i'.
The benefit of applying the logarithm to the noisy measurement projections is huge: One obtains a linear model and therefore one can apply a linear reconstruction algorithm which yields a unique solution. However, for negative values of y_i, the logarithm leads to an undefined expression. This is the case for a very high contribution of the electronic noise or in case of photon starvation. Fortunately, the detector noise can be neglected since in practical applications, its contribution is smaller than the signal of interest [377]. Furthermore, in clinical routine or in the field of industrial CT, photon starvation is not an issue, since the dose is typically quite high and there are enough photons hitting the detector cells. Another problem of applying the logarithm to the projections is the task of propagating the noise through the logarithm itself, e.g. in equation 2.16. This operation definitely changes the noise characteristics, since it changes the exact distribution of the log-domain noise. While this fact is negligible for high dose scans, for low dose scans and in case of accurate physical modeling of the log-converted projection data, the noise equivalent counts have to be found [257].

Due to the disadvantages of the log-conversion of the projection data, a more suitable and physically more accurate way is to formulate the Poisson distribution on the basis of the non-log converted projection data. Analog to equation 2.20 we then obtain:

$$POISSON(Y_i|Y_i') = P(Y_i|Y_i') = \prod_{i\in J_j} \frac{\left(d_0 e^{-\left(\sum\limits_{j\in I_i} l_{ij}\mu_j'\right)}\right)^{Y_i}}{Y_i!} e^{\left(-d_0 e^{-\left(\sum\limits_{j\in I_i} l_{ij}\mu_j'\right)}\right)} = P(Y_i|\mu_j'), \tag{2.21}$$

where Y_i' is the expected value for the non-log converted data.
Equation 2.21 is the Poisson distribution for the measured non-log-converted projection data or the likelihood of obtaining Y_i, given Y_i'. In iterative CT, we are interested in the expected sinogram that matches the observed sinogram most likely, or differently formulated: We want to find the Linear Attenuation Coefficient, μ_j', that best fits the sinogram data by including all available information about the physical model, the statistical model and the prior information about the object. To ease the computation, we take the logarithm of the likelihood, since it is a mathematically challenging task to compute the derivatives of the product sums. This operation is valid since the logarithm is a strictly monotonous function and it will not change the location of the maximum. We obtain the following log-likelihood function for the log-converted projection data:

$$L(y,\mu') = ln\left(L(y_i,\mu')\right) = \sum_{i\in J_j} y_i \ln\left(\sum_{j\in I_i} l_{ij}\mu_j'\right) - \ln(y_i!) - \sum_{j\in I_i} l_{ij}\mu_j' \tag{2.22}$$

and after obeying the constant term we define:

$$L(y,\mu') = \sum_{i\in J_j} y_i \ln\left(\sum_{j\in I_i} l_{ij}\mu_j'\right) - \sum_{j\in I_i} l_{ij}\mu_j', \tag{2.23}$$

For the non-log converted measured projection data we obtain the following analogous log-likelihood function [202, 200]:

$$L(Y,\mu_j') = \sum_{i\in J_j}\left(-d_0 e^{\left(-\sum\limits_{j\in I_i} l_{ij}\mu_j'\right)} - Y_i \sum_{j\in I_i} l_{ij}\mu_j'\right) \tag{2.24}$$

For iterative CT, there exist more complicated noise models which better correspond the reality and lead to an improved image quality: The CT transmission data can also be modeled as a Poisson-distributed quantum noise plus a Gaussian-distributed electronic noise [197, 367, 230, 325, 324]. Hereby, the noise of the detector itself is considered by the Gaussian term. The compound Poisson and Gaussian noise model is more accurate to describe the noise spectrum in CT than a simple Poisson or Gaussian noise model. The disadvantage is that it is more challenging to implement due to its complexity.
The noise models in this section assume a monochromatic ray. In fact, the X-ray spectrum is polychromatic and there are publications which account for the polychromatic nature of X-rays [65, 86, 87]. These methods divide the spectrum into a number of energy bins and then they compute each interaction within a voxel for each bin [3]. Scatter is modeled and estimated using Monte Carlo methods which approximate the overall result by simulating a large amount of photons and choosing interactions based on probabilities [393, 195]. Although these methods have been implemented on GPU clusters and computation clouds, execution times are still very high.

The cost function

Based on the noise model, where either a Gaussian or Poisson distribution was assumed for the raw measurements, a cost function can be derived. In case of Gaussian noise, a suitable cost function minimizes the distance between the measured projections and the simulated projections in each iteration, as measured by the Mean Squared Error. In case of Poisson noise, the cost function maximizes the probability that the measured projections match the simulated projection, as measured by the likelihood.
As a matter of principle, the cost function consists of a data term which cares for the data accuracy or data fit and a regularization term which constricts the data term in the sense that it removes noise and artifacts caused by non-idealities of the acquisition process and the scanner itself.
For the log-converted sinogram, based on equation 2.23, we can define the following regularized optimization function:

$$\mu^* = \underset{\mu'}{\operatorname{argmax}}\ L(y, \mu') - \beta\phi\left(\mu'\right), \tag{2.25}$$

leading to a **M**aximum **A** **P**osteriori (MAP) probability [64].
For the non-log converted sinogram, based on equation 2.24, the regularized optimization function reads as follows:

$$\mu^* = \underset{\mu'}{\operatorname{argmax}}\ L(Y, \mu') - \beta\phi\left(\mu'\right), \tag{2.26}$$

2.2.4.2 Statistical reconstruction methods

Among the iterative algorithms, statistical reconstruction methods are the most promising approaches to obtain the best image quality possible for CT reconstruction. These methods can lower the image noise in the reconstruction, improve the quantitative accuracy, spatial resolution, contrast, the SNR and they can remove streaking artifacts caused by under-sampling the object.
We want so summarize the most important iterative algorithms of the past years in the following time-line diagram and we then will classify these methods.

Time line digram of important iterative algorithms

- 1937: Linear least squares problem [175]
- 1963: Iterative algorithm for emission tomography [194]
- 1968: Iterative X-ray CT [146]
- 1970: Algebraic reconstruction Technique [116]
- 1972: Weighted Least Squares for Single Photon Emission Computed Tomography [113]
- 1974: Richardson/Lucy [288, 226] algorithm (familiar to ML-EM)
- 1976: Poisson-based likelihood for emission tomography [291]
- 1977: Maximum Likelihood Expectation Maximization [77]
- 1982: Poisson-based Expectation-Maximization for emission tomography [307]
- 1984: Poisson-based Expectation-Maximization for transmission tomography [202]
- (1984: Filtered Backprojection [93])
- 1990: Expectation Maximization and Gibbs smoothing prior [200]
- 1992: Simultaneous ART [279]
- 1994: Ordered Subsets ML Expectation Maximization method [153]
- 2000: **M**aximum **L**ikelihood for **Tr**ansmission Tomography (ML-TR) [64]

- 2004: Ordered Subsets SART [353]
- 2005: Ordered Subsets Convex algorithm [192]
- 2006: Penalized Weighted Least Squares [355]
- 2008: Adaptive Steepest Descent - Projection Onto Convex Sets reconstruction with TV constraint [313, 314]
- 2010: Fully GPU based CT reconstruction with TV constraint [165]
- 2012: Anisotropic Total Variation regularized EM reconstruction [71]
- 2013: Combined first order (isotropic) and second order (anisotropic) regularized EM reconstruction [70]
- 2015: Generalized Anisotropic TV for regularized, under-sampled, low-dose OSC reconstruction [69]

The tree diagram below classifies the reconstruction algorithms into analytical and iterative methods. The iterative algorithms subclassify into non-regularized and regularized approaches which again can be divided into two groups: Algebraic and statistical-based reconstruction methods. Statistical iterative methods are based on a (weighted) least squares objective function (in case Gaussian noise is assumed for the raw measurements) or a likelihood cost function (in case of Poisson noise is assumed for the sinogram). The tree diagram below presents the most important papers of the corresponding groups. [211] presents details of the various models for the data acquisition process in case of different modalities like SPECT or **P**ositron **E**mission **T**omography (PET) and presents an overview of the variety of reconstruction methods. Besides the fully statistical models which will be presented later, there are methods which include only parts of the statistics of X-ray CT, e.g. methods which operate mainly in the sinogram domain or the reconstructed image domain.

Common classes of reconstruction algorithms and the most important publications

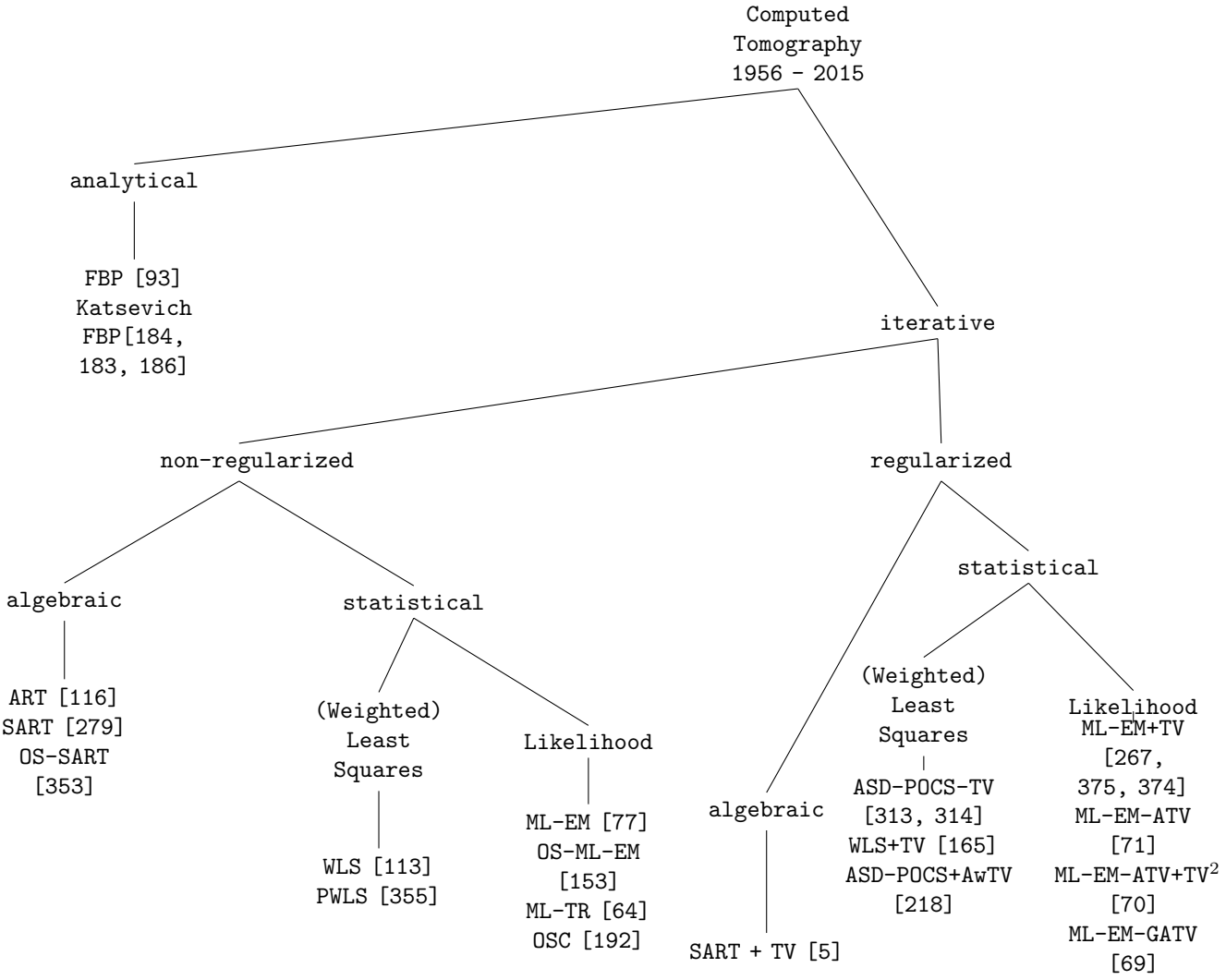

Tree diagram: The most important papers of CT published during the last years, categorized by their corresponding classes.

Methods which mainly operate in the sinogram domain

Many algorithms have been proposed which work mainly in the sinogram domain. The key idea is to reduce the complexity of an accurate physically modeling by modifying or precorrecting the sinogram, prior to the reconstruction. The methods aim at removing the noise or scatter from the raw measurements followed by analytic or iterative reconstruction. The sinogram can be denoised by adaptive [148, 299, 174, 76] or iterative [199, 102] filters. An alternative is the sinogram restoration based on penalized likelihood functions [196], [197] or by making use of a mean-variance dependent Gaussian density [355, 339]. The advantage of these methods is that they are relatively fast, even if they are iterative. However, an efficient denoising is not possible without a loss of resolution in the reconstructed image. The reason is that the precorrection destroys the noise statistics and therefore the results are worse compared to e.g. regularized iterative CT with an unmodified sinogram. Alternatively, the noise property can be modeled by a cost function in sinogram space. Then, an optimal solution for the Radon transform can be searched, followed by analytical or iterative reconstruction [224, 213, 198, 196].

Methods which operate on the reconstructed image domain

Algorithms which work on the reconstructed image domain are an alternative to those methods which mainly concentrate in the sinogram. They are very fast since they reconstruct the raw measurements by Filtered Backprojection and then they apply a post-processing filter on the reconstructed image [295, 225]. However, these algorithms cannot remove the streaks (caused by under-sampling) in the reconstructed images. Popular frameworks are the **A**daptive **S**tatistical **i**terative **r**econstruction algorithm (ASir) [316] or the **I**terative **R**econstruction in **I**mage **S**pace (IRIS), a framework of Siemens which can achieve a 60% dose reduction compared to FBP. Furthermore, it was reported that post-filtering of a reconstruction should be preferred over early stopping of an iterative algorithm [16], whereby both strategies are comparable in terms of the execution speed.

Other methods which include the CT statistics

Instead of accurately modeling the physics in X-ray CT, methods have been proposed which model the effective resolution loss [94]. Other alternatives are to modify the back-projection to dampen high frequencies [335], to filter every iteration during iterative reconstruction [317] or to apply a position dependent model, including a kernel modeling detector crosstalk [241]. Furthermore, there are accurate measures of the system matrix which is modeled as a combination of sinogram blurring, ideal projection and image blurring [398].

Fully statistical methods based on a Poisson or Gaussian noise model

Fully statistical methods are based on a noise model and a cost function which is minimized or maximized by iterative numerical algorithms. Publications which assume a Poisson noise model for the acquisition process are for example [92, 86, 97, 204]. Compared to Filtered Backprojection, the noise can be reduced by 20 to 30%, e.g. for an un-regularized **O**rdered **S**ubsets **C**onvex (OSC) algorithm [172]. Thus, efficient regularization functions have been proposed, which enable accurate reconstruction for some typical datasets in an under-sampled, low-dose scenario [313, 69].

The Maximum Likelihood Expectation Maximization algorithm

The likelihood function in equation 2.23 is the hypothetical probability that an event which has already occurred would yield a specific outcome. By maximizing the likelihood, the reconstruction algorithm tries to find the set of parameters that makes the measurements the most probable compared to the estimated data. The **M**aximum **L**ikelihood **E**xpectation **M**aximization (ML-EM) algorithm [77, 202, 201] can be used to find an estimate of μ' from y in equation 2.25. The standard ML-EM algorithm, however, leads to artifacts in the presence of noisy projection data [277]. The **O**ne **S**tep **L**ate strategy (OSL) [121], includes a regularization term $\phi(\cdot)$ in the algorithm and can overcome these shortcomings:

$$\mu_j'^{n+1} = \frac{\mu_j'^{n}}{\sum\limits_{i \in J_j} l_{ij} + \beta \left(\frac{\partial \phi(\mu_j'^{n})}{\partial \mu_j'} \right)} \sum_{i \in J_j} \frac{y_i l_{ij}}{\sum\limits_{k \in I_i} l_{ik} \mu_k'^{n}} \tag{2.27}$$

Parameter β controls the ratio between the fidelity term and the regularization term in equation 2.27. For $0 < \beta \ll 1$, the algorithm approaches the ML-EM solution, whereas for large values of $0 \ll \beta < 1$, the algorithm converges to the regularization function.

The Ordered Subsets Convex algorithm

A relaxed version of the Ordered Subsets Convex algorithm [192] is a typical solver for equation 2.26. In order to overcome multiple solutions [15], only one subset for the reconstruction is used in our implementation. The OSC algorithm is defined as:

$$\mu_j'^{n+1} = \mu_j'^{n} + \mu_j'^{n}\zeta \frac{\sum\limits_{i\in J_j} l_{ij}\left(d_0 e^{\left(-\sum\limits_{k\in I_i} l_{ik}\mu_k'^{n} - Y_i\right)}\right) - \tilde{\beta}\left(\frac{\partial\phi(\tilde{\mu}'^{n})}{\partial\tilde{\mu}_j'^{n}}\right)}{\sum\limits_{i\in J_j} l_{ij}\left(d_0 e^{\left(-\sum\limits_{k\in I_i} l_{ik}\mu_k'^{n}\right)}\right)\sum\limits_{k\in I_i} l_{ik}\mu_k'^{n}}, \tag{2.28}$$

where relaxation parameter $0 < \zeta \leq 1$ controls the convergence speed of the method [192]. Regularization term $\phi(\cdot)$ [200, 64] conditions the current solution μ'^{n}. Since the number of photons leaving the source, d_0, highly influence the balance between the fidelity term (depending on d_0) and the regularization term (not depending on d_0) in equation 2.28, we normalize $\tilde{\beta} = \beta \cdot d_0$, $(\beta \geq 0)$.
An alternative to the ML-EM and OSC approaches which assume that the raw measurements are corrupted by Poisson noise is the least-squares model, which assumes a Gaussian noise distribution of the acquired data. The goal is to minimize the distance between the measured projections and the simulated ones (obtained by the forward projection in every iteration). The distance is measured by the Mean Squared Error. Important publications for transmission tomography are [298, 29, 339], re-weighted least squared approaches [119], model-weighted least squares methods [6] and many others [339, 338], just to mention a few of them.
This section presented statistical reconstruction methods which can remarkably improve the reconstruction results. It is rather uncertain that further refinements in the statistical model could lead to higher image quality. As we will see in the next section, the regularization function is a powerful method to further improve the image quality for statistical iterative CT reconstruction.

2.2.4.3 The regularization term

Objective functions which are designed solely on the basis of measurement statistics (Poisson or Gaussian noise) perform poorly due to the ill-conditioned nature of tomographic reconstruction. Forcing too much data fit (a too high contribution of the data term) produces noisy images. The Maximum likelihood algorithm is even known to diverge in case the projection data is heavily corrupted by noise [277]. The reason is that ML-EM produces increasingly noisy images with succeeding iterations [326]. Regularization methods can overcome this problem, since regularization changes an ill-conditioned problem into a different well-conditioned problem. However, the choice of the parameters is complex, since these influence the convergence of the algorithm and they modify the final result. Some regularization techniques introduce additional artifacts [171, 285] or over-smooth prominent edges and therefore the spatial resolution of the result worsens. Other challenges which demand efficient regularization terms are the removing of undesired edges in the image, which were introduced only because of the noise, or the removing of artifacts introduced by bad detector bins or because of the under-sampling of the target. Regularization functions are computationally complex: Voxels have 26 neighbors in a three-dimensional setting and therefore a large neighborhood has to be processed.
A priori information can be obtained through various sources [286], which can be classified by the following categories:

- Full reference image: The a priori information is obtained from a reference image which is generated prior to the reconstruction, e.g. by a reconstruction of a previously acquired scan. A reference image can also be obtained by segmenting neighboring slices or by a blurred image obtained through the reconstruction from all available measured projection data in the first few iterations [50, 206, 334]. [369] use a full reference image as prior information to train a dictionary for dictionary-based reconstruction.

- Boundary and support information, e.g. through the pixel position: A priori information can be obtained through the boundary knowledge and support information of the scanned object.

This information is leveraged in the following three contributions of this thesis: [69, 70, 71]. The methods will be presented later.

- Attenuation information: The intensity values of the object are known, but not the exact pixel positions, see [286]. In [69], for example the LACs of objects being scanned in industrial CT are known beforehand and this information can be used for the design of an efficient regularization function, see chapter 5 for details.
- Other a priori information: E.g. smoothness of the noise-free image [215, 95].

Before we want to categorize the regularization techniques into the classes mentioned above, we want to present some simple, quadratic forms of regularization, which are convex and linear and are based on simple assumptions on the scanned object, e.g. "smoothness" of the noise-free image. The simplest form of regularization is definitely the entropy [58] or the identity norm, which is a form of Tikhonov-Miller regularization [343]. Later, Gibbs smoothing priors were introduced [137, 200], which were generalized in the past years [229] followed by Gamma priors [66] and Gaussian Markov Random fields formulated as quadratic forms [298, 333, 197, 96]. [381] propose an edge-preserving hyperbolic regularization function. [108] propose a line process to define the edge lattice during Bayesian restoration of images and [49] propose an auxiliary variable in the prior constraint to mark the discontinuities in the images.
Quadratic regularization functions are convex, easy to solve and implement. However, they globally smooth the image and therefore prominent edges get lost. In [96], a simple penalty was proposed, which weighs those pixels in an eight-connected neighborhood of the current pixel and it was proven that this penalty leads to a strictly convex objective function. However, when the weights are equal for the neighbors of equal distance, discontinuities are not considered in the image which leads to an over-smoothing of small edges and boundaries. Several edge-preserving regularization methods have been proposed to address this problem, for example the edge-preserving Huber penalty [86] which quadratically penalizes neighbors of small differences, while applying a linear penalty on neighbors of larger differences.
[356] take the difference in intensities of the neighboring voxels into account and they propose a quadratic regularization term with anisotropic weights for different neighbors. The non-linear weights enable a preservation of the edges and therefore researchers begun to concentrate more on non-quadratic and non-linear methods: Three-dimensional noise-filter algorithms are based on bilateral filters [371] or Nonlocal Means [372] have been proposed as well as Markov random fields with non-quadratic roughness penalty functions [28]. [381, 132, 231] present other non-linear regularization functions. The prior function proposed by [107] was introduced as a finite asymptotic edge-preserving function and is closely related to the Total Variation norm.

Compressed Sensing

The Compressed Sensing theorem [82, 81, 83, 40] proves that an image which consists of sparse signals could be reconstructed from far less measurements than the Nyquist sampling theorem assumes. This is possible if the associated transfer matrix of the sparse signals satisfies some conditions, such as the **R**estriced **I**sometry **P**ropety (RIP) [41]. Many algorithms have been proposed over the past few years which use increasingly less raw data [247, 271, 253, 73] or sparse projections: Sparse projections are obtained over a small number of equally or unequally distributed projection angles. Theoretically, exact reconstruction from under-sampled objects is impossible [140]. However, it was shown that for some simple objects, accurate reconstruction from under-sampled targets is possible: [247, 313, 69]. From the Compressed Sensing theorem we known that if the scanned object is sparse in some domain, the object can be accurately reconstructed. We therefore need a function to transform the object into a sparse domain.

Total Variation

The Total Variation is a non-linear sparseness transform for Compressed Sensing and it was proposed by [294]:

$$TV(\mu) = \int_{\Omega} |\nabla_{x,y}\mu| \, dxdy = \int_{\Omega} \sqrt{\left(\frac{\partial \mu_{x,y}}{\partial x}\right)^2 + \left(\frac{\partial \mu_{x,y}}{\partial y}\right)^2 + \varepsilon^2} \; dxdy, \tag{2.29}$$

where $\Omega \subset \mathbb{R}^2$ and $0 < \varepsilon \ll 1$ guarantees the differentiability of TV.
Equation 2.29 is the **G**radient **M**agnitude **T**ransform (GMT) and it quantitatively measures the "number" or "amount" of discontinuities in an image by computing the absolute value of the gradient in x- and y-direction of the image. The GMT is extremely sparse for piece-wise constant images, see figure 2.10: Excluding the background pixels in a) from computation (which are all zero), over 90% of the pixels of the GMT in b) are 0.

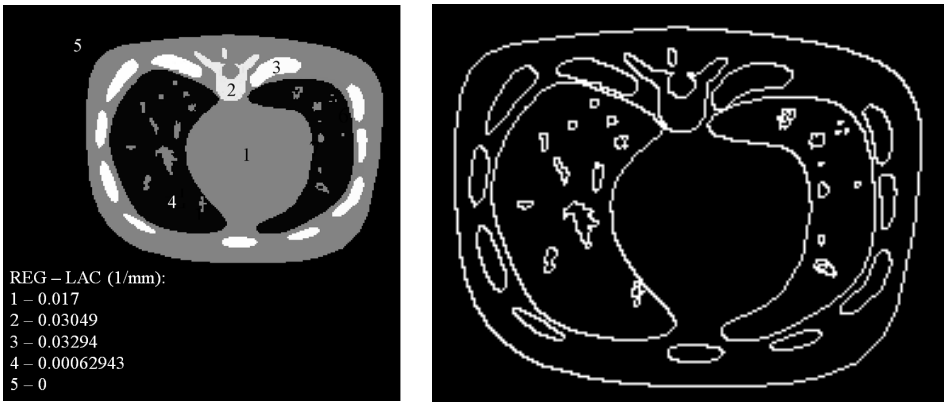

Figure 2.10: The lung phantom in a) and its Gradient Magnitude Transformation (equation 2.29) in b). The result in b) is extremely sparse. Not counting the zero intensity background pixels in a), over 90% of the pixels in b) are zero.

Intuitively, a noisy image has a higher Total Variation than a noise-free image, due to the "non-prominent" edge (pixels) which are introduced just because of the noise. A complete noise-free and piece-wise constant image has the lowest possible Total Variation. Phantoms, as presented in figure 2.2.1.3, are extremely sparse since they are piece-wise constant. Natural images, however, have a slightly higher Total Variation than the digitally simulated ones in figure 2.2.1.3, since there are some small fluctuations in homogeneous areas and usually these images are not completely noise-free, i.e. not perfectly sparse. Total Variation used as a regularization function in iterative CT can preserve edges. For some simple experiments (where the object is perfectly sparse in the Compressed Sensing sense); it preserves edges accurately. On the other side, it can smooth the noise up to a certain noise magnitude. The border where TV can distinguish noise and prominent edges will be evaluated heuristically, later in this dissertation. Due to the non-linearity of TV, it is extremely difficult to derive a meaningful analytic theory about its properties in general and in special cases as well. However, [331] managed to develop a precise quantitative theory for TV.

The properties of TV for both scenarios, noise-free and noisy projections, can be summarized as follows:

- TV regularization is useful in image restoration since it can remove the noise [351].
- TV can recover sharp edges in an image while simultaneously not penalizing smooth image features. For perfectly sparse, piece-wise constant objects it preserves edge locations exactly [313, 69].
- TV is especially effective in restoring images with larger-scaled features: It can restore high-contrast structures, like bones, quite well.
- TV can remove smaller-scaled noise, but it also removes or over-smoothes smaller-scaled important image features. It over-smoothes image features of smaller intensities as well, if the noise magnitude is too high.
- TV affects individual image features and changes their intensity values or in other words: The contrast (i.e. the variation) is reduced between individual image features. The change in intensity is inversely proportional to the scale of the feature and directly proportional to the regularization parameter.
- TV is local in its effects on image features. The effects on one feature in the image do not contribute to other features in the image which are further away in the image.
- TV introduces artificial patches, called stair-cases, in low-noise scenarios due to the restoration of edges which were solely introduced because of the noise.

The properties of TV have been investigated by other researchers: [18] discuss the conservation of shape and scale parameters controlling evolution within the TV-flow context and [46] present a study of TV regularization. [80] investigate how TV regularization affects the frequency distributions and they show that the effectiveness of TV image restoration depends on the size and gray-scale intensity of the image feature relative to its Total Variation. The authors conclude that TV regularization is particularly effective in restoring "blocky" images. [117] further investigate TV's problem of restoring blocky images, i.e. the introduction of stair-casing artifacts in regions which should be homogeneous. Furthermore, they conclude that TV is not effective for restoring detailed or textured images.
TV assumes that natural images are of bounded variation, i.e. they are piece-wise constant. For natural images, this assumption does not hold, the Total Variation is even not minimal for noise-free natural images. Furthermore, the Total Variation blows up to infinity with the increasing of resolution [117]. This is somehow intuitive, since only a constant image has a minimal Total Variation: Here the TV has a value of 0. However, the assumptions of TV are a good approximation of reality.
TV can be considered as state of the art in regularized tomography due to its extensive use; Google scholar counts more than 440,000 publications for the exact search word "Total Variation" everywhere in an article and more than 2,750 publications with the exact words in the title up to 2016.01.24. Total Variation has been evaluated thoroughly [336, 22, 332, 188]. It was used as a penalized likelihood estimation [277, 336, 259, 12], as a penalized weighted least-squares formulation for iterative CT reconstruction using a SART algorithm [165, 52] and for TV regularized Maximum-likelihood approaches [277]. ML-EM+TV regularization is based on Greens modified algorithm [120] which uses a belief about the smoothness of the noise-free image. TV was used for a constrained CT reconstruction with an adaptive steepest descent [313, 314, 311]. The algorithm was further improved by a weighted formulation [23] and used for low dose breast CT [23] and as superiorization, based on a block-iterative orthogonal projection algorithm [274, 45].
Due to the popularity and easy implementation of TV it is commonly used as regularization function in modern, iterative, statistical CT algorithms. Many improvements of TV have been proposed which address the main drawbacks of TV.

Anisotropic TV

Anisotropic TV [25] is a variant of TV and is defined as:

$$ATV(\mu) = \int_\Omega |\nabla_x \mu| \; dxdy + \int_\Omega |\nabla_y \mu| \; dxdy = \int_\Omega \sqrt{\left(\frac{\partial \mu_{x,y}}{\partial x}\right)^2} dxdy + \int_\Omega \sqrt{\left(\frac{\partial \mu_{x,y}}{\partial y}\right)^2} dxdy \quad (2.30)$$

By splitting the $x-$ and $y-$ coordinate in the TV regularization, i.e. by introducing anisotropy [309], a reduction of the stair-case effect and the suppression of artifacts can be achieved, as previous publications have reported [25, 118].
Many weighted formulations of TV have been proposed which aim at overcoming the problems of TV. [168] perform an ART reconstruction with a weighted TV term with 20 gradient descent steps per iteration for limited angle tomography. They define the anisotropic TV as follows:

$$ATV(\mu, A, B) = \int_\Omega \left|\nabla_{x,y}^{(A,B)} \mu\right| = \int_\Omega \sqrt{A\left(\frac{\partial \mu_{x,y}}{\partial x}\right)^2 + B\left(\frac{\partial \mu_{x,y}}{\partial y}\right)^2 + \varepsilon} \; dxdy, \quad (2.31)$$

where $\Omega \subset \mathbb{R}^2$ and $0 < \varepsilon \ll 1$ guarantees the differentiability of equation 2.31 and $A, B \in \mathbb{R}$. They chose A =1, B = 0.001 for x-axis symmetric projections and A = 0.001, B = 1 for y - axis symmetric projections. The main idea for the introduction of the constants A and B is to stop the smoothing of edges from radial directions. Typically, those edges are blurred because of the missing angular range of the projection views. Consequently, the method can better preserve edges from other radial ranges.
[292] propose to weigh the gradient of TV by a function. First, they detect an edge by use of the Canny edge detector [135]. Then, they update the weight for the TV term according to the detected isotropic case. For the anisotropic case, they apply sub-pixel edge detection (as described in [124]).
[341] propose and **E**dge **P**reserving TV (EPTV) with a weighted gradient inspired by [124]. The weight is formulated as an exponential function. The EPTV term can efficiently remove the noise and the artifacts. However, the derivative of EPTV is "cumbersome", as the authors indicate, see equation A.2 in [341].

Adaptive weighted Total Variation

The **A**daptive **w**eighted **T**otal **V**ariation (AwTV) [218] published at 15$^{\text{th}}$ of November 2012 is another formulation of a function-weighted TV. It is defined as:

$$AwTV(\mu) = \int_\Omega \left|\nabla_{x,y}^{w} \mu\right| = \int_\Omega \sqrt{\left(\frac{\partial \mu}{\partial x}\right)^2 e^{\left(-\left(\frac{\partial \mu}{\partial x}\right)^2/\sigma^2\right)} + \left(\frac{\partial \mu}{\partial y}\right)^2 e^{\left(-\left(\frac{\partial \mu}{\partial y}\right)^2/\sigma^2\right)} + \varepsilon} \; dxdy \quad (2.32)$$

where $w(\cdot)$ is a weighting function and $w(\cdot) = e^{\left(-\left(\frac{\partial \mu}{\partial z}\right)^2/\sigma^2\right)}$ and $z = x$ or y. The gradient is weighted by an exponential function. The exponential function contains a parameter, $\sigma > 0$, which acts like a threshold of the noise. AwTV can remove the noise and suppress stair-casing artifacts by smoothing longitudinally to the edge. For $\sigma < 1$, AwTV can preserve edges. In case parameter σ is set to 1, AwTV turns into TV. However, AwTV cannot maintain edges or fine structures below a certain noise level, since parameter σ is static during the optimization. Therefore, the edge-preserving capabilities are limited to the intensity of the noise magnitude left in the image. This holds true for the suppression of stair-cases, too: At a certain noise level, AwTV will introduce stair-cases, see [70]. For a similar definition of the Anisotropic Total Variation, see [71] or chapter 3 in this thesis. What is striking are the derivatives, which are not computed correctly for AwTV, see equation 2.37, taken from [218]. For ATV, the derivative is computed correctly, see equation 3.9.
Beside the previously discussed variations of TV, other improvements of TV have been proposed [368, 290].

Second order regularization functions

Higher order derivatives prefer smooth transitions over jumps. They are therefore used to overcome TV's problem of stair-casing, e.g. in the field of image denoising [228]. The second order Total Variation can be defined as follows:

$$TV^2(\mu) = \int_\Omega \left|\nabla^2_{x,y}\mu\right| dxdy = \int_\Omega \sqrt{\left(\frac{\partial^2\mu}{\partial x^2}\right)^2 + \left(\frac{\partial^2\mu}{\partial y^2}\right)^2 + \varepsilon}\ dxdy, \tag{2.33}$$

where $0 < \varepsilon \ll 1$ guarantees the differentiability of TV^2. Higher order regularization functions were used in regularized statistical, iterative reconstruction algorithms [217]. Therein, the higher order TV is based on the Total Variation stokes model [250]. The method tackles TV's problem of generating patchy artifacts in regions which should be homogeneous.

First and second order combined TV

Blurry results can be expected when solely second order derivatives are used in the regularization function, since they prefer smooth transitions over jumps. [48] proposed a combined first and second order Total Variation image restoration algorithm, which was later used in the field of tomography. [79] proposed to combine first order and second order derivatives for Total Variation regularization and hereby they profit from both advantages of the first and second order TV term: Edge-preservation and smoothing of noise. A parameter controls the contribution of the first and the second order term. As a result, a comparable SNR to a full-dose filtered back-projection can be achieved and at the same time, the stair-case effect of TV can be suppressed. [397] use the same regularization function as [79], but they use thresholds for the gradient of TV in order to decide where to apply first order and where to apply second order TV. [250] propose a Penalized Weighted Least Squares model with a combined first and second order regularization function for a stair-case free result. The regularization function was previously introduced by [31] and is called the **T**otal **G**eneralized **V**ariation (TGV).

Other methods using TV

There are numerous other papers related to TV reconstruction in CT. [74] present a TV algorithm to solve high-dimensional linear problems. [270] propose a fast algorithm using TV and the **B**arzilai-**B**orwein (BB) algorithm for fast online IGRT. [252] propose a TV regularized BB gradient projection algorithm. Later, they further improved the convergence speed using a modified Nesterov method [251]. TV was used to regulate the data terms of likelihood [267, 115, 374, 375] and least squares problems [402]. TV regularization was used in combination with the SART algorithm [382] and the Split Bregman theory (introduced in [114]) [348]. [394] show that FBP and post filtering achieves a comparable image quality as iterative, TV regularized reconstruction, while the non-iterative method has the advantage of requiring much shorter computation times. The **P**rior **I**mage **C**onstrained **C**ompressed **S**ensing (PICCS) [50] is a very promising approach. The regularization function is defined as the difference between the Total Variation of the current image estimate and the TV of a previously acquired image. The method was later improved [206] and it was introduced in the field of dual energy CT [334] and it was used in many other publications such as [284, 209]. Further improvements of PICCS were proposed [330, 206, 329] which include a refined noise model and can overcome blurring due to patient motion. TV regularization found its application in various other fields of CT, such as limited-angle tomography [350], duality-based methods [401] and discrete tomography [42].
Furthermore, there are fast and simplified implementations of the Total Variation, such as an iterative reconstruction algorithm suitable for parallel computation [308] and a fast and non-iterative direct algorithm for one-dimensional Total Variation denoising [54].
Beside the Total Variation as sparseness transform for the Compressed Sensing paradigm there are other transformations, such as wavelets, and these have been used in combination with TV for emission tomography [191]. [163] propose a GPU implementation with framelets (tight frames) and these are obtained by the **T**ight-**F**rame (TF) transform [60]. The tight frames generally provide sparser representations than traditional wavelets [163].

2.2.4.4 Strategies to reduce the dose and reconstruction time in CT

In this section we will present the various possibilities to reduce the dose and reconstruction time in CT.

Interior reconstruction

[382] proved that if an object under reconstruction is piece-wise constant, a local ROI can be exactly and stably reconstructed by Total Variation minimization; this is known as interior tomography. Interior reconstruction, also known as **L**imited **F**ield of **V**iew (LFV) reconstruction, can correct truncation artifacts caused by limited angle data. The method reconstructs only a small ROI inside the object. The dose can therefore be drastically reduced. If a sub-region of the object is known, accurate reconstructions are possible [378, 383]. Similar results were independently reported by other researchers [193, 56]. However, the interior method does not have a unique solution [247] and is therefore not used frequently.

GPU-based reconstruction

Since iterative CT is computationally demanding and the reconstruction time is the main concern why commercial scanners still employ Filtered Backprojection for reconstruction [264], many acceleration approaches have been proposed. Parallelization is a keyword here: One could solve the problem that multiple iterations of forward- and backward projections of large datasets cannot be completed in a clinically feasible time frame (e.g. < 1 min) by efficient parallel programming with proper hardware. A modern GPU has more than 2000 processors and over 6 GB of memory; a perfect basis to parallelize the iterative [165, 163, 364, 365, 122, 239, 268] or analytical ([238, 305, 373]) reconstruction, calculate doses [158, 142, 164] and then optimize the treatment plan [239, 240]; each of these tasks can be performed on the GPU. GPU based high-performance computing is very attractive in radiotherapy, as reviewed by [166]. [165] have found that 20 to 40 X-ray projections are sufficient to reconstruct images with satisfactory quality for IGRT, where "the reconstructions took from 77 to 130 s on an NVIDIA Tesla C1060, leading to an overall 36 to 72 times dose reduction" [165]. Furthermore,"a clinically-reasonable patient image from 91 views can be reconstructed in a total time of approximately 78 seconds using a single GPU card NVIDIA GTX 295", see table 1 on page 1810 in [270].

Algorithms which converge fast

Beside efficient parallel computing using modern hardware, one can define a mathematical formulation of an efficient search algorithm for fast-solution-convergence. The Ordered Subsets approach, for example, divides the projection data into ordered subsets and then group-wise updates each set instead of a whole update at once. OS methods are known as incremental gradient methods [20], or block iterative methods [39]. These methods provide an order-of-magnitude acceleration over EM in maximum likelihood problems. Due to their fast convergence rate, they can therefore accelerate the reconstruction in emission [153] and transmission tomography [182, 91, 15, 232, 258] by at least one order magnitude and reach almost the same image quality compared to non-OS methods. Furthermore, they can be easily implemented with any type of system model. Unfortunately, they individually converge to each subset and therefore a local optimum cannot be found. Another problem is the risk of over-correction if too many subsets are used and as a consequence, the methods introduce noise and artifacts in the reconstruction. Ordered Subsets Convex algorithms try to tackle these problems [182, 91, 15]. Besides these methods, there are iterative coordinate descent approaches [384, 298, 29, 339, 388] or block and group coordinate descent algorithms [99, 19, 98] for fast solution convergence. Coordinate descent methods can be realized by Ordered Subsets as well [207, 399].
[270] propose a Total Variation-norm regularized least squares problem based on the Barzilai-Borwein formulation for fast on-line IGRT. They can reconstruct a "clinically-reasonable patient image in 12 to 30 iterations and a total time of 34 to 78 seconds using a single GPU card" (e.g. the NVIDIA GTX 295). In [251], the **U**nknown **P**arameter **N**esterov (UPN) method [161] is used in a

previously proposed **A**ccelerated **B**arrier **O**ptimization **C**ompressed **S**ensing (ABOCS) framework [252]. The method can reconstruct a patient's head in 74 seconds. The patient was reconstructed from 91 projection views and the **R**elative **R**econstruction **E**rror (RRE) (defined in [400]) was reduced from 21% for the FBP method to 7.3% for the UPN-ABOCS method.

Reduction of the tube current or under-sampling the target

Among the available options for a reduction of the dose and reconstruction time discussed before, the following strategies are probably the most promising ones:

- Lower the X-ray flux towards each detector bin by reducing the tube current or the pulse length of the CT system. Articles are: [299, 357, 223, 76, 224, 86, 88, 213, 196, 197, 355, 236, 235, 69].
- Under-sampling the target by acquiring less projection views, uniformly distributed around the object. Publications are: [154, 246, 273, 212, 140, 128, 220, 313, 50, 205, 69].

Reducing the dose by lowering the pulse length or the current of the anode is one strategy to notably decrease the time for the acquisition process [355]. The disadvantage is a corruption of the image quality due to the introduction of excessive quantum noise [148]. Efforts have been made to compensate this effect by sinogram restoration [213, 196, 355, 230] and statistical, iterative algorithms have been proposed, which can accurately model the projection noise, e.g. the Statistical Iterative Reconstruction Technique [86], EM - Separable Paraboloidal Surrogates [91] and others [88].
Another strategy to decrease the acquisition and reconstruction time is to take fewer projections per full rotation around the object, known as sparse-view scanning. Acquiring projection views only for a limited angle setting, e.g. from 0 to 90 degrees, is another strategy but not an aim of this thesis. However, reducing the number of projections for the reconstruction of objects introduces strong streaking artifacts [34, 57] in images produced by conventional Filtered Backprojection [93], since the Shannon sampling theorem is not fulfilled [162]. As a matter of principle, there are two strategies to compensate under-sampling artifacts and noise in the image [363]. The first possibility is to propose efficient iterative reconstruction algorithms, such as the method of Gerchberg-Papoulis [109], convex projections [275, 380, 304], the Bayesian approach [130], dictionary learning [370], maximum entropy [104], short scan acquisition [271], truncated Hilbert transforms [253, 73], interpolation of additional projection views from measured data [263, 106] and morphologic techniques [35], just to mention a few of them. Probably the most famous algorithm, with more than 40,000 citations, which can handle incomplete data is Expectation Maximization [77]. There are other iterative algorithms, such as the **A**daptive **S**teepest **D**escent - **P**rojection **O**nto **C**onvex **S**ets (ASD-POCS) [314] algorithm, which can handle incomplete projections and remove the streaks in the reconstruction.
The second possibility to compensate under-sampling artifacts and noise in the image is to use true regularization. The Compressed Sensing [82] paradigm makes it possible to sample far below the Nyquist rate. Hereby, the Total Variation method plays an important role.
As mentioned earlier, Total Variation [294] is used as a sparsity transform for CS in iterative reconstruction algorithms and it can partially overcome data insufficiency problems [313, 314, 336, 22, 332]. Although FBP is still the standard reconstruction algorithm in industrial and medical CT [264], TV-regularized few-view tomography has reached a level of utility in terms of image quality [341] and reconstruction speed [165] and therefore has been used in many tomographic applications (e.g. [52, 277, 203, 50] and references therein, just to mention a few of them). Despite the success of TV in CT reconstruction, recent publications address further improvements. Convex optimization [312] and GPU implementations [165] reduce the time for reconstruction; anisotropic formulations of TV [356, 341, 218, 71] allow for higher spatial and contrast resolution and tackle the problem of over-smoothing of fine structures. If the noise-magnitude is too high, however, methods like the Adaptive weighted Total Variation [218] tend to over-smooth fine structures and they cannot reconstruct clear edges. The so-called "stair-casing effect" caused by TV, i.e. introducing blocky and patchy artifacts in homogeneous areas can be overcome by combining first and second order gradients [70]. An accurate solution to the interior problem based on TV

minimization (for a piece-wise constant ROI) has been proposed [382], generalized for piece-wise constant functions defined on a domain in any dimension [126] and extended to polynomial ROIs [376]. The **D**iscrete **A**lgebraic **R**econstruction **T**echnique (DART) [11], as an alternative to CS, is an algorithm for discrete tomography and it can reconstruct highly under-sampled data which consists only of a few gray-values. Apart from all these methods, there are hardware approaches, such as the modulation of the tube current [179], so as to use its optimal potential.

2.2.5 Discretization and derivatives

For the iterative algorithms, the discretization plays an important role, since it influences the final spatial resolution in the image. Discretization is a potential origin of danger for introducing (aliasing) artifacts. Discretization transfers a continuous object into its discrete counterpart. This enables numerical evaluation and in the end, facilitates the implementation routine, at the cost of a certain discretization error. Especially in the forward model, the discretization error plays an important role and can be even larger than the measurement error, if the discretization grid is too coarse. A finer grid improves the error rate at the cost of a higher computation cost. Therefore, one has to find a balance between discretization accuracy and computation precision. If the discretization error is far lower than the measurement error, it is negligible, otherwise severe artifacts are introduced in the reconstructed images, for practical examples see [176]. A possible solution to reduce the computational cost needed for finer grids could be a non-uniform discretization: Finer grids are only computed in regions of interest and at other regions in the image (where the introduction of artifacts does not impact the diagnostics), a coarser grid is used. [391] compute a reconstruction using a fine grid and then they subsequently fold back the result to obtain the final reconstruction.
Let us now concentrate on the discretization of the gradient and for simplicity, we analyze only the one-dimensional case. There are many possibilities to discretize the gradient, as reported in [111]:

- Left-sided differences: $(\nabla_x \mu)^2 \approx (\mu_x - \mu_{x-1})^2$
- Right-sided differences: $(\nabla_x \mu)^2 \approx (\mu_x - \mu_{x+1})^2$
- Central differences: $(\nabla_x \mu)^2 \approx \left(\frac{(\mu_x - \mu_{x+1}) \; + \; (\mu_x - \mu_{x-1})}{2} \right)^2$
- Geometric average: $(\nabla_x \mu)^2 \approx \frac{((\mu_x - \mu_{x+1}) \; + \; (\mu_x - \mu_{x-1}))^2}{2}$
- Minmod: $(\nabla_x \mu)^2 \approx \left(\frac{\text{sign}(\mu_x - \mu_{x+1}) \; + \; \text{sign}(\mu_x - \mu_{x-1})}{2} \right) \min\left(|\mu_x - \mu_{x+1}|, |\mu_x - \mu_{x-1}| \right)$
- Upwind discretization: $(\nabla_x \mu)^2 \approx \left(\max(\mu_x - \mu_{x+1}, 0)^2 + \max(\mu_x - \mu_{x-1}, 0)^2 \right) / 2$

In [111] it is reported that central differences should be avoided, since they miss thin structures. The following example (taken from [111]) illustrates this: "If μ has a 1-sample wide structure like $\mu_{0,y} = 1$ and $\mu_{x,y} = 0, \; \forall \; i \; \neq 0$, the variation at $\mu_{0,y}$ estimated by central differences is zero". This is not the case for left- or right-sided differences. We therefore use left-sided differences for the discretization in this thesis. The problem with left-sided differences is, however, they are not symmetric.
For the calculation of the derivative of TV, for example, it is practicable to use left-sided differences for the discretization of the gradient and right-sided differences for the derivative of the TV itself, so as to regain the symmetry. This was done in e.g. [313] and in this dissertation. Alternatively, the geometric average, minmod and upwind discretization could be used. However, these derivatives are non-linear. Furthermore, an improved numerical approximation of the first derivative [61] has been proposed which is very promising since it has a very high accuracy.

2.2.5.1 First order derivatives

Derivative of Total Variation

When the gradient in x-direction, ∇_x, is approximated by left-sided differences, the TV in equation 2.29 can then be discretized as follows:

$$\begin{aligned} \mathrm{TV}(\mu) &= \int_\Omega |\nabla_{x,y}\mu| \, dxdy \approx \\ &\sum_{x,y} \sqrt{\left(\mu_{x,y} - \mu_{x-1,y}\right)^2 + \left(\mu_{x,y} - \mu_{x,y-1}\right)^2 + \varepsilon} \;\; dxdy \end{aligned} \tag{2.34}$$

$0 < \varepsilon \ll 1$ guarantees the differentiability of TV. The partial derivatives of TV can then be evaluated by using the left-sided differences discretization scheme of for the gradient in x- or y-direction and a right-sided differences scheme for the derivative of TV, as described in [313, 267, 277]:

$$\begin{aligned} &\frac{\partial \mathrm{TV}\left(\mu_{x,y}\right)}{\partial \mu_{x,y}} = \frac{\partial \mathrm{TV}\left(\mu_{x,y}\right)}{\partial \mu_{x,y}} + \frac{\partial \mathrm{TV}\left(\mu_{x+1,y}\right)}{\partial \mu_{x,y}} + \frac{\partial \mathrm{TV}\left(\mu_{x,y+1}\right)}{\partial \mu_{x,y}} \approx \\ &\frac{\left(2\mu_{x,y} - \mu_{x-1,y} - \mu_{x,y-1}\right)}{\sqrt{\left(\mu_{x,y} - \mu_{x-1,y}\right)^2 + \left(\mu_{x,y} - \mu_{x,y-1}\right)^2 + \varepsilon^2)}} + \\ &\frac{\left(\mu_{x,y} - \mu_{x+1,y} - \mu_{x,y-1}\right)}{\sqrt{\left(\mu_{x+1,y} - \mu_{x,y}\right)^2 + \left(\mu_{x+1,y} - \mu_{x+1,y+1}\right)^2 + \varepsilon^2)}} + \\ &\frac{\left(\mu_{x,y} - \mu_{x,y-1} - \mu_{x,y-1}\right)}{\sqrt{\left(\mu_{x,y-1} - \mu_{x-1,y-1}\right)^2 + \left(\mu_{x,y-1} - \mu_{x,y}\right)^2 + \varepsilon^2)}} \end{aligned} \tag{2.35}$$

Derivative of Adaptive weighted Total Variation

Taking the left-sided differences approximated gradient as a basis, the AwTV in equation 2.32 can be discretized as follows:

$$\begin{aligned} &\mathrm{AwTV}(\mu) = \int_\Omega \left|\nabla^w_{x,y}\mu\right| dxdy \approx \\ &\sum_{x,y} \sqrt{\left(\left(\mu_{x,y} - \mu_{x-1,y}\right) e^{(-(\mu_{x,y} - \mu_{x-1,y})^2/\sigma^2)}\right)^2 + \left(\left(\mu_{x,y} - \mu_{x,y-1}\right) e^{(-(\mu_{x,y} - \mu_{x,y-1})^2/\sigma^2)}\right)^2 + \varepsilon} \; dxdy \end{aligned} \tag{2.36}$$

The partial derivatives were taken from [218]. The derivative of AwTV is then defined as:

$$\begin{aligned} &\frac{\partial \mathrm{AwTV}\left(\mu_{x,y}\right)}{\partial \mu_{x,y}} \approx \\ &\frac{2e^{\left(-(\mu_{x,y} - \mu_{x-1,y})^2/\sigma^2\right)}\left(\mu_{x,y} - \mu_{x-1,y}\right) + 2e^{\left(-(\mu_{x,y} - \mu_{x,y-1})^2/\sigma^2\right)}\left(\mu_{x,y} - \mu_{x,y-1}\right)^2}{\sqrt{e^{(-(\mu_{x,y} - \mu_{x-1,y})^2/\sigma^2)}\left(\mu_{x,y} - \mu_{x-1,y}\right)^2 + e^{(-(\mu_{x,y} - \mu_{x,y-1})^2/\sigma^2)}\left(\mu_{x,y} - \mu_{x,y-1}\right)^2 + \varepsilon}} + \\ &\frac{-2e^{\left(-(\mu_{x+1,y} - \mu_{x,y})^2/\sigma^2\right)}\left(\mu_{x+1,y} - \mu_{x,y}\right)}{\sqrt{e^{(-(\mu_{x+1,y} - \mu_{x,y})^2/\sigma^2)}\left(\mu_{x+1,y} - \mu_{x,y}\right)^2 + e^{(-(\mu_{x+1,y} - \mu_{x+1,y-1})^2/\sigma^2)}\left(\mu_{x+1,y} - \mu_{x+1,y-1}\right)^2 + \varepsilon}} + \\ &\frac{-2e^{\left(-(\mu_{x,y+1} - \mu_{x,y})^2/\sigma^2\right)}\left(\mu_{x,y+1} - \mu_{x-1,y}\right)}{\sqrt{e^{(-(\mu_{x,y+1} - \mu_{x,y})^2/\sigma^2)}\left(\mu_{x,y+1} - \mu_{x,y}\right)^2 + e^{(-(\mu_{x,y+1} - \mu_{x-1,y+1})^2/\sigma^2)}\left(\mu_{x,y+1} - \mu_{x-1,y+1}\right)^2 + \varepsilon}} + \end{aligned} \tag{2.37}$$

Looking closely at the derivative of AwTV, one can directly see that it was not calculated in a mathematically correct way. Instead, the derivative was approximated by taking the correctly

calculated derivative of TV in equation 2.35 as a basis and then weighting each term by the corresponding $e^{(\cdot)}$ functions for the computation of the AwTV. This is not correct in the mathematical sense. The derivative of AwTV should be calculated as follows:

$$\frac{\partial \mathrm{AwTV}\left(\mu_{x,y}\right)}{\partial \mu_{x,y}} = \frac{\partial \mathrm{AwTV}\left(\mu_{x,y}\right)}{\partial \mu_{x,y}} + \frac{\partial \mathrm{AwTV}\left(\mu_{x+1,y}\right)}{\partial \mu_{x,y}} + \frac{\partial \mathrm{AwTV}\left(\mu_{x,y+1}\right)}{\partial \mu_{x,y}} \tag{2.38}$$

The definition of the ATV in chapter 3 is equal to the AwTV of [218]. However, the derivative of ATV was computed correctly, compare equation 3.9 with equation 2.37. The derivative of AwTV is in fact a weighted approximation of the derivative of TV.
We would like to point out that there are other publications where the derivative of the regularization function was not correctly computed. In these publications the derivatives were arbitrarily approximated by a routine which is not further explained, see e.g. the derivative of the EpTV penalty of [342] (see A.2 and A.3). The authors indicate in their paper that their approximation scheme is "cumbersome" [61]. To improve the stability of the algorithms, it seems that it is a common practice to numerically modify the derivatives and to customize them to the current problem. However, there is a strong risk of these methods to introduce additional artifacts in the image since this leads to arbitrary functions with no distinct mathematical background.

2.2.5.2 Second order derivative

The left-sided differences discretized second order Total Variation can be defined as follows:

$$\begin{aligned} &\mathrm{TV}^2(\mu) = \int_\Omega \left|\nabla^2_{x,y}\mu\right| dxdy \approx \\ &\sum_{x,y} \sqrt{\left(\mu_{x,y} - 2\mu_{x-1,y} + \mu_{x-2,y}\right)^2 + \left(\mu_{x,y} - 2\mu_{x,y-1} + \mu_{x,y-2}\right)^2 + \varepsilon^2}\ \ dxdy \end{aligned} \tag{2.39}$$

Analog to the first order derivative of TV, the second order derivative of TV can then be computed as follows:

$$\begin{aligned} &\frac{\partial \mathrm{TV}^2\left(\mu_{x,y}\right)}{\partial \mu_{x,y}} = \frac{\partial \mathrm{TV}^2\left(\mu_{x,y}\right)}{\partial \mu_{x,y}} + \frac{\partial \mathrm{TV}^2\left(\mu_{x+1,y}\right)}{\partial \mu_{x,y}} + \frac{\partial \mathrm{TV}^2\left(\mu_{x,y+1}\right)}{\partial \mu_{x,y}} \approx \\ &\frac{\left(2\mu_{x,y} - 2\mu_{x-1,y} - 2\mu_{x,y-1} + \mu_{x-2,y} + \mu_{x,y-2}\right)^2}{\sqrt{\left(\mu_{x,y} - 2\mu_{x-1,y} + \mu_{x-2,y}\right)^2 + \left(\mu_{x,y} - 2\mu_{x,y-1} + \mu_{x,y-2}\right)^2 + \varepsilon^2}} + \\ &\frac{\left(-2\mu_{x,y} + \mu_{x-1,y} - 2\mu_{x+1,y}\right)^2}{\sqrt{\left(\mu_{x+1,y} - 2\mu_{x,y} + \mu_{x-1,y}\right)^2 + \left(\mu_{x+1,y} - 2\mu_{x+1,y-1} + \mu_{x+1,y-2}\right)^2 + \varepsilon^2}} + \\ &\frac{\left(-2\mu_{x,y+1} + \mu_{x,y-1} - 2\mu_{x,y}\right)^2}{\sqrt{\left(\mu_{x,y+1} - 2\mu_{x-1,y+1} + \mu_{x-2,y+1}\right)^2 + \left(\mu_{x,y+1} - 2\mu_{x,y} + \mu_{x,y+1}\right)^2 + \varepsilon^2}} \end{aligned} \tag{2.40}$$

2.3 Analytic-based image reconstruction

Analytic-based algorithms are widely used in practical CT applications. They model the fact that there are a continuous number of rays and the object is assumed to be continuous as well. This is advantageous, since the discretization is applied after the solution has been obtained and this leads to less artifacts than a vice versa approach. The methods are very well understood, they are fast, linear and common methods to measure the spatial resolution and variance are applicable. On the other hand side, the methods over-simplify the physics, which causes a drastic image corruption when conventional dose reduction strategies are applied, e.g. few-view tomography or anode current reduction.

2.3.1 Projection theorem

As we have seen in section 2.2.2.3, the intuitive way to back-project the image from the available sinogram, $p(r, \theta)$ results in a blurred image. We therefore need a better solution. Recall, vector r belongs to the rotated coordinate system (r,s) in figure 2.6, and it basically represents the detector coordinate. We are interested in the LAC distribution, $\mu(x, y)$. Mathematically, this can be expressed as the inverse Radon transform:

$$\mu(x, y) = \Re^{-1}\left(p(r, \theta)\right) \tag{2.41}$$

We need to find a mathematical solution to this equation. The **Central Slice theorem** or **Projection theorem** can solve equation 2.41. The following notation and explanation is taken from [65].
Let $F(k_x, k_y)$ be the two-dimensional **F**ourier **T**ransform (FT) of $\mu(x, y)$:

$$F(k_x, k_y) = \int_{-\infty}^{\infty}\int_{-\infty}^{\infty} \mu(x, y) e^{(-2\pi i(k_x x + k_y y))}\, dx\, dy \tag{2.42}$$

where $i = \sqrt{-1}$ and let $P(k, \theta)$ be the one-dimensional FT of $p(r, \theta)$ with respect to r:

$$P(k, \theta) = \int_{-\infty}^{\infty} p(r, \theta) e^{(-2\pi i(kr))}\, dr \tag{2.43}$$

Then, the Central Slice theorem states that:

$$P(k, \theta) = F(k_x, k_y), \tag{2.44}$$

where $k_x = k\cos(\theta)$ and $k_y = k\sin(\theta)$. In other words: The one-dimensional FT with respect to the vector r of the Radon Transform of a two-dimensional function (or distribution $\mu(x, y)$) is the two-dimensional Fourier transform of that function. We can therefore compute $\mu(x, y)$ for each point of (x, y), based on the sinogram $p(r, \theta)$ by varying θ between 0 and π.

2.3.2 Direct Fourier reconstruction

Based on the projection theorem, it is possible to directly reconstruct $\mu(x, y)$ by:

1. Calculate the one-dimensional FT, F_1, of the sinogram, $p(r, \theta)$, with respect to r: $F_1\{p(r, \theta)\} = P(k, \theta)$
2. Calculate the two-dimensional inverse FT, F_2^{-1} of $F(k_x, k_y) = P(k, \theta)$: $F_2^{-1}\{F(k_x, k_y)\} = \mu(x, y)$

Direct Fourier reconstruction involves an interpolation step, since for the discretization, one has to sample from a polar grid to a cartesian grid, see figure 2.11. This step makes direct Fourier reconstruction less popular.

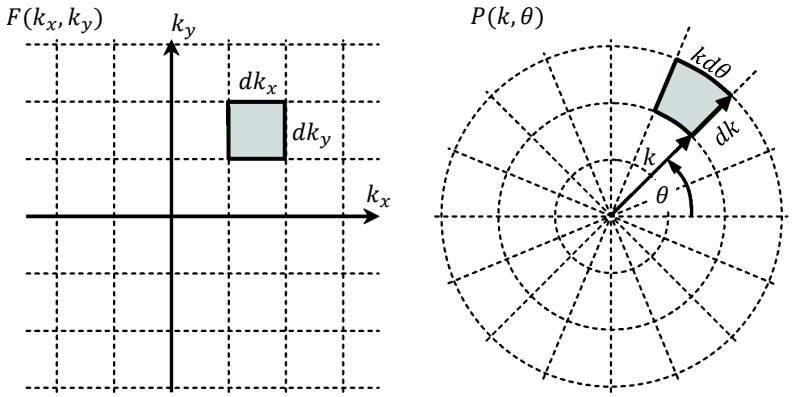

Figure 2.11: Schematic view of a cartesian grid and a polar grid.

2.3.3 Filtered Backprojection

The Filtered Backprojection algorithm [93] is still the standard reconstruction method for commercial scanners [264] and it has been used for many decades now [281, 30, 26, 306]. FBP and its (weighted) improvements [151, 337, 337] are often used for CBCT reconstruction. However, FBP algorithms require that the number of projections should satisfy the Shannon sampling theorem [162]; otherwise they introduce strong (streaking) artifacts. [214, 366] propose iterative FBP based methods which are not based on any cost function. New, exact analytical reconstruction algorithms were proposed, in which the scanner moves along helical [184, 254] and other more exotic acquisition trajectories [262].
Filter Backprojection directly operates on the polar grid and there is no need to re-sample to a cartesian grid, compared to direct Fourier reconstruction. [65]. Therefore, the Filtered backprojection can be derived as a result of the coordinate transformation, see figure 2.11. As a first step, the inverse Fourier Transform of $\mu(x, y)$ must be expressed in polar coordinates:

$$\mu(x, y) = \int_{-\infty}^{\infty} \int_{-\infty}^{\infty} F(k_x, k_y) e^{i2\pi(k_x x + k_y y)} \, dk_x \, dk_y, \tag{2.45}$$

where $k_x = k\cos(\theta)$ and $k_y = k\sin(\theta)$. Then the infinitesimal area integration element k_x and k_y in equation 2.45 is transformed to its Jacobian J:

$$J \equiv det \begin{bmatrix} \frac{\partial k_x}{\partial k} & \frac{\partial k_y}{\partial k} \\ \frac{\partial k_x}{\partial \theta} & \frac{\partial k_y}{\partial \theta} \end{bmatrix} = k\left(\cos^2(\theta) + \sin^2(\theta)\right) = k \tag{2.46}$$

Equation 2.45 can then be expressed in polar coordinates:

$$\mu(x, y) = \int_0^{2\pi} \int_0^{\infty} F(k_x, k_y) e^{i2\pi(k_x x + k_y y)} k \, dk \, d\theta \tag{2.47}$$

Equation 2.47 can be rewritten to:

$$\mu\left(x,y\right)=\int_{0}^{\pi}\int_{-\infty}^{\infty}F(k_x,k_y)e^{i2\pi(k_x x+k_y y)}\left|k\right|\ dk\ d\theta, \tag{2.48}$$

Recall, the Fourier slice theorem in equation 2.44 states that:

$$P(k,\theta)=F(k_x,k_y), \tag{2.49}$$

and we can therefore write:

$$\mu\left(x,y\right)=\int_{0}^{\pi}\int_{-\infty}^{\infty}P\left(k,\theta\right)\left|k\right|\,e^{i2\pi kr}\ dk\ d\theta, \tag{2.50}$$

where $r=x\cos(\theta)+y\sin(\theta)$ and $|k|$ is the absolute value of the Jacobian of the polar transformation. In fact, $|k|$ is a ramp filter, but other filters than the ramp filter can be defined.
We define a convolution kernel in the position space as follows:

$$q(r)=F^{-1}\left\{\left|k\right|\right\}=\int_{-\infty}^{\infty}\left|k\right|\ e^{i2\pi kr}\ dk \tag{2.51}$$

The reconstruction scheme can therefore be summarized as:

1. **filter the sinogram,** $p(r,\theta)$**:** $\forall\ \theta$ do: $p'(r,\theta)=p(r,\theta)*q(r)$ or $P'(k,\theta)=P(k,\theta)\left|k\right|$
2. **back project the filtered sinogram:** $\mu(x,y)=\int_{0}^{\pi}p'(x\cos(\theta)+y\sin(\theta),\theta)\ d\theta$

The ramp filter is not used in practice. Although it can remove low frequencies and keep high frequencies, it magnifies the noise of the projection data. From the discrete projection data we know that the useful Fourier content is limited to frequencies smaller than $k_{\max}=1/2\ \Delta r$, where Δr is the sampling distance. **Ram**achandran and **Lak**shminarayanan (Ram-Lak) [283] therefore propose an efficient filter, the so called Ram-Lak filter. It does not magnify the noise and is limited to frequencies smaller than $k_{\max}=1/2\ \Delta r$ and cut off at $k_{\max}$. It is defined as:

$$q(r)=\frac{k_{\max}\sin\left(2\pi k_{\max}r\right)}{\pi r}-\frac{1-\cos\left(2\pi k_{\max}r\right)}{2\pi^2r^2} \tag{2.52}$$

FBP reconstructions

Figure 2.12 shows FBP reconstructions (filter: Ram-Lak) of a human head for different numbers of noise-free projections. The noise-free sinogram was acquired by a forward projection of a completely noise-free reconstruction of a human head. FBP needs at least 200 views to reconstruct artifact-free results. For less than 200 views, the images are heavily corrupted by streaking artifacts.

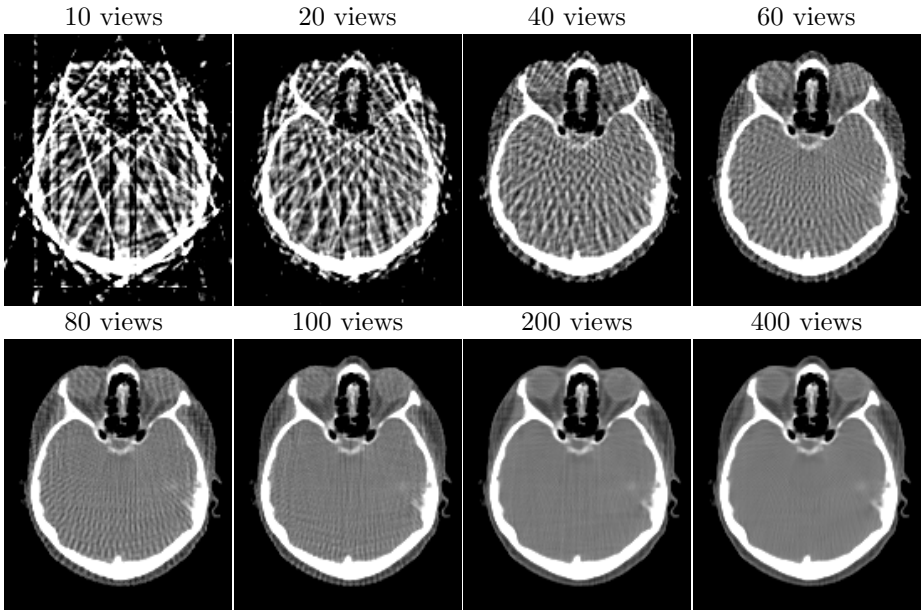

Figure 2.12: FBP reconstructions (filter: Ram-Lak) of a patient head, based on noise-free projections. The results are heavily corrupted by streaking artifacts if less than 200 projection views are considered. The display range is [0.0100,0.0178].

Figure 2.13 shows FBP reconstructions (filter: Ram-Lak) of a patient head from 400 uniformly sampled projections views and different SNRs of the sinogram. The results are extremely noisy if the SNR is smaller than 707.

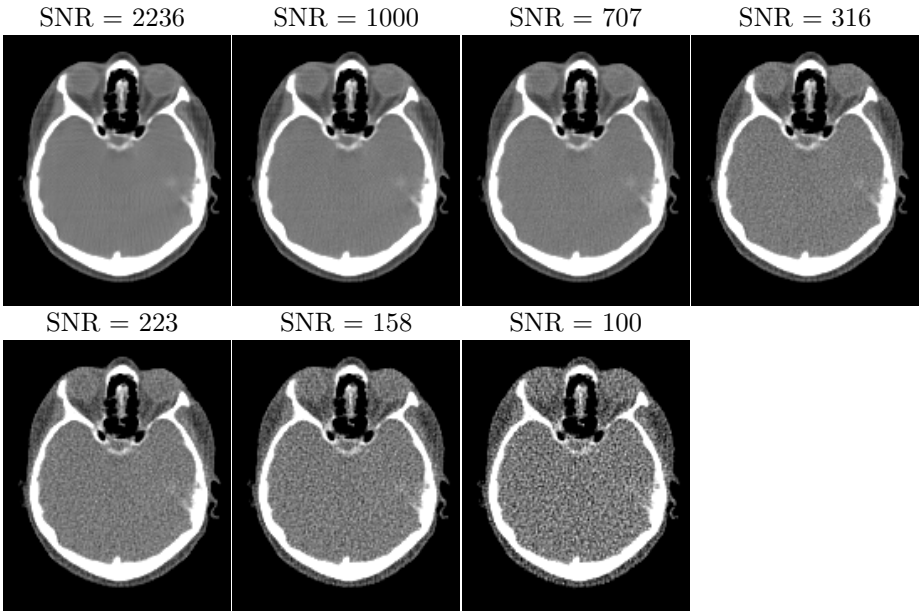

Figure 2.13: FBP reconstruction (filter: Ram-Lak) of noisy projections. 400 uniform measurements of a patient head were acquired. The results are extremely noisy for a SNR smaller than 316. The display range is [0.0100,0.0178].

2.4 Further reading

We want to provide a useful literature list on the topic of Computed Tomography for further reading.
[360] covers the early history of imaging and pioneering works towards CT. [38] describes in overwhelming detail the fundamentals of X-ray physics, like X-ray Generation and photon-matter interaction. The author then continues with the milestones of Computed Tomography, like micro-CT, PET-CT and two-dimensional Fourier-Based reconstruction methods, like the Radon transformation, simple Backprojection and Filtered Backprojection. The next chapters cover algebraic and statistical reconstruction methods and iterative reconstruction approaches, like ART and Maximum Likelihood. The author then discusses image quality and assessment, followed by presenting common artifacts in CT reconstructions, like the partial volume effect, beam hardening and artifacts caused by motion, sampling, electronic or detector nature, scatter or metal implants.
The Essential Physics for Medical Imaging [37] covers the topics of image quality, contrast, spatial resolution, noise, detective quantum efficiency, sampling and aliasing in digital images, contrast-detail curves, diagnostic radiology, nuclear medicine, radiation protection, dosimetry and biology.
[139] is advisable to consult for an overview of the process of CT. It covers the main goal of CT from traditional tomography over data collection, representation by voxels (three-dimensional case) and pixels (two-dimensional case), the polychromatic nature of X-rays, physical problems associated with data collection in CT, like photon statistics, beam hardening, as well as acquisition modes and other sources of error.
[149] presents the principles, design, artifacts and recent advances of Computed Tomography. The author leads the reader through important chapters, like different generations of CT Scanners, measurement of line integrals and data conditioning, sampling geometry and the sinogram, the Fourier Slice Theorem, fan-beam reconstruction, helical or spiral CT, multi-slice CT, X-ray radiation and dose-reduction techniques. Furthermore, there are other handbooks on medical imaging worth to consider, e.g. [21, 8].
Nowadays, **G**raphics **P**rocessing **U**nits (GPUs) contain approximately 2000 processors, which make it possible to overcome the computational burden in CT if the algorithms are parallelized efficiently. The GPU is therefore a strong tool to speed up the reconstruction process. Books that cover the topic of General-Purpose GPU are [190] or [297], which includes practical examples of Nvidia GPU programing as well. [301] provides a good overview on topics like linear inverse problems, regularization methods for ill-posed problems, Compressive Sensing, EM algorithms, energy minimization methods, tomography in general, statistical methods in imaging and Total Variation in imaging.
[395] is a good paper for physicians who do not have a strong mathematical background. It shows basic principles of image reconstruction in nuclear medicine. Many review articles on X-ray tomographic imaging have been proposed and are worth to consider so as to obtain a good overview on the field [72, 178, 265, 248, 211, 72, 264, 22, 256].

Three new regularization methods for low-dose, under-sampled, iterative CT reconstruction which successively improve the reconstruction results of TV

In the following chapters we propose three new regularization methods for low-dose, under-sampled, iterative CT reconstruction which successively improve the results of the current state of the art methods. These are: FBP in case of analytical reconstruction and Total Variation in case of iterative reconstruction.

CT Reconstruction from Few-Views by Anisotropic Total Variation Minimization
→ Chapter 3, published in [71].

In this chapter, we propose a gradient re-definition so as to overcome TV's problem of over-smoothing of fine structures. The re-definition is accomplished by multiplying the gradient of TV by an exponential function. The exponential function is parametrized by σ and this parameter acts like a threshold of the noise and controls which structures (noise and prominent edges) to penalize. The consequences of such a formulation in the application of regularized iterative tomographic reconstruction is examined. We reconstruct noise-free projections obtained by an under-sampled digitally simulated lung phantom, as well as real data scans acquired by an Elekta XVI CBCT. We define a visual acceptance test for the reconstructions, where the most valuable results are selected manually by means of visual inspection. Based on the visual acceptance test, we conclude that our method can produce piece-wise constant results with sharper and clearer edges and a higher spatial resolution than the common state of the art methods, TV and FBP.

CT Reconstruction from Few-Views by Higher Order Anisotropic Total Variation Minimization
→ Chapter 4, published in [70].

The method we present in this chapter focuses on the main drawbacks of TV: The production of stair-casing artifacts in regions which should be homogeneous and the over-smoothing of fine structures. To overcome the stair-casing effect of TV and at the same time to reconstruct high resolution images, we discuss a novel combination of a first order Anisotropic Total Variation and a second order Total Variation regularization for under-sampled, low-dose iterative CT reconstruction and compare it to the standard methods, Total Variation and Filtered Backprojection. We combine first order anisotropic gradients with second order isotropic gradients, creating a new formulation of a regularization function. Our proposed method is up to 1.57 times more homogeneous than AwTV and up to 7.7 times more homogeneous than TV. In contrast to TV, our new method can restore small details of a single pixel width. The spatial resolution of our proposed method is 26% higher than TV and equal to AwTV. Combined first order anisotropic gradients and second

order isotropic gradients thus do not influence the spatial resolution and can reconstruct piece-wise constant CT images of high quality.

Accurate Low-Dose Iterative CT Reconstruction from Few Projections by Generalized Anisotropic Total Variation Minimization for Industrial CT
→ Chapter 5, published in [69].

In this chapter, we discuss a novel generalized Total Variation regularization for under-sampled, low-dose iterative CT reconstruction. We propose a novel regularization function which uses *a priori* information about the Gradient Magnitude Distribution of the underlying object for the reconstruction. We provide a general parameterization scheme and evaluate the efficiency of our new algorithm for many different noise levels and many different numbers of projection views. We compare the results to the standard methods, Total Variation and Filtered Backprojection. For each combination of noise level and projection view, we perform 10 different measurements, where the noise random variable was varied. In total we perform 560 measurements for each method. We simulate projections based on under-sampled digitally simulated phantoms and rate the image quality produced by our method on the basis of quality measures such as the Relative Root Mean Squared Error, the Kullback-Leibler distance, the Contrast to Noise Ratio and subjective human assessment by examining the image quality. When noise is not present, our proposed method can accurately reconstruct piece-wise constant objects from only 40 projections. In cases where noise is simulated, our strategy achieves a Relative Root Mean Square Error that is up to one order of magnitude lower than Total Variation-based iterative statistical reconstruction. To obtain the same reconstruction quality as achieved by Total Variation, the projection number, the pulse length and the acquisition time and the dose, respectively can be reduced by a factor of approximately 3.5, when AwTV is used and by a factor of approximately 7, when our proposed method is used.

Comparison of the three methods in a common framework
→ Chapter 6.

All of the three innovations, the ATV in chapter 3, the combined first order ATV + second order TV in chapter 4 and the Generalized Anisotropic Total Variation in chapter 5 successively improve the resulting image quality for low-dose scans and under-sampled objects. Each method, ATV, ATV+TV^2 and GATV, produces better results than its preceding method. Furthermore, each method can successively improve the reconstruction results of the current state of the art method, Total Variation. This is shown in chapter 6. In this chapter, we compare these three methods in a common reconstruction framework so as to draw an overall conclusion of this dissertation. We evaluated the methods in a large experiment with 560 measurements where we tested different noise levels, different numbers of projection views and 10 realizations of the noise random variable. The main findings of this chapter include that an extreme dose reduction factor of 15.81 can be achieved compared to TV for all of the proposed methods. Furthermore, at this dose reduction factor (40 projections and a SNR of 707), ATV, ATV+TV^2 and GATV can further lower the RRMSE by 10.93%, 19.65% and 33.13%, respectively, compared to the RRMSE of TV at 200 projections and a SNR of 2236.

Chapter 3

CT Reconstruction from Few-Views by Anisotropic Total Variation Minimization

3.1 Outline

The method we present in this chapter was published at the **IEEE** *Nuclear Science Symposium and Medical Imaging Conference* in October, 2012 [71]. The abstract submission deadline was 13^{th} May, 2012. The key idea of the publication originates from April, 2011 and was already developed in the diploma thesis of Maurice Debatin [68]. The work presented in this chapter was submitted to the **Journal of Medical Physics** on the 24^{th} February 2012 and **IOP Science** *Physics in Medicine and Biology* on the 8^{th} May 2012.
In this chapter we introduce a generalized gradient re-definition. The classical definition of the derivative goes back in history to formulations of Newton and Leibniz in the 17^{th} century. The re-definition of the gradient is accomplished by multiplying the derivative with an exponential weighting function and we examine the consequences of such a formulation in the application of regularized Computed Tomography reconstruction. Based on visual inspection, our proposed method produces piece-wise constant results with a higher spatial resolution compared to the results of Total Variation regularized, iterative reconstruction and Filtered Backprojection. In contrast to FBP, our proposed method can remove the streaks caused-by under-sampling the target and it can produce smooth, noise-free results.

3.2 Introduction

In section 2.2.4.4, we have presented promising strategies to reduce the dose and acquisition time in CT. In this chapter, we want to concentrate on the most promising approaches for dose reduction: Under-sampling the target and lowering the tube current of the CT machine. Many regularization functions have been proposed to compensate the under-sampling artifacts, which are introduced in the reconstruction results when only few projections are considered for the reconstruction, or to remove the noise in the reconstructions which is caused by reducing anode current, see section 2.2.4.3.
Among the available regularization methods, Total Variation, described in section 2.2.4.3 and defined in equation 2.29 is very effective for removing the streaks. In section 2.2.4.3 the properties of TV are described. These are in short: Removal of under-sampling artifacts and noise at the cost of over-smoothing of small structures. There are many variants of TV, which try to solve these problems, for example in equation 2.31 the TV gradient was weighted by parameters and in [341] the TV gradient was isotropically weighted by an exponential function. In November 2012, the Adaptive Weighted Total Variation [218] was proposed, see equation 2.32. AwTV anisotropically weights the TV gradient by introducing exponential functions. Although these weighted formula-

tions of the TV address the aforementioned problems of TV, as described in section 2.2.4.3, the derivatives are wrong in the mathematical sense, for a description see section 2.2.5.1. The derivative of AwTV is presented in equation 2.37.
In this chapter, we propose a re-definition of the gradient by weighting it with an exponential function so as to overcome TV's problem of over-smoothing fine structures. The definition is analog to [218]; we however compute the derivative of the TV in a mathematically correct way leading to a different regularization function. Furthermore, our proposed method was published before [218] in [68].

3.3 Material and methods

The mathematical notation and the abbreviations we use in this chapter are listed in table 1.
X-Ray Computed Tomography can be modeled linearly by equation 2.14. In our experiments, we operate at a low-dose regime. This minimizes the acquisition time in industrial CT and hence maximizes the throughput. For medical CT, it notably reduces the patient dose. We therefore consider a Poisson noise model for imaging, see equation 2.16. The detector noise can be neglected, since its contribution is much smaller than the signal of interest [377].
Note that equation 2.16 is valid if at least 1000 photons per pixel are detected. This value was empirically measured in [287] and is related to the Central Limit Theorem. One can compare incident photon counts, d_0, directly to assess differences in the squared SNR of the sinogram datum, as described in section 2.2.4.1. Therefore, artificial Poisson noise can be applied to the projection data such that the resulting projection has a specific SNR. The relation between the SNR of a projection and the tube current was examined in [332], see table 2.3. The measurement associated with a larger SNR will have a greater impact on the solution. Based on the Poisson noise model in equation 2.16 and the log-likelihood in equation 2.23, an objective function can pe proposed:

$$\mu^* = \underset{\mu'}{\operatorname{argmax}}\ L(y, \mu') - \beta\phi\left(\mu'\right), \tag{3.1}$$

see section 2.2.4.1 for details. The regularized Maximum Likelihood Expectation Maximization algorithm presented in equation 2.27 is a solver for this optimization function. In the following, we describe a new regularization function $\phi(\cdot)$ for low-dose, under-sampled, iterative CT reconstruction.

3.3.1 The proposed method: Anisotropic Total Variation

To describe the idea of the method, we start from the initial point of the classical definition of the derivative. The derivative is defined as the approximation of the gradient of the tangent of a function $f : U \to \mathbb{R}$, with an open interval $U \subset \mathbb{R}$ at the point $x \in U$, by its secant. To compute the gradient of the tangent of f, one analyzes the limit of f:

$$\lim_{h \to 0} \frac{f_{x+h} - f_x}{h}, \tag{3.2}$$

when $h \in \mathbb{R}$ (defined as the step size) borders 0. In computer vision, one has to deal with discrete signals. A digital image for example has to be discretized before it can be processed, and for the discretization a finite step size $h \geq 1$ has to be selected. In the following, we therefore consider a discretized function $f^d : U^d \to \mathbb{R}$, $U^d \subset \mathbb{R}$ and the points $x, h \in \mathbb{N}^+$. The "gradient of the secant" then reads as follows:

$$\nabla_x f \approx \frac{f_{x+\triangle x} - f_x}{(x + \triangle x) - x} = \frac{f_{x+\triangle x} - f_x}{\triangle x}, \tag{3.3}$$

where $\triangle x = (x + h) - x$. When the sampling lattice h is set to 1, it is adequate that the left-sided differences formulation (also called backward difference) of the gradient at point x in the discretized image can be expressed as:

$$\nabla_x f^d \approx \frac{f_x - f_{x-1}}{(x-1) - x} = f_x - f_{x-1}, \tag{3.4}$$

For other discretization strategies of the gradient, see section 2.2.5. In a discretized image, the gradient, $\nabla_x f^d$ of any point x within the image refers to the most important image feature: the image's edges. The gradient yields the direction of the steepest descent of a point in the image and the Gradient Magnitude (GM), $|\nabla_{x,y} f|$, the corresponding slope in that direction.
In CT, for the calculus of the variation in the reconstructed image in terms of the edge intensities, it is therefore practical to compute the Total Variation of the Linear Attenuation Coefficient μ^n at the current iteration n. The TV is defined in equation 2.29. When the gradient $\nabla_{x,y}$ is approximated by left-sided differences (equation 3.4), the discretization of TV can be formulated, see equation 2.34. In equation 2.35, we compute the derivative of TV.
The novelty we present in this chapter is that the Total Variation is generalized by introducing a gradient re-definition, that is: to multiply the gradient with a common function $w : \mathbb{R} \to \mathbb{R}$.

$$\begin{aligned} \mathrm{ATV}(\mu) &= \int_\Omega \left| \nabla^w_{x,y} \mu \right| dxdy = \\ &\int_\Omega \sqrt{\left(\left(\frac{\partial \mu}{\partial x} \right) \cdot w \left(\frac{\partial \mu}{\partial x} \right) \right)^2 + \left(\left(\frac{\partial \mu}{\partial y} \right) \cdot w \left(\frac{\partial \mu}{\partial y} \right) \right)^2 + \varepsilon} \; dxdy \end{aligned} \tag{3.5}$$

Depending on the choice of the weighting function $w(\cdot)$, the computation of the gradient now becomes directionally independent as opposed to TV in equation 2.29 which implies identical properties in all directions (x and y) of the image. Due to the anisotropic property of equation 3.5, we call the method Anisotropic Total Variation. Do not mix our proposed method, ATV, with the ATV defined in equation 2.30 which just splits the $x-$ and $y-$ coordinate computation of TV: From now on, the term "ATV" denotes equation 3.5.
Next, we will motivate a specific choice for the function $w(\cdot)$. But before, let us have a look at the properties of Total Variation regularization. The application of Total Variation minimization recovers prominent edges and restores piece-wise constant images by removing noise and streaking artifacts caused by under-sampling the target. However, we can find typical shortcomings from this type of regularization function:
The choice of the regularization parameter of Total Variation based techniques is always a compromise between increased sparsity and the loss of small structures. Furthermore, TV-based regularization leads to piece-wise homogeneous results when the noise magnitude is high – the so-called "stair-casing effect", [70]. In Computed Tomography, where TV is used as a penalty term, e.g. in regularized iterative optimization functions, one usually assumes that the underlying true image which is noise and artifact free has a minimal Total Variation. However, this assumption is not true for all parts of the image. Especially this is not the case for the edges themselves, where the (Total) Variation is locally maximal. Let us have a look at figure 3.1 c), where the Gradient Magnitudes of figure 3.1 a) (the lung phantom) are visualized: The edges are the dominant part in the Gradient Magnitude Transform (GMT) – as TV is called. In figure 3.1 e), the histogram of the GMs of figure 3.1 c) is visualized. The small numbers of true Gradient Magnitudes (black squares) indicates the sparsity of the GM transformed image. Most of the GMs are 0. However, at the edges, the (Total) Variation is maximal. Therefore, in practical applications, where the TV is minimized to obtain a smoothed, piece-wise constant result, the Gradient Magnitudes related to noise and the GMs related to prominent edges are penalized at an equal amount (isotropic smoothing). This leads to an over-smoothing of fine structures and a blurring of edges.
Figure 3.1 d) shows the GMT of the Poisson noise corrupted lung phantom. A SNR of 1000 of the bones was chosen, see figure 3.1 b) for the noise-corrupted image. Figure 3.1 e) shows the corresponding GMs (gray dots with a black border) related to noise. Poisson noise blurs the original peaks and introduces additional peaks near the GM of intensity 0.

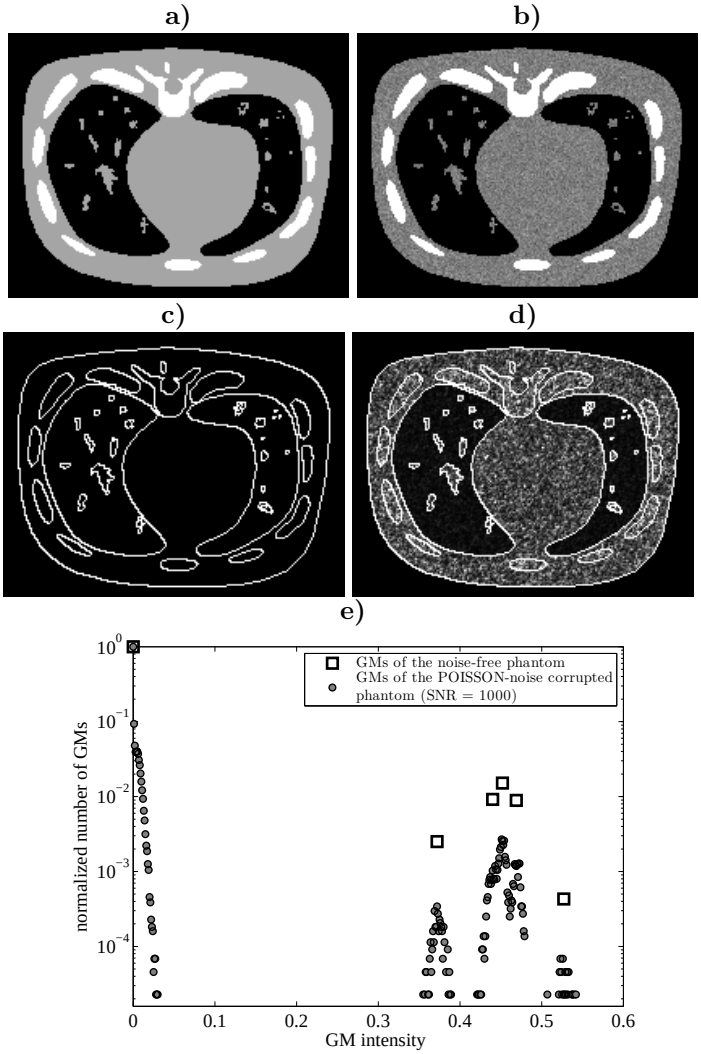

Figure 3.1: a) The digitally simulated lung phantom containing small bronchi (window-level: [0,0.0329]). b) The phantom corrupted by Poisson noise with a SNR of 1000 at the bones (window-level: [0,0.0391]). c) The Gradient Magnitude transform of a). d) The GMT of b) ((window-level of c) and d): [0.4453,0.5547]). e) The Gradient Magnitude Distribution of c) and d).

A possible solution to tackle the problems of TV could be to solely penalize the Gradient Magnitudes related to noise during the optimization and leave all other GMs which are related to true prominent edges untouched, i.e. enabling a separation of GMs related to noise and GM related to prominent edges (anisotropic smoothing). In figure 3.1 e), for example, one can clearly see that in principle it is possible to achieve this characteristic by just thresholding all low intensity GMs $< 10^{-1}$ related to noise. A more controllable version than simple thresholding could be achieved by re-defining the classical definition of the gradient operator in equation 3.4 and generalize it by multiplying it with a weighting function:

$$\nabla_x^w f^d \approx (f_x - f_{x-1}) \cdot w\,(f_x, f_{x-1}) \tag{3.6}$$

In the next step we want to keep a close eye on the formulation of a *specific* weighting function out of the set of possible weighting functions in equation 3.6. $\nabla_x^w f^d$ obviously conditions the gradient operator and intuitively one can question which positive effects can be expected. One can question:

- *Which* gradients in the Gradient Magnitude Distribution of the current image estimate should be weighted?
- *How* can the weight contribution be controlled for the optimization of the objective function?

For the design of a specific weighting function, we want to comprise the answers of the previous two questions. Concerning the first question, it is evident that minimizing the Total Variation of an image (estimate) during the optimization process should lead to a noise-free and artifact-free result. However, by definition, when the TV method is used in penalized cost functions, all gradients related to noise and prominent edges are penalized at an equal amount. It could be more efficient to solely penalize GMs related to noise and leave all other GMs untouched during the optimization. In such a way, the data term of the objective function can then restore the prominent edges. A specific weighting function should therefore be able to separate noise and prominent edges.
Concerning question two, a specific weighting function should produce weights in a useful interval of $[0, 1]$, ranging from zero contribution (weight = 1) to full contribution (weight = 0) of the weight at the current pixel location and intensity. Furthermore, a parameter which can be manually adjusted should control which Gradient Magnitudes (of a certain intensity) should be considered for the weighting. Typically, GMs related to noise have a lower intensity than GMs related to prominent edges (see the noisy GMs in figure 3.1 e). This fact enables the separability of the GMs. The precondition we impose on the data to be reconstructed is therefore twofold:

1. The Gradient Magnitude Distribution of the examined object consists of a small set of isolated peaks (see the true GMs (squares) in figure 3.1 e)).

2. The distance between the peaks is much bigger than the noise standard deviation in the image (see the noisy GMs (dots) in figure 3.1 e)).

Concentrating the previous information on a reasonable choice of a specific weighting function for ATV in equation 3.6, we therefore define $w(\cdot)$ as:

$$w\left(\nabla_x f^d\right) \approx e^{\left(-\frac{1}{2}(f_x - f_{x-1})^2/\sigma^2\right)} \tag{3.7}$$

due to the following reasons:

- By definition, the non-linear weighting function can control which Gradient Magnitudes are weighted, by tuning parameter σ. If the squared difference in the $e^{(\cdot)}$ function, $(f_x - f_{x-1})^2$, is high (representing a true edge) and σ is low, the weight $w(\cdot)$ is close to 0 and therefore, the true Gradient Magnitude can be restored. If the squared difference, $(f_x - f_{x-1})^2$, is low (representing an edge related to noise) and σ is low, the weight $w(\cdot)$ is close to 1 and the Gradient Magnitude related to noise is penalized. Therefore, the lowest possible value for σ should be chosen such that still a noise-free image can be achieved. A suitable value for parameter σ depends on the intensity of the actual GM in the image and therefore has to be found heuristically.

- By definition, the non-linear weighting function produces useful weights in the interval of $[0, 1]$, ranging from 0 contribution, where the weight is equal to 1, to full contribution, where the weight is 0.

The discrete and specific version of our proposed regularization function therefore reads as follows:

$$\begin{aligned} \mathrm{ATV}(\mu) &= \int_\Omega \left|\nabla^w_{x,y}\mu\right| dxdy \approx \\ &\sum_{x,y} \sqrt{\left(\left(\mu_{x,y} - \mu_{x-1,y}\right) e^{\left(-\frac{1}{2}(\mu_{x,y} - \mu_{x-1,y})^2/\sigma^2\right)}\right)^2 + \\ &\left(\left(\mu_{x,y} - \mu_{x,y-1}\right) e^{\left(-\frac{1}{2}(\mu_{x,y} - \mu_{x,y-1})^2/\sigma^2\right)}\right)^2 + \varepsilon}\; dxdy \end{aligned} \tag{3.8}$$

Parameter $0 < \varepsilon \ll 1$ enables the differentiability of equation 3.8. By definition, the Total Variation does not distinguish between GMs related to noise (which have small intensities) and large GMs related to prominent edges (which have high intensities). Our proposed method, however, can differentiate between these features: It can separate GMs of different intensities.

When parameter σ is tuned efficiently, ATV acts like a threshold of the noise, where GMs which have a low intensity and are related to noise can be separated from those GMs which have a high value and are related to prominent edges. The following experiment underlines these basic findings.

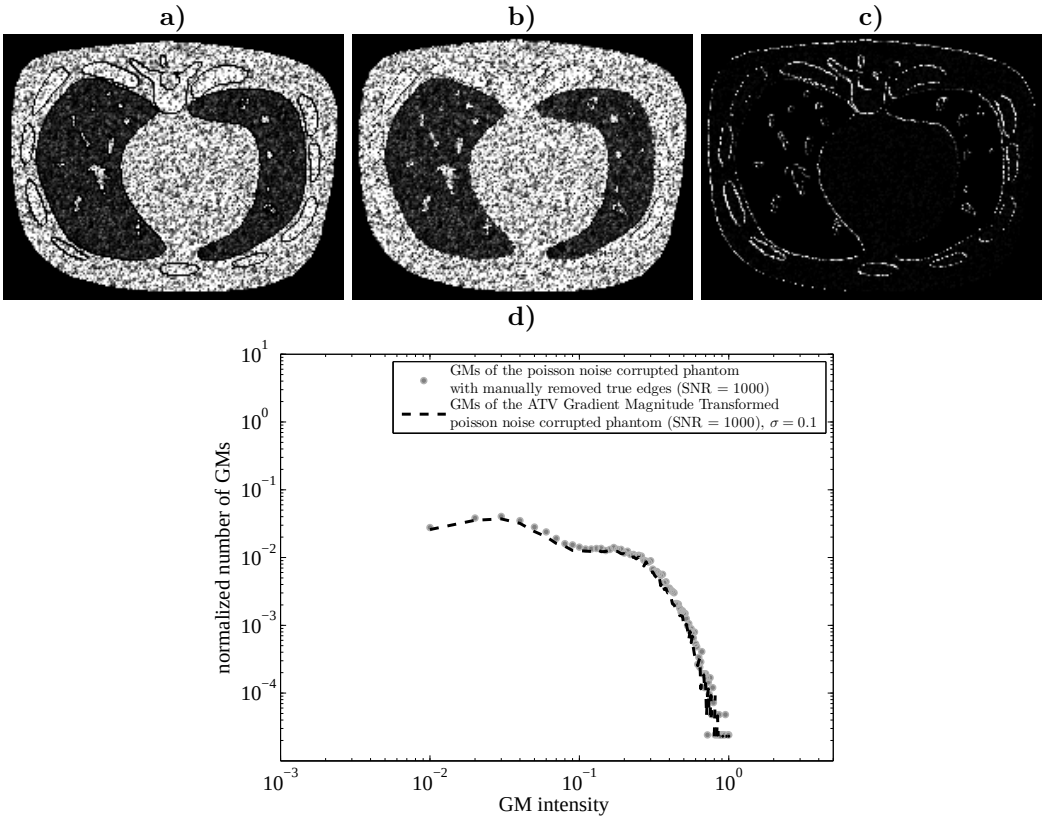

Figure 3.2: a) The Gradient Magnitude Transform of the POISSON noise corrupted lung phantom (SNR of the bone = 1000) with manually removed true GMs. b) The ATV Gradient Magnitude transform of the Poisson noise corrupted lung phantom. c) The difference between a) and b) (window-level of all figures 0.0105 - 0.2366). d) The Gradient Magnitude distribution of a) and b).

Figure 3.2 a) is equal to figure 3.1 d), however, the true GMs (displayed in figure 3.1 c)) were manually removed. What remains are the GMs related to noise. Now we want to show that if a suitable parameter for σ is selected, ATV, equation 3.8, can remove the true GMs, too, such that only GMs related to noise remain: Figure 3.2 b) shows the ATV Gradient Magnitude transform of the Poisson noise corrupted lung phantom in figure 3.1 b) for a specific value of σ. In figure 3.2 d), one can clearly see that given a suitable parameter for σ, the GMD of ATV (dashed line) can approximate the GMD related to noise (dots) of figure 3.2 a) quite well. A high quality CT image can therefore be reconstructed if ATV is used as a penalty term. The reason is that ATV solely penalizes GMs related to noise during the optimization and does not penalize all other GMs. In addition to that, the aforementioned problems of TV could be addressed as well.
It should be noticed that not all true GMs can be removed by ATV in contrast to manual thresholding, compare figure 3.2 b) with figure 3.2 a). The difference of those figures is displayed in figure 3.2 c). Only the true edges which were not suppressed by ATV remain in image c). The reason is that noisy GMs which have the same intensity as the prominent GMs cannot be separated by ATV. This could be a limitation of the method, especially in extremely noisy scenarios.
The effects of the gradient re-definition with application to Anisotropic Total Variation minimization in regularized tomographic reconstruction are experimentally evaluated in the next sections and compared to the state of the art methods, Total Variation and Filtered Backprojection.

The derivative of ATV is defined as follows:

$$
\begin{aligned}
&\frac{\partial \mathrm{ATV}(\mu_{x,y})}{\partial \mu_{x,y}} = \frac{\partial \mathrm{ATV}(\mu_{x,y})}{\partial \mu_{x,y}} + \frac{\partial \mathrm{ATV}(\mu_{x+1,y})}{\partial \mu_{x,y}} + \frac{\partial \mathrm{ATV}(\mu_{x,y+1})}{\partial \mu_{x,y}} \approx \\
&\Big(- \Big((\mu_{x,y} - \mu_{x-1,y})^3 e^{\left(-\frac{1}{2}(\mu_{x,y}-\mu_{x-1,y})^2/\sigma^2\right)} \Big) /\sigma^2 + (\mu_{x,y} - \mu_{x-1,y}) e^{\left(-\frac{1}{2}(\mu_{x,y}-\mu_{x-1,y})^2/\sigma^2\right)} \\
&- \Big((\mu_{x,y} - \mu_{x,y-1})^3 e^{\left(-\frac{1}{2}(\mu_{x,y}-\mu_{x,y-1})^2/\sigma^2\right)} \Big) /\sigma^2 + (\mu_{x,y} - \mu_{x,y-1}) e^{\left(-\frac{1}{2}(\mu_{x,y}-\mu_{x,y-1})^2/\sigma^2\right)} \Big) / \\
&\sqrt{(\mu_{x,y} - \mu_{x-1,y})^2 e^{\left(-\frac{1}{2}(\mu_{x,y}-\mu_{x-1,y})^2/\sigma^2\right)} + (\mu_{x,y} - \mu_{x,y-1})^2 e^{\left(-\frac{1}{2}(\mu_{x,y}-\mu_{x,y-1})^2/\sigma^2\right)} + \varepsilon^2} \\
&- \\
&\Big((\mu_{x,y} - \mu_{x+1,y}) e^{\left(-\frac{1}{2}(\mu_{x,y}-\mu_{x+1,y})^2/\sigma^2\right)} \Big) /\sigma^2 \left((\mu_{x,y} - \mu_{x+1,y})^2 - \sigma^2 \right) / \\
&\sqrt{(\mu_{x,y} - \mu_{x+1,y})^2 e^{\left(-\frac{1}{2}(\mu_{x,y}-\mu_{x+1,y})^2/\sigma^2\right)} + (\mu_{x+1,y} - \mu_{x+1,y+1})^2 e^{\left(-\frac{1}{2}(\mu_{x+1,y}-\mu_{x+1,y+1})^2/\sigma^2\right)} + \varepsilon^2} \\
&- \\
&\Big((\mu_{x,y} - \mu_{x,y+1}) e^{\left(-\frac{1}{2}(\mu_{x,y}-\mu_{x,y+1})^2/\sigma^2\right)} \Big) /\sigma^2 \left((\mu_{x,y} - \mu_{x,y+1})^2 - \sigma^2 \right) / \\
&\sqrt{(\mu_{x,y} - \mu_{x,y+1})^2 e^{\left(-\frac{1}{2}(\mu_{x,y}-\mu_{x,y+1})^2/\sigma^2\right)} + (\mu_{x-1,y+1} - \mu_{x,y+1})^2 e^{\left(-\frac{1}{2}(\mu_{x-1,y+1}-\mu_{x,y+1})^2/\sigma^2\right)} + \varepsilon^2}
\end{aligned}
\tag{3.9}
$$

3.3.2 Data acquisition

We test the proposed algorithm on a noise-free digitally simulated lung phantom, displayed in figure 2.4 a) and b) and a real patient measurement of a human head, displayed in figure 2.5 a) and b). For more details on the phantoms, see sections 2.2.1.3 and 2.2.1.4. The human head was scanned with an Elekta XVI CBCT, located at the University Medical Center in Mannheim. The detector has a size of 409.6mm×409.6mm and consists of 1024×1024 pixels. The source-to-isocenter distance is 100cm and the source-to-detector center is 153.6cm. The detector bin scale is 0.4mm ×0.4mm. We performed a scan, where 72 projections were acquired at equidistant rotation angles in the interval $[0, \pi]$. The sinogram data was then internally down-sampled to 512×512 pixels by the CT machine using the method of bilinear interpolation. The tube voltage was 120kV, the tube current 10mA and the pulse length was 10ms resulting in a dose of 0.1mAs per projection. The LACs of the lung phantom were normalized between $[0, 1]$ using equation 5.5. We selected a cone-beam configuration similar to the settings of the Elekta XVI CBCT. The source-to-isocenter distance is 100cm and the source-to-detector distance is 130cm. The number of detector bins is 256×256 and the detector bin scale is 1mm×1mm. 40 projections were acquired at equidistant rotation angles in the interval $[0, \pi]$. The same projector for forward- and back-projection is chosen. To compute the length of the projection line i that intersects pixel j, a fast ray tracing algorithm was used [310]. The projection set was normalized by $\tilde{Y} = \frac{Y}{\max(Y)}$ prior to the iterative reconstruction.

3.3.3 Quality metrics

We assess the quality of the reconstructions by subjective human judgment, since this type of evaluation is still the best quality evaluation method compared to ongoing research for optimal objective image quality metrics [352].
We define a visual quality acceptance test for the algorithms by judging the reconstruction results solely on a visual basis. As a common rule of passing the visual acceptance test the resulting images should:

- be as close as possible to the reference image.
- be piece-wise constant, no noise should be left in the image.
- not introduce additional artifacts in the image.
- have sharp edges, with a high acutance and which are not blurred.
- preserve small-scaled image features and those of small intensity.

This ensures on one hand that a high resolution image is reconstructed, since even small structures can be restored; and on the other hand, the noise is completely removed, since the resulting image consists of piece-wise constant areas. The visual acceptance test does not rate the accurate reconstruction of the contrast level. This property is neglected, since the contrast can always be adapted to a certain level by e.g. contrast-limited adaptive histogram equalization or contrast-enhancing methods. All of the points above have an equivalent weighting for the evaluation of the best achievable reconstruction result, but, of course, a balanced ratio of the points is important, too. For example an image which contains only very few artifacts but is perfectly sharp, piece-wise constant and small-structures are reconstructed quite well, is valuable, too.

3.3.4 Parameterization of FBP

For the definition of FBP, see section 2.3.3. We selected the Ram-Lak filter [283] for FBP, since this filter has the characteristic to restore images with the highest spatial resolution among other possible filter choices like the Shepp-Logan filter or the Hanning filter [227] and it does not magnify the noise.

3.3.5 Parameterization of TV

The Total Variation depends on two parameters: ε and β. $\varepsilon = 10^{-8}$ ensures the differentiability of equation 2.29. The value was found empirically. It is not sensitive. Regularization parameter β controls the impact of TV on the fidelity term in equation 3.1. We empirically found that a too low value of $\beta \ll 10^{-3}$ leads to a result with remaining under-sampling artifacts and noise left in the image, whereas a too high value of $\beta \gg 10^{-3}$ causes an over-smoothing of fine structures. We start the evaluation of a suitable β with a low value of $\beta = 10^{-4}$, which still yields a noise and artifact-corrupted result. Then, successively increasing β for each reconstruction, removes the noise in the reconstructions more an more for each updated value of β. We stop the process of increasing β if the visual acceptance test is passed. The scheme is summarized in algorithm 1.

Algorithm 1 Parameterization of ML-EM-TV

1: **normalize** Y: $\tilde{Y} = \frac{Y}{\max(Y)}$
2: **initialize** $\mu = 0.001$, $\beta = 0.0001$
3: **while** (**visual acceptance test in section 3.3.3 has not passed**) **do**
4: **solve** equation 3.1 using ML-EM in equation 2.27, where $\phi(\cdot) = TV$
5: **update** $\beta = \beta + 0.0001$ in equation 2.35
6: **visually** check reconstructed output
7: **end while**

$\beta = 0.03$ passes the visual acceptance test for the reconstructions of the lung phantom in figure 2.4 a) and b). $\beta = 0.035$ was selected for the head data in figure 2.5 a) and b).

3.3.6 Parameterization of ATV

The selection of a suitable parameter for σ in ATV depends on the "amount" of noise in the current image (estimate). When ATV is parametrized efficiently, it can separate GMs related to noise and true GMs in the GMD of the current image estimate. We observed that noise is not the only source of corruption the regularization method has to deal with. In fact, under-sampling artifacts are dominating at the first iterations. The "amount" of the under-sampling artifacts in the initial image estimate cannot be quantified a priori, since it highly depends on the experimental setup, for example on how many projections are considered for the reconstruction and which algorithm is chosen for the back-projection. Consequently, the best parameter for σ in equation 3.9 has to be found heuristically.
As a basis, we take the optimal regularization parameter found for TV in section 3.3.5, since our proposed regularization function, ATV, is a generalization of TV and especially for $\sigma = \infty$ the weight $w(\cdot)$ equals 1 and then TV and ATV are equal as well. We set $\beta = 0.03$ in case of digitally simulated phantom data and $\beta = 0.035$ for the patient data reconstructions. A suitable choice for σ yields a balanced ratio between smoothing and edge detail. We therefore test several parameters of σ, which lead to the best separation of prominent GMs and noisy GMs. We start with an extreme low value of $\sigma = 5 \cdot 10^{-8}$, so as not to loose any important structure and we then successively increase sigma for each experiment. We stop the process of finding best parameters if the visual acceptance test is passed. Algorithm 2 summarizes the scheme.

Algorithm 2 Parameterization of ML-EM-ATV

1: **normalize** Y: $\tilde{Y} = \frac{Y}{\max(Y)}$
2: **initialize** $\mu = 0.001$, $\beta = 0.03$ (as found for TV, lung phantom) or $\beta = 0.035$ (as found for TV, head data), $\sigma = 5 \cdot 10^{-8}$
3: **while** (**visual acceptance test in section 3.3.3 has not passed**) **do**
4: **solve** equation 3.1 using ML-EM in equation 2.27, where $\phi(\cdot) = ATV$
5: **update** $\sigma = \sigma + 5 \cdot 10^{-8}$ in equation 3.9
6: **visually** check reconstructed output
7: **end while**

Based on the visual acceptance test, we found that $\sigma = 5 \cdot 10^{-7}$ produces the best result for both, the lung phantom and the head data with the highest image quality.

3.4 Results

We examine the reconstruction results on the basis of human perception. We selected a typical result which passed the visual acceptance test. The reconstructed images of the digital lung phantom and real patient data is visualized in figures 3.3 and 3.4 respectively.
When only 40 projections are obtained during the CT scan, ML-EM-ATV can reconstruct a piece-wise constant result, see figure 3.3 a). ML-EM-TV, however, produces stair-cases in regions which should be flat, see figure 3.3 c). The image produced by Filtered Backprojection in 3.3 d) is heavily corrupted by streaking artifacts and noise. In case of 72 projections, both methods, ML-EM-TV and ML-EM-ATV, can produce a piece-wise smooth result, see figure 3.4 a), b), d) and e).
The results in figure 3.3 and figure 3.4 show that the spatial resolution for the ATV regularized reconstruction is by far higher than for TV, since small structures of only a single pixel width, marked by an arrow in the images, are better and more clearly restored by ML-EM-ATV compared to ML-EM-TV or FBP, where they are over-smoothed or blurred.
ML-EM-ATV reconstructions have edges which visually have a higher acutance and are sharper, compared to the results of ML-EM-TV, see figures 3.3 and 3.4. For ML-EM-TV, the edges are blurred and from a visual perspective they have a low acutance.

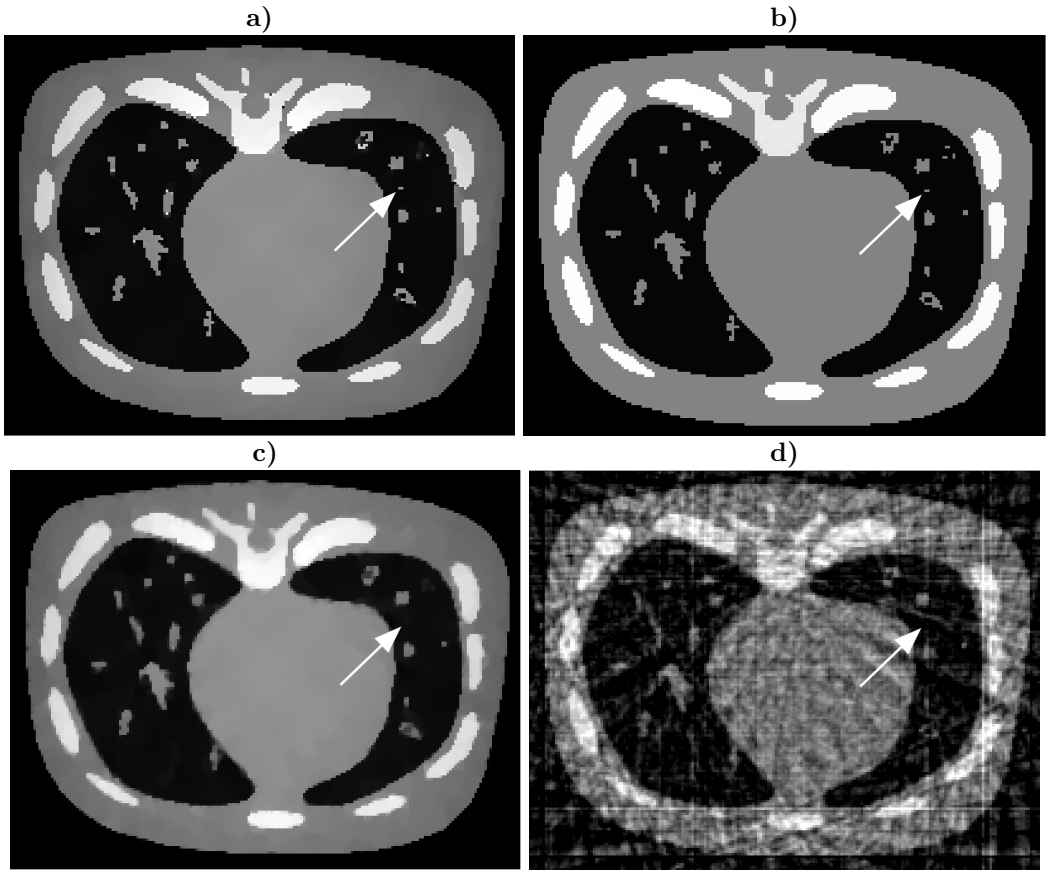

Figure 3.3: The lung phantom was reconstructed from 40 projections. a) ML-EM-ATV (window-level: [0.0039,0.6433]). b) The ground truth (window-level: [0,1]). c) ML-EM-TV (window-level: [0,0.9953]). d) Filtered Backprojection (window-level: [0.0039,0.8008]).

Based on human perception, the same level of edge sharpness and spatial resolution can be achieved for ML-EM-ATV in case of an under-sampled scenario of 72 projections compared to the FBP-reference, where 360 projections have been considered, compare figures 3.4 b) with c) and figure 3.4 e) with f). For ML-EM-TV, however, the edges are blurred, compare figures 3.4 a) with c) and figure 3.4 d) with f).

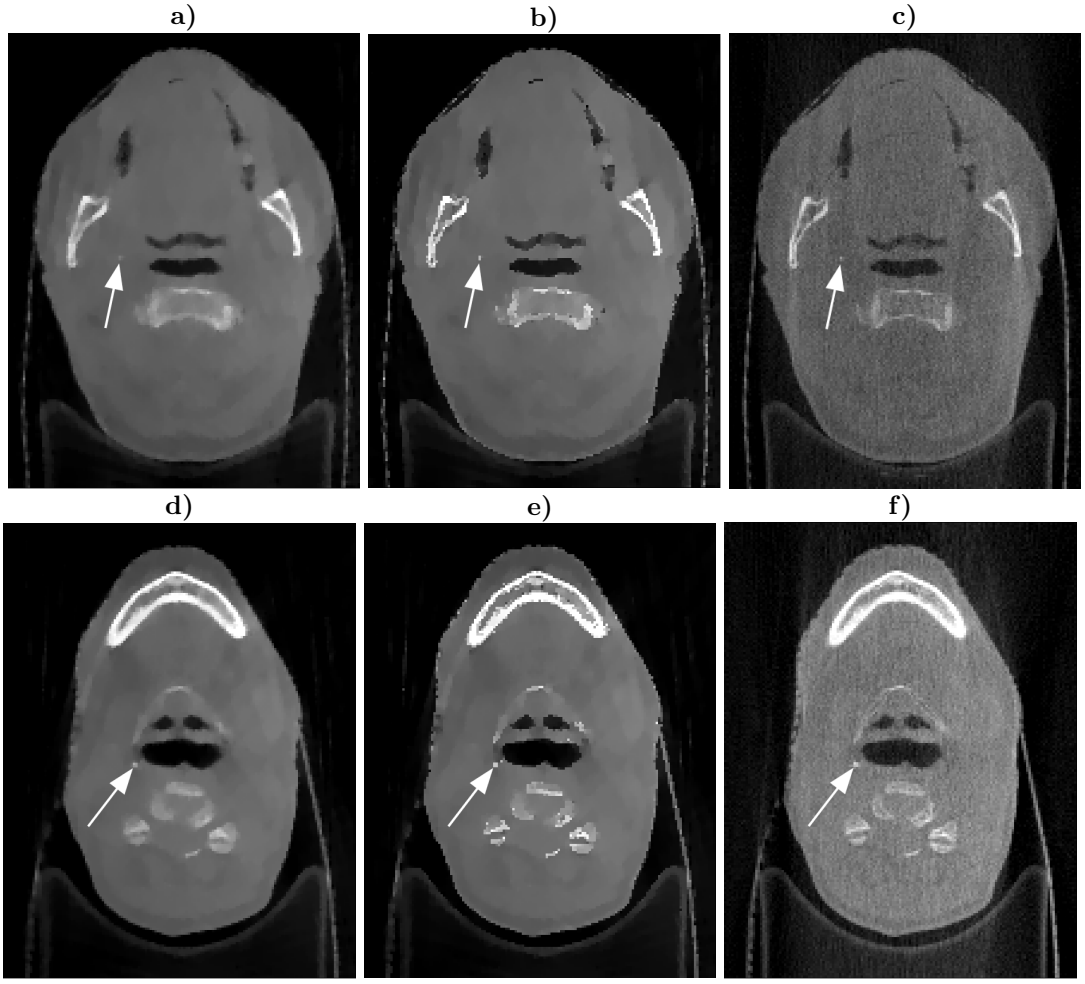

Figure 3.4: A patient's head data set obtained by an Elekta XVI CBCT was taken for the reconstruction. a) and d) Reconstruction results of the ML-EM-TV (window-level: [0.0208,0.0970]). b) and e) ML-EM-ATV (window-level: [0.0208,0.0970]). An under-sampled scenario of 72 projection views was chosen. c) and f) The reference-FBP method. 360 projection views were selected (window level of image c) [0,0.8947], window-level of image f) [0,0.7164]).

3.5 Discussion

The results show the positive effects of using ATV as a regularization function and the consequences of a gradient re-definition, where solely GMs related to noise are penalized during the reconstruction. ATV can produce piece-wise constant results with sharp and clear edges and single pixel accuracy. This can be achieved by anisotropically smoothing longitudinal to the edge. The TV, however, aims at minimizing the (Total) Variation (i.e. the sum of all GMs) for the whole image at an equal measure, not respecting image features of small scale or small intensity. That is to say: The TV does not differentiate between GMs related to noise and GMs related to prominent edges and therefore over-smoothes small details and blurs the edges.
The results of FBP are not usable for medical or industrial diagnostics since they are heavily corrupted by streaking artifacts and noise.

The fact that the optimal regularization parameter, β, is equal for ML-EM-TV and ML-EM-ATV, is an indicator that the edge-preserving properties of ML-EM-ATV solely depend on the correct choice of σ. Our specific version of the weighting function for the gradient re-definition is appropriate to separate GMs related to noise and true GMs, as the resulting high quality images indicate. In an extremely noisy scenario, ATV cannot separate GMs related to noise and true GMs, since they have the same intensity. As a consequence, the resulting reconstruction will be noisy. This is a limitation of the method.
Contrary to the ML-EM-TV reconstructions, ML-EM-ATV reconstructions suffer from a loss of contrast, e.g. for the under-sampled case of the digital lung phantom reconstructions. The loss of contrast can be compensated by a posteriori window-level enhancement. The equal window-levels of the ML-EM-TV and ML-EM-ATV-based real data reconstructions indicate that there is no contrast loss for real data reconstructions.
The evaluation method which is based on subjective human perception is fast and in many cases more reliable than objective quality methods. A disadvantage is that subjective human perception is not so precise in every case and therefore, a more valuable parameter σ for ML-EM-ATV could be found by including objective quality metrics.

3.6 Conclusion

The work in this chapter represents a proof-of-concept. We showed that the gradient can be re-defined by multiplying it with a specific function and we discussed the consequences of such an approach for few-view tomography on digital phantoms and real patient data as well. Our proposed method can produce results with a better image quality than the current state of the art methods, TV and FBP. Based on visual inspection, the results of our method are shaper, have a higher resolution and small objects of single pixel width can be reconstructed as well. Whether this approach is also suitable for dose reduction requires a further investigation of the method using quantitative quality metrics and a larger set of measurement experiments. This will be done in chapter 6 of this dissertation.
The performance of the proposed method could be evaluated in the context of limited-angle tomography or **D**igital **B**reast **T**omography (DBT), where strong regularization functions are demanded. In future, other specific functions for $w(\cdot)$ in equation 3.7 could be found which can produce even better results than ML-EM-ATV.
A more valuable parameter for σ in ML-EM-ATV, which does not lead to a huge loss of contrast when synthetical data is reconstructed, could be found by including objective quality metrics into the process of finding suitable parameters. An evaluation of the robustness of ATV under clinical assurance conditions, as presented in [332], could be a further topic of interest.

Chapter 4

CT Reconstruction from Few-Views by Higher Order Adaptive Weighted Total Variation Minimization

4.1 Outline

The work in this chapter was presented at the **Fully 3D** conference and published in the conference proceedings [70] in July, 2013. We show that higher order derivatives enable a suppression of the stair-case artifact produced by TV and modern AwTV. We combine first order anisotropic and second order isotropic gradients into a new regularization function. For the first order part, we take the AwTV (described in section 2.2.4.3 and defined in equation 2.32) and for the second order part, we take conventional TV (defined in equation 2.33). We evaluated the new method on digitally simulated phantom data and simulated real data. Our proposed method is up to 1.57 times more homogeneous than AwTV and up to 7.7 times more homogeneous than TV. Furthermore, in contrast to TV, prominent edges, small details and structures are preserved by our method. The spatial resolution of our proposed method is 26% higher than TV and equal to AwTV. We therefore conclude that introducing second order derivatives does have an effect on the spatial resolution if they are combined with first order gradients. Furthermore, stair-casing artifacts of TV can be suppressed since second order derivatives prefer smooth transitions over jumps. The examination of the contour map indicates that our method produces the best result concerning the homogeneity, since all level lines in constant regions lie far apart. This is not the case for the other methods, TV and AwTV. Here, the level lines which are close to each other or even overlap indicate an edge, which is undesired in regions which should be constant.

4.2 Introduction

Since dose reduction is an important issue in medical CT, our experiments in this chapter are based on a low-dose scenario which can be achieved by under-sampling the target and decreasing the current of the X-ray machine; see section 2.2.4.4 for recent publications and further details. The consequences for under-sampling the target and a tube current reduction are on one hand positive effects regarding the possibility to reduce the dose in medical CT and the acquisition time in industrial CT, but on the other hand, a demand of efficient reconstruction algorithms which can remedy the resulting image quality corruption. Total Variation regularization, described in section 2.2.4.3 and defined in equation 2.29, is very effective for removing the streaks and noise caused by a reduction of the tube current, since it is a sparsity transform of the Compressed Sensing paradigm, see section 2.2.4.3. We describe the properties of TV in section 2.2.4.3. A draw-back of Total Variation is the introduction of stair-casing artifacts in regions which should

be homogeneous, since edges are introduced in the results which are related to the noisy pixels but not to prominent features of the underlying true object itself. Another problem of TV is that it over-smoothes fine structures of small scale and intensity. The proposed method in this chapter addresses these disadvantages and we will analyze the results from a qualitative point of view by means of inspecting the reconstructed images and quantitative means, by applying error measurement metrics. We will show that our method can reduce the stair-casing effect of TV and at the same time reconstruct small objects, which are over-smoothed by TV.

4.3 Material and Methods

The mathematical notation and the abbreviations we use in this chapter are listed in table 1.
The acquisition model of X-ray Computed Tomography can be described by a linear equation, see equation 2.14. We apply a Poisson noise model for the measurements, defined in equation 2.16. We do not model the detector noise, since its contribution is much smaller than the signal of interest [377]. If at least 1000 photons per pixel are captured, equation 2.16 is valid [287]. This can be explained by the Central Limit theorem. Since the variance of a Poisson Distribution equals its mean and the standard deviation of Poisson noise is equal to the square root of the average number of events, a relation of the SNR of the projection data to the number of incident photon counts, d_0, exists. It is therefore possible to apply artificial Poisson noise to the projection data such that the resulting projection has a specific SNR. For a relation of the tube current and the SNR of the sinogram see [332] and table 2.3. Based on a Poisson noise model, a likelihood function can be derived; see equation 2.23. The corresponding objective function then reads as follows:

$$\mu^* = \underset{\mu'}{\operatorname{argmax}}\ L(y, \mu') - \beta\phi\left(\mu'\right), \tag{4.1}$$

see section 2.2.4.1 for details. The Maximum Likelihood Expectation Maximization algorithm presented in equation 2.27 finds a unique solution to this cost function. For the regularization term, $\phi(\cdot)$, we propose to combine first and second order gradients. The first order Adaptive Weighted Total Variation regularization function is introduced in [218], described in section 2.2.4.3, defined in equation 2.32, discretized and deviated in equation 2.37. We combined this first order AwTV with a second order Total Variation, see section 2.2.4.3 for details, equation 2.39 for a definition and a discretization and equation 2.40 for the derivative of the second order TV.
Let us now concentrate on the proposed regularization function.

4.3.1 Idea of the method

As discussed in the previous chapter of this thesis, the discretized *first order* gradient of a function $f^d : U^d \to \mathbb{R}$, can be approximated by a left-sided differences expression; $U^d \subset \mathbb{R}$, the points $x, h \in \mathbb{N}^+$ and a grid size of $h = 1$:

$$\nabla f^d\left(x\right) \approx \frac{f\left(x\right) - f\left(x-1\right)}{(x-1) - x} = f\left(x\right) - f\left(x-1\right), \tag{4.2}$$

The corresponding discretized *second order* gradient reads as follows:

$$\begin{aligned} &\nabla^2 f^d\left(x\right) \approx \frac{f\left(x\right) + 2f\left(x-1\right) - f\left(x-2\right)}{(x-1) - x} = \\ &f\left(x\right) + 2f\left(x-1\right) - f\left(x-2\right) \end{aligned} \tag{4.3}$$

For other discretization possibilities see section 2.2.5. A typical application of the gradient is found in Rudin Osher and Fatemis' Total Variation minimization algorithm [294], often applied as regularization term in CS-based reconstruction algorithms for reducing noise and under-sampling artifacts. For a description of the properties of TV, see section 2.2.4.3, for the definition of the TV, see equation 2.29.
As a matter of principle, medical and industrial images can be transformed into a sparse domain by equation 2.29 (see the black squares in the GMD of figure 3.1 e)). Minimizing the Total Variation in

CS-based reconstruction algorithms is based on the assumption that noise and artifact-free medical and industrial images are smooth everywhere in the image. This assumption is inadequate, since the variation in the image is definitely not minimal in *every part* of the image: The variation is maximal, especially at the edges. Consequences associated with this assumption for TV regularized CT are the over-smoothing of fine structures and the blurring of edges, especially in scenarios of high noise. In chapter 3, we discussed that a gradient re-definition with application to Anisotropic Total Variation minimization can overcome these limitations by smoothing longitudinally to the edge and therefore, preserving small structures:

$$\begin{aligned} \mathrm{ATV}(\mu) &= \int_{\Omega} \left|\nabla^{w}_{x,y}\mu\right| dxdy = \\ &\int_{\Omega} \sqrt{\left(\frac{\partial \mu}{\partial x} e^{\left(\left(\frac{\partial \mu}{\partial x}\right)^2/\sigma^2\right)}\right)^2 + \left(\frac{\partial \mu}{\partial y} e^{\left(\left(\frac{\partial \mu}{\partial y}\right)^2/\sigma^2\right)}\right)^2 + \varepsilon}\ dxdy \end{aligned} \tag{4.4}$$

where parameter $0 < \varepsilon \ll 1$ enables the differentiability of equation 4.4 and parameter $\sigma > 0$ controls the separation of high and low intensity Gradient Magnitudes. When parameter σ is tuned efficiently, ATV acts like a threshold of the noise. A similar expression (but not a re-definition of the gradient) is the Adaptive weighted Total Variation, introduced by [218], described in section 2.2.4.3 and defined in equation 2.32. The AwTV was the current state of the art at the time the proposed algorithm in this chapter was developed. Although the paper addressing the ATV method [71] was developed long before the publication of [218], it was published at a later date in [71]. We therefore use the AwTV method in this chapter.
ATV and AwTV respectively, can overcome TV's problem of over-smoothing fine structures and blurring the edges, since these functions smooth longitudinally to the edge.
The problem concerning the AwTV method of [218] is that the derivative is not computed in a mathematically correct way, see equation 2.37 and compare with the correct derivative of ATV in equation 3.9. In fact, the derivative of AwTV is just a weighted formulation of the TV derivative in equation 2.35, where each term in the derivative of TV was just multiplied by the corresponding $e^{(\cdot)}$ functions.
A remaining problem of TV is the production of "stair-cases" in regions which should be flat. Total Variation tends to yield piece-wise constant images. The effect can be best described in one dimension: "Let us consider a 1 dimensional line through the true image μ_x and the fact that the pixel intensities are monotonically increasing around a point in μ_0, i.e. $\mu_{-1} < \mu_0 > \mu_1 < \mu_2$. The Total Variation model cannot preserve this monotonicity since $\nabla\mu_{-1} < \nabla\mu_0 = \nabla\mu_1 < \nabla\mu_2$ and then, visually $\nabla\mu$ looks like a staircase at μ_0 instead of a monotonically increasing signal" (explanation taken from [47]).
Intuitively, to preserve the monotonicity of neighboring pixel values one could penalize jumps, or GMs, stronger. This can be achieved by incorporating higher order derivatives. "For example, consider a discrete step function at a height of $h = 1$ (e.g. equation 3.2). The first order derivate (equation 4.2) of this function is $1/h$ and the second order derivative (equation 4.3) is $1/(h^2) \gg 1/h$, when $h \approx 0$" (explanation taken from [48]). Consequently, higher order derivatives prefer smooth transitions over jumps and can preserve the monotonicity of neighboring pixel values even in noisy environments.
To avoid the stair-casing effect of TV, one could just penalize jumps stronger by using the second order discretization scheme. Regularization functions which solely use second order gradients, e.g. equation 2.33, can suppresses the stair-casing artifact, since jumps are penalized stronger. However, they lead to a blurring of edges, too, since slopes are penalized stronger compared to the first-order case (conventional TV, equation 2.29).

We therefore propose a regularization function which combines first order (anisotropic) gradients with second order (isotropic) gradients. Our proposed function reads as follows:

$$\begin{aligned}
&\text{AwTV+TV}^2(\mu) = \int_\Omega (1-\lambda)\ \left|\nabla^w_{x,y}\mu\right| + \lambda\ \left|\nabla^2_{x,y}\mu\right|\ dxdy = \\
&(1-\lambda)\ \cdot \int_\Omega \sqrt{\left(\frac{\partial\mu}{\partial x}\right)^2 e^{\left(\left(\frac{\partial\mu}{\partial x}\right)^2/\sigma^2\right)} + \left(\frac{\partial\mu}{\partial y}\right)^2 e^{\left(\left(\frac{\partial\mu}{\partial y}\right)^2/\sigma^2\right)} + \varepsilon}\ dxdy + \\
&\lambda\ \cdot \int_\Omega \sqrt{\left(\frac{\partial^2\mu}{\partial x^2}\right)^2 + \left(\frac{\partial^2\mu}{\partial y^2}\right)^2 + \varepsilon}\ dxdy,
\end{aligned} \tag{4.5}$$

The first term of equation 4.5, $\left|\nabla^w_{x,y}\mu\right|$, computes the first order AwTV, equation 2.32. As discussed in chapter 3, ATV, respectively AwTV, can preserve small structures and smooth longitudinally to the edges since they can separate prominent edges and edges related to noise. The second term of equation 4.5, $\left|\nabla^2_{x,y}\mu\right|$, computes the second order TV^2, and penalizes jumps to a greater extend. One can thus say that ATV and AwTV, respectively threshold the image and exclude the prominent edges from penalization such that the second order TV can penalize these edges. A stronger penalization of slopes can be achieved by incorporating higher order derivatives.
A balanced ratio between edge separation, as achieved by ATV and AwTV and edge penalization, as achieved by TV^2 is able to suppress the stair-cases and to maintain a high resolution image, since solely GMs related to noise are penalized while other GMs are left untouched. At the same time, there is no penalization of small structures and true edges and they can be restored. The ratio of the influence of the first and the second term in equation 4.5 is controlled by parameter λ. The discretization and derivative of AwTV and TV^2 is given in equation 2.37 and equation 2.40 respectively.

4.3.2 Reconstruction data

We reconstruct the digital lung phantom presented in figure 2.4 a) and b). The Catphan phantom in figure 2.5 c) is used for quality control in CT. It contains several modules, for example the resolution module with 21 **l**ine-**p**airs (lp). The gauge accuracy is ± 0.5 line-pairs. The gauge is cast into epoxy and cut from 2mm thick aluminum sheets. In figure 4.1, ROIs and a line selection were placed on the lung and the Catphan data for the purpose of image quality assessment.

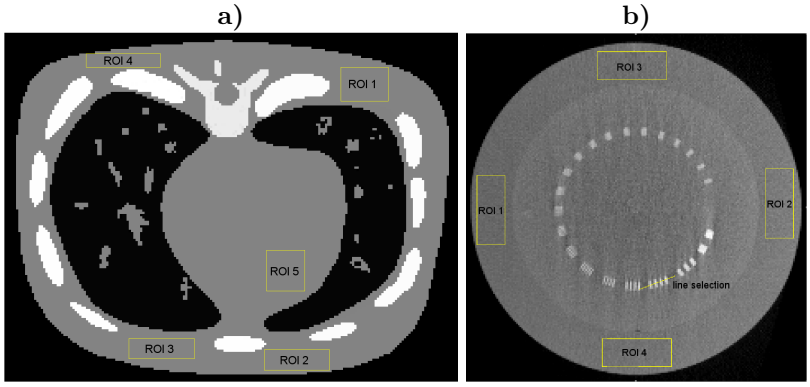

Figure 4.1: a) A digitally simulated lung phantom with small bronchi. b) A FBP reconstruction from 360 views of a Catphan 600 phantom scanned on an Elekta XVI CBCT.

4.3.3 Properties of the CT system

We simulated noise-free, two-dimensional projections based on a digitally three-dimensional artificial lung phantom, displayed in figure 4.1 a) and a Catpahn phantom in figure 4.1 b). We selected a cone-beam configuration similar to the settings of an Elekta XVI CBCT. The source-to-isocenter distance is 100cm and the source-to-detector distance is 130cm. The detector bin

scale is 1mm×1mm and the number of detector bins is 256×256. 40 projections were acquired at equidistant rotation angles in the interval $[0, \pi]$. The same projector is chosen for the forward- and backprojection operator. To compute the length of the projection line i that intersects pixel j, a ray tracing algorithm was used [310].
The scanner we use to acquire the real data is an Elekta XVI CBCT with 1024×1024 pixels mapped on the scanner field of 409.6mm×409.6mm. The sinogram data is internally down-sampled to 512×512 by the hardware of the CT machine using the method of bilinear interpolation.
The source-to-isocenter distance is 100cm and the source-to-detector center is 153.6cm. The detector bin scale is 0.4mm×0.4mm. For the scan we selected a tube voltage of 120kV, a tube current of 20mA and a pulse length of 10ms, resulting in a dose of 0.2mAs per projection. We performed a measurement, where 360 projections were acquired at equidistant rotation angles in the interval $[0, \pi]$. The projections were reconstructed using the FBP algorithm [93]. We then used the FBP reconstruction result to simulate 80 two-dimensional projections by a simple forward projection (equation 2.10). Since the forward projection is linear and FBP does not remove the noise, the same "amount" of noise is left in the simulated projections. We can therefore test our algorithm in a noisy scenario. The LACs of the phantoms were normalized between $[0, 1]$ (using equation 5.5) and the projection set was normalized before the reconstruction: $\tilde{Y} = \frac{Y}{\max(Y)}$. This makes it possible to use the same parameter settings for the methods in case of different modalities, scanning configurations and phantoms.

4.3.4 Figures of merit

We introduce a new quality measure to assess the non-homogeneity of an image: The **N**on-**U**niformity **E**rror **I**ndex (NUEI). It is computed over a manually pre-defined three-dimensional Region Of Interest where the true image is known to be homogeneous, e.g. ROI 1-5 in figure 4.1 a). As an intermediate step, we compute the 2×2×2 neighborhood variance of the pixels within the ROI resulting in the **P**ixel **V**ariance **M**ap (PVM) of the specified region. Then, the **S**tandard **D**eviation (SD) of the PVM is calculated to determine the homogeneity of the results:

$$\mathrm{NUEI(ROI)} = \frac{\sum_t (\mathrm{SD}(\mathrm{PVM}(\mathrm{ROI}_t)))}{\mathrm{T}}, \tag{4.6}$$

where $\mathrm{ROI_t}$ is the ROI number and $\mathrm{t} \in \mathrm{T}$ is the number of ROIs. For the NUEI, a value of 0 refers to a completely homogeneous result.
To visually determine the images' homogeneity, we compute the contour plot of the resulting images. Level-lines of the contour plot which lie close to each other refer to an edge, whereas level-lines which are a long distance away from each other indicate a constant region.

To compute the spatial resolution of an image one usually analyzes the **M**odulation **T**ransfer **F**unction (MTF). However, the regularization functionals $\phi(\cdot)$ we selected in this dissertation are non-linear. Therefore the interpretation of the MTF would be meaningless since images of arbitrary resolution could be generated. For non-linear systems, we need a different measure to rate the spatial resolution of the results. Intuitively the assessment of the spatial resolution is based on the ability to visually differentiate objects in an image from the background, e.g. line-pairs in the Catphan phantom in figure 4.1 b). We therefore analyze the profile plot of a linear selection through the line pair number 3 by the following strategy: After normalizing the pixels of the ROI to 1 (by dividing every pixel of the ROI by the maximum pixel intensity of the ROI), the intensities can be measured. Peaks in the plot refer to the line itself whereas valleys are denoted as background of the ROI. The ratio of the peaks and valleys can be determined by computing the Euclidean Distance. A value of 1 would then correspond to the highest resolution possible.
Furthermore, we judge the reconstruction results based on human visual assessment, since in many cases, it is still more adequate than objective image quality metrics [352]. The detailed description and conditions for passing the visual acceptance test are provided in section 3.3.3.

4.3.5 Parameterization of FBP

The FBP method is still the standard reconstruction routine in industrial and medical imaging [264]. There are several filter choices for the FBP algorithm [93], (e.g. Shepp-Logan or Hanning [227]). We selected the Ram-Lak filter [283] since it is known to produce images with the highest spatial resolution.

4.3.6 Parameterization of TV

Since the scanning modality, the objective function and the reconstruction algorithm we selected in this chapter is equal to the settings in chapter 3, we use the optimal parameters found for ML-EM-TV, see section 3.3.5. These are: $\beta = 0.03$ for the reconstructions of the digital lung phantom in figure 4.1 a) and $\beta = 0.035$ for the reconstructions of the Catphan real data in figure 4.1 b).

4.3.7 Parameterization of AwTV + TV^2

Our proposed regularization method, AwTV+TV^2, is a combination of 2 functions: AwTV and TV^2 and it depends on three parameters: σ, λ and β. For β, we apply the same parameter found for TV, since our proposed regularization function can be understood as a generalization of TV: If $\sigma = 1$ and $\lambda = 0$ in equation 4.5 we obtain standard TV.
For σ, we selected the value reported in [218]: $\sigma = 5 \cdot 10^{-6}$. To find an optimal value for λ, we employed the visual acceptance test described in detail in section 3.3.3 by empirically testing several parameters for $\lambda \in [0.01, 0.5]$. The best value of λ balances the edge-preserving properties of AwTV and the smoothing properties of TV^2 in such a way that a smooth image can be reconstructed with a high resolution. A too high value for $\lambda > 0.3$ does not suppress stair-cases and a too low parameter of $\lambda < 0.1$ over-smoothes the result and blurs the edges.

Algorithm 3 Parameterization of AwTV+TV^2

normalize Y: $\tilde{Y} = \frac{Y}{\max(Y)}$
initialize $\mu = 0.001$, $\beta = 0.03$ (in case of the lung phantom) or $\beta = 0.035$ (in case of the Catphan data), $\sigma = 5 \cdot 10^{-6}$, $\lambda = 0$
while (**visual acceptance test in section 3.3.3 has not passed**) **do**
  solve equation 3.1 using ML-EM in equation 2.27, where $\phi(\cdot)$ =AwTV+TV^2
  update $\lambda = \lambda + 0.01$ in equation 4.5
  visually check reconstructed output
end while

We found that $\lambda = 0.17$ for the reconstructions of the lung phantom (synthetic data) and $\lambda = 0.25$ for the reconstructions of the Catphan phantom (real data) produces the best results based on the human visual acceptance test in section 3.3.3.

4.4 Results

In figure 4.2 we show the reconstructions of the lung phantom from 40 projections. The true phantom is displayed in a). Visually, ML-EM-AwTV in b) and ML-EM-AwTV+TV^2 in d) can reconstruct sharp edges with a high acutance. Furthermore, these methods can preserve even small structures, e.g. bronchi of single pixel width as marked by an arrow. For ML-EM-TV in b), most of the edges are blurred and small structures are over-smoothed.

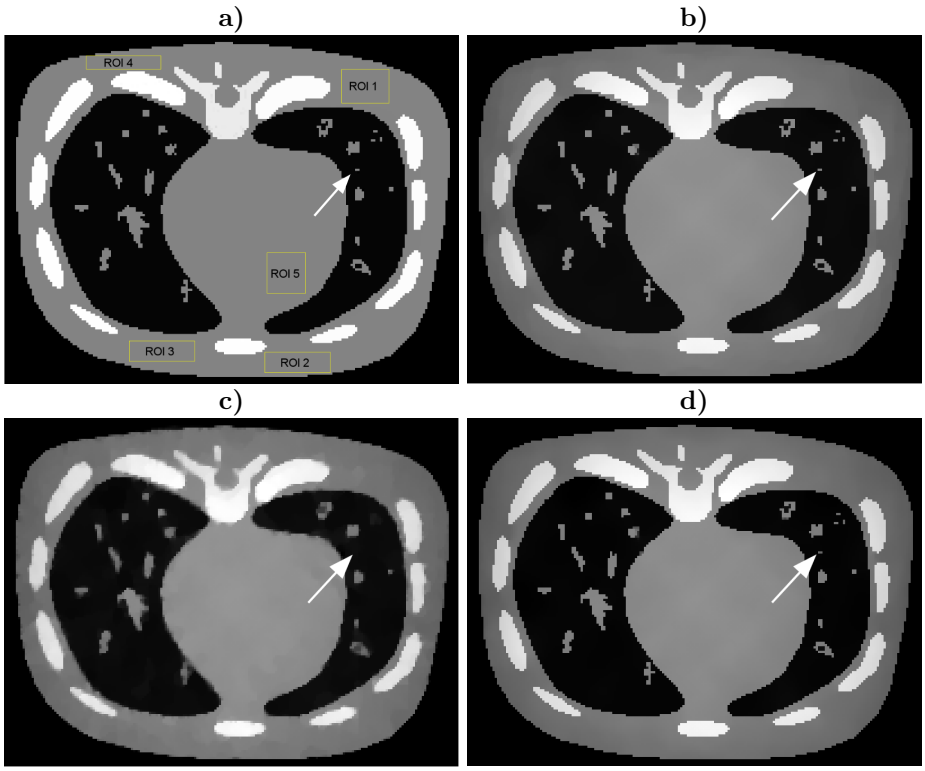

Figure 4.2: Reconstructions from 40 projections of the three-dimensional lung phantom. The gray-value interval for all images is $[0, 1]$. a) The true image containing five ROIs, where the homogeneity is measured, b) ML-EM-AwTV, c) ML-EM-TV, d) ML-EM-AwTV+TV^2. The white arrow indicates a small bronchi of a single pixel width which can be reconstructed by ML-EM-AwTV and ML-EM-AwTV+TV^2. For ML-EM-TV it is over-smoothed.

Our proposed method, ML-EM-AwTV+TV^2, can reduce the stair-casing effect of TV and produce smooth, piece-wise constant results, see figure 4.2 d). The images produced by ML-EM-AwTV in figure 4.2 b) and ML-EM-TV in figure 4.2 c) however suffer from stair-casing artifacts in regions where the true image in figure 4.2 a) is constant. The artifacts become visually clearer at a different window-level, see figure 4.3. The arrow in this figure indicates an area where stair-cases are dominant for ML-EM-AwTV and ML-EM-TV. For ML-EM-AwTV+TV^2, the area is smooth.

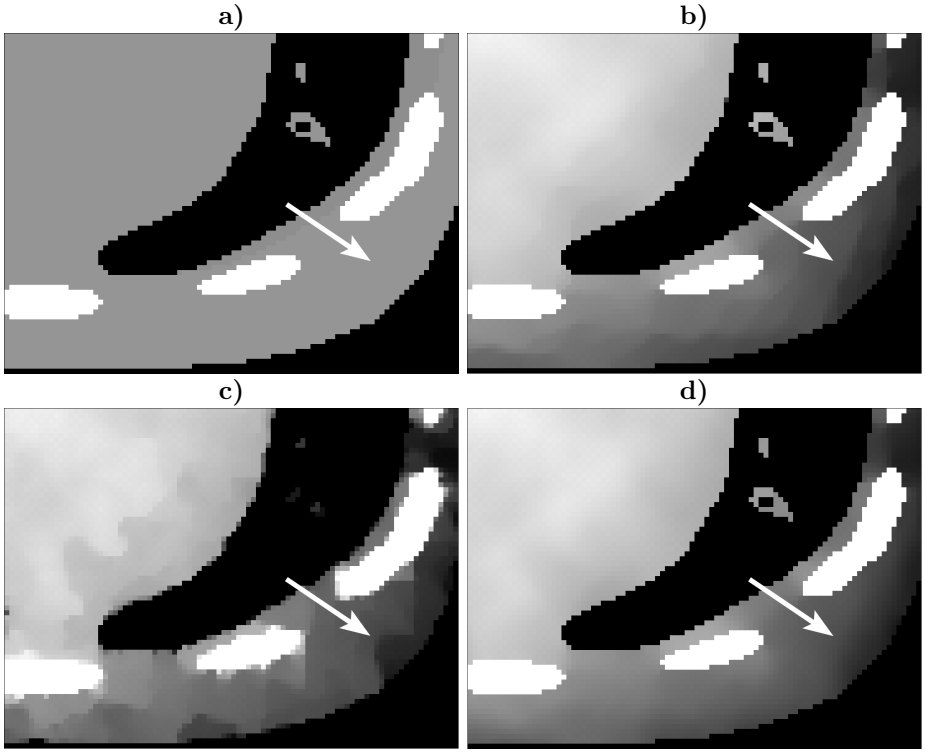

Figure 4.3: Cropped regions of the reconstructions presented in figure 4.2 at a different window-level: [0.38,0.61]. a) The true image, b) ML-EM-AwTV, c) ML-EM-TV, d) ML-EM-AwTV+TV^2.

The contour plots in figure 4.4 show level lines of the reconstruction results presented in figure 4.3. Level-lines which lie close to one another indicate an edge, whereas lines which are a long distance away from each other represent a constant area. It is evident that ML-EM-TV in figure 4.4 c) produces many edges in regions where the true image in a) is flat. ML-EM-AwTV can better suppress these undesired edges; however, they are still visible. The results of our proposed method, ML-EM-AwTV+TV^2, in d) has level-lines which are almost all spaced a long distance away from each other in regions where the true image is constant.

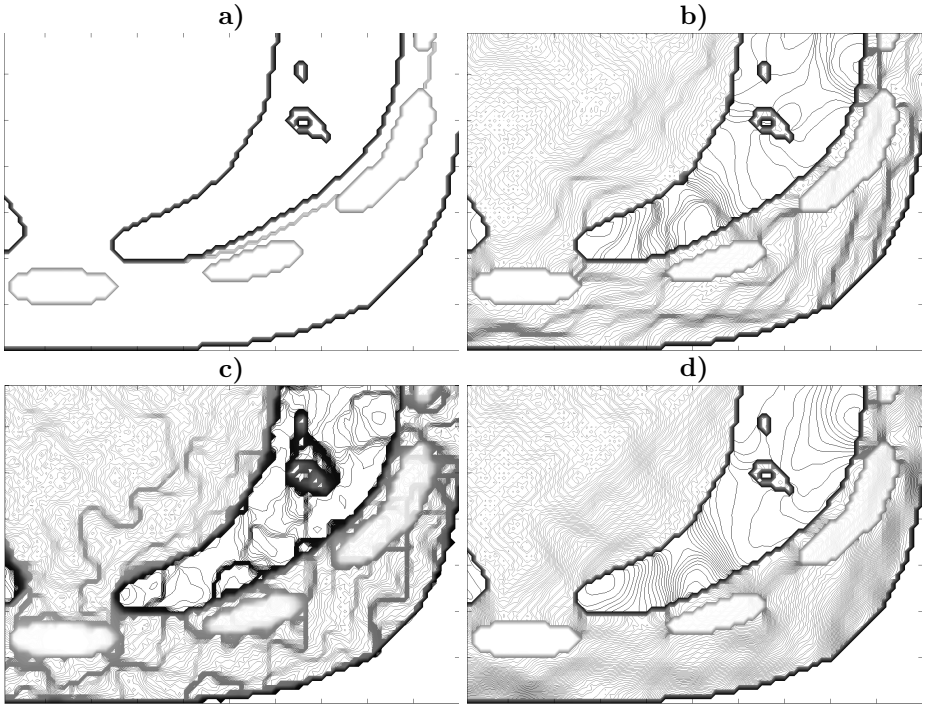

Figure 4.4: Contour plots of the reconstructions presented in figure 4.3. Level-lines which are close to one another indicate an edge whereas level-lines which lie a long distance away from each other represent a constant area. One can clearly see that ML-EM-AwTV+TV^2 in image d) has level-lines which are a long distance away from each other whereas the other methods, ML-EM-TV in image c) and ML-EM-AwTV in image b), produce edges and stair-cases respectively in regions which should be constant, cf. the original image in a).

The real data measurements of the Catphan phantom in figure 4.5 show that both methods, ML-EM-AwTV in b) and ML-EM-AwTV+TV^2 in d), can produce images with a high spatial resolution. This is not the case for ML-EM-TV in a). Judging visually, the line-pair number three of b) and d) is sharper compared to c). Furthermore, the line-pair of the result of our proposed method is more complete compared to ML-EM-AwTV, where some pixels of the lines are over-smoothed. In table 4.1, the mean value ratio of the pixel-intensities of the peaks and valleys in the normalized line pair number three of figure 4.5 are computed. The table indicates that our proposed method produces results which have nearly the same spatial resolution as those of ML-EM-AwTV and a resolution which is approximately 26% higher than the reconstruction results of ML-EM-TV.

SPATIAL RESOLUTION OF LP NO. 3, CATPHAN RESOLUTION MODULE

method	ML-EM-AwTV+TV^2	ML-EM-AwTV	ML-EM-TV
mean resolution	**0.77**	**0.78**	0.61

Table 4.1: The mean value of the Euclidean distance of the peaks and valleys in the normalized line pair number 3 in figure 4.5. ML-EM-AwTV+TV^2 and ML-EM-AwTV have nearly the same spatial resolution, but clearly outperform ML-EM-TV which has a spatial resolution which is 26% lower. A value of 1 refers to the highest resolution possible.

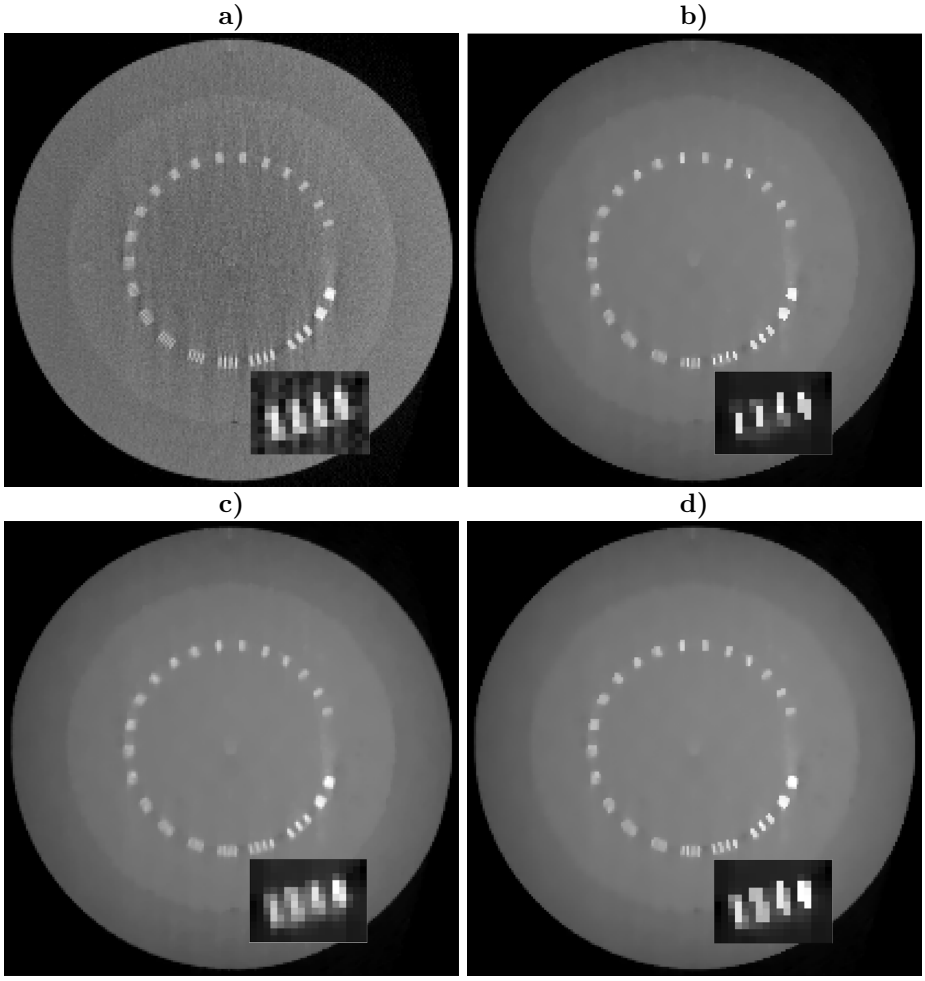

Figure 4.5: Reconstructions of the under-sampled Catphan phantom. The window-level for all images is $[0, 1]$. a) FBP, b) ML-EM-AwTV, c) ML-EM-TV, d) ML-EM-AwTV+TV^2. Image d) has a higher spatial resolution than images c) and b), since all pixels of the line-pair number 3 (cropped image) are clearly restored and not blurred. In a), 400 projections were used for the reconstruction and in b), c) and d) 80 projections were used.

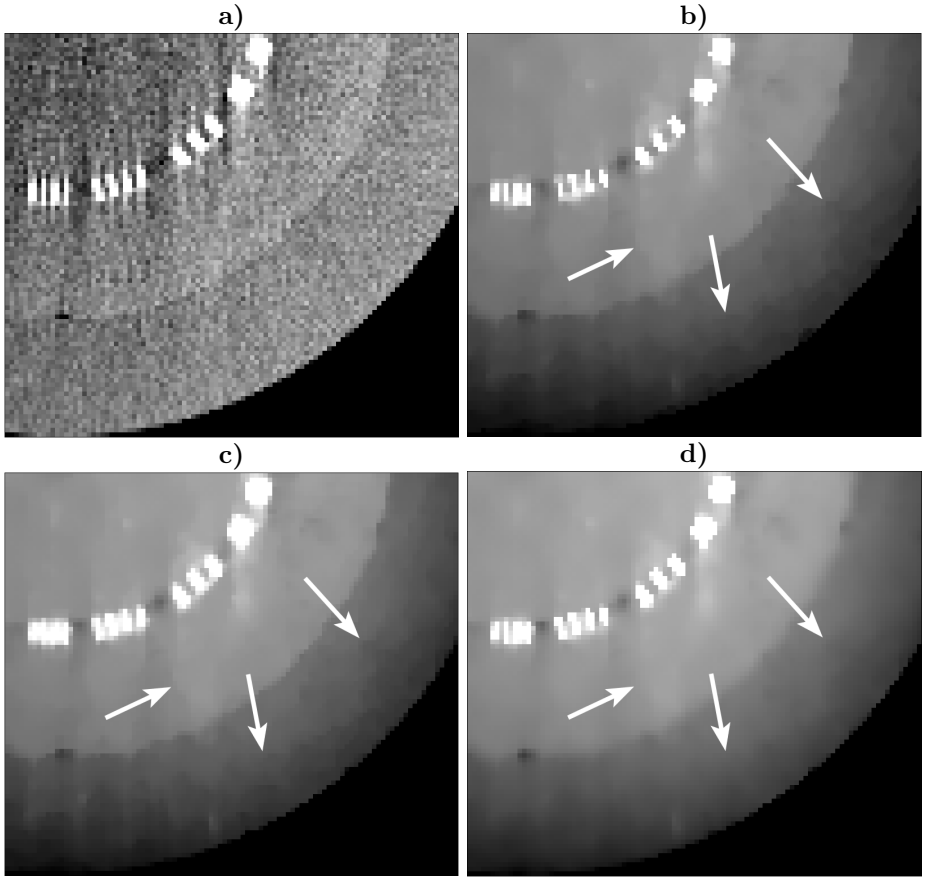

Figure 4.6: Cropped regions of the reconstructions presented in figure 4.5. Image a) shows the reconstruction result of FBP from 400 projections, b) - d) are reconstructions from 80 projections. The arrows indicate the regions where strong stair-casing effects occur. In d), which shows the result of ML-EM-AwTV+TV^2, there are no additional edges at the arrow marks. Window-level: [0.31,0.62].

Let us analyze the homogeneity of the results in figure 4.5 by selecting a different window-level and a cropped region. In figure 4.6, the arrows indicate a strong production of stair-casing artifacts in regions which should be homogeneous and one can clearly see that ML-EM-AwTV+TV^2 in figure 4.6 d) yields the image with the least stair-casing artifacts, followed by ML-EM-AwTV in 4.6 c) and ML-EM-TV in figure 4.6 b). This can also be seen in the contour plot measurements in figure 4.7 of figure 4.6. For ML-EM-AwTV+TV^2 in figure 4.7 d), the level lines are all spaced a long distance away in regions where the true image is homogeneous, compared to ML-EM-AwTV in 4.7 c) and ML-EM-TV in figure 4.7 b) where the level-lines are spaced close to one another, indicating an undesired edge.

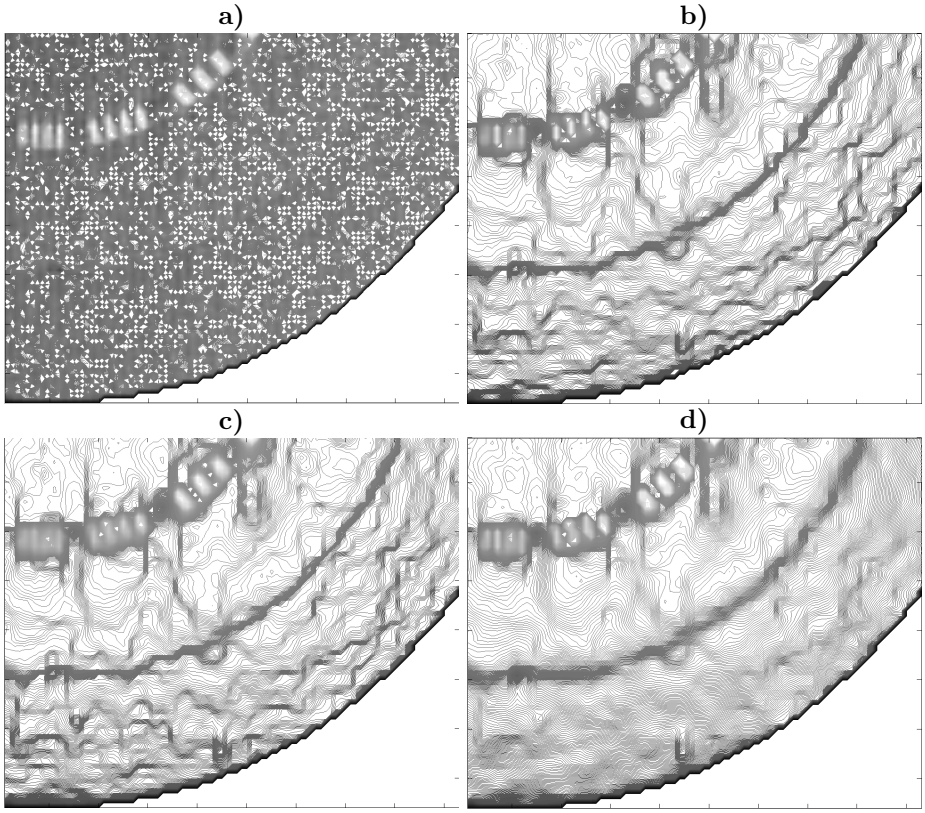

Figure 4.7: Contour plots of the results presented in figure 4.6. a) FBP, b) ML-EM-AwTV, c) ML-EM-TV, d) ML-EM-AwTV+TV^2. Our proposed method, ML-EM-AwTV+TV^2 in d) can produce piece-wise constant results, as the level-lines of the plot indicate: They are all a long distance away from each other in regions where the true image is homogeneous. This is not the case for the ML-EM-TV in c) and ML-EM-AwTV in b) where level-lines which are close to one another represent an edge in regions where the true image in a) is constant. The FBP algorithm cannot suppress the noise in figure 4.5 a). Consequently, the level-lines of the contour plot in a) are close to one another, forming constant areas. This is due to the variation of the noisy pixels.

The Non Uniformity Error Index in table 4.2 assesses the non-homogeneity of a predefined ROI in a reconstruction result. As ROIs we selected the ones in figures 4.1 a) and b). Our proposed method, ML-EM-AwTV+TV^2, is 1.38 times more homogeneous than ML-EM-AwTV and 1.34 times more homogeneous than ML-EM-TV considering the reconstructions of the Catphan phantom. In case of the lung phantom, ML-EM-AwTV+TV^2 produces results which are 1.57 times smoother than those of ML-EM-AwTV and 7.72 times smoother than those of ML-EM-TV, respectively.

NON-UNIFORMITY ERROR INDEX

method	ML-EM-AwTV+TV^2		ML-EM-AwTV		ML-EM-TV	
phantom	Catphan	lung	Catphan	lung	Catphan	lung
NUEI	**1.58**	**0.94**	2.18	1.48	2.12	7.26

Table 4.2: The Non-Uniformity Error Index of the ROIs selected in 4.1 a) and b). ML-EM-AwTV+TV^2 has the smallest NUEI since it can suppress the stair-casing artifacts in constant regions. All values have been scaled by a factor of 10^6. A value of 0 refers to a completely homogeneous result.

4.5 Discussion

By introducing a second order penalty term in the regularization function, the stair-case artifact of TV can be suppressed since edges are stronger penalized. A combination of a second order term with an anisotropic, edge-preserving first order term can restore high resolution images where even small structures of single pixel width can be reconstructed. One can thus conclude that there is practically no trade-off regarding resolution when ML-EM-AwTV+TV^2 is used as a regularization since the results are equal to ML-EM-AwTV in terms of the spatial resolution. Quality metrics such as the NUEI or the measurement of the spatial resolution underline these facts.
It should be noticed that even ML-EM-AwTV can reduce the stair-casing effect of TV up to a certain noise level. The reason is that function $w(\cdot)$ acts like a threshold of the undesired edge. If the noise level is too high, ML-EM-AwTV and ML-EM-AwTV+TV^2, however, introduce edges in regions which should be flat.
The derivative of AwTV is wrong in the mathematical sense, see equation 2.37. In fact it is a weighted approximation of the TV derivative in equation 2.35. In chapter 6, we therefore use the ATV regularizer proposed in equation 3.5 (which is analog to AwTV but the derivative was computed correctly here) combined with a second order TV and we independently compare all methods (from chapters 3, 4 and 5) proposed in this thesis.

4.6 Conclusion

Our proposed regularization function, ML-EM-AwTV+TV^2, produces results which are up to 7 times more homogeneous than the images of ML-EM-TV and 1.57 times more homogeneous than the images of AwTV. At the same time, the spatial resolution is approximately 26% higher for ML-EM-AwTV-TV^2 compared to ML-EM-TV and almost equal to ML-EM-AwTV.
Whether the proposed regularization function is suitable for dose reduction in CT requires a further investigation of the method, using quantitative quality metrics and a larger set of experiments. This is done in chapter 6.
In future, we will concentrate on other possible formulations of regularization techniques. A combination of higher order anisotropic gradients and higher order isotropic gradients might further enhance the image quality when only few projections are considered for the reconstruction.

Chapter 5

Accurate Low-Dose Iterative CT Reconstruction from Few Projections by Generalized Anisotropic Total Variation Minimization for Industrial CT

5.1 Outline

In this chapter, we propose a novel generalized Anisotropic Total Variation regularization for low-dose iterative CT reconstruction. The method was published in **IOS** *Journal Of X-Ray Science and Technology*, [69], in 2015.
Short acquisition and reconstruction times decrease the availability time of the X-ray machine and therefore increase the sales. This can be realized by decreasing both, the dose and the pulse length of the CT system and under-sampling the target. In this chapter, we propose a generalization of Total Variation for accurate, low-dose, under-sampled CT reconstruction. We compare our method to the standard methods, Total Variation, Adaptive weighted Total Variation and Filtered Backprojection. The novel regularization function uses *a priori* information about the Gradient Magnitude Distribution of the scanned object for the reconstruction. We provide a general parameterization scheme and evaluate the efficiency of our new algorithm for different noise levels and different numbers of projection views. When noise is not present, error-free reconstructions are achievable for AwTV and GATV from 40 projections. In cases where noise is simulated, our strategy achieves a Relative Root Mean Square Error that is up to 11 times lower than Total Variation-based and up to 4 times lower than AwTV-based iterative statistical reconstruction (e.g. for a SNR of 223 and 40 projections). To obtain the same reconstruction quality as achieved by Total Variation, the projection number and the pulse length, and the acquisition time and the dose, respectively, can be reduced by a factor of approximately 3.5, when AwTV is used and a factor of approximately 7, when our proposed algorithm is used.

5.2 Introduction

X-ray Computed Tomography is a modality used for quality control in industrial radiography, e.g. for void, crack and defect detection. It enables a nondestructive testing of different (composite) materials. Typical industrial CT scanners acquire several hundreds to thousands of projection views [187] and this process can take up to several minutes [156]. Short acquisition and reconstruction times decrease the availability time of the X-ray machine and therefore increase the sales. One strategy to decrease the acquisition time is to take fewer projections per full rotation around

the object, known as sparse-view scanning. Reducing the dose by lowering the pulse length of the anode is another strategy to notably decrease the time for the acquisition process, see section 2.2.4.4 for details.
Taking into consideration that machine parts consist of homogeneous regions of one alloy (and air), these objects can, in principle, be represented by a limited number of gray values or (considering the boundaries of these homogeneous regions) discrete Gradient Magnitudes.
As an alternative to discrete tomography [11] and to overcome the problems of TV (see section 2.2.4.3) and AwTV reconstructions, we propose a new generalization of a TV-based regularizer which uses *a priori* information of the Gradient Magnitude Distribution in typical data sets. Our proposed regularization method is called Generalized Anisotropic TV. We investigate the properties of such a regularizer and compare its performance to the known special cases of GATV, e.g. standard Total Variation [294], described in section 2.2.4.3 and defined in equation 2.29 and AwTV [218], described in section 2.2.4.3 and defined in equation 2.32. FBP, TV and AwTV are considered as reference and state of the art techniques in many publications.
This chapter is organized as follows: Section 5.3 introduces the imaging model and the GM distribution of typical objects in industrial CT. The implementation of the GATV method and its parametrization are then explained. In section 5.4, we evaluate FBP, TV, AwTV and GATV and we investigate the properties of GATV. We finally discuss the potential and limitations of GATV compared to the state of the art techniques and finish the chapter with a conclusion.

5.3 Materials and Methods

The notation we use for the mathematical expressions can be found in table 1, as well as the abbreviations of the methods and corresponding parameters and their ranges. Components of a vector are indexed by subscripts, whereas e.g. iteration indices are denoted by a superscript.
We apply a Poisson model for the raw CT measurements, see equations 2.17 and 2.21. Based on the measurements and a Poisson noise model, an objective function can be formulated:

$$\mu^\star = \underset{\mu'}{\operatorname{argmax}}\ L(Y, \mu') - \beta \cdot \phi(\mu'), \tag{5.1}$$

where $L(Y, \mu')$ is the likelihood in equation 2.24 and $\phi(\cdot)$ is the regularization function, controlled by regularization parameter β. The relaxed Ordered Subsets Convex algorithm, presented in section 2.2.4.2 and defined in equation 2.28 is a typical solver of equation 5.1. The algorithm is a variant of the well-known Maximum Likelihood Expectation Maximization [77], suitable for transmission CT scans. In this chapter, we denote ML-EM-TV for $\phi(\cdot) = TV(\cdot)$, ML-EM-AwTV for $\phi(\cdot) = AwTV(\cdot)$ and ML-EM-GATV for $\phi(\cdot) = GATV(\cdot)$. GATV uses the normalized vector as input, $\tilde{\mu}^n = (\mu^n - \min(\mu^n))/(\max(\mu^n) - \min(\mu^n))$. For Total Variation regularization [294] calculated for the two-dimensional case, we use equation 2.29, discretization 2.34 and derivative 2.35. A variant of TV is ATV in equation 2.30. In this case the coordinate variables x and y are splitted to compute the TV. The method is called Anisotropic Total Variation [309], since the computation of the TV is not directionally dependent anymore. ATV can suppress artifacts, like the stair-casing of TV, as previous publications have demonstrated [25, 118].
The Adaptive weighted Total Variation described in section 2.2.4.3 and defined in equation 2.32 has recently been proposed in [218] to tackle TV's problem of over-smoothing fine structures and to improve the noise-resolution trade-off. For a similar definition (but a correctly computed derivative) c.f. [71] and the method presented in chapter 3. AwTV can smooth longitudinally to the edge since the TV gradient is weighted by an exponential function and this exponential function acts like a threshold of the noise if the parameter $\sigma > 0$ is properly set. For $\sigma = 1$, the AwTV method turns into the standard TV method. For parameter $\sigma < 1$, AwTV can preserve edges. However, since parameter σ is static, the edge-preserving capabilities are limited to the intensity of the noise magnitude, which means that AwTV cannot maintain edges or fine structures below a certain noise level. This holds true for the suppression of stair-cases, too: At a certain noise level, AwTV will introduce stair-cases, see [70] and chapter 4. The discretization of AwTV is presented in 2.36 and the derivative of AwTV is defined in equation 2.37.

5.3.1 The proposed method: Generalized Anisotropic Total Variation

For the generalization, we start from equation 2.30, where ATV was defined. Having a close look at this equation, we observe that the regularization term is in general a linear function of the Gradient Magnitude. To generalize the TV, we choose a function ϕ of the absolute of the considered gradient component (either in x- or y-direction) instead of a linear function. We then define GATV as follows:

$$\mathrm{GATV}_z(u) = \int_\Omega \phi\left(u(x,y)\right)\ dxdy, \tag{5.2}$$

where $u = \left|\frac{\partial \mu_{x,y}}{\partial z}\right|$ and z is used either as x or y component.
Equation 5.2 is the Generalized Anisotropic Total Variation. As mentioned above, machine parts often consist of few distinct materials and hence can be represented by a piecewise constant function with given attenuation coefficients. This property leads to a discrete spectrum of Gradient Magnitudes in the GMD. Defects such as cracks or inclusions or deviations from the ideal geometry typically do not modify this spectrum. Limited sampling would widen the individual peaks due to sampling-induced blurring (in order to obey the Shannon Theorem). For simplicity, we omit this issue in the following since the blurring is typically very small.
Let us illustrate these findings by considering an **e**ngine **b**lock (**eb**) as an example which consists of an arrangement of homogeneous metal alloys surrounded by air. We enumerate these compounds by:

$$eb = \{\text{iron, aluminium, air}\}. \tag{5.3}$$

The elements' Linear Attenuation Coefficients at 2MeV are:

$$\mu^{eb} = \{0.03294,\ 0.01881,\ 0.00000536\}\,\frac{1}{\mathrm{mm}}, \tag{5.4}$$

where the first entry of vector μ^{eb} corresponds to the LAC of iron, the second entry to the LAC of aluminum and the third entry to the LAC of air. The Mass Attenuation Coefficients were taken from [152], see table 2.1. For practical reasons and to achieve a level of generality when the object consists of different elements and LACs respectively, we normalize μ^{eb} between 0 and 1 by:

$$\widetilde{\mu}^{eb} = \frac{\mu^{eb} - \min\left(\mu^{eb}\right)}{\max(\mu^{eb}) - \min(\mu^{eb})} \tag{5.5}$$

and hereby force that the LAC with the lowest value (the LAC corresponding to air), is set to 0. The vector of normalized LACs then reads as:

$$\widetilde{\mu}^{eb} = \{1,\ 0.57078,\ 0\} \tag{5.6}$$

When the gradient of the LACs, $\nabla_x \widetilde{\mu}^{eb}$, is approximated by left-sided differences (c.f. section 2.2.5):

$$\frac{\partial \widetilde{\mu}^{eb}}{\partial x} \approx \widetilde{\mu}^{eb}_x - \widetilde{\mu}^{eb}_{x-1}, \tag{5.7}$$

all possible combinations of resulting GMs of $\widetilde{\mu}^{eb}$ can be computed, see table 5.1.

GRADIENT MAGNITUDE COMBINATIONS OF THE ENGINE BLOCK

$\widetilde{\mu}^{eb}_x$ \ $\widetilde{\mu}^{eb}_{x-1}$	air	aluminum	iron
air	0	0.57078	1
aluminum	0.57078	0	0.42922
iron	1	0.42922	0

Table 5.1: All combinations of Gradient Magnitudes (approximated by left-sided differences) of the normalized Linear Attenuation Coefficients of the industrial CT engine.

Therefore, the GM intensities of $\widetilde{\mu}^{eb}$ in the GMD are:

$$GM_{\text{intensity}}\left(\widetilde{\mu}^{eb}\right) = \{1,\, 0.57078,\, 0.42922,\, 0\} \tag{5.8}$$

The object and Gradient Magnitude spectrum of this example is shown in figure 5.1.

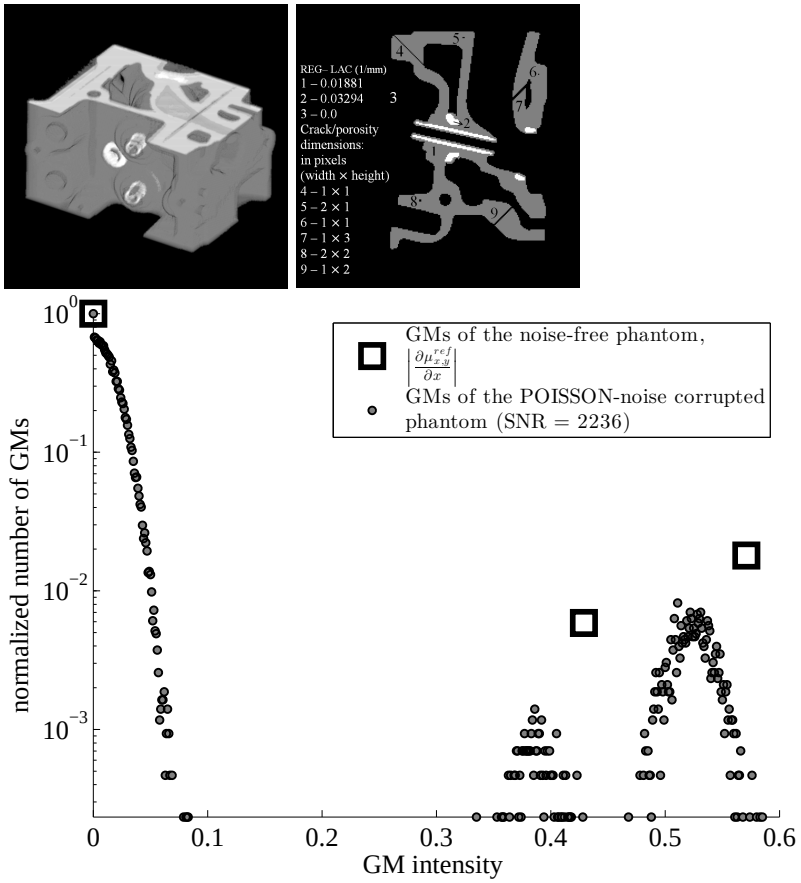

Figure 5.1: Top: A three-dimensional surface reconstruction of an industrial CT engine and a reconstructed slice of it with simulated cracks and porosities (display range: $[0, 0.0329]$). Bottom: Gradient Magnitudes (in x-direction) of the noise-free and Poisson-noise corrupted (SNR = 2236) industrial CT engine of the top right image. The true GMs are marked as squares. Poisson noise causes a widening of the true GMs (dots). The histogram was created from 580 bins where one bin corresponds to a GM intensity of 0.001. Note, in this data GMs = 0 are not displayed for the sake of clarity.

The GMD displays the normalized-to-1 amount (y-axis) and the intensities (x-axis) of the true GMs in equation 5.8, which are marked as black squares. GM = 1 is missing, since the highest LAC of the engine block is not surrounded by air or a cavity. Furthermore, GMs of intensity 0 are not displayed for the sake of clarity. Poisson noise corrupted data is represented by gray dots with a black border and shows a blurring of the original spectrum. Based on the GMD of this data, we formulate the *a priori* knowledge in the following way:

1. The Gradient Magnitude Distribution of noise-free objects consists of a discrete spectrum (see the GMs of the reference data in figure 5.1).

2. The distance between the true GM peaks is much higher than the blurring of the peaks by noise (see the GMs of the noisy data in figure 5.1).

In the next step we want to keep a close eye on the formulation of a *specific* function out of the set of possible functions for $\phi(\cdot)$ in equation 5.2. Intuitively, one can ask:

- *Which* gradients in the Gradient Magnitude Distribution of the current image estimate should be penalized?
- *How* can the penalization of GMs be controlled for the optimization of the objective function?

For the design of a specific function for GATV we want to comprise the answers of the previous two questions. Concerning the first question, it is evident that minimizing the Total Variation of an image (estimate) during the optimization process should lead to a noise-free and piece-wise constant result. However, by definition, when the TV method is used in penalized cost functions, all GMs related to noise and GMs related to prominent edges are penalized at an equal amount. It could be more efficient to solely penalize GMs related to noise and leave all other GMs untouched during the optimization process. In such a way the data term of the objective function can then restore the prominent edges. A specific function for GATV should therefore be able to separate noise and prominent edges and solely penalize GMs related to noise whereas GMs related to prominent edges should be left untouched.
Concerning question two, a specific function for GATV should produce (penalization) weights in a useful interval of $[0, 1]$, ranging from no contribution (weight = 1) to full contribution (weight = 0). Furthermore, a parameter which can be automatically or manually adjusted controls which Gradient Magnitudes (of a certain intensity) are penalized. Typically, GMs related to noise have a lower intensity than GMs related to prominent edges. This fact enables the separability of the GMs. Concentrating the previous information on a reasonable choice of a specific function for GATV in equation 5.2, we therefore define GATV as:

$$\begin{aligned} &\text{GATV}\left(\mu_{x,y}\right) = \\ &\int_\Omega \phi\left(\left|\frac{\partial \mu_{x,y}}{\partial x}\right|\right) dxdy + \int_\Omega \phi\left(\left|\frac{\partial \mu_{x,y}}{\partial y}\right|\right) dxdy = \\ &\int_\Omega e^{-\left(\frac{\left|\frac{\partial \mu_{x,y}}{\partial x}\right|^2}{2\tau^2}\right)} dxdy + \int_\Omega e^{-\left(\frac{\left|\frac{\partial \mu_{x,y}}{\partial y}\right|^2}{2\tau^2}\right)} dxdy \end{aligned} \tag{5.9}$$

where μ is the Linear Attenuation Coefficient distribution in the reconstructed image and $\left|\frac{\partial \mu_{x,y}}{\partial z}\right|$ is its Gradient Magnitude, z either stands for x or y.
By tuning parameter τ in the non-linear function in equation 5.9, one can control which Gradient Magnitudes should be penalized. Starting the optimization with a high value of τ and varying τ during the iterations, different Gradient Magnitudes in the spectrum can be penalized. At the end of the optimization, τ should arrive at the lowest possible value, which is still bigger than the current noise magnitude, so as to still obtain a noise-free image.
The explicit parametrization strategy and the derivative of GATV is presented in the next section.

5.3.2 Parameterization of GATV

Our new regularization function depends on τ which selects those GMs in the spectrum to be penalized. We observed that it is of high importance that parameter τ has to be chosen carefully and that it should change over the iterations: τ should have a start value, τ_{start}, chosen such that in the beginning of the optimization, all Gradient Magnitudes are penalized. This removes the blurring on large GMs. τ_{end} represents the end value and has to be chosen such that in the end, only GMs related to noise are penalized. During the optimization, the value of τ is reduced and the way how τ is reduced is controlled by a cooling scheme. Figure 5.2 shows this mechanics, where the industrial CT engine phantom was reconstructed from 40 projections and a SNR = 2236 using ML-EM-GATV. The GMs of the reconstruction of ML-EM-GATV are marked as gray spots with a black border. The true GMs of the noise-free phantom are marked as black squares. The GATV penalty (equation 5.9) is a solid line and all GMs underneath this line are currently penalized.
The reconstructed image in the top row shows that under-sampling artifacts and blurring are the main source of corruption at the first iteration. It is therefore natural to select a value of τ so that GATV penalizes the whole spectrum; in this case $\tau = 0.3$. We call this initial step, where all possible GMs of the current image estimate are penalized, *optimization step 1*. Next, for *optimization step 2*, the parameter value τ is decreased and the way of reduction is described by a *cooling scheme*. As cooling scheme, we select an exponential rule, parameterized by $\kappa > 0$. κ controls the speed of the exponential reduction of τ by setting $\tau^{(n)} = \tau^{(n-1)} + (\tau_{\text{start}} - \tau_{\text{end}}) \cdot \frac{e^{(-\mathrm{n}\cdot\kappa)} - e^{(-\mathrm{N}\cdot\kappa)}}{\left(1 - e^{(-\mathrm{N}\cdot\kappa)}\right)}$, $\forall\ n = 1, ..., N$. N is the overall number of iterations. For low values of κ (such as $\kappa \leq 0.0001$), τ decreases almost linearly, whereas for higher values of κ (like $\kappa > 0.0001$), τ decreases exponentially. The empirical argument for selecting such a cooling scheme is that the time to reduce a given fraction of the remaining GMs related to noise typically increases exponentially in an optimization process and hence, the system should be given appropriate time to do this before going to the next value of τ.
The lowest possible value of τ is restricted to the lowest GM intensity related to noise left in the current image estimate. A further reduction of τ introduces noise in the reconstruction due to a lack of penalty. At this point, the cooling is stopped. This level is reached in our example case for $\tau = 0.007$ (middle of figure 5.2). Then, the value of τ is fixed and the regularization parameter $\tilde{\beta}$ can be drastically increased to penalize the remaining low-intensity GMs related to noise until the algorithm has converged (bottom of figure 5.2).
Algorithm 4 summarizes the parameterization and reconstruction scheme for ML-EM-GATV.

Algorithm 4 Parameterization of ML-EM-GATV

1: **initialize** $\mu = 1 \cdot 10^{-7}$, $\zeta = 1.0$, see table 5.3 for the following parameters: N, β, τ_{start}, τ_{end}, κ.
2: {*optimization step* 1: restore prominent high-contrast edges, penalize edges related to noise/artifacts}
3: **for** $n = 0$ to N **do**
4: **update** $\tau^{(n-1)} + (\tau_{\text{start}} - \tau_{\text{end}}) \cdot \frac{e^{(-\mathrm{n}\cdot\kappa)} - e^{(-\mathrm{N}\cdot\kappa)}}{\left(1 - e^{(-\mathrm{N}\cdot\kappa)}\right)}$ in equation 5.12
5: **solve** equation 2.28, where $\phi(\cdot)$ = GATV in equation 5.12
6: **end for**
7: {*optimization step* 2: produce a smooth result, iterate until convergence }
8: **set** $\beta = 60.0$, $\tau_{\text{start}} = \tau_{\text{end}}$, $\zeta = 0.01$
9: **for** $n = 0$ to 20,000 **do**
10: **solve** equation 2.28, where $\phi(\cdot)$ = GATV in equation 5.12
11: **end for**

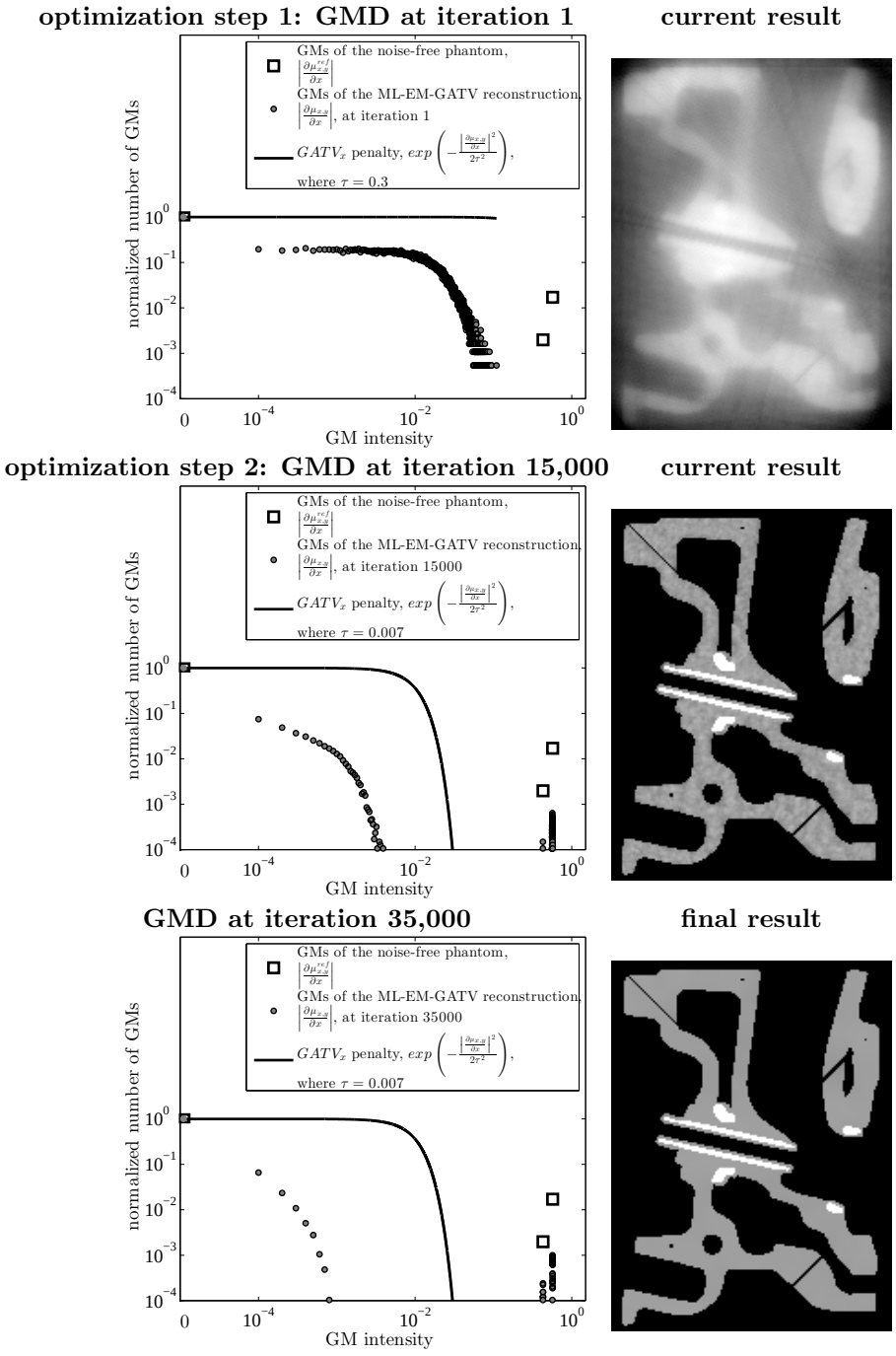

Figure 5.2: The figure shows the GMDs at iteration 1 (top), 15,000 (middle) and 35,000 (bottom) on the left side and the corresponding reconstruction of ML-EM-GATV on the right side. The reconstruction settings were: 40 projections, SNR = 2236. The GMDs show the true Gradient Magnitudes of the reference data (squares), the GMs of ML-EM-GATV (gray dots with a black border) and the currently penalized GMs (represented by a solid line) at different optimization steps. Note, we do not display a GM of intensity 0 for the the sake of clarity.

Next, we want to provide the derivative of GATV. Discretizing the gradient in equation 5.9 by a left-sided differences approximation (c.f. section 2.2.5) leads to:

$$\mathrm{GATV}\left(\mu_{x,y}\right) \approx \sum_{x,y} \mathrm{e}^{-\frac{1}{2}\left(\frac{\left(\mu_{x,y}-\mu_{x-1,y}\right)}{\tau}\right)^2} + e^{-\frac{1}{2}\left(\frac{\left(\mu_{x,y-1}-\mu_{x,y}\right)}{\tau}\right)^2}, \tag{5.10}$$

where x and y are the pixel indices and τ controls the penalization of Gradient Magnitudes in the GMD. The partial derivatives were evaluated using a left-sided differences discretization scheme for the gradient $\frac{\partial \mu_{x,y}}{\partial z}$ in x or y - direction and a right-sided differences scheme for the derivative of GATV [313]:

$$\begin{aligned}
&\frac{\partial \mathrm{GATV}\left(\mu_{x,y}\right)}{\partial \mu_{x,y}} = \frac{\partial \mathrm{GATV}\left(\mu_{x,y}\right)}{\partial \mu_{x,y}} + \frac{\partial \mathrm{GATV}\left(\mu_{x+1,y}\right)}{\partial \mu_{x,y}} + \frac{\partial \mathrm{GATV}\left(\mu_{x,y+1}\right)}{\partial \mu_{x,y}} \approx \\
&\frac{\left(\mu_{x,y}-\mu_{x-1,y}\right)\mathrm{e}^{-\frac{1}{2}\left(\frac{\left(\mu_{x,y}-\mu_{x-1,y}\right)}{\tau}\right)^2}}{\tau^2} + \frac{\left(\mu_{x,y}-\mu_{x,y+1}\right)\mathrm{e}^{-\frac{1}{2}\left(\frac{\left(\mu_{x,y}-\mu_{x+1,y}\right)}{\tau}\right)^2}}{\tau^2} + \\
&\frac{\left(\mu_{x,y}-\mu_{x+1,y}\right)\mathrm{e}^{-\frac{1}{2}\left(\frac{\left(\mu_{x,y}-\mu_{x+1,y}\right)}{\tau}\right)^2}}{\tau^2} + \frac{\left(\mu_{x,y}-\mu_{x,y-1}\right)\mathrm{e}^{-\frac{1}{2}\left(\frac{\left(\mu_{x,y}-\mu_{x,y-1}\right)}{\tau}\right)^2}}{\tau^2}
\end{aligned} \tag{5.11}$$

Recall, parameter τ in $e^{-\left(\frac{\left|\frac{\partial \mu_{x,y}}{\partial x}\right|^2}{2\tau^2}\right)}$ selects which GMs to penalize. Due to the differentiation of GATV in equation 5.11, this parameter occurs in every denominator of each term, which makes the control of the behavior of GATV (and the systematic penalization of GMs) complicated. We therefore omit parameter τ in each denominator of equation 5.11 (except τ in the denominator of the $e^{(\cdot)}$ functions) and approximate the derivative of GATV by:

$$\begin{aligned}
&\frac{\partial \mathrm{GATV}\left(\mu_{x,y}\right)}{\partial \mu_{x,y}} \approx \\
&\left(\mu_{x,y}-\mu_{x-1,y}\right)\mathrm{e}^{-\frac{1}{2}\left(\frac{\left(\mu_{x,y}-\mu_{x-1,y}\right)}{\tau}\right)^2} + \left(\mu_{x,y}-\mu_{x,y+1}\right)\mathrm{e}^{-\frac{1}{2}\left(\frac{\left(\mu_{x,y}-\mu_{x+1,y}\right)}{\tau}\right)^2} + \\
&\left(\mu_{x,y}-\mu_{x+1,y}\right)\mathrm{e}^{-\frac{1}{2}\left(\frac{\left(\mu_{x,y}-\mu_{x+1,y}\right)}{\tau}\right)^2} + \left(\mu_{x,y}-\mu_{x,y-1}\right)\mathrm{e}^{-\frac{1}{2}\left(\frac{\left(\mu_{x,y}-\mu_{x,y-1}\right)}{\tau}\right)^2}
\end{aligned} \tag{5.12}$$

Note, instead of omitting parameter τ in each denominator of equation 5.11, the multiplication of the regularization parameter β by τ in equation 2.28 would have the same effect. We, however, do not follow this strategy and we use equation 5.12 for the derivative of GATV.

5.3.3 Simulation conditions

We neglect the detector noise in our experiments since its contribution its contribution is much smaller than the signal of interest [377]. For investigating the properties of the algorithm, simulated projections of given CT data sets are used. Scatter and beam hardening are therefore ignored. Poisson noise is modeled, given the average number of photons hitting the detector pixels [230]. An Elekta XVI CBCT examined in [332], is chosen as reference. The noise levels we used are listed in table 2.3.
We consider a parallel beam configuration in which the number of detector bins equals 256 and each detector bin scale is 1mm. The reconstructed image has 256×256 pixels with a 1mm×1mm pixel size.
The projections were acquired at equidistant rotation angles in the interval $[0, \pi]$. Projections were calculated using an accelerated version of Siddon's algorithm [157]. A Matlab implementation for calculating the intersection lengths l_{ij} in equation 2.9, provided by Munir Ahmad [1] is used. In particular the same projector for forward- and backprojection is chosen. The whole reconstruction is performed on a Nvidia GTX 780 Ti graphics card.
For a particular reconstruction setting, namely the industrial CT engine block, 40 projections and 7 different noise levels (SNR = 2236, 1000, 707, 316, 223, 158, 100), we derived a useful set of parameters for each noise level and reconstruction method, ML-EM-TV, ML-EM-AwTV and ML-EM-GATV, with the goal of a minimal RRMSE. For ML-EM-TV, for example, we tested different values for β in the interval $[0.05, 1]$, where e.g. $\beta = 0.05$ produced a very noisy result and $\beta = 1$ produced a piece-wise homogeneous image with extremely over-smoothed structures. For ML-EM-AwTV, we first fixed parameter β and then iterated over different values for δ. Then, we increased β and again iterated over different values for δ. For GATV, we obtained the best parameter set in an analog way: We iterated over the following 4 parameters: β, τ_{start}, τ_{end} and κ. The parameter ranges we tested are listed in table 5.2.

EXAMINED PARAMETERS FOR THE ALGORITHMS

parameter / method	β	τ_{start}	τ_{end}
ML-EM-GATV	$[5 \cdot 10^{-2}, 1]$	$[10^{-1}, 5 \cdot 10^{-1}]$	$[10^{-4}, 10^{-1}]$
ML-EM-AwTV	$[5 \cdot 10^{-2}, 1]$	**n**ot **a**pplicable (n.a.)	n.a.
ML-EM-TV	$[10^{-4}, 5 \cdot 10^{-3}]$	n.a.	n.a.
parameter / method	κ	ζ	δ
ML-EM-GATV	$[10^{-5}, 5 \cdot 10^{-3}]$	$[10^{-3}, 1]$	n.a.
ML-EM-AwTV	n.a.	n.a.	$[1 \cdot 10^{-4}, 1 \cdot 10^{-2}]$
ML-EM-TV	n.a.	n.a.	n.a.

Table 5.2: Parameter ranges we evaluated for the ML-EM-TV, ML-EM-AwTV and ML-EM-GATV reconstructions.

From the evaluation results which produced the lowest RRMSE, we selected constants for ML-EM-TV, ML-EM-AwTV and ML-EM-GATV, see table 5.3. The constants are applicable to other phantoms such as the Forbild phantom in figure 2.4 e).

CONSTANTS FOR ML-EM-TV, ML-EM-AwTV and ML-EM-GATV

GATV	SNR	N	β	τ_{start}	τ_{end}	κ
	∞	$2 \cdot 10^6$	0.2	0.3	$1.0 \cdot 10^{-4}$	$1.0 \cdot 10^{-5}$
	2236	$1.5 \cdot 10^4$	0.3	0.3	$7.0 \cdot 10^{-3}$	$8.0 \cdot 10^{-4}$
	1000	$1.5 \cdot 10^4$	0.3	0.3	$4.1 \cdot 10^{-3}$	$8.0 \cdot 10^{-4}$
	707	$1.5 \cdot 10^4$	0.3	0.3	$1.0 \cdot 10^{-2}$	$8.0 \cdot 10^{-4}$
	316	$1.5 \cdot 10^4$	0.3	0.3	$2.0 \cdot 10^{-2}$	$8.0 \cdot 10^{-4}$
	223	$1.5 \cdot 10^4$	0.3	0.3	$3.5 \cdot 10^{-2}$	$8.0 \cdot 10^{-4}$
	158	$1.5 \cdot 10^4$	0.3	0.3	$3.8 \cdot 10^{-2}$	$8.0 \cdot 10^{-4}$
	100	$1.5 \cdot 10^4$	0.3	0.3	$6.0 \cdot 10^{-2}$	$8.0 \cdot 10^{-4}$
AwTV	SNR	N	β	δ		
	∞	$3.5 \cdot 10^4$	$4.1 \cdot 10^{-4}$	$5.0 \cdot 10^{-4}$		
	2236	$3.5 \cdot 10^4$	$4.1 \cdot 10^{-4}$	$5.0 \cdot 10^{-4}$		
	1000	$3.5 \cdot 10^4$	$2.1 \cdot 10^{-4}$	$9.0 \cdot 10^{-4}$		
	707	$3.5 \cdot 10^4$	$1.7 \cdot 10^{-4}$	$1.1 \cdot 10^{-3}$		
	316	$3.5 \cdot 10^4$	$1.3 \cdot 10^{-4}$	$1.3 \cdot 10^{-3}$		
	223	$3.5 \cdot 10^4$	$7.0 \cdot 10^{-5}$	$2.7 \cdot 10^{-3}$		
	158	$3.5 \cdot 10^4$	$5.0 \cdot 10^{-5}$	$3.7 \cdot 10^{-3}$		
	100	$3.5 \cdot 10^4$	$9.0 \cdot 10^{-5}$	$4.1 \cdot 10^{-3}$		
TV	SNR	N	β			
	∞	$3.5 \cdot 10^4$	$8.0 \cdot 10^{-4}$			
	2236	$3.5 \cdot 10^4$	$1.1 \cdot 10^{-3}$			
	1000	$3.5 \cdot 10^4$	$1.3 \cdot 10^{-3}$			
	707	$3.5 \cdot 10^4$	$1.8 \cdot 10^{-3}$			
	316	$3.5 \cdot 10^4$	$2.0 \cdot 10^{-3}$			
	223	$3.5 \cdot 10^4$	$5.0 \cdot 10^{-3}$			
	158	$3.5 \cdot 10^4$	$8.7 \cdot 10^{-3}$			
	100	$3.5 \cdot 10^4$	$1.8 \cdot 10^{-2}$			

Table 5.3: Constants for ML-EM-GATV, ML-EM-AwTV and ML-EM-TV applicable to all phantoms, noise-levels, realizations of the noise random variable and projection views used in this chapter. Note, a SNR of ∞ corresponds to a noise-free sinogram, where d_0 has been set to 2236^2; however, no Poisson noise was applied in equation 2.17.

The values show that ML-EM-GATV is not sensitive to the parameters β, τ_{start} and κ, since they are equal for the different SNRs. Only τ_{end} severely depends on the noise level. To evaluate the robustness of the reconstruction methods, ML-EM-TV, ML-EM-AwTV and ML-EM-GATV and the usability of the selected constants for the different methods, we performed reconstructions with 10 different realizations of the noise random variable and all combinations of projection views and noise levels listed in table 5.4

SELECTED NUMBER OF PROJECTIONS AND NOISE LEVELS

Projection views	10	20	30	40	60	80	100	200
Noise levels	2236	2236	2236	2236	2236	2236	2236	2236
	1000	1000	1000	1000	1000	1000	1000	1000
	707	707	707	707	707	707	707	707
	316	316	316	316	316	316	316	316
	223	223	223	223	223	223	223	223
	158	158	158	158	158	158	158	158
	100	100	100	100	100	100	100	100

Table 5.4: We evaluated the new method on all combinations of the projection views and noise levels. For each projection view, we considered 10 different realizations of the noise random variable. Thus, in total, we performed 560 reconstructions.

Industrial CT datasets have a limited number of Linear Attenuation Coefficients, since the objects consist of some few solid materials of the same kind. We selected iron and aluminum as elements representing metal. Such datasets are therefore well suited to evaluate the reconstruction quality of the proposed method. We reconstruct the industrial CT engine data, simulated at an energy of 2MeV. The phantom is described in detail in section 2.2.1.3 and displayed in figure 2.4 c), d). The Forbild head phantom in figure 2.4 e), f) and g) was simulated at 80keV. It is well suited to measure the CNR of the results since it contains elements of small intensity variation.
Since we ignore the partial volume effect during the acquisition for all phantoms, the objects' edges have a high acutance. Consequently, the GMD is discrete (see black squares in figure 5.1) and has a shape as described in section 5.3.1.

5.3.4 Figures of merit

The Relative Root Mean Squared Error [336] is a reliable measure to rate the image quality and is used to evaluate the final reconstruction μ^n:

$$\mathrm{RRMSE}^n\left(\mu^n, \mu^{\mathrm{ref}}\right) = \sqrt{\frac{\sum_j \left(\mu_j^n - \mu_j^{\mathrm{ref}}\right)^2}{\sum_j \left(\mu_j^{\mathrm{ref}}\right)^2}}, \tag{5.13}$$

where μ^{ref} is the reference phantom.
Plotting the log-likelihood function (equation 2.24) versus the iteration number displays the convergence behavior of the algorithm.
The Gradient Magnitude Distribution of the reconstruction and reference image displays deviations very well: The better their coincidence, the smaller is the reconstruction error. As quantitative measure, the symmetric Kullback-Leibler distance [169] of reconstructed and true GMD spectrum is used:

$$\mathrm{KLD} = \frac{\mathrm{kld}'\left(\mathrm{GMD}\left(\mu^n\right), \mathrm{GMD}\left(\mu^{\mathrm{ref}}\right)\right)}{2} + \frac{\mathrm{kld}'\left(\mathrm{GMD}\left(\mu^{\mathrm{ref}}\right), \mathrm{GMD}\left(\mu^n\right)\right)}{2}, \tag{5.14}$$

where:

$$\mathrm{kld}'\left(\mathrm{GMD}\left(\mu^n\right), \mathrm{GMD}\left(\mu^{\mathrm{ref}}\right)\right) = \sum_x \mathrm{GMD}\left(\mu^n\right)_b \log\left(\frac{\mathrm{GMD}\left(\mu^n\right)_b}{\mathrm{GMD}\left(\mu^{\mathrm{ref}}\right)_b}\right), \tag{5.15}$$

where b corresponds to the binned GMs in the GMD. The GM frequency at bin b is therefore $\mathrm{GMD}\left(\mu\right)_b$.
The **C**ontrast to **N**oise **R**atio (CNR) [165] was used to evaluate the image quality in selected low-contrast Regions of Interest (ROIs):

$$\mathrm{CNR}\left(\mu^n\right) = \frac{\left|\mathrm{mean}\left(\mu^{t\_\mathrm{ROI}}\right) - \mathrm{mean}\left(\mu^{\mathrm{bg}}\right)\right|}{\mathrm{sd}\left(\mu^{t\_\mathrm{ROI}}\right) + \mathrm{sd}\left(\mu^{\mathrm{bg}}\right)}, \tag{5.16}$$

where *t_ROI* represents the target ROIs and the whole **b**ack**g**round (bg), of the object which is selected in figure 2.4 f). $\mu^{(n)}$ is the reconstruction result at iteration n, $\mathrm{mean}\left(\cdot\right)$ and $\mathrm{sd}\left(\cdot\right)$ denote the mean and the standard deviation computed over the areas.
We measure the degree of homogeneity (H) of the results by computing the closeness of the distribution of elements in the **G**ray-**L**evel **C**o-occurence **M**atrix [134] (GLCM) compared to the GLCM diagonal. Given the reconstructed image μ of size M×M and its spatial positions x and y, the GLCM at the spatial positions o and p can be computed:

$$GLCM_{o,p}(\mu^\star(x,y)) = \sum_{x=1}^{M}\sum_{y=1}^{M} \begin{cases} 1, & \textbf{if } \mu^\star(x,y) = o \textbf{ and} \\ & \mu^\star(x+\Delta x, y+\Delta y) = p \\ 0, & \text{otherwise} \end{cases} \tag{5.17}$$

Note, to compute the GLCM, the reconstruction result μ was normalized between 0 and 1 (using equation 5.5), resulting in $\mu^\star$. Δx and Δy are offsets, specifying the distance between the pixel-of-interest and its neighbor. We set $\Delta x = \Delta y = 1$; however, rotation invariant solutions for the choice of Δx and Δy have been proposed [90]. We compute the degree of homogeneity H of the reconstruction result by:

$$H = \sum_{o,p} \frac{\mathrm{GLCM}_{o,p}(\mu^\star)}{1 + |o - p|}, \tag{5.18}$$

$H \in [0, 1]$, where 1 is found in a diagonal GLCM, i.e. a constant image.
The difference measure:

$$\sum_{x,y} \left| \mu^{\mathrm{ref}}_{x,y} - \mu_{x,y} \right| \tag{5.19}$$

computes the closeness of the reconstruction, μ, compared to the reference, μ^{ref}. We used it to calculate the difference between single pixels like cracks, cavities or flaws at manually selected ROIs.

5.4 Results

In this section, we analyze the reconstruction results of FBP, ML-EM-TV, ML-EM-AwTV and the proposed method, ML-EM-GATV. We judge the results qualitatively by analyzing the reconstruction images and quantitatively using the metrics presented in section 5.3.4.

5.4.1 Reconstruction results: Execution time

We measured the execution time of ML-EM-GATV for the given simulation conditions in section 5.3.3. The execution time for both methods, ML-EM-GATV and ML-EM-AwTV, is approximately 0.00114 seconds per iteration, performed on a Nvidia GTX 780 Ti graphics card. The execution time of our FBP method (implemented on the CPU) is 0.03853 seconds.

5.4.2 Reconstruction results: Overall evaluation

Figure 5.3 shows an overall evaluation of the reconstruction methods, ML-EM-TV, ML-EM-AwTV and ML-EM-GATV and the dependency of mean RRMSE on the number of projections and the noise level for the engine phantom simulation. A two-dimensional contour plot shows the interpolated mean RRMSE at a discrete set of measurements points. Each point corresponds to 10 different measurements, where the noise random variable varied for each of the measurements and a specific combination of the number of projections (10, 20, 30, 40, 60, 80, 100 or 200) and SNRs (2236, 1000, 707, 316, 223, 158 or 100) was selected. The **r**ed-**g**reen-**b**lue-valued (rgb) and gray-valued color bars represent the mean and standard deviation of the RRMSE of the 10 different measurements respectively.

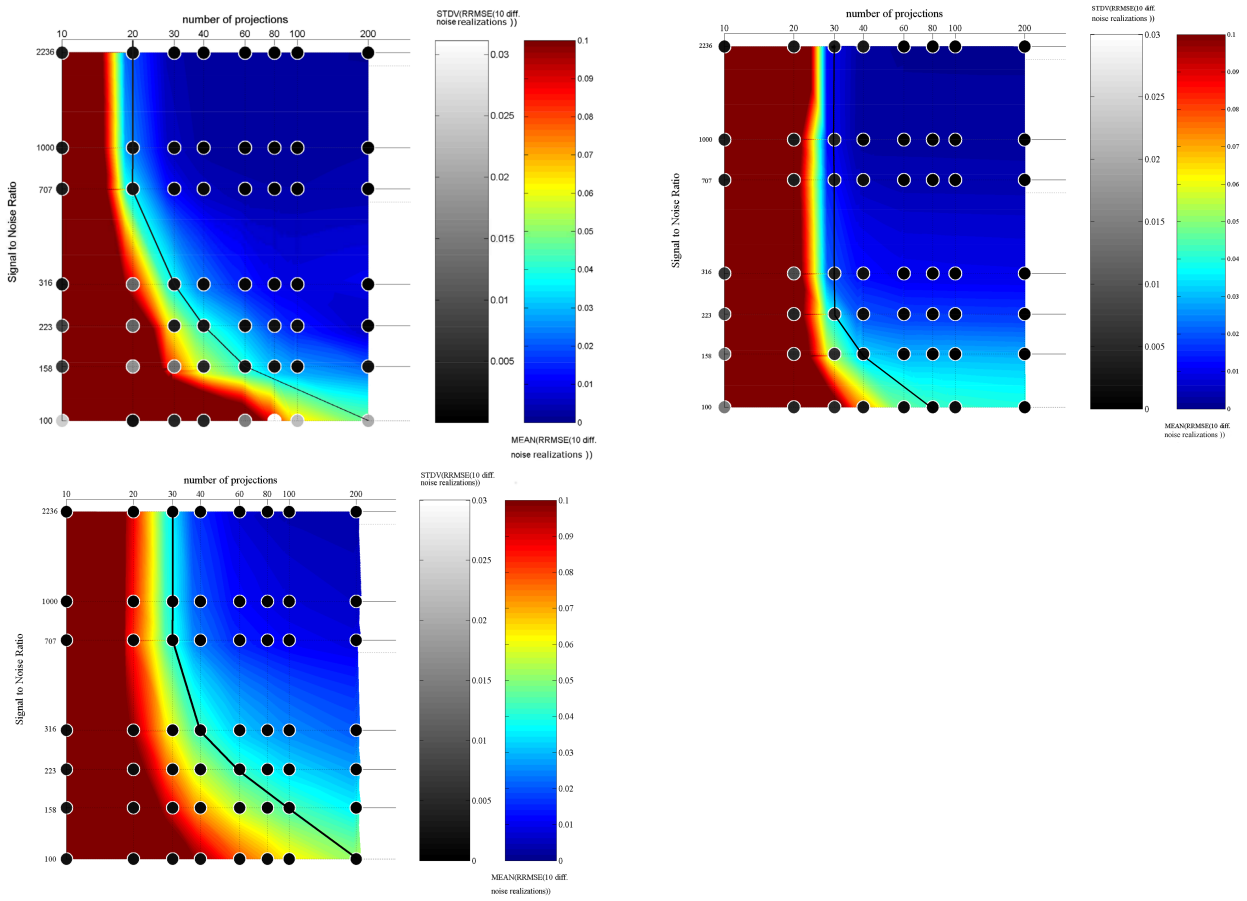

Figure 5.3: Result of the overall evaluation of the industrial CT engine phantom. 10 realizations of the noise random variable and different combinations of noise-levels and projection views were evaluated, given the constants for the algorithms in table 5.3. Gray-valued colorbar: Standard deviation of the RRMSE of the measurements (points), rgb-valued colorbar: Mean value of the RRMSE of the measurements (contour plot). Top left: ML-EM-GATV, top right: ML-EM-AwTV, bottom left: ML-EM-TV.

To compare the plots of ML-EM-GATV (top left) with ML-EM-AwTV (top right) and ML-EM-TV (bottom left), we exemplary drew a black line along the measurement points which are in the region of a RRMSE of [0.03, 0.05]. This interval contains the highest possible RRMSE values which were found suitable, regarding the image quality for industrial inspection purposes. One can see that the results of ML-EM-TV are more robust compared to the results of ML-EM-AwTV and ML-EM-GATV. Especially in the case of a high noise-level (SNR < 316) and few projections (SNR < 40), the standard deviation of the latter 2 methods have fluctuations. However, the variation is only approximately 10%, since these points lie in a RRMSE region which is close to 0.1 and there, the standard deviation is about 0.1. All measurement points on the right side of the black line have nearly the same standard deviation which is close to 0, indicating that these valuable results (where the RRMSE is greater than 0.04) are robust. The tendency of the RRMSE graph in all of the 3 plots is that the reconstruction methods produce worse results the higher the noise-level/under-sampling combination is. When the SNR is greater than 316, ML-EM-GATV can reconstruct a high quality image from 20 projections, where ML-EM-AwTV needs at least 30 and ML-EM-TV at least 40 projections for a similar RRMSE. ML-EM-AwTV can, by trend, better reconstruct images in case of low SNR / less projection settings. However, taking more projections (≥ 40) into consideration, ML-EM-GATV outperforms ML-EM-AwTV and ML-EM-TV for all examined SNRs and has much lower RRMSE values. SNR $= 100$ constitutes a special case, where ML-EM-AwTV outperforms ML-EM-GATV and ML-EM-TV in terms of a minimal RRMSE value, e.g. in case of 40 to 100 projection views.

5.4.3 Reconstruction results: 40 projections, different noise levels

In the following, we will discuss the properties of the algorithms by considering one column of figure 5.3, where the number of projections are 40 and different noise levels (SNR = 2236, 1000, 707, 316, 223, 158 or 100) are selected.
Figure 5.4 and 5.5 show the reconstruction results of ML-EM-TV, ML-EM-AwTV, ML-EM-GATV and FBP of the industrial CT engine data. The reconstructions produced by FBP are extremely noisy and show typical streaking artifacts caused by the under-sampling of the object. A tremendous loss of contrast for the FBP-results can be seen. Hence, it is impossible to identify the correct edge shape and location of structures. The results produced by FBP are unacceptable for industrial imaging.
Visually, the edge detail of the ML-EM-TV reconstructions in figures 5.4 and 5.5 is extremely poor, even for the noise-free case, and further worsens with higher noise levels. The correct shape of high and low-contrast edges cannot be recognized, either due to the introduction of additional artifacts, or due to a lowered contrast (pixel intensity) at the edges, e.g. for SNR = 2236 and lower SNRs. Visually, ML-EM-AwTV does not introduce additional artifacts in the reconstructed image down to a SNR of 707 and the edge detail is strong down to a SNR of 316. The results of ML-EM-GATV are artifact-free, down to a SNR of 223, which is the lower bound for a visually strong edge detail as well.

Figure 5.4: Reconstructions of an under-sampled industrial CT engine phantom from 40 projections and different noise levels. (Left to right) ML-EM-TV, ML-EM-AwTV, ML-EM-GATV, FBP (filter: Ram-Lak [283]) and the reference; (Top to bottom) SNR = ∞ (no noise), SNR = 2236, SNR = 1000, SNR = 707. The display range is [0.0173 - 0.0203].

Figure 5.5: Reconstructions of an under-sampled industrial CT engine phantom from 40 projections and different noise levels. (Left to right) ML-EM-TV, ML-EM-GATV, FBP (filter: Ram-Lak [283]) and the reference; (Top to bottom) SNR = 316, SNR = 223, SNR = 158, SNR = 100. The display range is [0.0173 - 0.0203].

5.4.3.1 Ability to restore fine structures

The visual impression of the reconstruction quality of the flaws can be judged in figures 5.4 and 5.5. Starting from a noise level of SNR = 707, cavities and cracks cannot be clearly identified for ML-EM-TV, due to a reduced contrast (pixel intensity) at the edges. Judging visually, the lower bound for identifying cracks and porosities for ML-EM-AwTV and ML-EM-GATV is a SNR of 158. The ability to restore fine structures, such as defects, cavities and cracks of one pixel width, can be measured by calculating the sum of the absolute difference between the reconstructed flaw pixel intensities $\mu_{\text{flaw-position}}$ and the true flaw pixel intensities $\mu^{\text{ref}}_{\text{flaw-position}}$. We calculated the mean over 10 different measurements, where the noise random variable was varied for each measurement. Concerning the true flaw pixel intensities and the reconstructed ones, the difference for ML-EM-GATV is up to one order of magnitude lower than for ML-EM-TV, see figure 5.6. For low noise levels, where the SNR is in the range of 2236 to 707, the difference between the reconstructed flaw pixel intensities and the true flaw pixel intensities for the results of ML-EM-AwTV is up to 1.76 times lower compared to the results of ML-EM-GATV. For lower noise levels, where the SNR is smaller than 316, ML-EM-GATV outperforms ML-EM-AwTV in terms of the quantitative difference measure, which is up to 1.4 times lower for ML-EM-GATV.

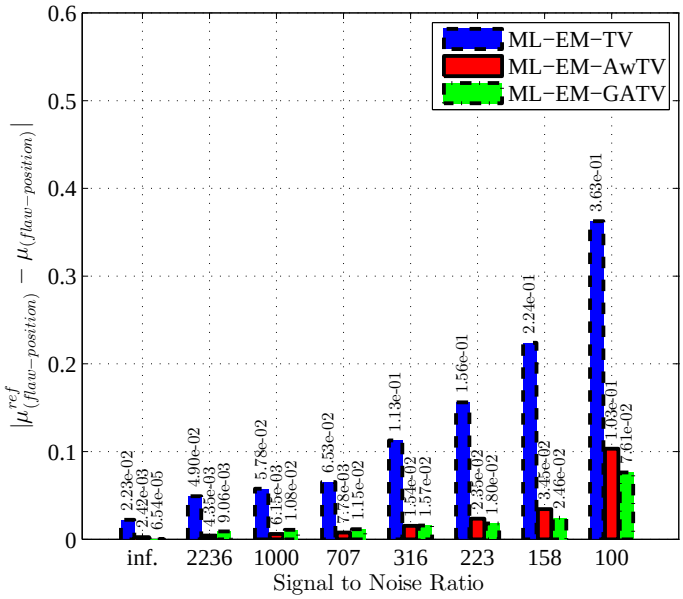

Figure 5.6: The mean of the sum of the difference between the true flaw pixel intensities and the reconstructed ones. 40 projections and different SNRs were used for the reconstruction and the mean over 10 different experiments, where the noise random variable was varied, was computed.

5.4.3.2 Convergence analysis

In figure 5.7, we plotted the log-RRMSE (left side) and log-likelihood behavior (right side) for ML-EM-TV, ML-EM-AwTV and ML-EM-GATV over the iterations for the under-sampled CT engine data (40 projections), top: SNR = 2236, bottom: SNR = 100. We first analyze the case of SNR = 2236: ML-EM-GATV has a much lower RRMSE than ML-EM-TV and ML-EM-AwTV, starting at iteration 100. The reason is that parameter τ decreases more quickly from this point on. As a consequence, the data term can restore the specific GMs which are then not penalized anymore. This leads to a higher data consistency which can be measured by the RRMSE. Near the converged solution at iteration 15,000, there is a clear drop of the RRMSE of ML-EM-GATV to be noticed. This is the point where the optimization step 2 begins. At this point, parameter τ is fixed and solely the remaining GMs related to noise are penalized. The RRMSE value of the result produced by ML-EM-GATV is approximately 10 times lower at the convergence point at iteration 35,000 compared to the RRMSE of ML-EM-TV and approximately 5.6 times lower than ML-EM-AwTV, indicating a better image quality. In case of SNR = 100, the convergence behavior is different:

In the beginning, the RRMSE of ML-EM-TV and ML-EM-AwTV is even higher compared to ML-EM-GATV. However, near the converged solution at iteration 15,000, there is a clear drop of the RRMSE of ML-EM-GATV to be noticed and it falls far below the RRMSE of ML-EM-AwTV and ML-EM-TV, by analogy with the case SNR = 2236.
The log-likelihood for an SNR of 2236 is monotonic and all methods converge to a high maximum likelihood. Under-relaxation, as achieved by parameter $\zeta = 0.01$ in algorithm 4, can influence the convergence behavior of ML-EM-GATV, as it can be seen in the likelihood at iteration 15,000 and SNR = 100. At this point, the likelihood of ML-EM-GATV drops below the likelihood of ML-EM-AwTV and ML-EM-TV. However, this effect has no impact on the RRMSE on the left side and the image quality respectively.

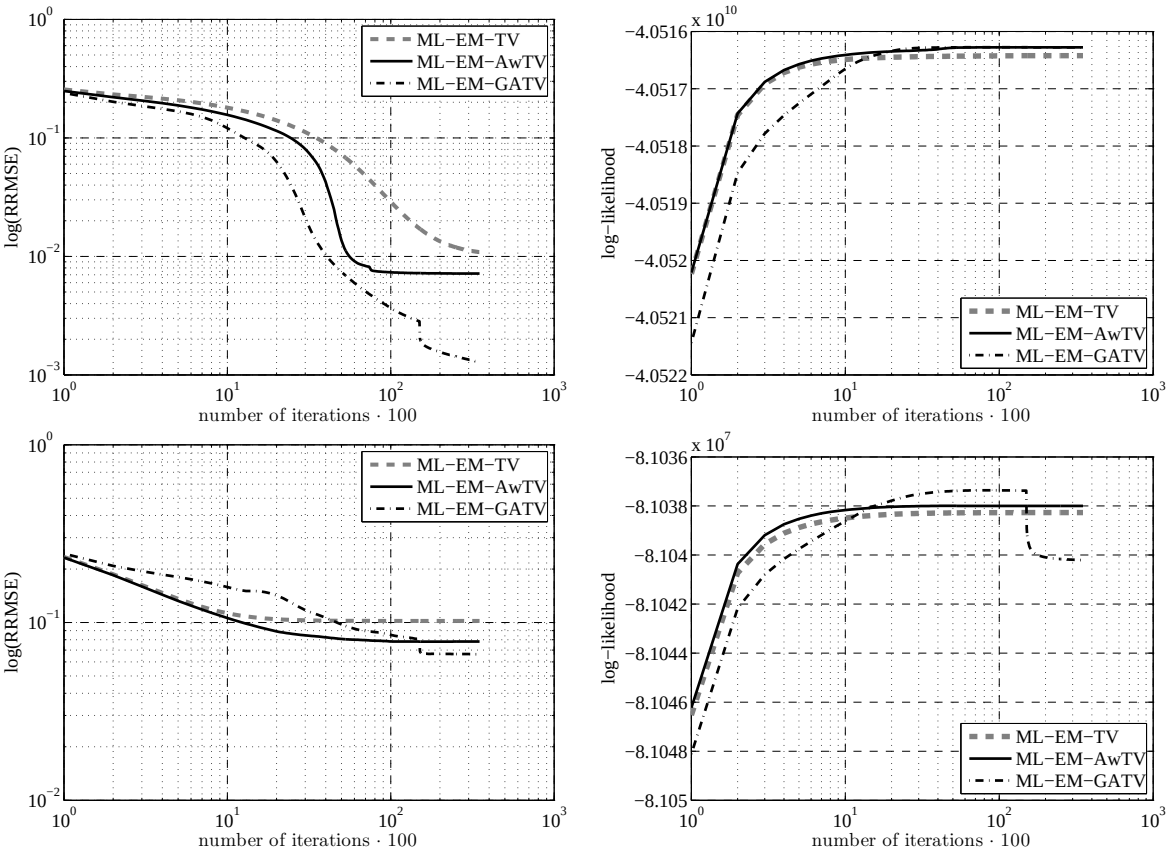

Figure 5.7: The log-RRMSE and the log-likelihood of the industrial CT reconstructions from 40 projections and the different algorithms: ML-EM-TV, ML-EM-AwTV and ML-EM-GATV. Top: SNR=2236, bottom: SNR = 100.

5.4.3.3 Ability to restore the true Gradient Magnitude Distribution

Figure 5.9 shows the performance of the algorithms and the utility of the chosen constants in table 5.3 to reconstruct the true GMD. One can see that the GMDs of the ML-EM-GATV results (cross) better approach the true GMD (square) compared to the GMDs of the results of ML-EM-TV (dot) or the GMDs of the results of ML-EM-AwTV (plus), irrespective of the noise level.
The Kullback-Leibler Distance of the reconstructed GMDs serves as a measure for the reconstruction quality of high and low contrast edges, since a correctly reconstructed GMD correlates with the edge preserving properties of the reconstruction algorithm. In figure 5.8, we measured the KLD of the true GMD and the reconstructed GMD of ML-EM-AwTV and ML-EM-TV. ML-EM-GATV can accurately restore the GMD for noise-free and noisy projections of SNR = 2236; there, the KLD is 0. For the other noise levels, the KLD of the GMDs of ML-EM-GATV is in most of the cases more than 1 order of magnitude lower compared to the KLD of the GMDs of ML-EM-TV and up to 7.8 times lower than the KLD of the GMDs of ML-EM-AwTV, except for SNR = 100, where the results for ML-EM-AwTV and ML-EM-GATV are almost similar.

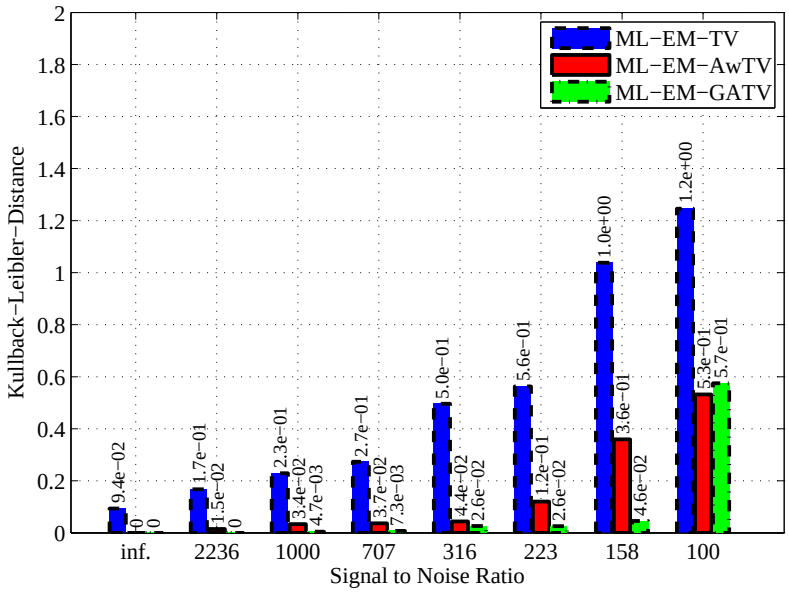

Figure 5.8: The Kullback-Leibler distance of the GMDs shown in figure 5.9. 40 projections were used for the reconstruction.

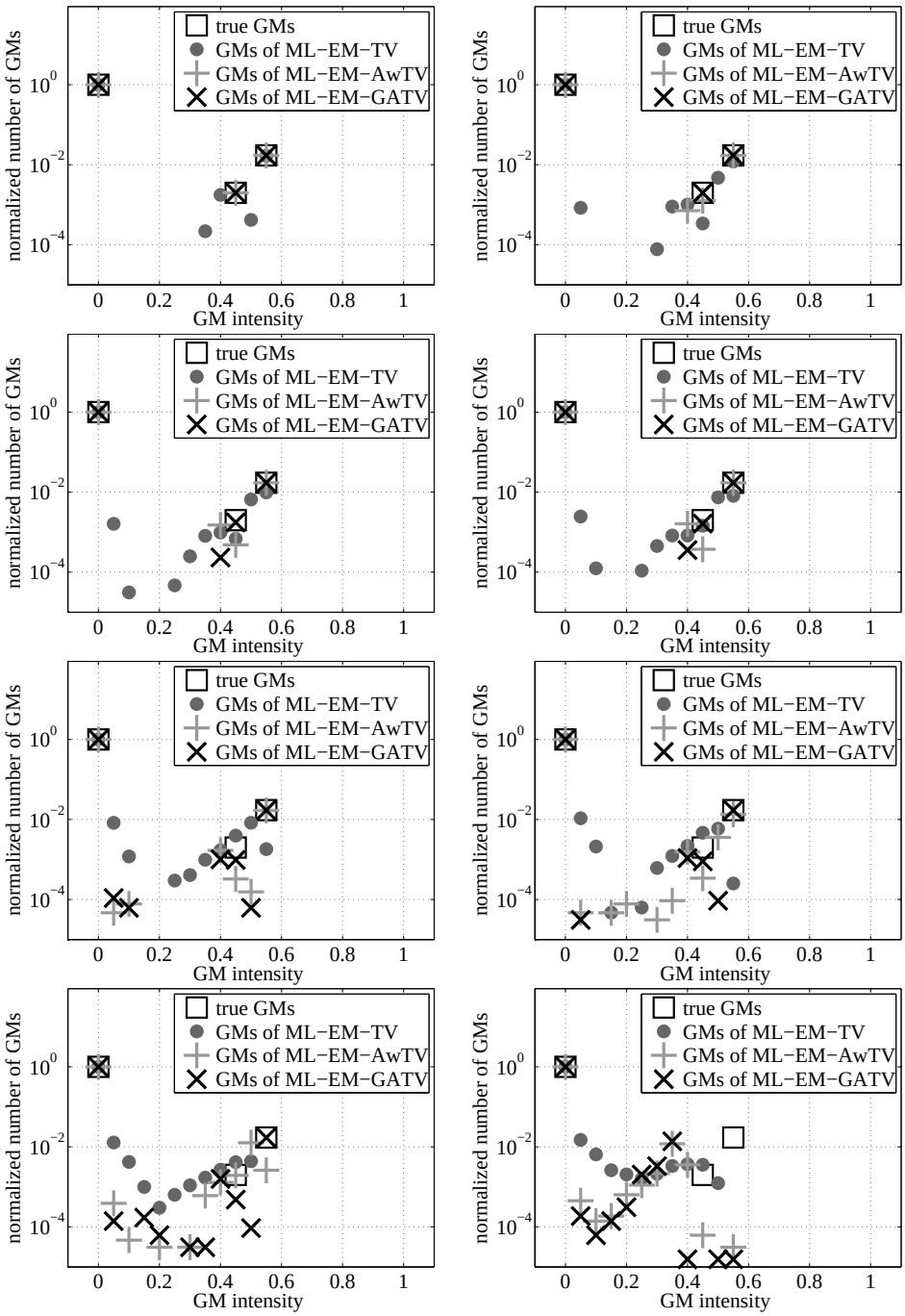

Figure 5.9: The GMDs of the ML-EM-TV (dot), the ML-EM-AwTV (plus) and the ML-EM-GATV (cross) industrial CT engine reconstructions of figures 5.4 and 5.5 compared to the GMD of the reference (square) at different noise levels (left to right): SNR = ∞, SNR = 2236, SNR = 1000, SNR = 707, SNR = 316, SNR = 223, SNR = 158, SNR =100. We selected 40 projections for the reconstructions. To compute the GMD, 12 bins were used, where one bin corresponds to the GM intensity of 0.05. Note, a GM intensity of 0 is not displayed for the sake of clarity. The GMs were computed in x-direction.

5.4.3.4 Ability to restore piece-wise constant images

The TV model prefers sudden over smooth transitions, the so-called "stair-casing effect". This effect results in undesired edges in regions which should be constant; and it further dominates in the image when the noise level increases (see [70] for details). ML-EM-TV introduces stair-cases in regions which should be flat, even for a high SNR of 2236, and this effect further intensifies with lower tube currents. ML-EM-AwTV and ML-EM-GATV can drastically reduce the stair-casing effect of ML-EM-TV, see figures 5.4 and 5.5. Independently of the noise level, ML-EM-GATV can produce a piece-wise constant result. For ML-EM-AwTV, the lower bound for restoring piece-wise constant results is a SNR of 707. Figure 5.10 shows the effect of checkerboards introduced by TV, which are best visible when directly displaying the derivative of TV (see e.g. [313], equation 7) at the last iteration of the noisy industrial CT phantom reconstruction. In figure 5.10, the derivatives of AwTV (see [218], equation 10) and GATV (see equation 5.11) are checkerboard-free.

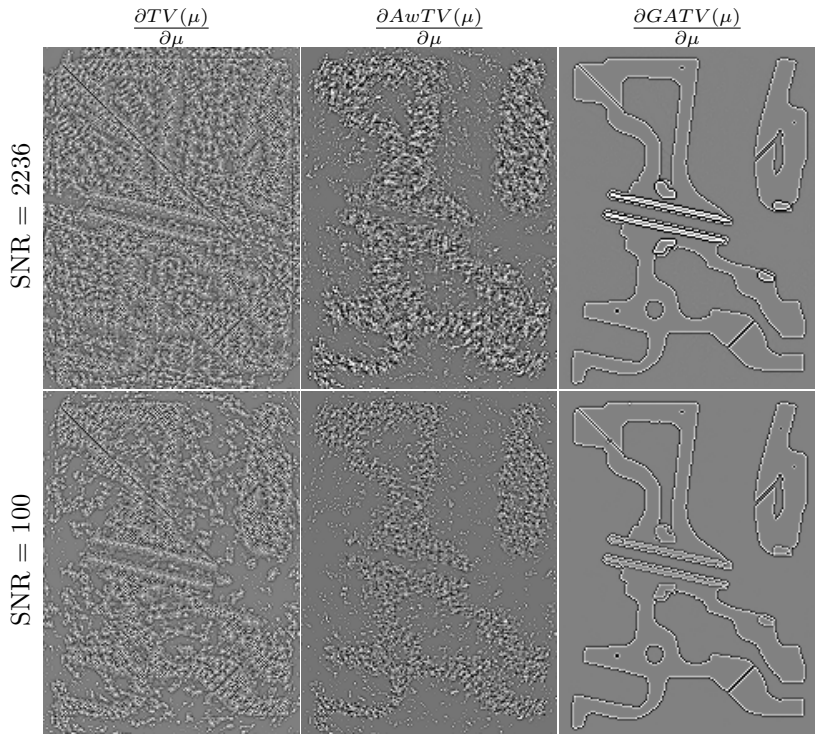

Figure 5.10: The derivative of TV (see [313], equation 7, window-level in case of SNR = 2236 and 100: $[-3.41, 3.41]$), AwTV (see [218], equation 10, window-level in case of SNR = 2236: [-4.95,5.82] and 100: $[-425.97, 507.72]$) and GATV (equation 5.12, window-level in case of SNR = 2236: [-0.0011,0.0011] and SNR = 100: [-0.037 - 0.036]) at the last iteration of the noisy industrial CT engine reconstruction (40 projections, SNR = 2236 and SNR = 100). The derivatives of AwTV and GATV are checkerboard-free.

We measured the homogeneity of the reconstruction results of ML-EM-TV, ML-EM-AwTV and ML-EM-GATV by analyzing the closeness of the distribution of elements in the Gray-Level Co-occurrence Matrix compared to the GLCM diagonal. Since the degree of homogeneity correlates with the introduction of artifacts, such as stair-cases and checkerboards, (piece-wise) homogeneous results are an indicator for artifact-free reconstructions. We performed 10 different measurements, where the noise random variable was varied for each measurement, and we then calculated the mean homogeneity for the reconstructions of the Forbild and industrial CT phantom from 40 projections and different SNRs. For all phantoms reconstructed by ML-EM-GATV, the reconstructions have nearly the same level of homogeneity (≈ 0.981), see figure 5.11. For ML-EM-TV, however, the results become less homogeneous for higher noise levels (starting from 0.982 for SNR = 2236 down to 0.969 for SNR = 100), the same for ML-EM-AwTV (starting from 0.982 for SNR = 2236 down

to 0.978 for SNR = 100). A reason for the inhomogeneity of ML-EM-TV reconstructions are stair-cases or the occurrence of regular patterns similar to a checkerboard in the results, or for ML-EM-AwTV, noise which is left in the reconstructed image. Comparing the results of ML-EM-AwTV for the engine phantom and the Forbild phantom in figure 5.11, one can see that they differ. The homogeneity of the Forbild phantom is even lower at a SNR of 2236, compared to a SNR of 1000. The reason is that the parameter set we found for ML-EM-AwTV in table 5.3 is only applicable to the engine phantom and new, optimal parameters have to be found for ML-EM-AwTV when other phantoms are used.

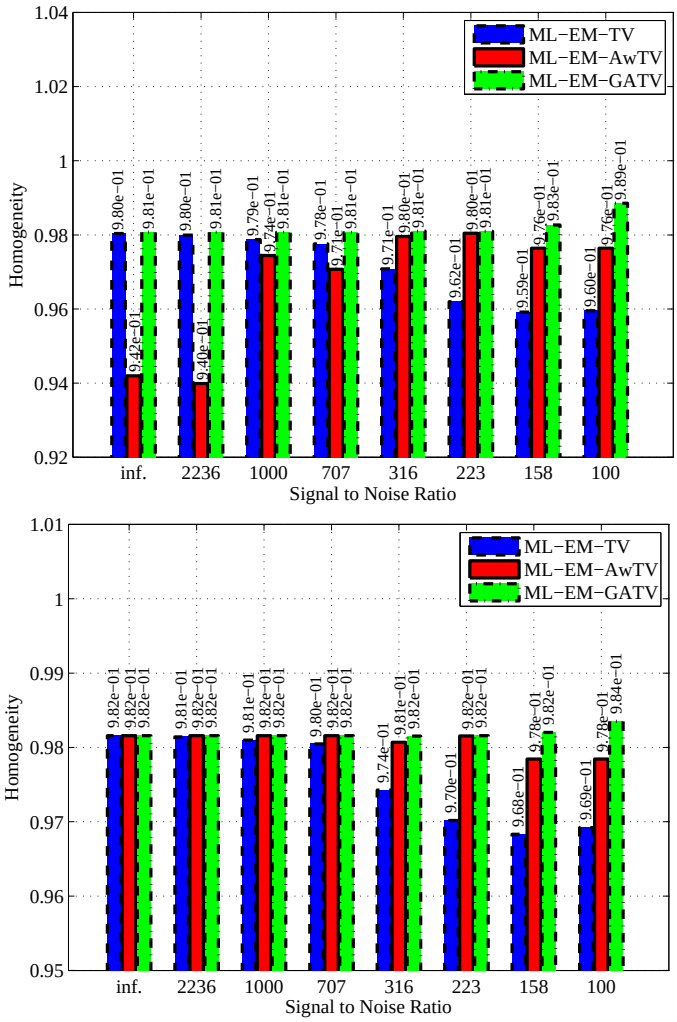

Figure 5.11: The mean homogeneity H of the reconstructions of the Forbild (top) and industrial CT engine (bottom) phantom. 40 projections and different SNRs were used for the reconstruction and then the mean over 10 different measurements, where the noise random variable was varied for each measurement, was calculated. Note, for AwTV, the parameters were optimized for the engine phantom.

5.4.3.5 Reconstruction quality in terms of RRMSE

In figure 5.12, we computed the mean RRMSE over 10 different measurements (by varying the noise random variable) of the under-sampled Forbild phantom (top) and engine block (bottom). ML-EM-GATV outperforms ML-EM-TV and ML-EM-AwTV in terms of RRMSE, irrespective of nearly all phantoms, number of projections or noise levels considered. The RRMSE of ML-EM-GATV is up to one order of magnitude lower compared to the results of ML-EM-TV and up to four times lower compared to the results of ML-EM-AwTV. SNR = 100 constitutes a special case where ML-EM-TV and ML-EM-AwTV outperform ML-EM-GATV and have a slightly lower RRMSE value. Note, for ML-EM-AwTV, the parameters were optimized for the engine phantom; therefore, theoretically, better results could be achieved when the parameters are optimized for the Forbild phantom. We evaluated at which dose level our proposed method, GATV, and AwTV produce the same (mean) RRMSE (over 10 different measurements) as TV: Considering the Forbild phantom, ML-EM-GATV has still a lower RRMSE at a SNR of 158 compared to TV at a SNR of 1000 and ML-EM-AwTV has the same RRMSE value at a SNR of 223 compared to TV at a SNR of 1000. We conclude that the dose and the acquisition time respectively can be reduced by a factor of approximately 7 for GATV and approximately 3.5 for AwTV.

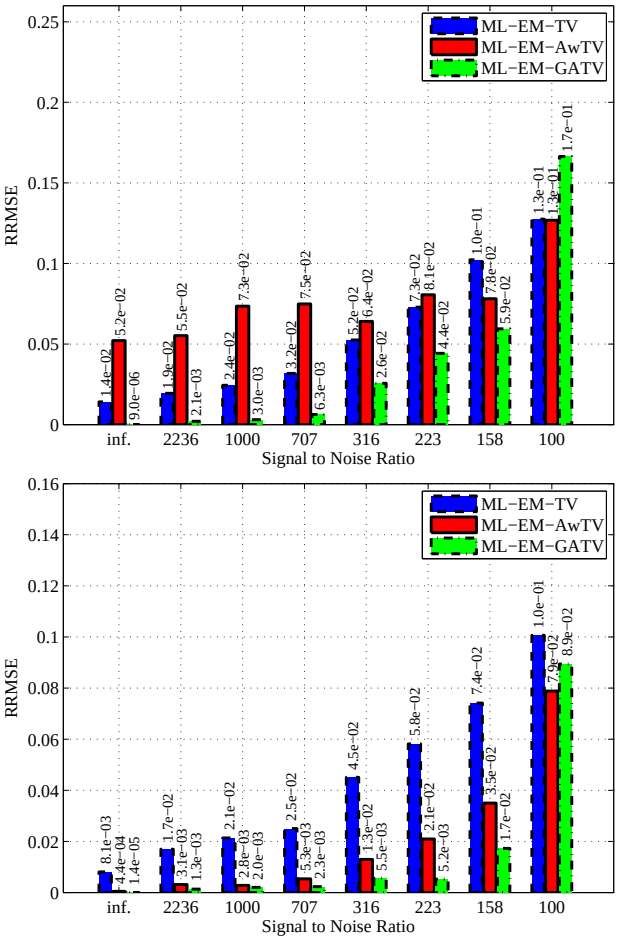

Figure 5.12: The mean Relative Root Mean Squared error (for 10 different measurements with a varying noise random variable) of the reconstruction results in figure 5.4 and 5.5 for ML-EM-TV, ML-EM-AwTV and ML-EM-GATV. Top: Forbild phantom, bottom: Industrial CT engine phantom. 40 projections and different SNRs were chosen for the reconstruction. Note, for AwTV, the parameters were optimized for the engine phantom.

5.4.3.6 Ability to restore a high contrast level

We computed the mean CNR of 10 different measurements, where the noise random variable was varied for each measurement in selected regions within the noise-free Forbild reconstructions (40 projections, different SNRs). Figure 5.13 shows that the CNR of the ML-EM-GATV reconstructions is up to a factor of 146 higher compared to the results of ML-EM-TV and up to a factor of 1277 higher than ML-EM-AwTV, e.g. region one and region six for the noise-free case respectively. For a SNR of 316 and lower SNR values, the CNR of all methods is more or less equal. Again, due to the fact that the parameters for ML-EM-AwTV were optimized for the engine phantom and not for the Forbild phantom, better results for ML-EM-AwTV could be theoretically achievable.

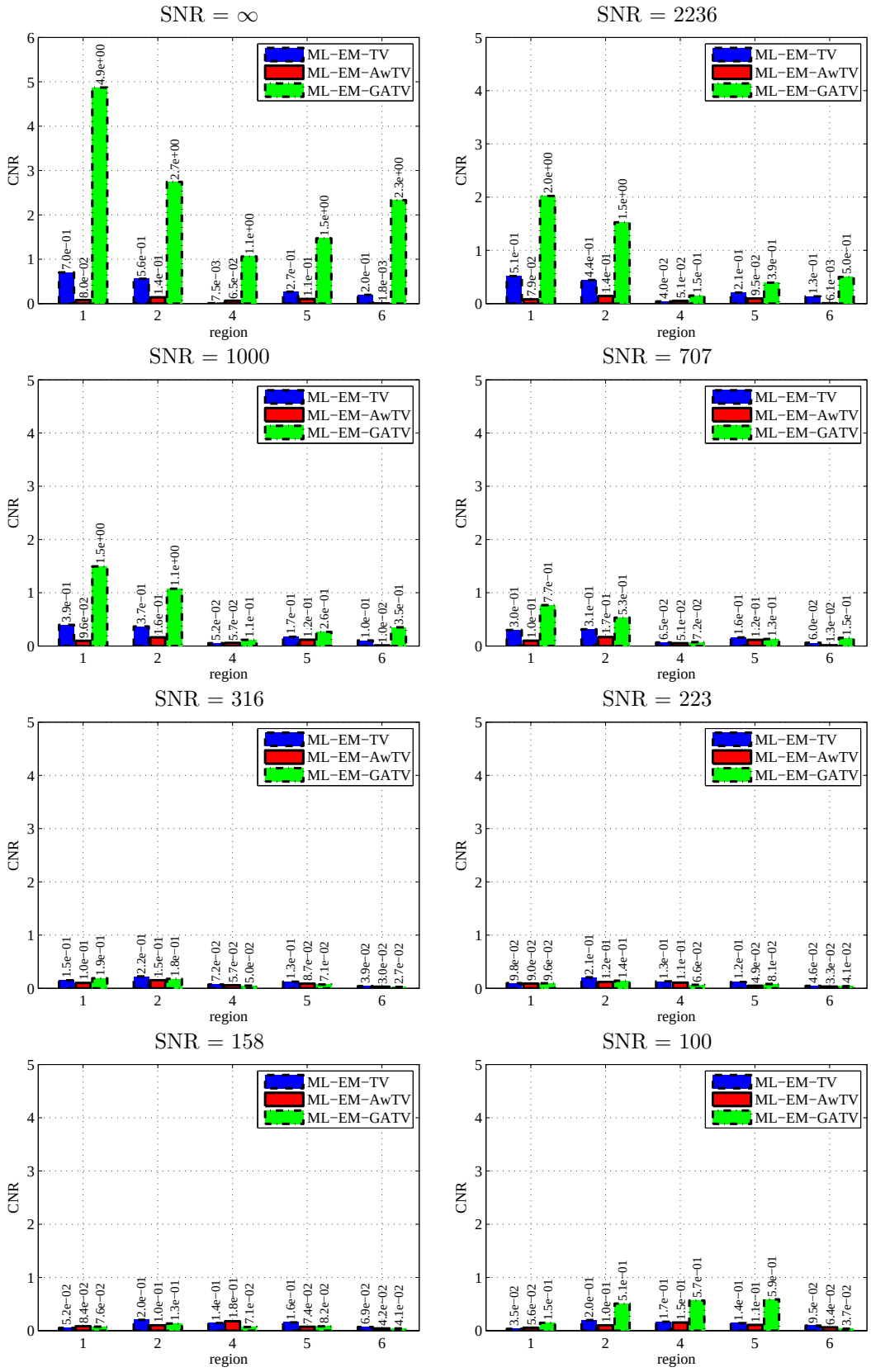

Figure 5.13: The mean CNR (for 10 different measurements with varying noise random variable) of the ML-EM-TV, ML-EM-AwTV and ML-EM-GATV reconstructions of the Forbild phantom. 40 projections were used for the reconstruction and different noise levels were chosen. The CNR was computed in the selected regions of figure 2.4 f).

5.5 Discussion and conclusion

The achieved results demonstrate the superiority of the proposed strategy compared to ML-EM-TV and ML-EM-AwTV. The new regularization function does not penalize large GMs for the reconstruction of objects only consisting of few material types. This can only be achieved if the regularization function varies over time.
What is of high practical relevance is the ability of this strategy to reconstruct even small cracks or porosities in the object as long as the boundary of the object features is described by large Gradient Magnitudes related to the surrounding material.
It can be observed that the limit of this method is reached when homogeneous structures are not reconstructed as flat objects anymore. Before this stage, however, the risk of incorrectly reconstructing porosities and cracks still increases.
The field of application of this method is limited to cases where the Gradient Magnitude Distributions are such that small GMs do only occur infrequently in the true data object. In case of blurred boundaries, small contrast structures or structures that are much smaller than the resolution of the CT, the regularization term either removes the structures or sharpens the edges.
Another observation is that our proposed method does not introduce additional artifacts like a checkerboard pattern or stair-cases as produced by TV or AwTV. This results in smooth, piecewise homogeneous reconstruction images.
We observed that the knowledge about the whole GM spectrum of the scanned object is actually not needed to find suitable parameters for ML-EM-GATV which produce high quality CT images. Considering parameter τ for example, τ_{start} is selected in such a way to penalize the whole spectrum in the beginning of the optimization and τ_{end} is restricted to the amount of noise in the image, i.e. τ_{end} cannot be smaller than the noise magnitude to avoid artifacts in the image. Since τ_{start} is not sensitive, further investigation on the GATV method can solely concentrate on the cooling scheme (and κ within this scheme).
For AwTV, the parameters highly depend on the phantom and have to be optimized for each phantom individually. This is not the case for TV or GATV, where the parameters are applicable to all of the investigated phantoms.
This chapter discussed the potential, limitation and mechanics of a Generalized Anisotropic Total Variation regularizer, which is well-suited for industrial CT. It shows extraordinary superiority compared to ML-EM-TV and ML-EM-AwTV. In addition, we can use the same strategy of non-penalizing structures and penalizing noise directly in dedicated transforms in the same way we performed here in order to use problem-specific information. Whether this approach is of use in medical CT, still needs to be investigated. In cases where noise is simulated, our strategy achieves a Relative Root Mean Square Error that is up to 11 times lower than Total Variation-based and up to 4 times lower than AwTV-based iterative statistical reconstruction (e.g. for a SNR of 223 and 40 projections). To obtain the same reconstruction quality as achieved by Total Variation, the projection number and the pulse length, and the acquisition time and the dose, respectively, can be reduced by a factor of approximately 3.5, when AwTV is used and a factor of approximately 7, when our proposed algorithm is used.

Chapter 6

Comparison of the Three Proposed Regularization Methods for Low-Dose, Under-Sampled Iterative CT Reconstruction

6.1 Outline

In the previous chapters, we proposed three new regularization methods for accurate, under-sampled, low-dose iterative CT reconstruction. All of these methods improve the reconstruction results of FBP and TV.
In this chapter, we want to examine the three methods, ATV, ATV+TV^2 and GATV in one general framework and we want to show in a large experiment with 560 reconstructions that these methods successively improve the resulting images. Each method, ATV, ATV+TV^2 and GATV, produces better results than its preceding method: We will show that ATV [71] produces better results than TV, ATV+TV^2 [70] produces better results than ATV and GATV [69] produces better results than ATV+TV^2. Furthermore, each method can successively improve the reconstruction results of the current state of the art method, Total Variation. The main goal of this chapter is to quantitatively determine the highest possible dose-reduction factor[1] in case of low-dose reconstructions from few projections under the assumption that still better reconstruction images can be obtained compared to TV reconstructions from many views and a high dose setting. Besides that, we are interested in the visual impression of the reconstruction images, the CNR and the homogeneity of the results.

6.2 Materials and Methods

The properties of TV and the other three regularization methods, ATV, ATV+TV^2 and GATV, have been discussed extensively in the previous chapters. Now we want to evaluate the methods in a common framework. For that purpose we consider a Poisson noise model for imaging, see equation 2.17 and equation 2.21. Note, the raw-measurements were not log-converted, resulting in the likelihood function defined in equation 2.24 and the following objective function:

$$\mu^* = \underset{\mu'}{\operatorname{argmax}}\ L(Y, \mu') - \beta\phi\left(\mu'\right), \tag{6.1}$$

[1]The dose-reduction factor is obtained by a multiplication of the maximum reduction value of the tube current with the under-sampling rate compared to the settings of a reference reconstruction. It yields a possible overall dose reduction value.

The regularized and relaxed Ordered Subsets Convex algorithm described in section 2.2.4.2 and defined in equation 2.28 is a typical solver for this objective function. As regularization term we select $\phi(\cdot) = \left\{\text{TV},\ \text{ATV},\ \text{ATV} + \text{TV}^2,\ \text{GATV}\right\}$ and we denote the reconstruction algorithm OSC-TV, OSC-ATV, OSC-ATV+TV^2 and OSC-GATV.
The simulation and reconstruction conditions are equal to those described in section 5.3.3. These are summarized in short:

- We reconstruct two-dimensional digitally simulated phantom data presented in section 2.2.1.3 using the regularized OSC algorithm. In order to overcome multiple solutions [15], only one subset for the reconstruction is used in our implementation.
- We apply an inverse Crime study and we use the Siddon method [310] for generating the projection data and the Siddon method for the forward model in the reconstruction with the same parameters.
- For all of the four methods, TV, ATV, ATV+TV^2 and GATV and the examined noise levels, we derived an optimal parameter set on the basis of a particular phantom by testing all combinations of corresponding parameters of each method in a useful range with the goal of a minimal overall RRMSE of the reconstruction. For OSC-TV, OSC-ATV, OSC-ATV+TV^2, we chose the Forbild phantom and 40 projections to find optimal parameters. For OSC-GATV, we selected the industrial CT engine phantom and 40 projections. The resulting constants of this evaluation are listed in table 6.1. We used this parameter set for the reconstruction of the lung and engine phantom as well.
- Let us establish a sequence of methods to ease the discussion in this chapter: If we talk about a preceding or successive method, we refer to the element before and after an element in the sequence: OSC-TV (1), OSC-ATV (2), OSC-ATV+TV^2 (3) and OSC-GATV (4). Hereby, OSC-TV is referred to the first method, OSC-ATV is denoted the second method, OSC-ATV+TV^2 is the third method and OSC-GATV is the fourth method.
- We evaluated the four methods on all combinations of the projection views and noise levels in table 5.4. For each noise level and projection view combination we evaluated 10 different realizations of the Poisson noise random variable, resulting in 560 experiments.
- To quantitatively evaluate the reconstruction results, we apply the figures of merit introduced in section 5.3.4 and we computed the mean over 10 different measurements, where the noise random variable has been varied for each measurement.
- To qualitatively evaluate the reconstruction results, we computed the mean of the resulting 10 images for each noise level and projection number combination, so as to draw a meaningful conclusion on the reconstruction quality of the methods.

CONSTANTS FOR OSC-GATV, OSC-ATV+TV^2, OSC-ATV and OSC-TV

GATV	SNR	N	β	τ_{start}	τ_{end}	κ
	∞	$2.0 \cdot 10^6$	0.2	0.3	$1.0 \cdot 10^{-4}$	$1.0 \cdot 10^{-5}$
	2236	$1.5 \cdot 10^4$	0.3	0.3	$7.0 \cdot 10^{-3}$	$8.0 \cdot 10^{-4}$
	1000	$1.5 \cdot 10^4$	0.3	0.3	$4.1 \cdot 10^{-3}$	$8.0 \cdot 10^{-4}$
	707	$1.5 \cdot 10^4$	0.3	0.3	$1.0 \cdot 10^{-2}$	$8.0 \cdot 10^{-4}$
	316	$1.5 \cdot 10^4$	0.3	0.3	$2.0 \cdot 10^{-2}$	$8.0 \cdot 10^{-4}$
	223	$1.5 \cdot 10^4$	0.3	0.3	$3.5 \cdot 10^{-2}$	$8.0 \cdot 10^{-4}$
	158	$1.5 \cdot 10^4$	0.3	0.3	$3.8 \cdot 10^{-2}$	$8.0 \cdot 10^{-4}$
	100	$1.5 \cdot 10^4$	0.3	0.3	$6.0 \cdot 10^{-2}$	$8.0 \cdot 10^{-4}$
ATV+TV^2	SNR	N	β	δ	λ	
	∞	$3.5 \cdot 10^4$	$9.0 \cdot 10^{-4}$	$5.0 \cdot 10^{-3}$	$4.0 \cdot 10^{-2}$	
	2236	$3.5 \cdot 10^4$	$2.1 \cdot 10^{-3}$	$5.0 \cdot 10^{-3}$	$2.0 \cdot 10^{-2}$	
	1000	$3.5 \cdot 10^4$	$4.1 \cdot 10^{-3}$	$5.0 \cdot 10^{-3}$	$3.0 \cdot 10^{-2}$	
	707	$3.5 \cdot 10^4$	$5.5 \cdot 10^{-3}$	$4.0 \cdot 10^{-3}$	$3.0 \cdot 10^{-2}$	
	316	$3.5 \cdot 10^4$	$9.7 \cdot 10^{-3}$	$9.0 \cdot 10^{-3}$	$1.6 \cdot 10^{-1}$	
	223	$3.5 \cdot 10^4$	$1.1 \cdot 10^{-2}$	$7.0 \cdot 10^{-3}$	$1.0 \cdot 10^{-1}$	
	158	$3.5 \cdot 10^4$	$1.3 \cdot 10^{-2}$	$8.0 \cdot 10^{-3}$	$1.5 \cdot 10^{-1}$	
	100	$3.5 \cdot 10^4$	$1.4 \cdot 10^{-2}$	$1.0 \cdot 10^{-2}$	$2.0 \cdot 10^{-1}$	
ATV	SNR	N	β	δ		
	∞	$3.5 \cdot 10^4$	$1.2 \cdot 10^{-3}$	$4.8 \cdot 10^{-3}$		
	2236	$3.5 \cdot 10^4$	$1.7 \cdot 10^{-3}$	$5.0 \cdot 10^{-3}$		
	1000	$3.5 \cdot 10^4$	$4.1 \cdot 10^{-3}$	$4.0 \cdot 10^{-3}$		
	707	$3.5 \cdot 10^4$	$5.0 \cdot 10^{-3}$	$4.0 \cdot 10^{-3}$		
	316	$3.5 \cdot 10^4$	$8.0 \cdot 10^{-3}$	$6.0 \cdot 10^{-3}$		
	223	$3.5 \cdot 10^4$	$1.0 \cdot 10^{-2}$	$7.0 \cdot 10^{-3}$		
	158	$3.5 \cdot 10^4$	$1.4 \cdot 10^{-2}$	$1.6 \cdot 10^{-2}$		
	100	$3.5 \cdot 10^4$	$7.4 \cdot 10^{-3}$	$2.5 \cdot 10^{-2}$		
TV	SNR	N	β			
	∞	$3.5 \cdot 10^4$	$8.0 \cdot 10^{-4}$			
	2236	$3.5 \cdot 10^4$	$1.1 \cdot 10^{-3}$			
	1000	$3.5 \cdot 10^4$	$1.3 \cdot 10^{-3}$			
	707	$3.5 \cdot 10^4$	$1.8 \cdot 10^{-3}$			
	316	$3.5 \cdot 10^4$	$2.0 \cdot 10^{-3}$			
	223	$3.5 \cdot 10^4$	$5.0 \cdot 10^{-3}$			
	158	$3.5 \cdot 10^4$	$8.7 \cdot 10^{-3}$			
	100	$3.5 \cdot 10^4$	$1.8 \cdot 10^{-2}$			

Table 6.1: Constants for GATV, ATV+TV^2, ATV and TV applicable to all phantoms, noise-levels, realizations of the noise random variable and projection views used in section 2.2.1.3. Note, a SNR of ∞ corresponds to a noise-free sinogram, where d_0 was set to 2236^2 ($\approx 5,000,000$), however, no Poisson noise was applied in equation 2.17.

6.3 Results

6.3.1 Overall evaluation

We performed an overall evaluation of the reconstruction methods, TV, ATV, ATV+TV^2 and GATV for the different phantoms. The results are visualized in figure 6.7 (Forbild phantom), figure 6.8 (engine phantom) and figure 6.9 (lung phantom). The graph shows the dependency of mean RRMSE on the number of projections and the noise level for the different phantoms. A two-dimensional contour plot shows the interpolated mean RRMSE at a discrete set of measurement points. Each point corresponds to 10 different measurements, where the noise random variable varied for each of the measurements and a specific combination of the number of projections (10, 20, 30, 40, 60, 80, 100 or 200) and SNRs (2236, 1000, 707, 316, 223, 158 or 100) was selected. The rgb-valued and gray-valued color bars represent the mean and standard deviation of the RRMSE of the 10 different measurements respectively.
Let us restrict the following analysis to a color-region which can be classified as an acceptable image quality: The RRMSE is in the interval $[0, 0.04]$, representing a dark-blue to light-blue color area in the plot. In figures 6.7, 6.8 and 6.9, one can directly see that based on the plot in a) (result of TV), this region subsequently expands more and more to the left and to the lower part of the plot for each graph in b) (result of ATV), c) (result of ATV + TV^2) and d) (result of GATV). This means that each method can successively improve the RRMSE in case less projections (left part in the plot) and a higher noise level (lower part in the plot) are selected. Furthermore, considering the rgb-colored environment of each measurement point, one can directly see that for each method, the point lies in an environment which has a darker blue color than its preceding method. This means that each method produces a better result based on the preceding method (RRMSE(TV) > RRMSE(ATV) > RRMSE(ATV+TV^2) > RRMSE (GATV)). This holds true for each of the measurement points in the interval of RRMSE: $[0, 0.04]$.
All methods produce a robust result for each measurement point in figures 6.7, 6.8 and 6.9, since the standard deviation for all points is close to 0 (black color). The only exception are the measurement points for OSC-ATV+TV^2 and OSC-GATV in case of a high noise contribution (SNR $\leq$ 316) and a small number of projections ($\leq$ 30). There, the SD of the points can reach a value of 0.03 and compared to the mean values at these points, which vary in between [0.06,0.1], this represents a deviation of approximately 50%, worst case. However, it is clear that the results can strongly deviate for low-quality images, since they are often corrupted by artifacts or noise left in the image and the results of repeated experiments therefore differ quite much from each other. The important thing is that the results do not deviate in regions where the mean value is in the interval [0,0.04], since these values represent an acceptable image quality. As we can see from figures 6.7, 6.8 and 6.9 the standard deviation of the measurements is close to 0 in this interval.

6.3.2 Reconstruction results: 40 projections, different noise levels, 10 different noise random variables

Let us now have a closer look at the resulting images and quality metrics (RRMSE, CNR, homogeneity) in case of a specific number of projections (40), different SNRs (2236, 1000, 707, 316, 223, 158 or 100) and 10 different measurements, where the noise random variable varied for each of the measurement. We computed the mean for each result (image or quality metric). Figures 6.1, 6.3 and 6.5 present the noise-free reconstructions of the Forbild, engine and lung phantom data and figures 6.2, 6.4 and 6.6 present the corresponding results of the noise-corrupted data.

Reconstructed images

In case of noise-free projections, GATV can accurately reconstruct the Forbild phantom from 20 projections. TV, ATV and ATV+TV^2, however, produce results which are heavily corrupted.

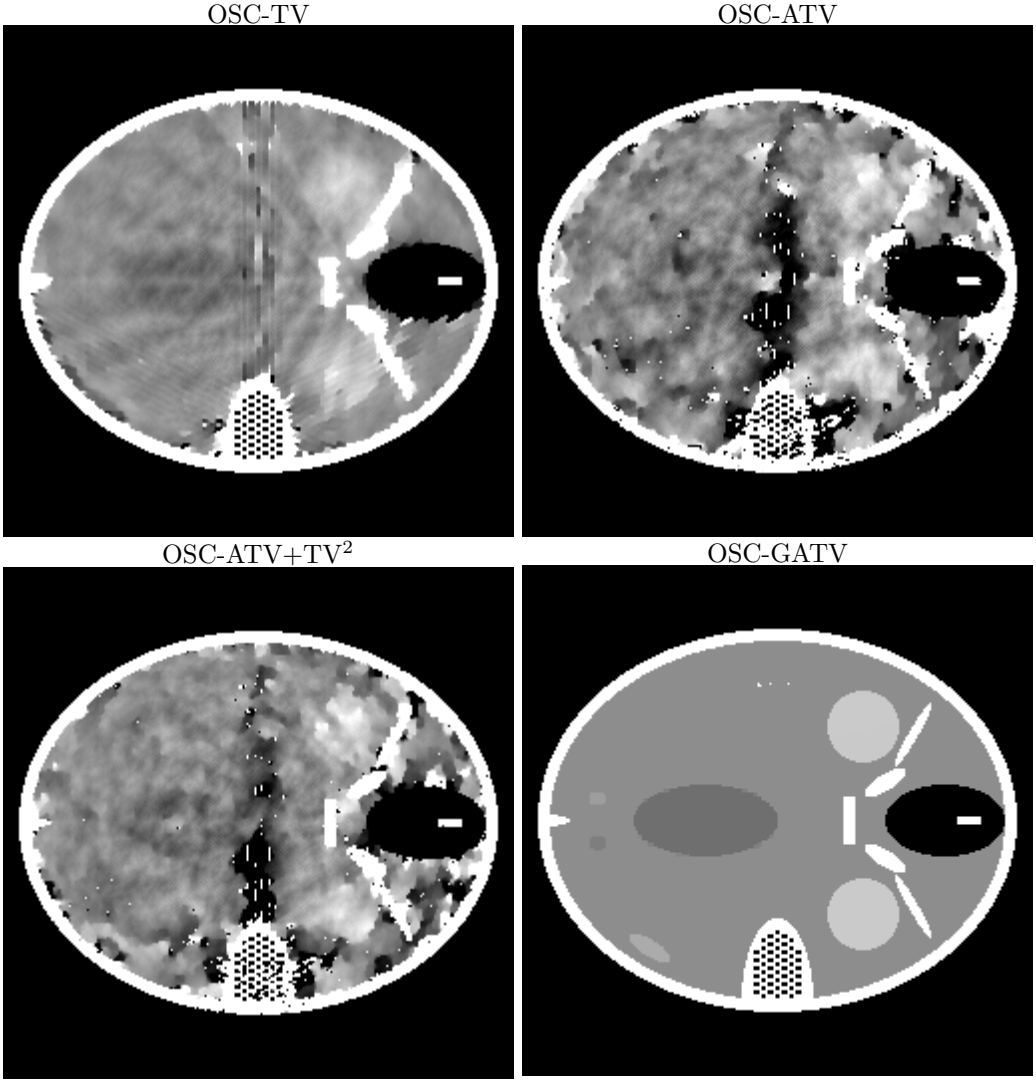

Reconstructions of the Forbild phantom from 20 noise-free projections, window-level: [0.0188,0.0196].

For GATV and ATV+TV^2, a visually acceptable result can be obtained from 30 projections, not so for TV and ATV. Low-contrast objects in the result of ATV+TV^2, however, are blurred.

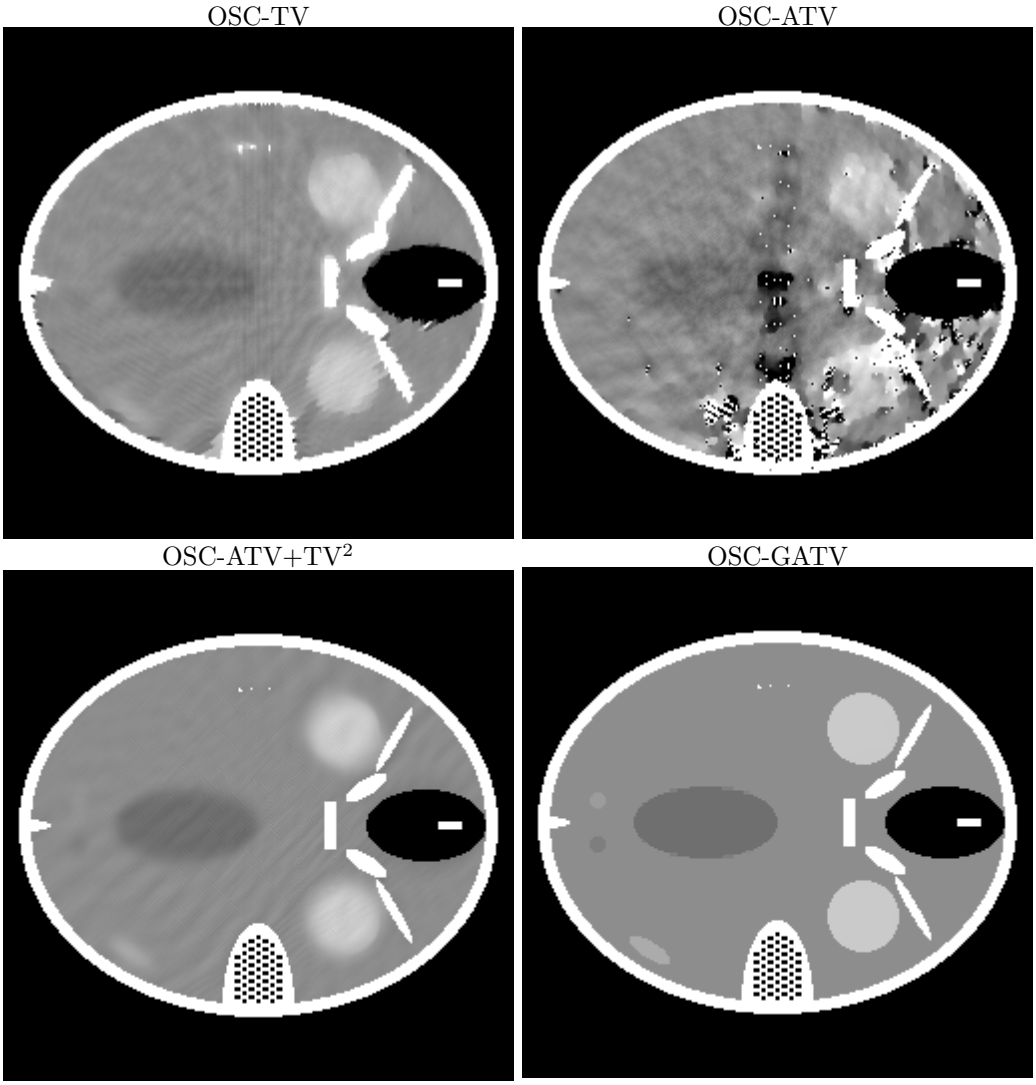

Reconstructions of the Forbild phantom from 30 noise-free projections, window-level: [0.0188,0.0196].

For OSC-ATV and OSC-TV, at least 40 projections are needed to obtain a reasonable image quality in case of the Forbild phantom reconstruction. Low-contrast objects in the result of TV, ATV and ATV+TV^2, however, are blurred.

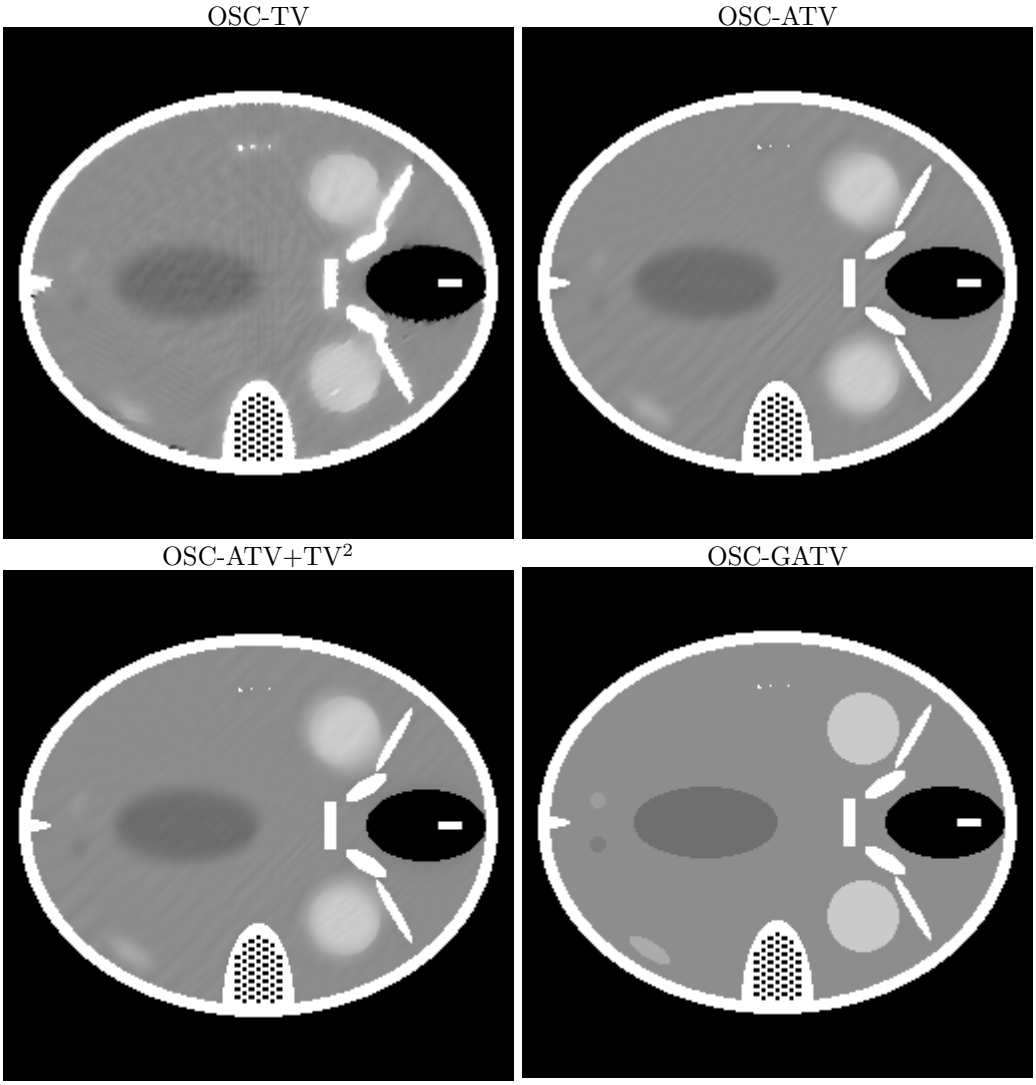

Reconstructions of the Forbild phantom from 40 noise-free projections, window-level: [0.0188,0.0196].

In case of the engine data, OSC-TV and OSC-ATV+TV^2 need at least 40 projections and OSC-ATV needs at least 60 views for an accurate result, see figure 6.3. For more than 40 views, the results of OSC-TV, OSC-ATV, OSC-ATV+TV^2 and OSC-GATV do not differ much, except for the Forbild phantom in figure 6.1, where OSC-GATV can better restore extreme low-contrast edges than OSC-TV, OSC-ATV and OSC-ATV+TV^2: Those features are sharper and clearer for GATV.

In case of noisy projections and the Forbild phantom, OSC-GATV cannot restore the extreme low-contrast objects, even for a noise-level of SNR = 2236. Here, the other methods, OSC-TV, OSC-ATV and OSC-ATV+TV^2 can yield slightly sharper edges concerning these features.

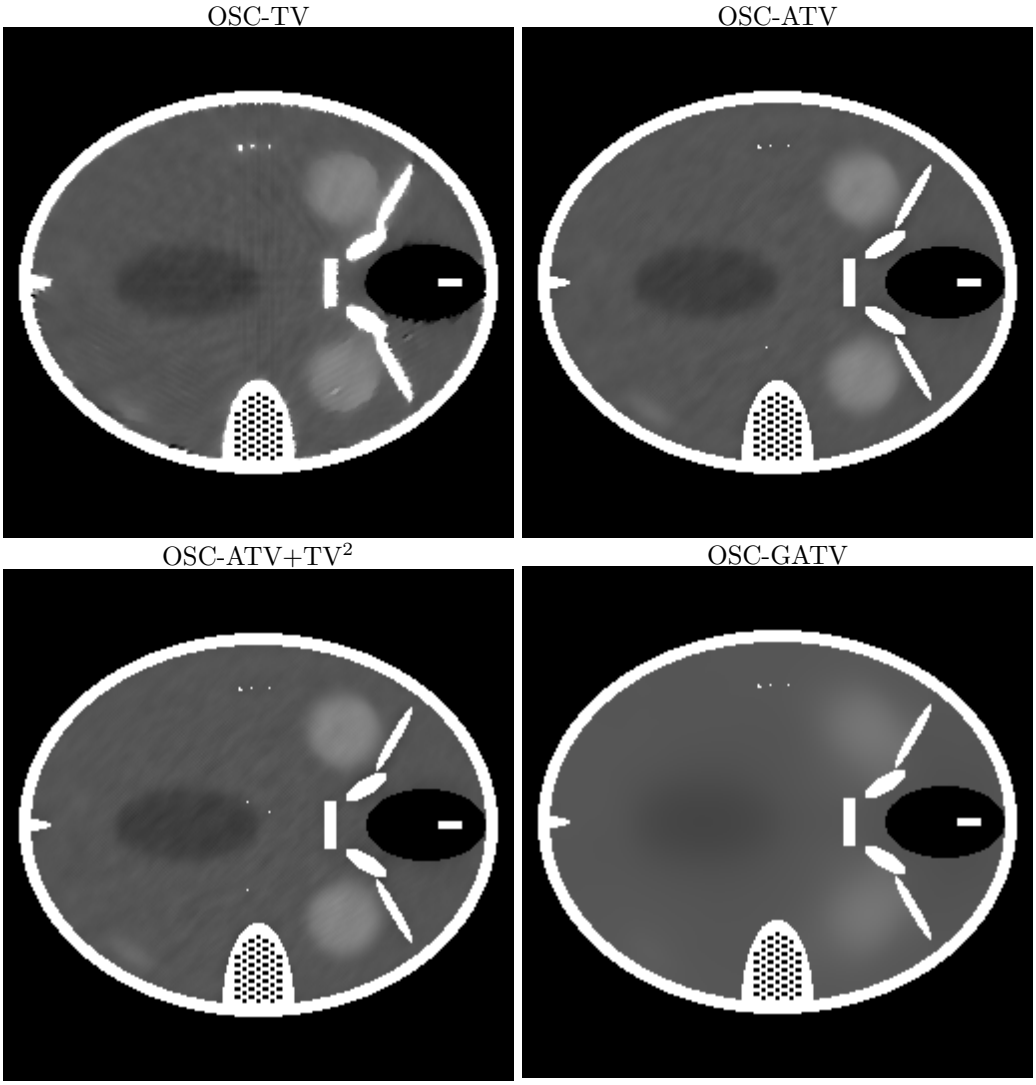

Reconstructions of the Forbild phantom from 40 projections. A SNR of 2236 was chosen and the mean over 10 different realizations of the noise random variable was computed, window-level: [0.0188,0.0196].

Figures 6.2, 6.4 and 6.6 show the reconstructions of the Forbild, engine and lung phantom respectively from noisy projections. By trend, each method, OSC-ATV, OSC-ATV+TV^2 and OSC-GATV can successively improve the visual impression of the edge detail and edge sharpness. Let us consider the reconstruction results of the different methods OSC-TV, OSC-ATV and OSC-ATV+TV^2 in case of the lung phantom as a typical example to analyze the image quality. A SNR of 158 and 40 projections were selected and the mean over all resulting images of the 10 different experiments, where the random noise variable was varied or each experiment, was computed.

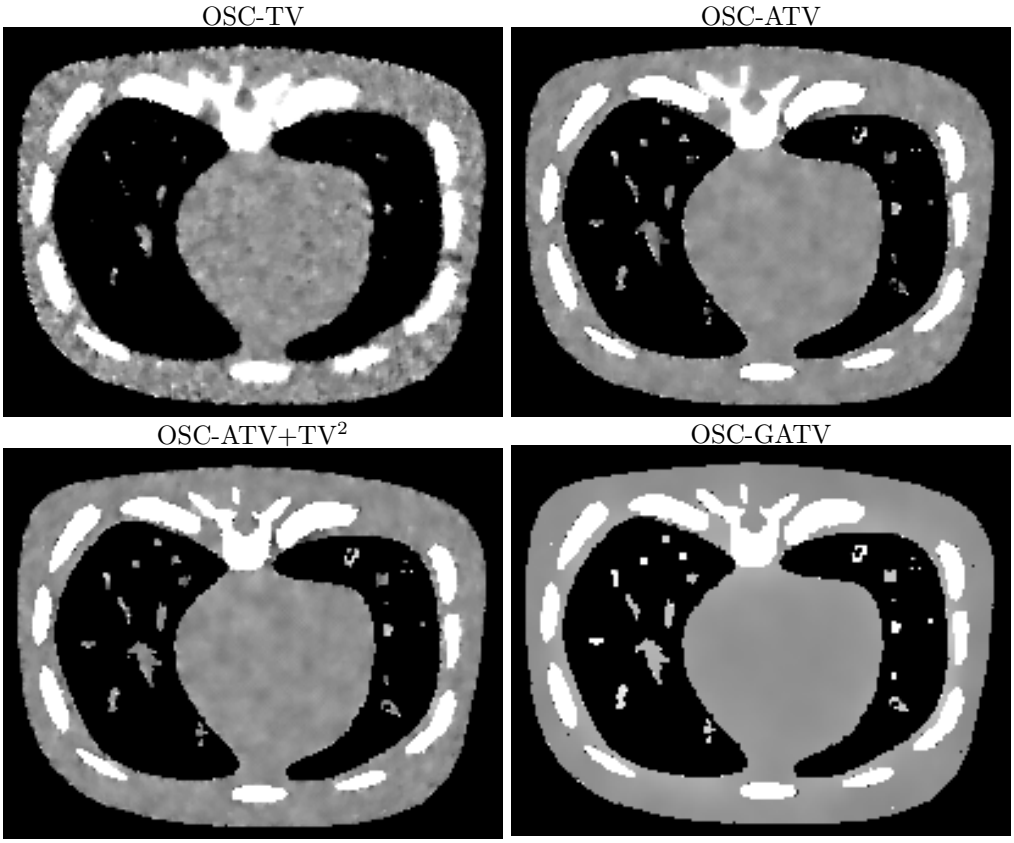

Reconstructions of the Forbild phantom from 40 projections. A SNR of 158 was chosen and the mean over 10 different realizations of the noise random variable was computed, window-level: [0.016,0.0178].

One can see that OSC-TV cannot produce a homogeneous result. Furthermore, small structures (bronchi of single pixel width) are over-smoothed and the edge detail of the bones is very weak: The edges of the bones are blurred and cannot be clearly identified. OSC-ATV can produce a visually much better image than OSC-TV, since it can better preserve small structures like the bronchi. Furthermore, the bones are sharper and the reconstructed image is much more homogeneous. All these characteristics are further improved by the other 2 methods OSC-ATV+TV^2 and OSC-GATV. OSC-ATV+TV^2 can produce images with a better edge sharpness than OSC-ATV. Furthermore, OSC-ATV+TV^2 can better preserve small-scaled features like the bronchi compared to OSC-ATV. OSC-GATV produces the best result which is completely homogeneous and therefore piece-wise constant. It is very close to the true data, except for some single pixels which do not have the correct intensity. OSC-GATV is the method which can best preserve small-scaled features and features of small intensity, compared to the other methods, OSC-ATV, OSC-ATV+TV^2. All these findings concerning the image quality of the methods hold true for different noise levels and the other phantoms in figures 6.2, 6.4 and 6.6 as well.

Relative Root Mean Squared Error Measurements

Figures 6.10, 6.11 and 6.12 display the mean RRMSE of the results for the different methods and the Forbild, engine and the lung data respectively. Let us first analyze the RRMSE which relate to the noisy measurements. For many projection view and SNR combinations, it can be seen that the methods improve successively. This means that the RRMSE for each method is smaller than the RRMSE of the preceding method: RRMSE(OSC-TV) > RRMSE(OSC-ATV) > RRMSE(OSC-ATV+TV^2) > RRMSE (OSC-GATV). This is the case for the following projection view and SNR combinations (marked as a $\times$):

RRMSE of the Forbild phantom reconstructions in figure 6.10

Noise levels \ projection views	200	100	80	60	40	30	20	10
2236						$\times$		
1000				$\times$				
707		$\times$	$\times$	$\times$				
316		$\times$	$\times$	$\times$	$\times$			
223	$\times$	$\times$	$\times$	$\times$	$\times$			
158					$\times$			
100					$\times$			

Noise level and projection view combinations for the Forbild phantom in figure 6.10 where the following condition for the RRMSE holds true: RRMSE(OSC-TV) > RRMSE(OSC-ATV) > RRMSE(OSC-ATV+TV^2) > RRMSE (OSC-GATV), marked as a cross.

RRMSE of the engine phantom reconstructions in figure 6.11

Noise levels \ projection views	200	100	80	60	40	30	20	10
2236								
1000		$\times$	$\times$					
707	$\times$	$\times$	$\times$	$\times$				
316	$\times$	$\times$						
223	$\times$	$\times$	$\times$	$\times$	$\times$			
158	$\times$	$\times$	$\times$	$\times$	$\times$			
100								

Noise level and projection view combinations for the engine phantom in figure 6.11 where the following condition for the RRMSE holds true: RRMSE(OSC-TV) > RRMSE(OSC-ATV) > RRMSE(OSC-ATV+TV^2) > RRMSE (OSC-GATV), marked as a cross.

RRMSE of the lung phantom reconstructions in figure 6.12

Noise levels \ projection views	200	100	80	60	40	30	20	10
2236								
1000								
707	×							
316	×							
223	×	×		×				
158	×	×		×				
100								

Noise level and projection view combinations for the lung phantom in figure 6.12 where the following condition for the RRMSE holds true: RRMSE(OSC-TV) > RRMSE(OSC-ATV) > RRMSE(OSC-ATV+TV^2) > RRMSE (OSC-GATV), marked as a cross.

One can thus conclude that the biggest difference of all three methods is at a rather low noise level in the range of SNR = 100 to SNR = 158 and 40 to 200 projections. For all other combinations, where the number of projections is greater than 40, the RRMSE of OSC-ATV, OSC-ATV+TV^2 and OSC-GATV is in most of the cases smaller than the RRMSE of OSC-TV. Furthermore, in most of the cases, the RRMSE of OSC-ATV+TV^2 is either smaller than ATV or has at least a comparable value.
Let us express this in concrete numbers for the noisy case:

- The RRMSE of OSC-ATV is up to **18.75** times smaller than the RRMSE of OSC-TV, e.g. for the lung phantom in figure 6.12, a SNR of 2236 and 40 projections.
- The RRMSE of OSC-ATV+TV^2 is up to **18.99** times smaller than the RRMSE of OSC-TV, e.g. for the lung phantom in figure 6.12, a SNR of 2236 and 40 projections.
- The RRMSE of OSC-GATV is up to **35.71** times smaller than the RRMSE of OSC-TV, e.g. for the lung phantom in figure 6.12, a SNR of 2236 and 40 projections.
- The RRMSE of OSC-GATV is up to **6** times smaller than the RRMSE of OSC-ATV+TV^2, e.g. for the Forbild phantom in figure 6.10, a SNR of 1000 and 40 projections.
- The RRMSE of OSC-ATV+TV^2 is up to **2.45** times smaller than the RRMSE of OSC-ATV, e.g. for the Forbild phantom in figure 6.10, a SNR of 1000 and 80 projections.

Let us now provide concrete numbers for the noise-free case:

- The RRMSE of OSC-ATV is up to **32** times smaller than the RRMSE of OSC-TV e.g. for 40 projections of the lung reconstructions in figure 6.12.
- The RRMSE of OSC-ATV+TV^2 is up to **68** times smaller than the RRMSE of OSC-TV e.g. for 30 projections of the lung reconstructions in figure 6.12.
- The RRMSE of OSC-GATV is up to **1770** times smaller than the RRMSE of OSC-TV e.g. for 40 projections of the Forbild reconstructions in figure 6.10.

Dose reduction factor

Recall, the dose-reduction factor is obtained by a multiplication of the maximum reduction value of the tube current with the under-sampling rate compared to the settings of a reference reconstruction. Based on the RRMSE measurements, let us now compute the highest possible dose reduction factor for the proposed methods. For that purpose, we take the measurement with the highest dose as a basis: a SNR of 2236 and 200 projection views. At this point, the result of OSC-TV has a RRMSE of 0.0027, see figure 6.12. Compared to this measurement point:

- the RRMSE of OSC-ATV is still **10.93**% lower at the point where the projections are 40 and the SNR is 707, see figure 6.12.
- the RRMSE of OSC-ATV+TV^2 is still **19.65**% lower at the point where the projections are 40 and the SNR is 707, see figure 6.12.
- the RRMSE of OSC-GATV is still **33.19**% lower at the point where the projections are 40 and the SNR is 707, see figure 6.11.

One can thus conclude that an extreme dose reduction factor of approximately **15.81** is achievable for all of the three methods OSC-ATV, OSC-ATV+TV^2 and OSC-GATV, compared to OSC-TV, since the projections can be reduced from 200 to 40 (factor of 5) and the SNR can be lowered from 2236 to 707 (factor of 3.16). Furthermore, at this point, all methods successively improve the RRMSE of OSC-TV by further lowering it by approximately 11% for OSC-ATV, 20% for OSC-ATV+TV^2 and 33% for OSC-GATV.

CNR

We computed the mean CNR of 10 different measurements, where the noise random variable was varied for each measurement in selected regions within the noise-free Forbild reconstructions. The results for different numbers of projections are displayed in figures 6.13 (10 projections), 6.14 (20 projections), 6.15 (30 projections), 6.16 (40 projections), 6.17 (60 projections), 6.18 (80 projections), 6.19 (100 projections) and 6.20 (200 projections).
For example in case of noise-free projections, OSC-GATV produces results with the highest CNR compared to the other methods OSC-TV, OSC-ATV and OSC-ATV+TV^2. In case of 20 projections and region 6 of the Forbild phantom in figure 6.14, the CNR of OSC-GATV is **86.36** times higher than the CNR of OSC-TV, **44.19** times higher than the CNR of OSC-ATV and **250** times higher than the CNR of OSC-ATV+TV^2.
For the noisy case, the tendency is the following: CNR(OSC-ATV+TV^2) $\gg$ CNR(OSC-ATV) $>$ CNR(OSC-GATV) $>$ CNR(OSC-TV):

- The CNR of OSC-ATV+TV^2 is up to **29.38** times smaller than the CNR of OSC-TV e.g. for region 1 in figure 6.19, where 100 projections and a SNR of 223 were selected for the reconstructions of the Forbild phantom.
- The CNR of OSC-ATV is up to **4.8** times higher than the CNR of OSC-TV e.g. for region 1 in figure 6.20, where 200 projections and a SNR of 316 were selected for the reconstructions of the Forbild phantom.
- The CNR of OSC-GATV is up to **3.42** times higher than the CNR of OSC-TV e.g. for region 1 in figure 6.16, where 40 projections and a SNR of 707 were selected for the reconstructions of the Forbild phantom.

Homogeneity

In figures 6.21, 6.22 and 6.23 we compute the mean homogeneity of the results presented in figures 6.2 (Forbild phantom), 6.4 (engine phantom) and 6.6 (lung phantom). For many projection view and SNR combinations, it can be seen that the homogeneity of the methods successively improves. This means that the homogeneity, H, for each method is bigger than the homogeneity of the preceding method: H(OSC-TV) $<$ H(OSC-ATV) $<$ H(OSC-ATV+TV^2) $<$ H(OSC-GATV). This is the case for the following projection views/SNR combinations, marked as a cross:

Homogeneity of the Forbild phantom reconstructions in figure 6.21

Noise levels \ projection views	200	100	80	60	40	30	20	10
2236							×	
1000							×	
707							×	
316			×		×	×		
223	×	×	×		×			
158	×	×			×			
100				×				

Noise level and projection view combinations for the homogeneity values of the Forbild phantom in figure 6.21 where the following condition for the Homogeneity holds true: H(OSC-TV) $<$ H(OSC-ATV) $<$ H(OSC-ATV+TV^2) $<$ H (OSC-GATV), marked as a cross.

Homogeneity of the engine phantom reconstructions in figure 6.22

Noise levels \ projection views	200	100	80	60	40	30	20	10
2236								
1000								
707								
316						×		×
223		×	×	×	×	×	×	×
158	×	×	×	×				
100		×	×	×	×			

Noise level and projection view combinations for the engine phantom in figure 6.22 where the following condition for the Homogeneity holds true: H(OSC-TV) $<$ H(OSC-ATV) $<$ H(OSC-ATV+TV^2) $<$ H (OSC-GATV), marked as a cross.

Homogeneity of the lung phantom reconstructions in figure 6.23

Noise levels \ projection views	200	100	80	60	40	30	20	10
2236								×
1000		×						
707		×	×		×			×
316	×							×
223					×		×	×
158			×					
100						×		

Noise level and projection view combinations for the lung phantom in figure 6.23 where the following condition for the Homogeneity holds true: H(OSC-TV) $<$ H(OSC-ATV) $<$ H(OSC-ATV+TV^2) $<$ H (OSC-GATV), marked as a cross.

One can thus conclude that the biggest difference of all three methods is at a rather low noise level in the range of SNR = 316 to SNR = 158 and 20 to 200 projections. Let us summarize these findings by concrete values by further analyzing a meaningful scenario, e.g. 200 projections and a SNR of 158 and the Forbild phantom in figure 6.21. The result of each method is more homogeneous than its preceding method:

- The homogeneity of OSC-ATV is **3.03**% higher than the homogeneity of OSC-TV.
- The homogeneity of OSC-ATV+TV^2 is **3.42**% higher than the homogeneity of OSC-TV.
- The homogeneity of OSC-GATV is **3.52**% higher than the homogeneity of OSC-TV.

Furthermore, the homogeneity of OSC-ATV+TV^2 is up to **3.33**% higher than the homogeneity of OSC-ATV and the homogeneity of OSC-GATV is up to **1.65**% higher than the homogeneity of OSC-ATV+TV^2, e.g. for the Forbild phantom in figure 6.21, a SNR of 158 and 100 projections. These values underline that all of the three methods successively improve the homogeneity of the results compared to TV. In case of noise-free projections and more than 40 views, all methods have almost the same level of homogeneity.

6.3.3 Reconstructed images and results of the quality metrics

In this chapter we have performed a large evaluation of 560 measurements. We examined the reconstruction results of the proposed regularization algorithms in a general framework so as to draw a meaningful conclusion of the overall performance of the methods in relation of each method to its succeeding method and in relation of each method versus the state of the art, TV. Next, we want to present the reconstructed images and the corresponding graphs and plots of this evaluation. The final discussion and conclusion of this evaluation is presented in chapter 7.

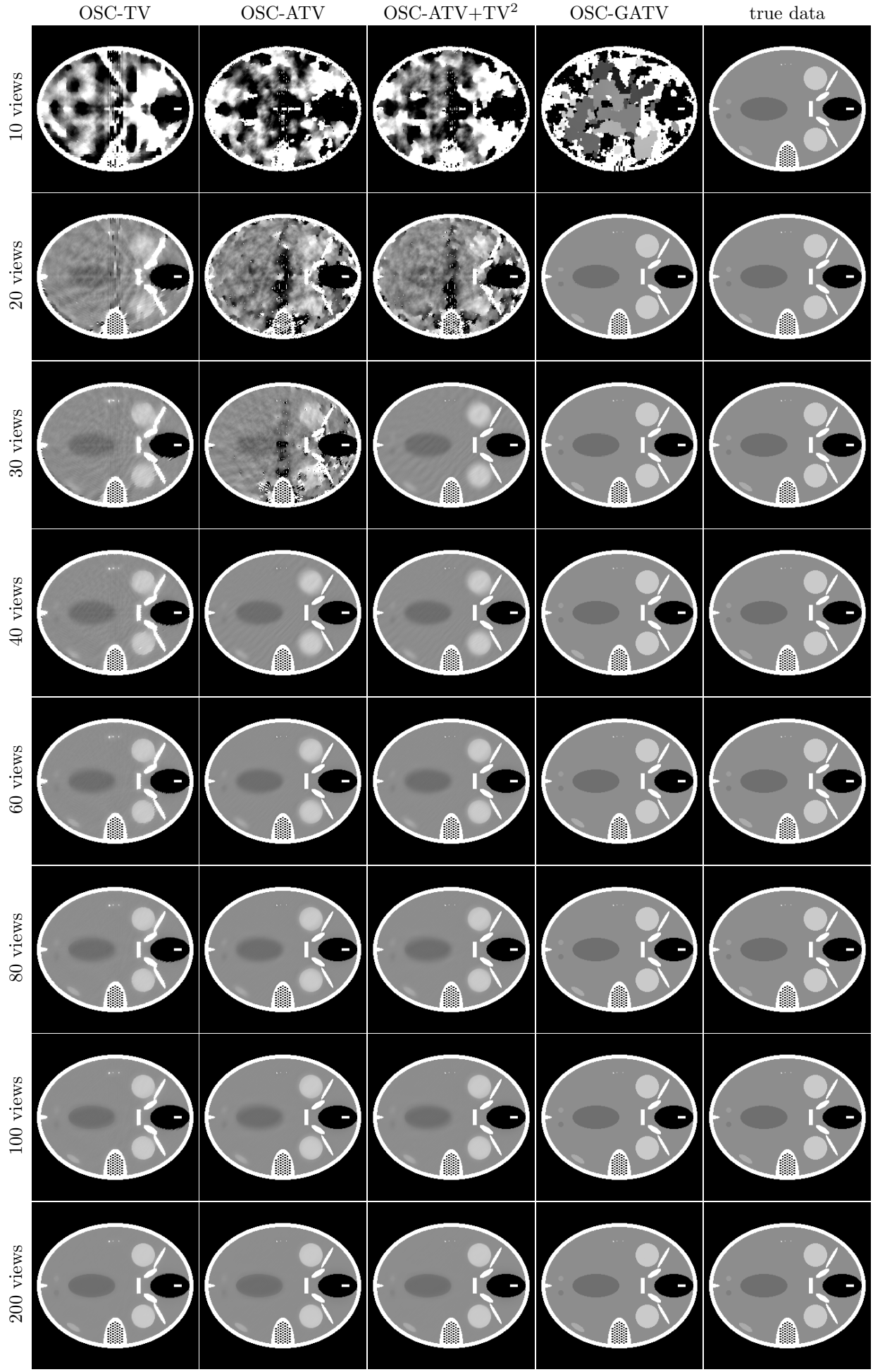

Figure 6.1: Reconstructions of the Forbild phantom from different numbers of noise-free projections, window-level: [0.0188,0.0196].

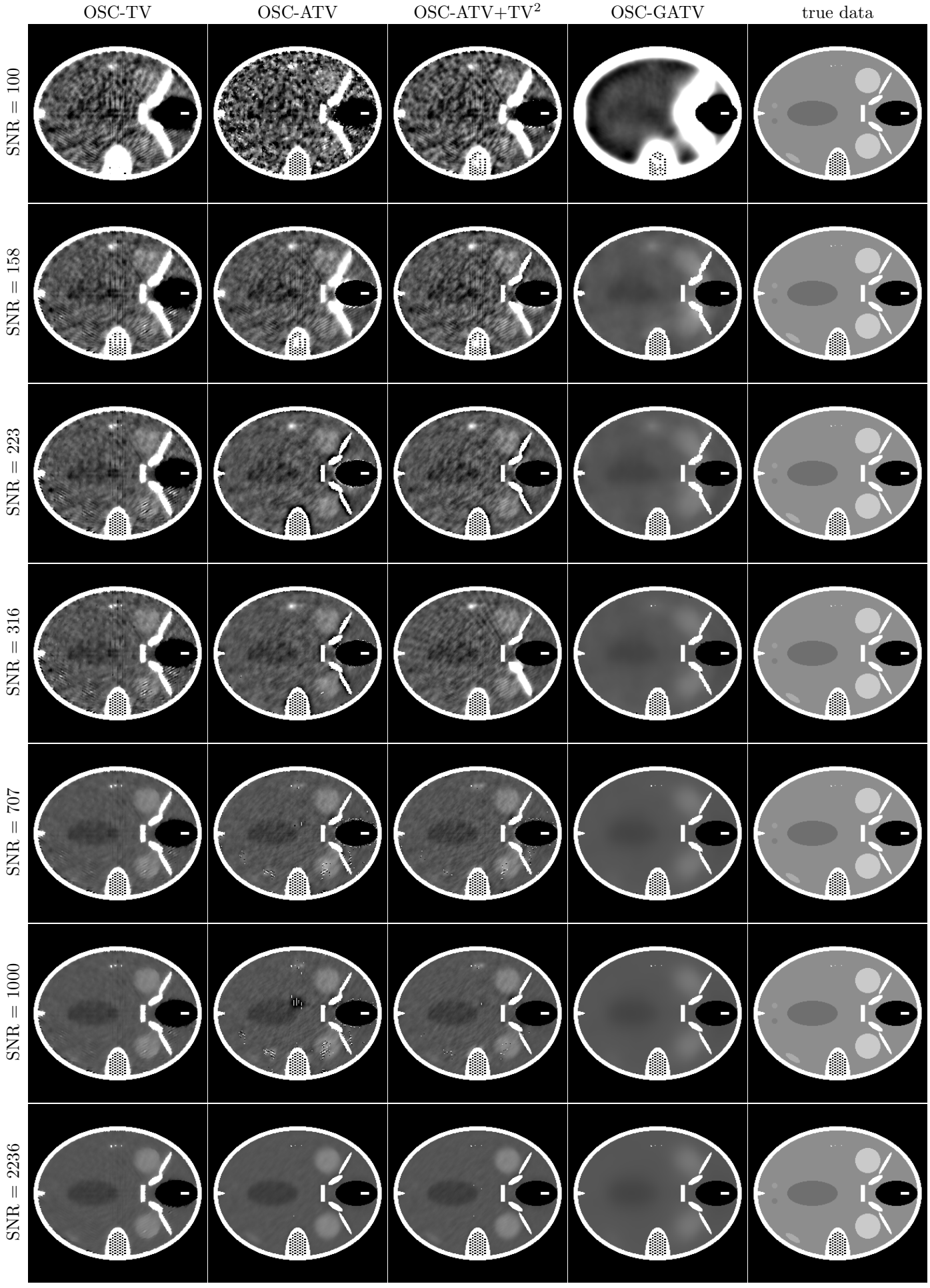

Figure 6.2: Reconstructions of the Forbild phantom from 40 projections, different noise levels and 10 different realizations of the random noise variable. The mean of the results is displayed, window-level: [0.0188,0.0196].

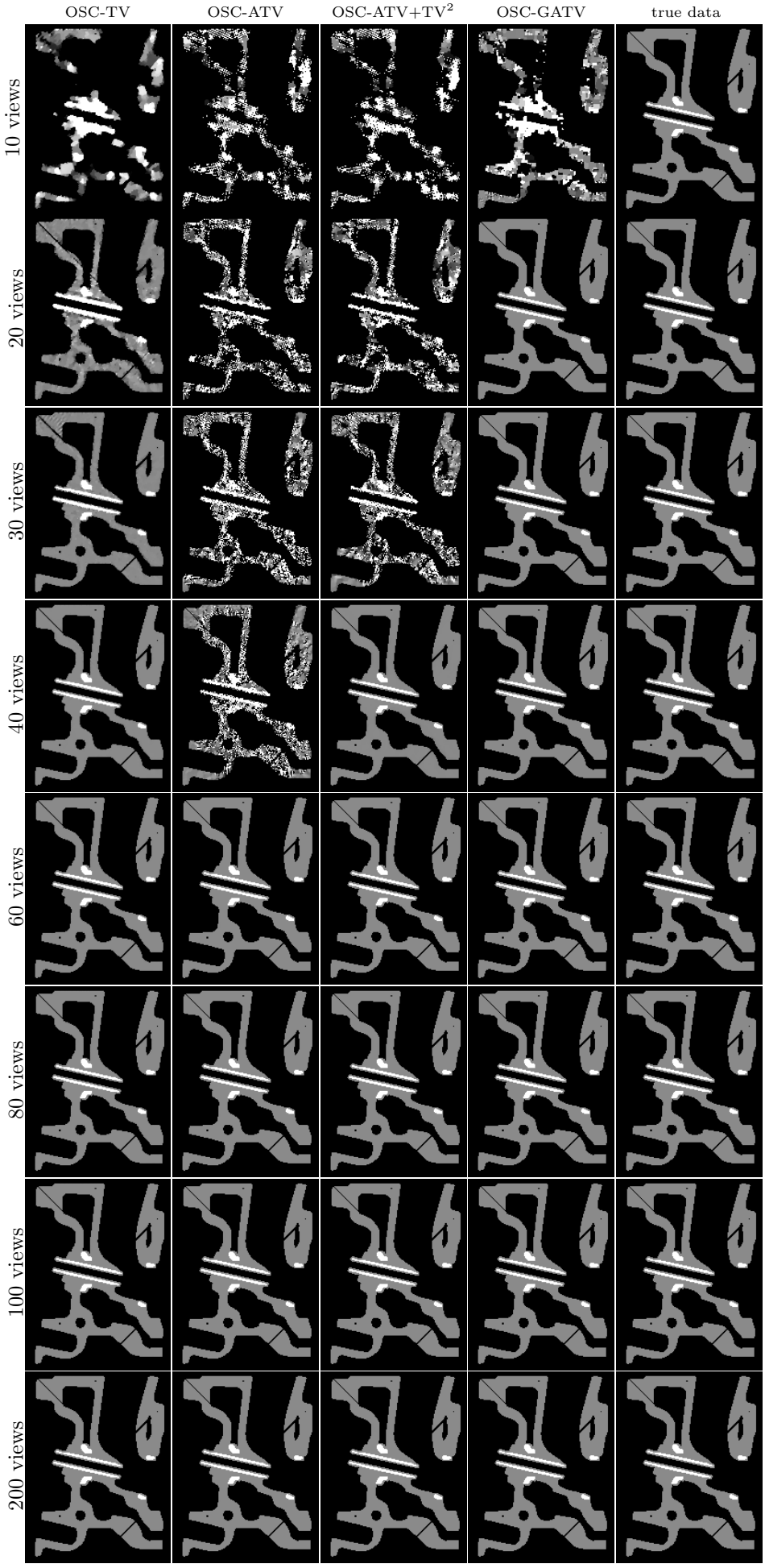

Figure 6.3: Reconstructions of the engine phantom from different numbers of noise-free projections, window-level: [0.0168,0.0205].

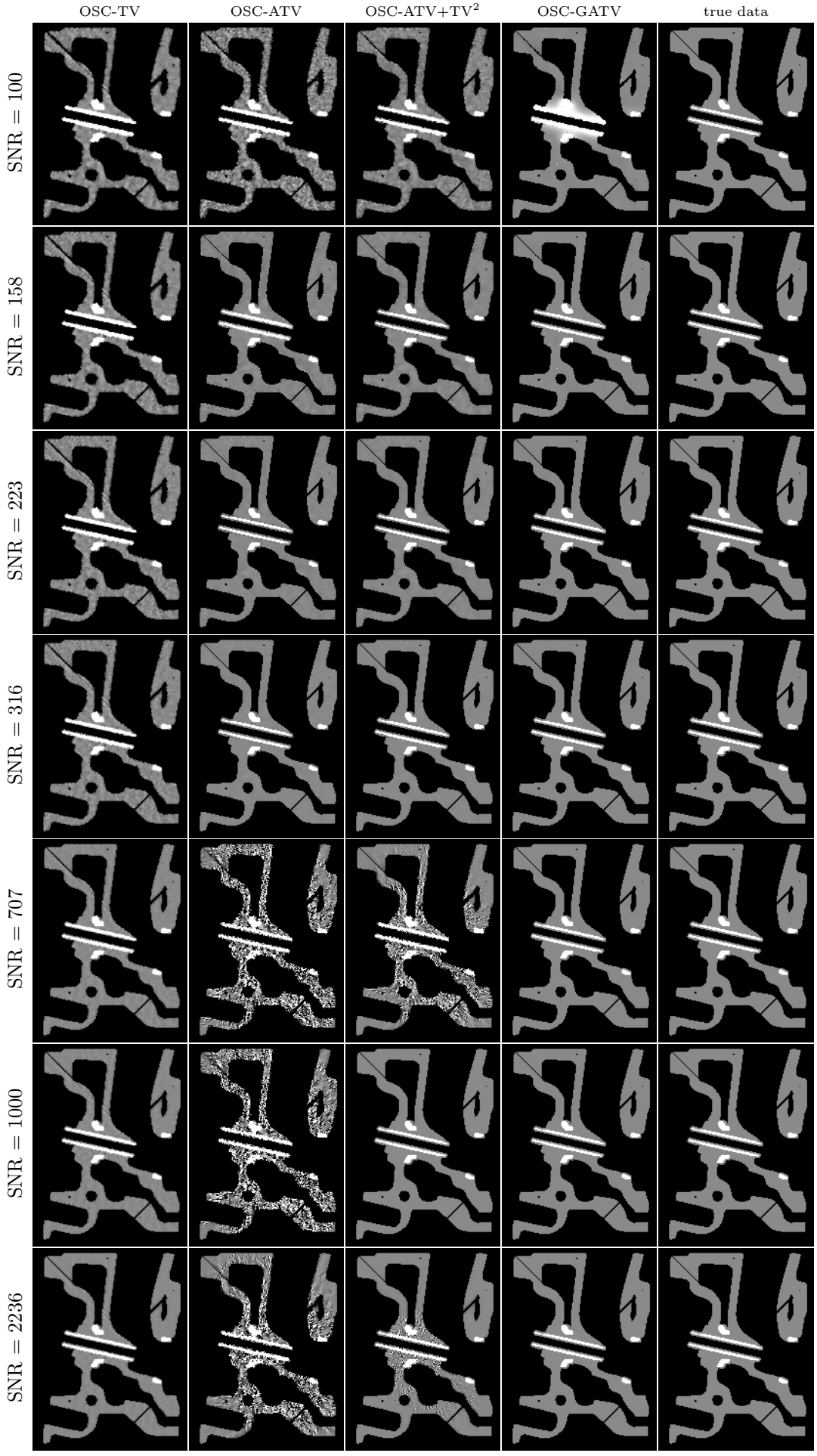

Figure 6.4: Reconstructions of the engine phantom from 40 projections, different noise levels and 10 different realizations of the random noise variable. The mean of the results is displayed, window-level: [0.0168,0.0205].

Figure 6.5: Reconstructions of the lung phantom from different numbers of noise-free projections, window-level: [0.0160,0.0178].

Figure 6.6: Reconstructions of the lung phantom from 40 projections, different noise levels and 10 different realizations of the random noise variable. The mean of the results is displayed, window-level: [0.0160,0.0178].

Forbild phantom

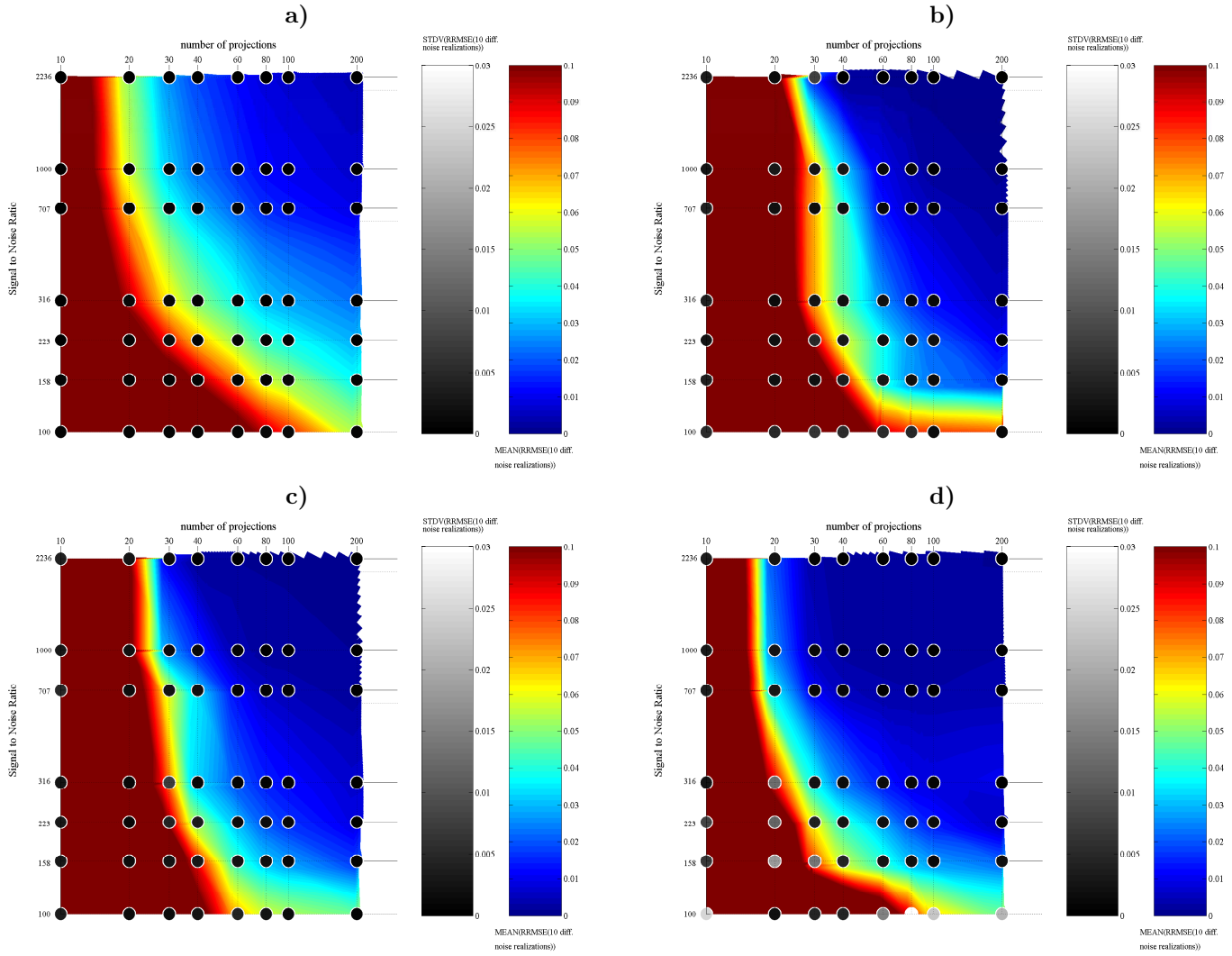

Figure 6.7: Result of the overall evaluation of the Forbild phantom. 10 realizations of the noise random variable and different combinations of noise-levels and projection views were evaluated, given the constants for the algorithms in table 6.1. Gray-valued colorbar: Standard deviation of the RRMSE of the measurements (points), rgb-valued colorbar: Mean value of the RRMSE of the measurements (contour plot). a) OSC-TV, b) OSC-ATV, c) OSC-ATV+TV^2, d) OSC-GATV.

Engine phantom

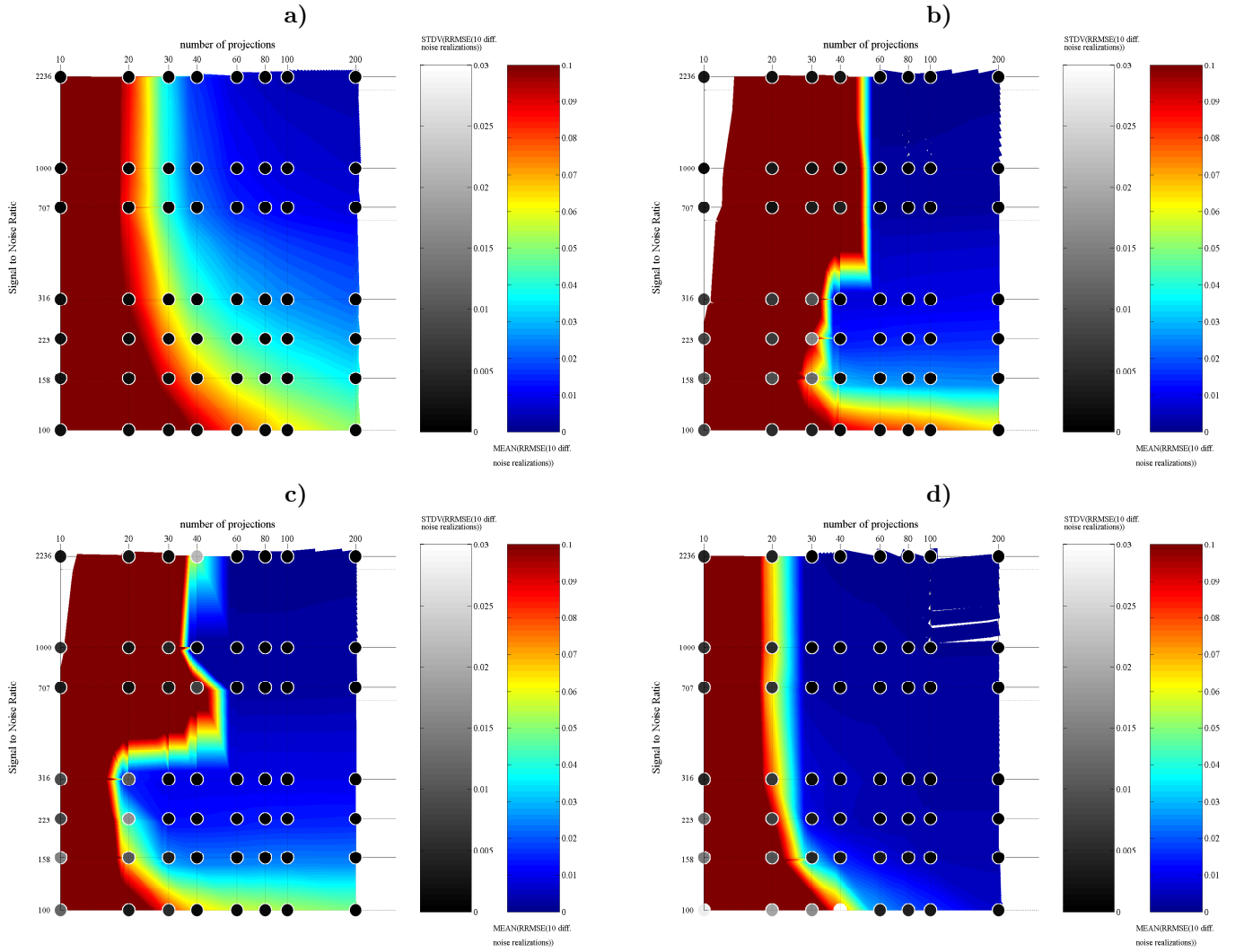

Figure 6.8: Result of the overall evaluation of the engine phantom. 10 realizations of the noise random variable and different combinations of noise-levels and projection views were evaluated, given the constants for the algorithms in table 6.1. Gray-valued colorbar: Standard deviation of the RRMSE of the measurements (points), rgb-valued colorbar: Mean value of the RRMSE of the measurements (contour plot). a) OSC-TV, b) OSC-ATV, c) OSC-ATV+TV^2, d) OSC-GATV. The white gaps in the plots of b), c) and d) are display errors and do not represent the actual RRMSE value.

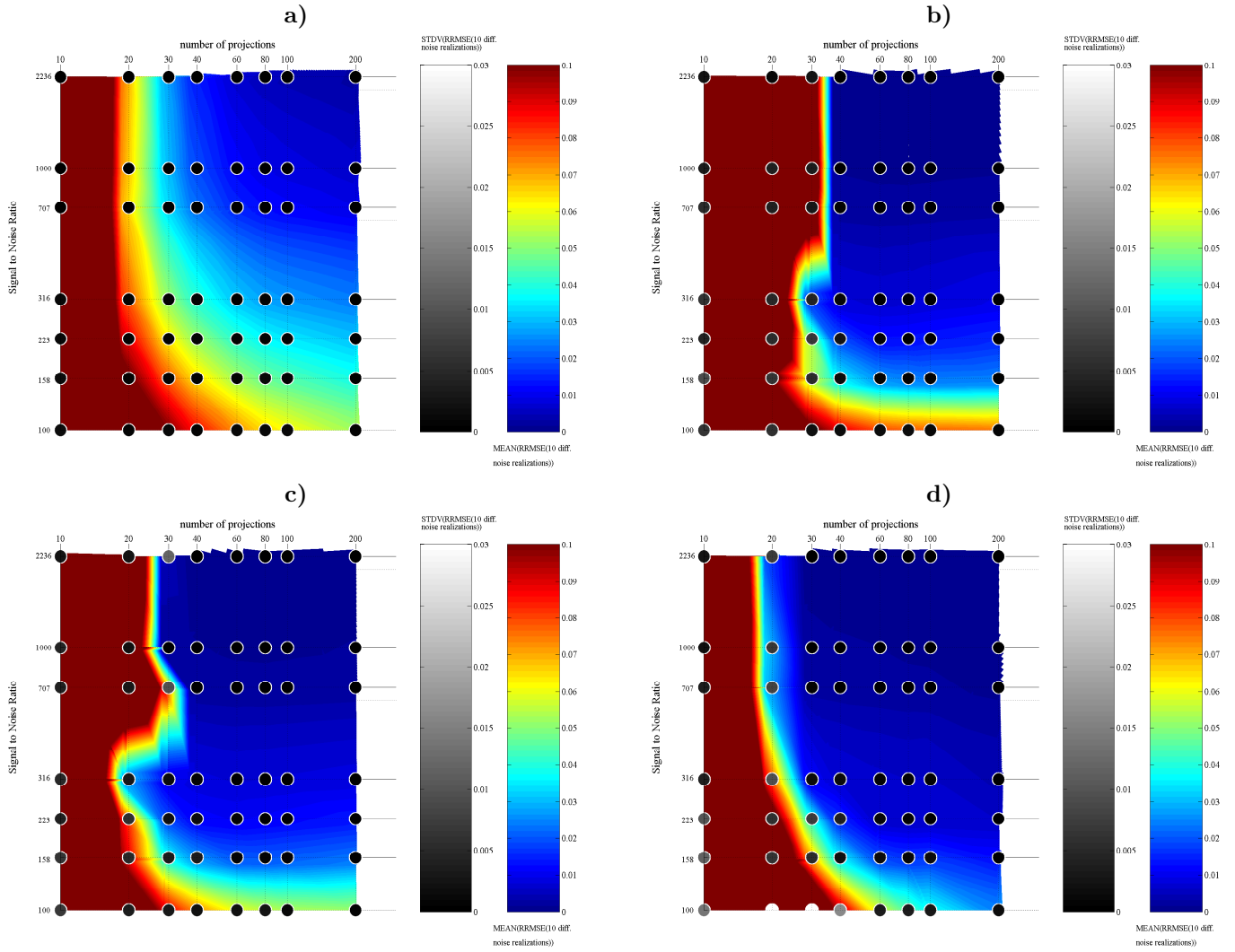

Figure 6.9: Result of the overall evaluation of the lung phantom. 10 realizations of the noise random variable and different combinations of noise-levels and projection views were evaluated, given the constants for the algorithms in table 6.1. Gray-valued colorbar: Standard deviation of the RRMSE of the measurements (points), rgb-valued colorbar: Mean value of the RRMSE of the measurements (contour plot). a) OSC-TV, b) OSC-ATV, c) OSC-ATV+TV^2, d) OSC-GATV.

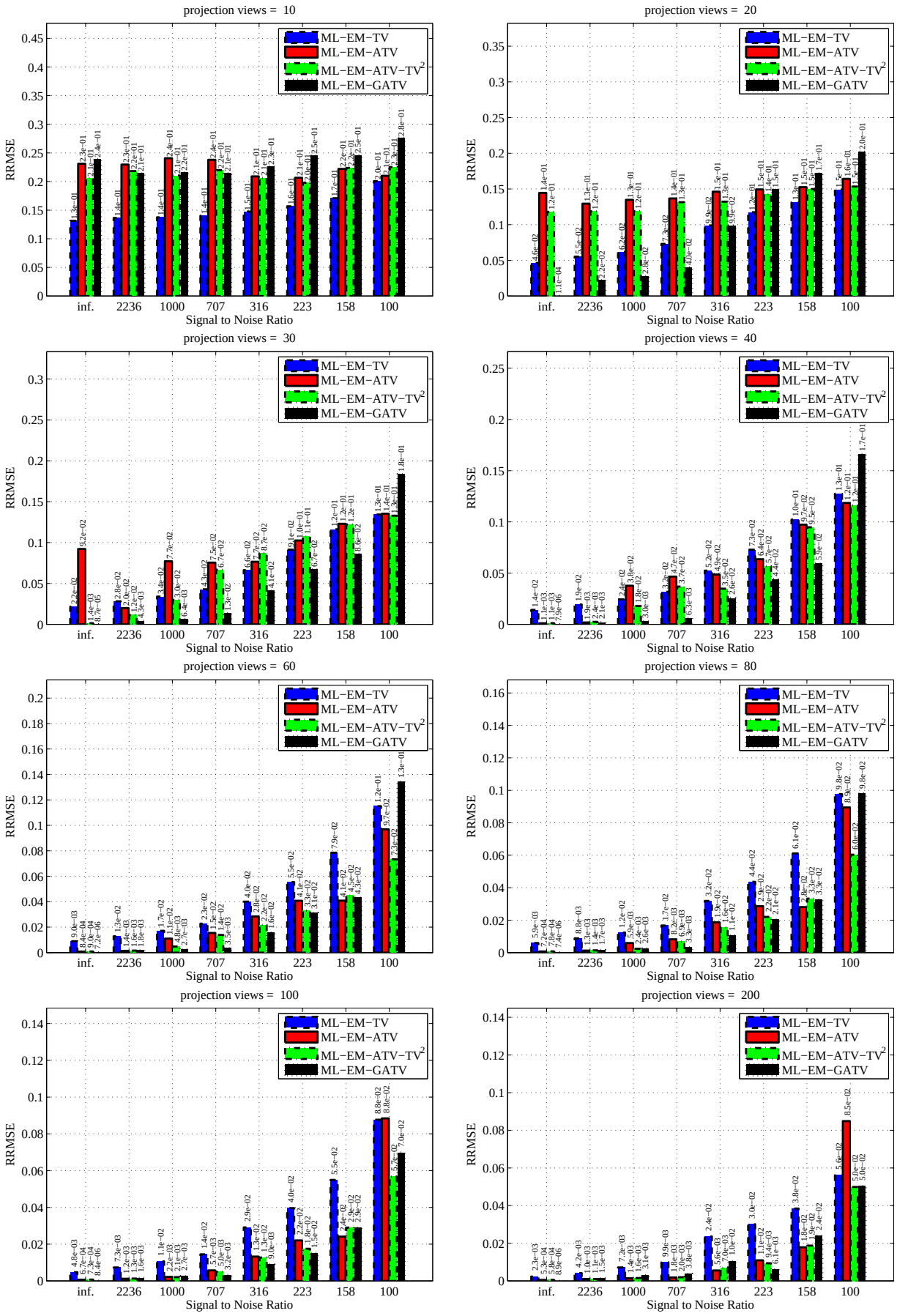

Figure 6.10: The RRMSE of the Forbild phantom reconstructions from different numbers of projection views and noise levels.

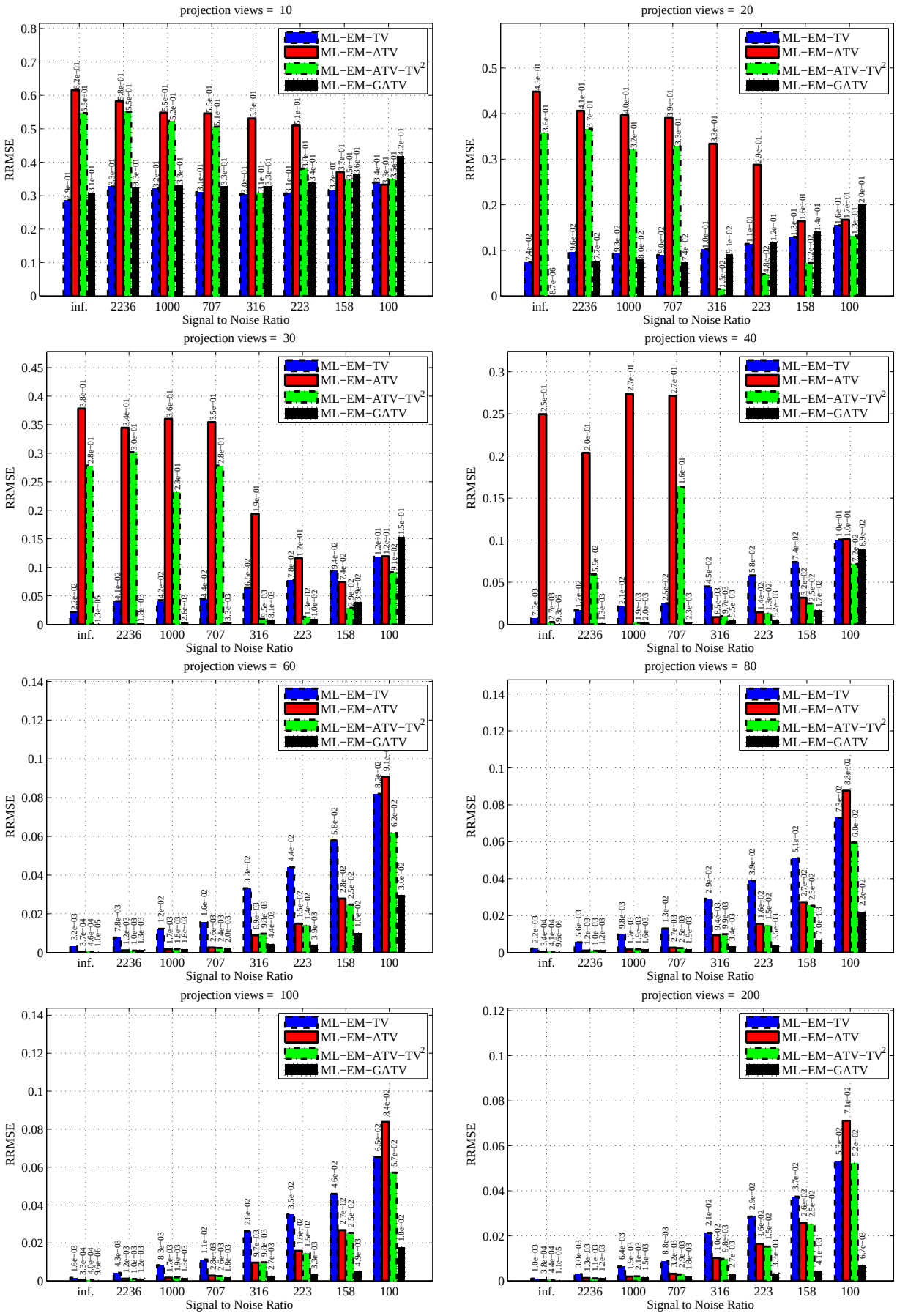

Figure 6.11: The RRMSE of the engine phantom reconstructions from different numbers of projection views and noise levels.

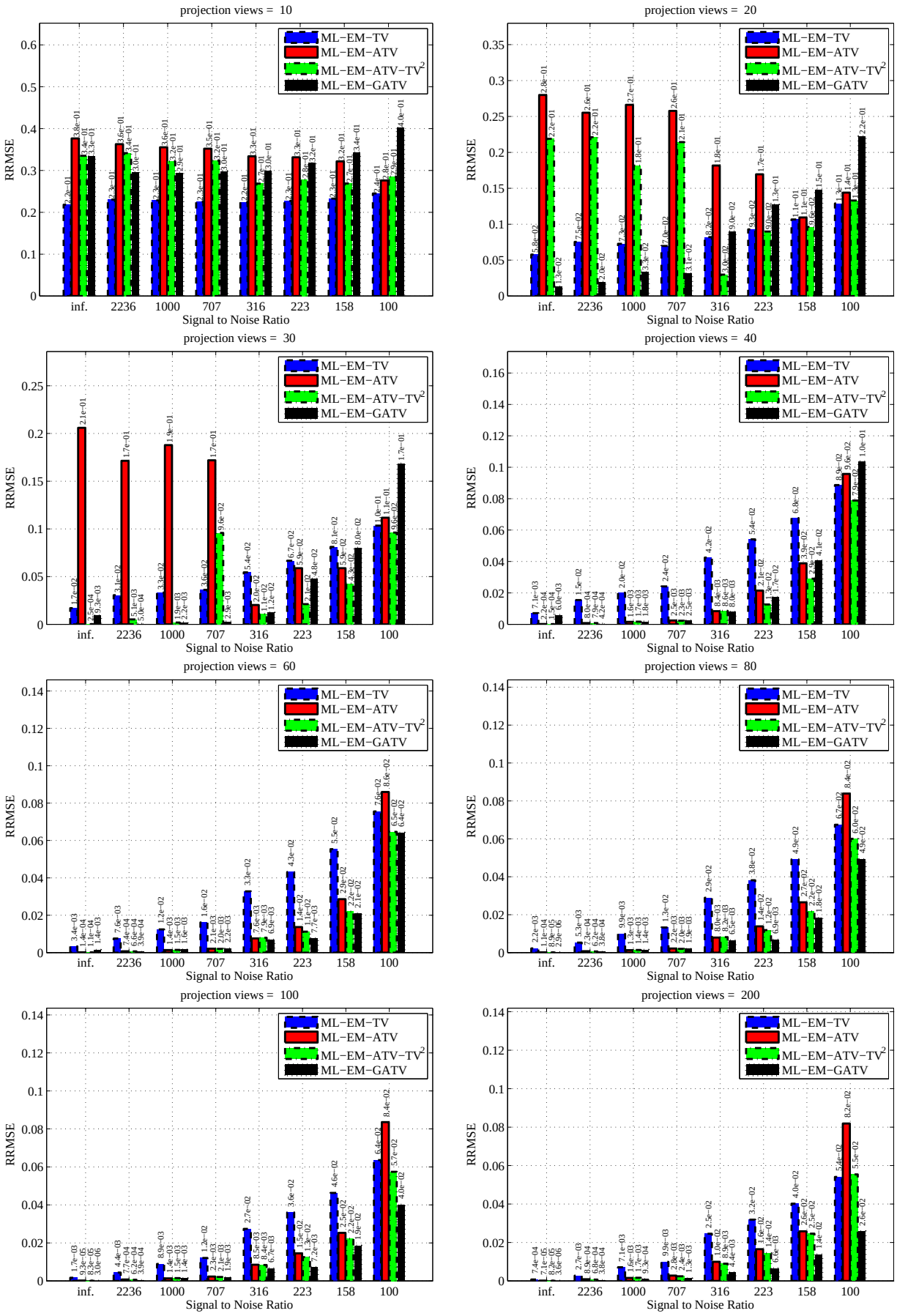

Figure 6.12: The RRMSE of the lung phantom reconstructions from different numbers of projection views and noise levels.

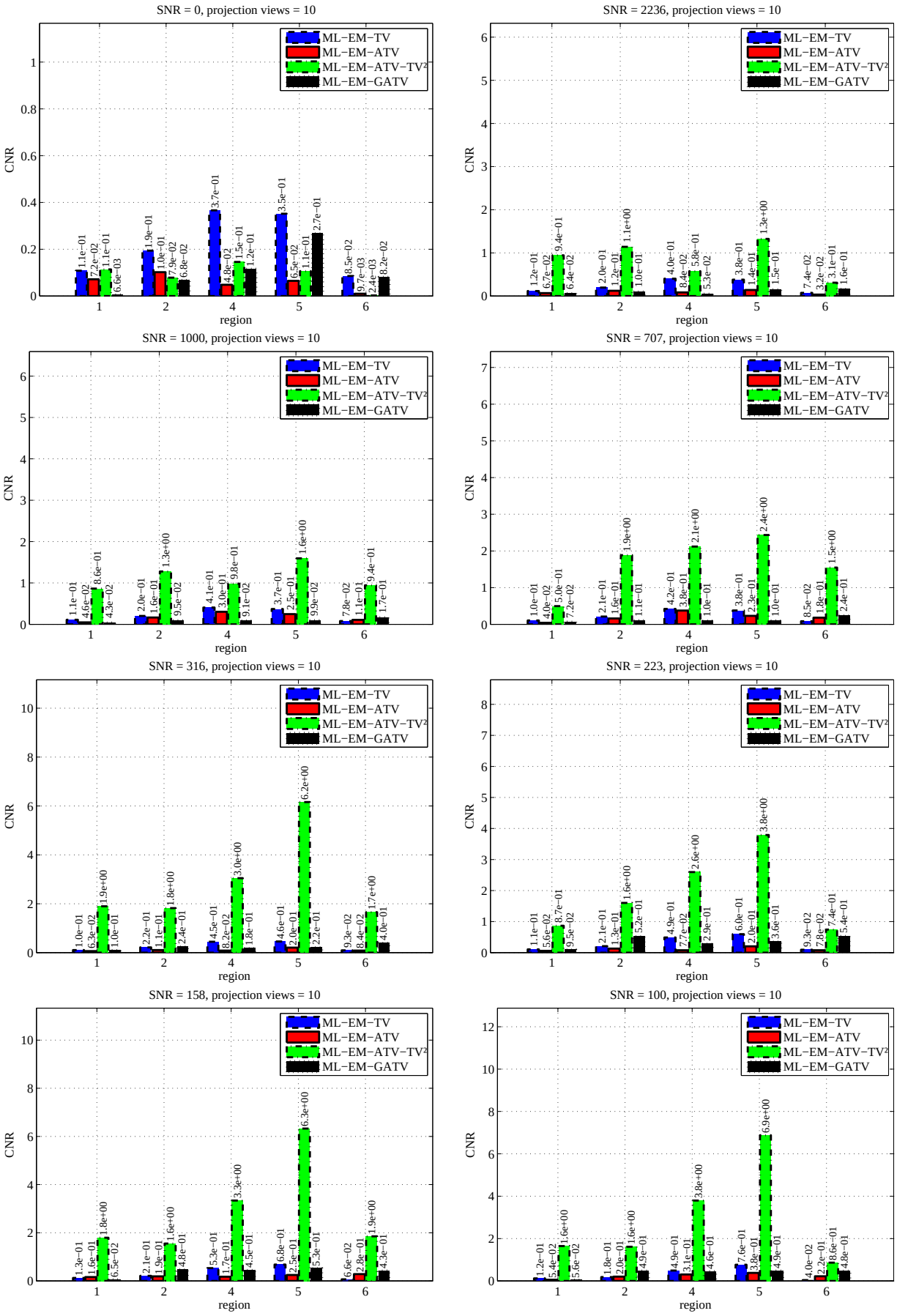

Figure 6.13: The CNR of the Forbild phantom reconstructions from 10 projection views and different noise levels.

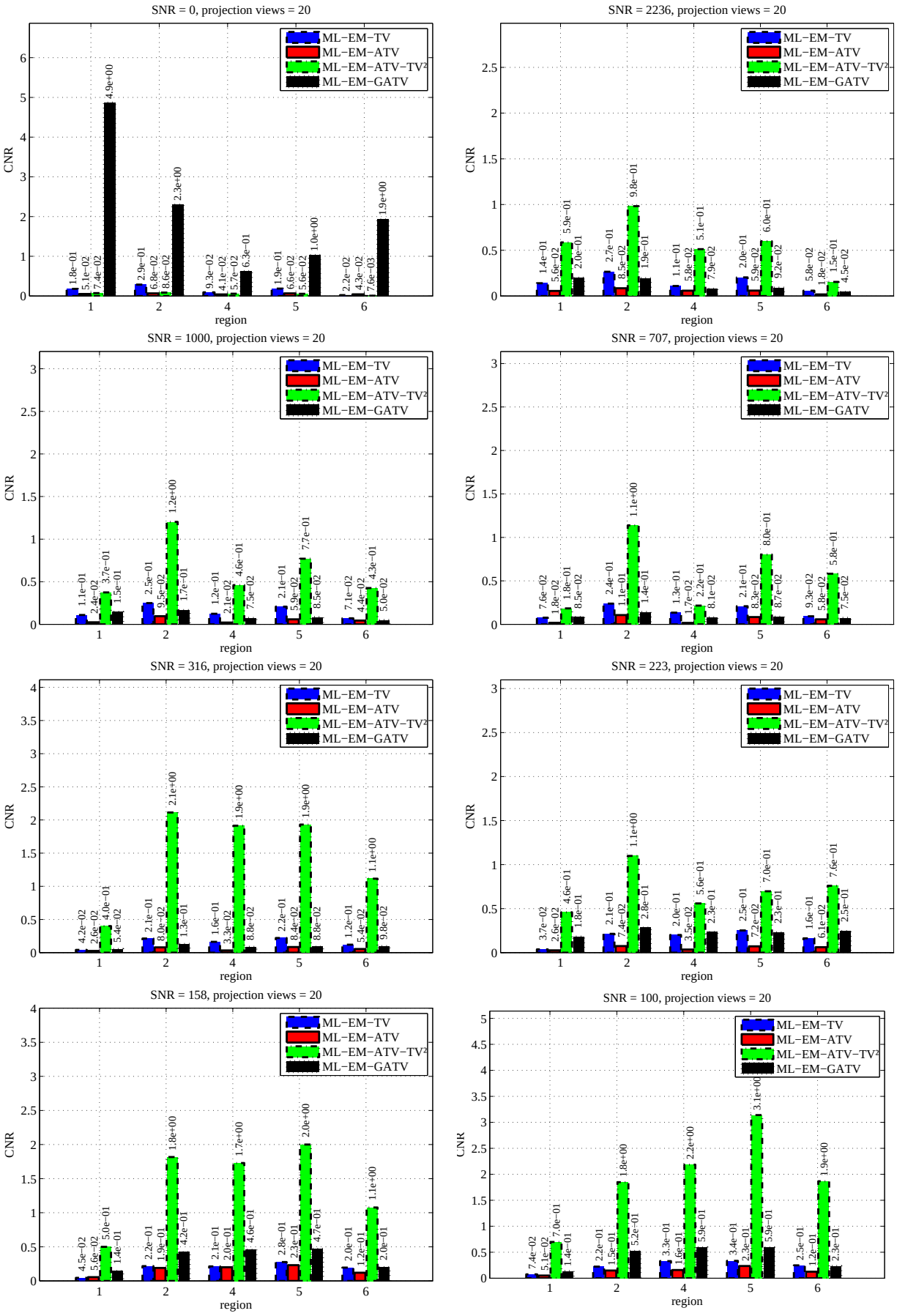

Figure 6.14: The CNR of the Forbild phantom reconstructions from 20 projection views and different noise levels.

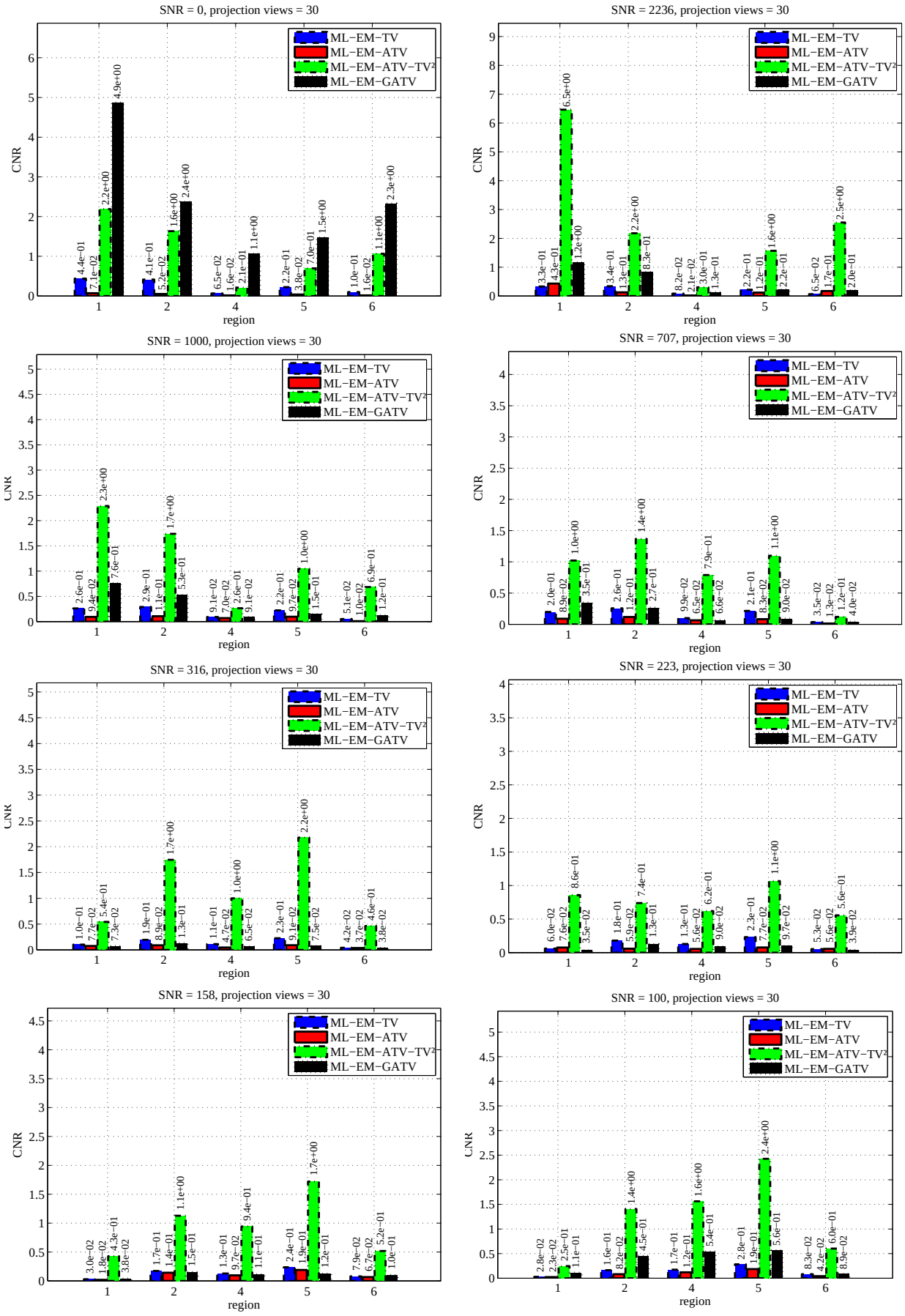

Figure 6.15: The CNR of the Forbild phantom reconstructions from 30 projection views and different noise levels.

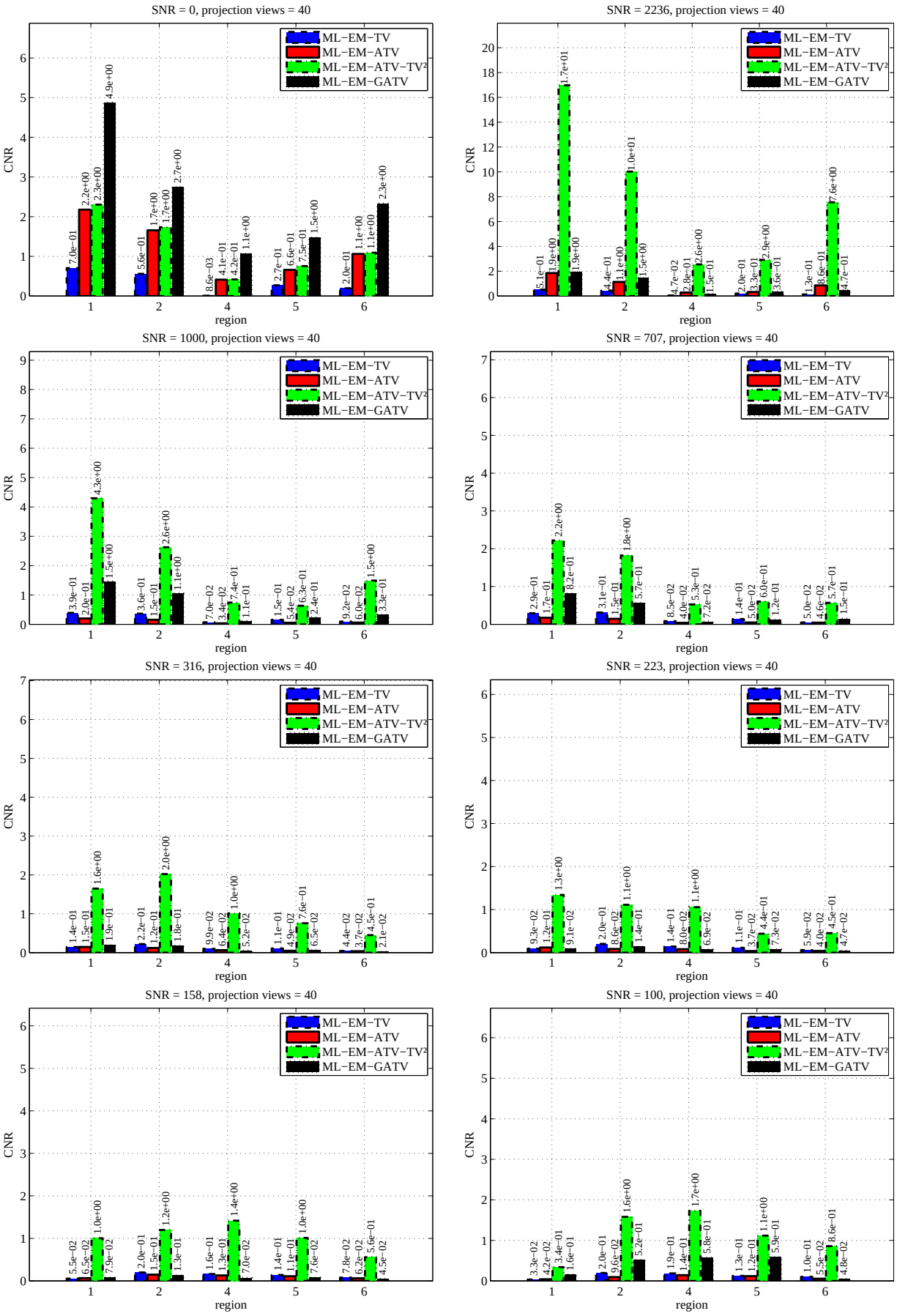

Figure 6.16: The CNR of the Forbild phantom reconstructions from 40 projection views and different noise levels.

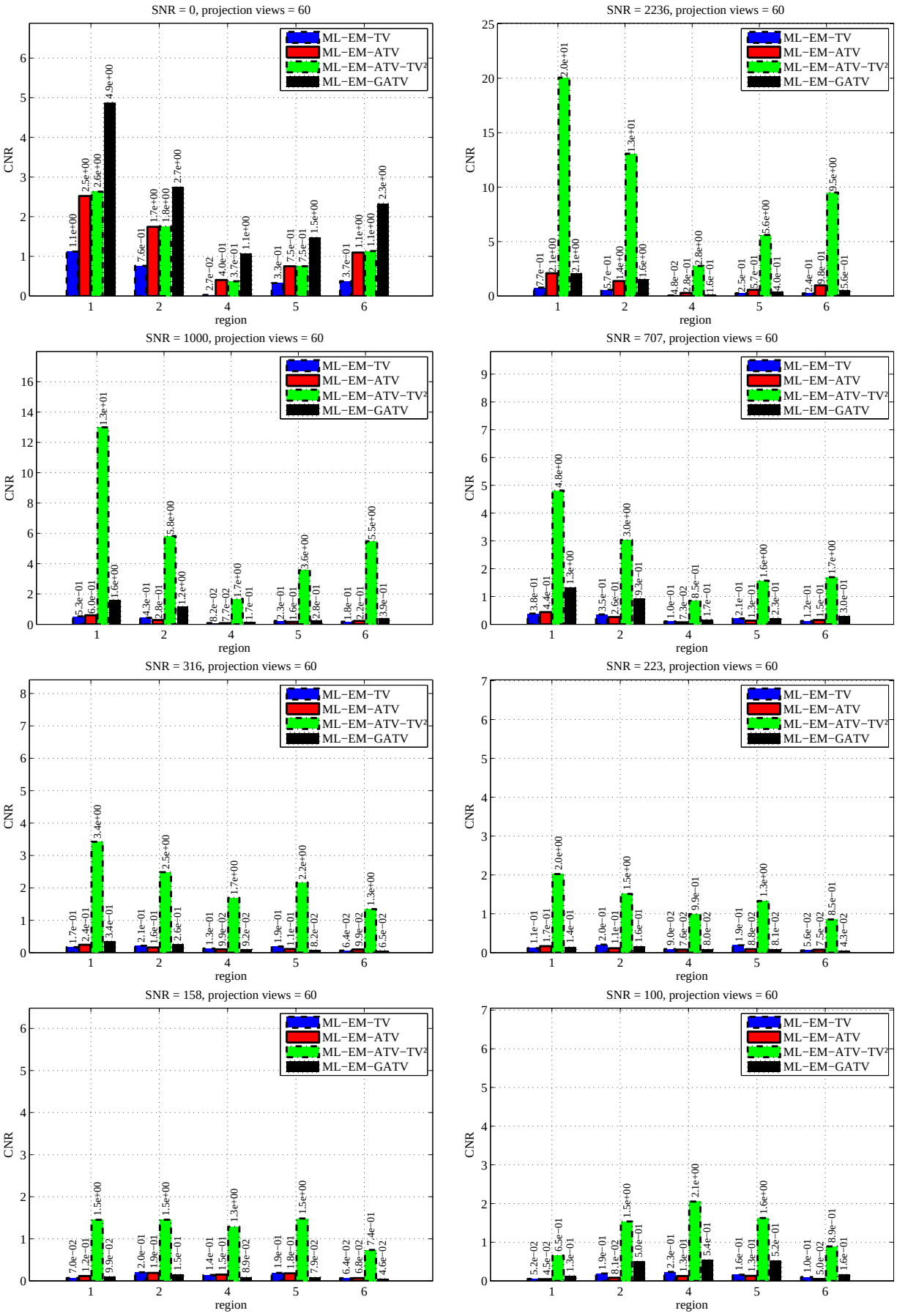

Figure 6.17: The CNR of the Forbild phantom reconstructions from 60 projection views and different noise levels.

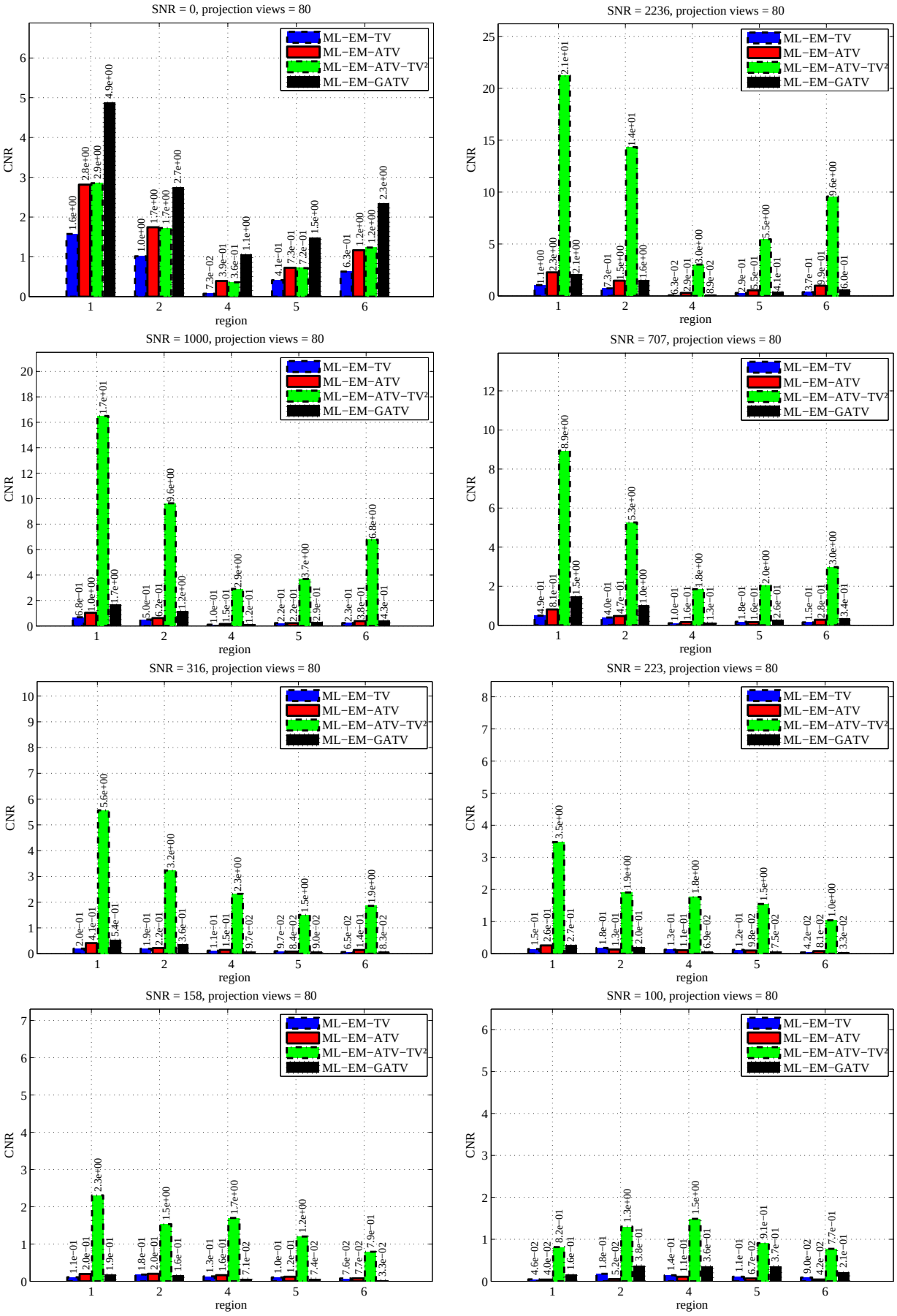

Figure 6.18: The CNR of the Forbild phantom reconstructions from 80 projection views and different noise levels.

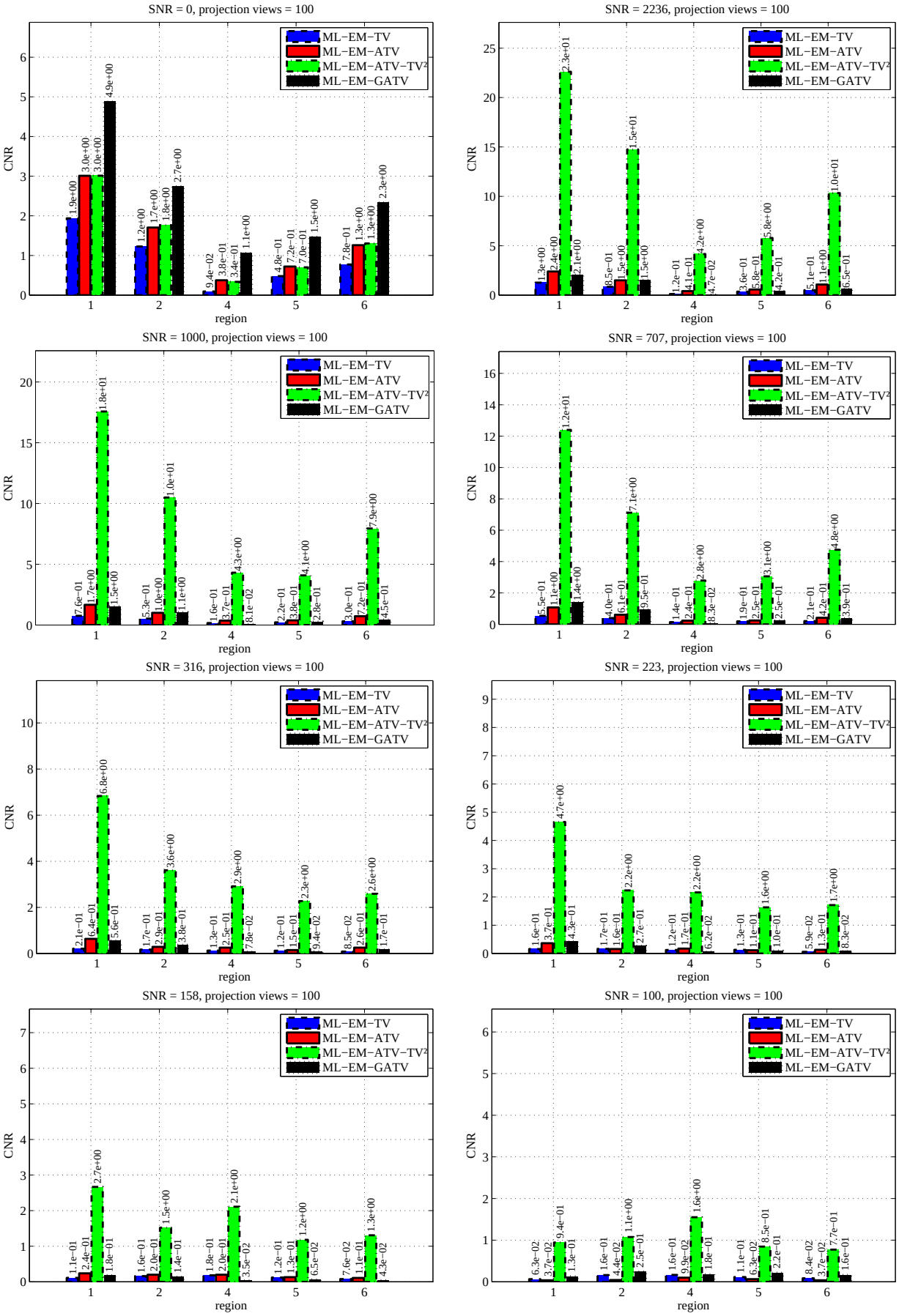

Figure 6.19: The CNR of the Forbild phantom reconstructions from 100 projection views and different noise levels.

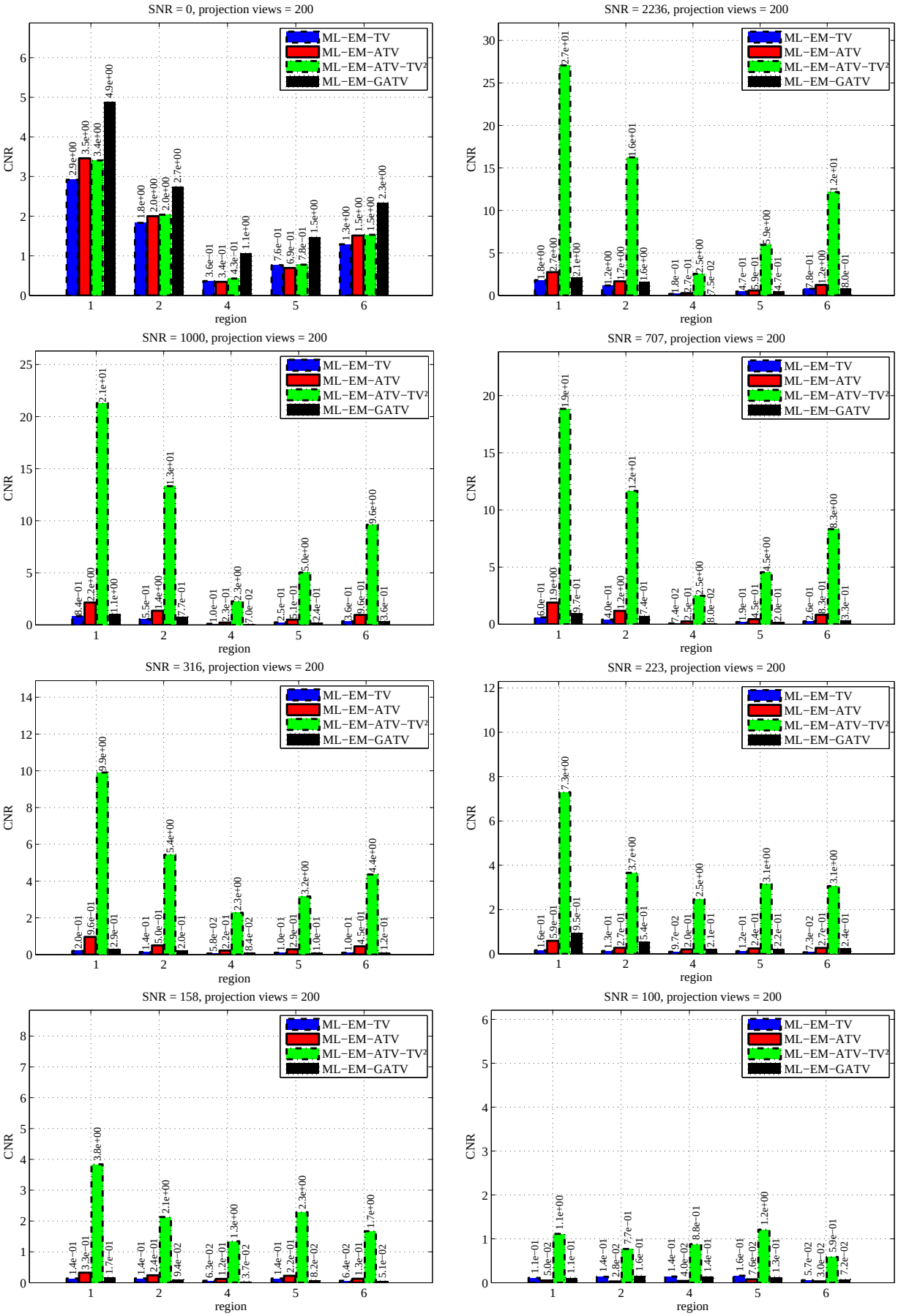

Figure 6.20: The CNR of the Forbild phantom reconstructions from 200 projection views and different noise levels.

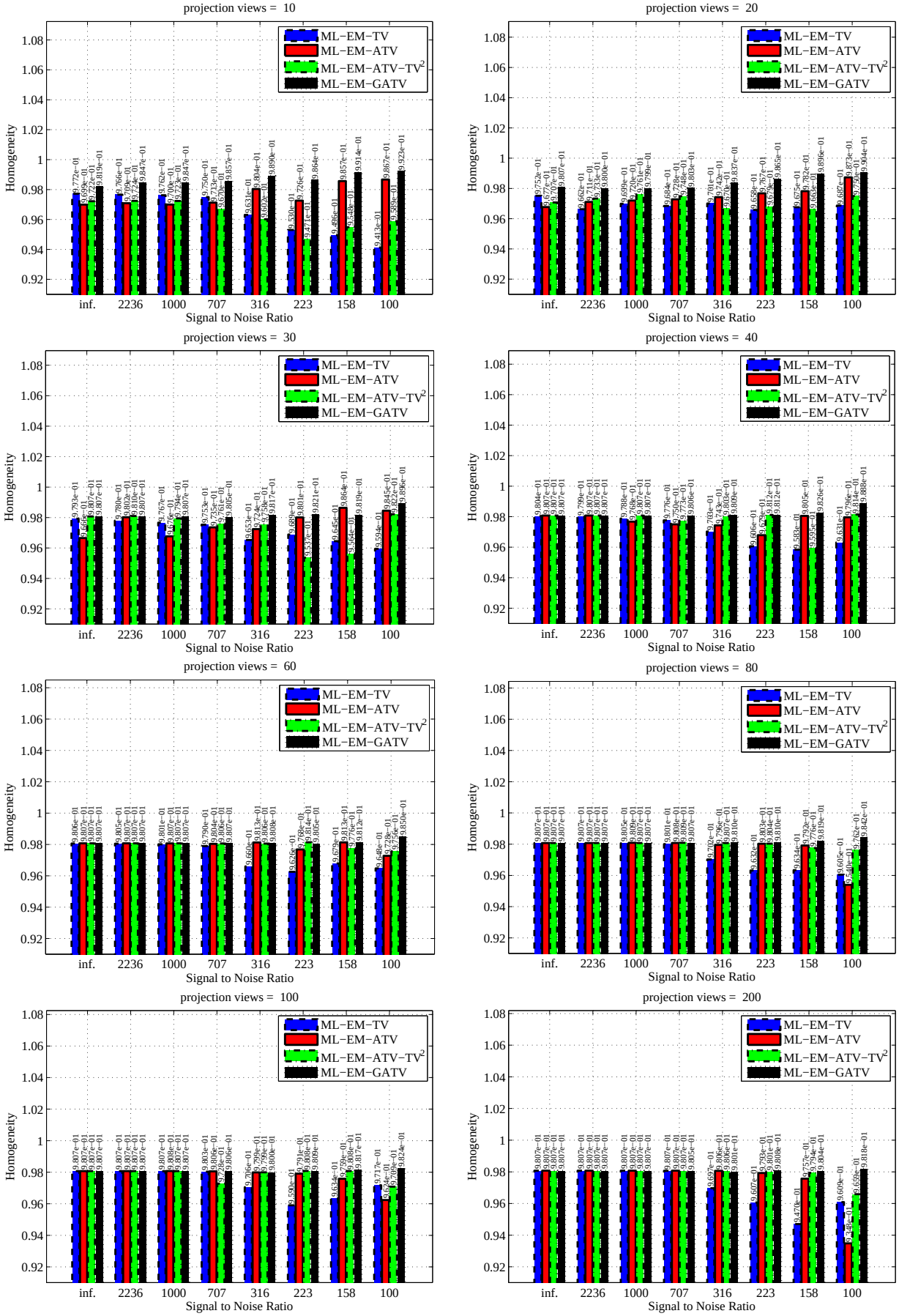

Figure 6.21: The homogeneity of the Forbild phantom reconstructions from different numbers of projection views and noise levels.

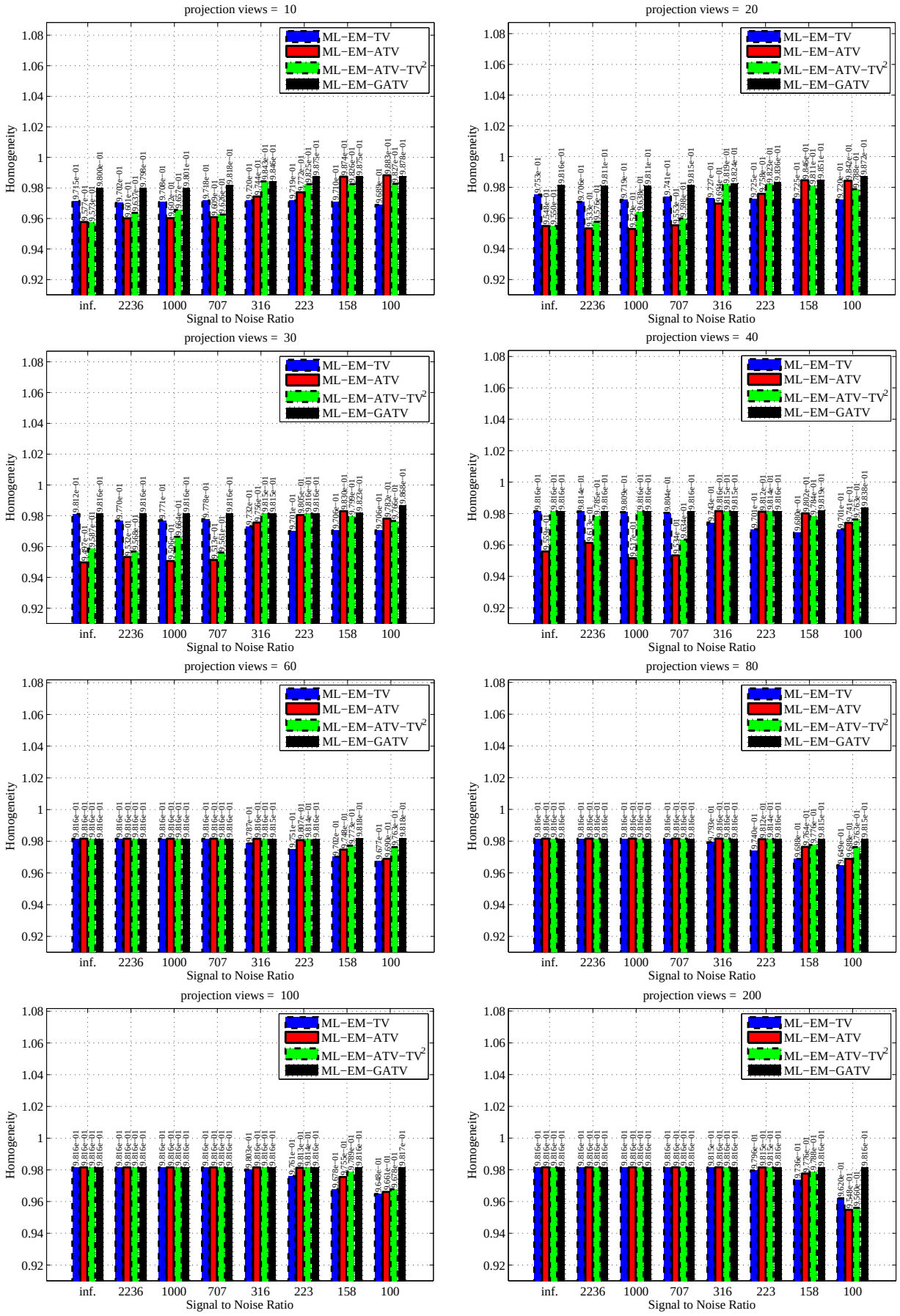

Figure 6.22: The homogeneity of the engine phantom reconstructions from different numbers of projection views and noise levels.

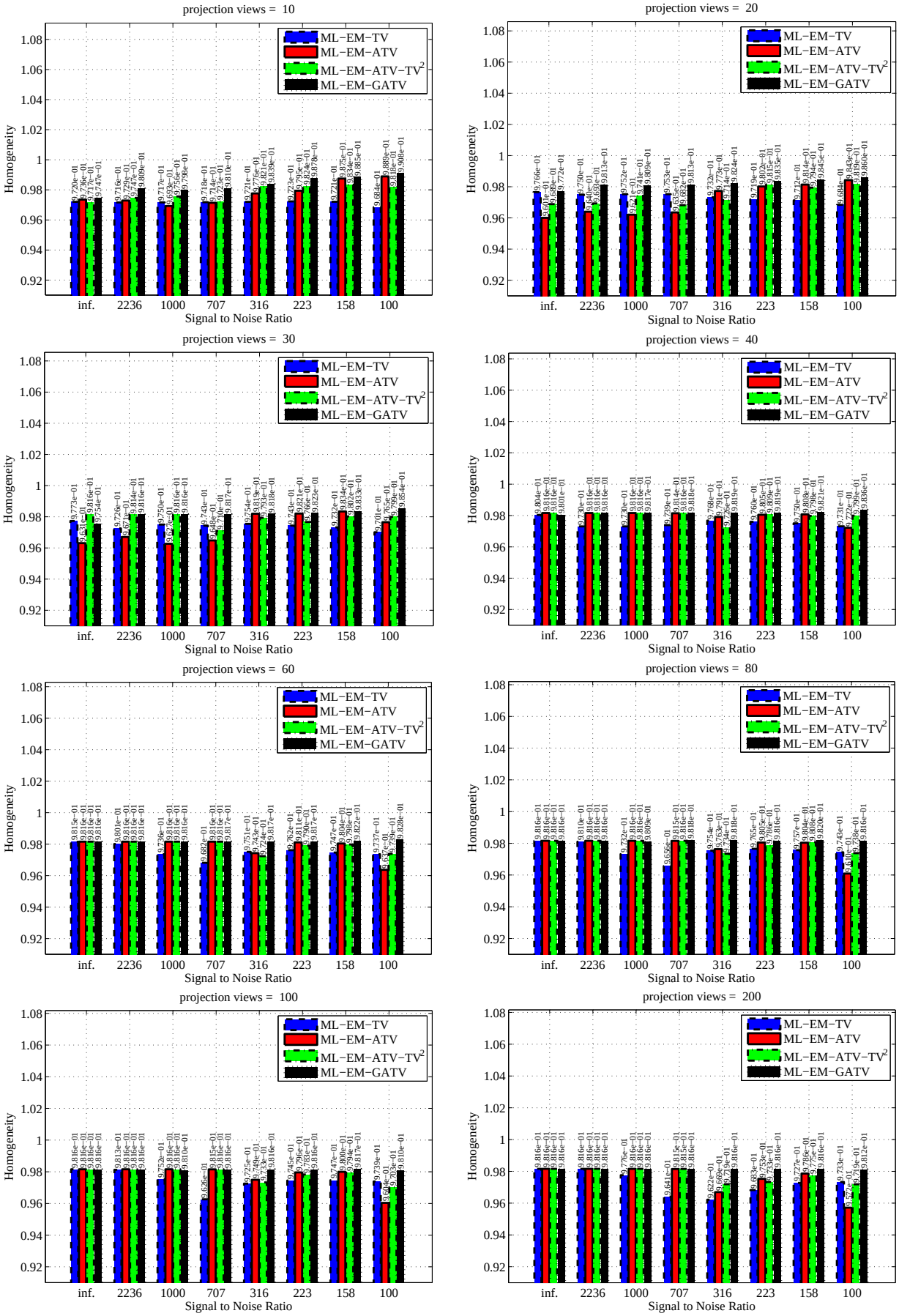

Figure 6.23: The homogeneity of the lung phantom reconstructions from different numbers of projection views and noise levels.

Chapter 7

General Discussion and Conclusion

In this dissertation, we proposed three new regularization methods for accurate, low-dose, iterative CT reconstruction from under-sampled projections which successively improve the reconstruction results of Total Variation. All quality measures presented in this dissertation are well suited to quantify the reconstruction results of the methods. Since the result of a single experiment would not be meaningful, as in principle, it could be obtained by chance and as a result of a random process (since the noise is random as well), we changed the noise random variable 10 times for each experiment and we then computed the mean over these 10 results for both, the resulting images and error metrics, so as to draw a meaningful overall conclusion on the proposed methods.
The main findings of this work include that all of the three methods, ATV, ATV+TV^2 and GATV, successively improve the visual impression of the reconstruction results in terms of preservation of small-scaled image features and those of small intensity. Furthermore, they can improve the edge sharpness, spatial resolution, image contrast and homogeneity. These methods have the potential to extremely decrease the dose in CT.
In case of noise-free projections, the RRMSE of OSC-ATV is up to 32 times smaller than the RRMSE of OSC-TV. The RRMSE of OSC-ATV+TV^2 is up to 68 times smaller than the RRMSE and the RRMSE of OSC-GATV is up to 1770 times smaller than the RRMSE of OSC-TV.
In case of noisy projections, an extreme dose reduction factor of 15.81 can be achieved, when the proposed methods in this dissertation are used, compared to TV: The number of projections can be reduced from 200 to 40 and at the same time, the SNR of the projections can be lowered from 2236 to 707. Furthermore, at this measurement point (projections: 40, SNR: 707), OSC-ATV, OSC-ATV+TV^2, OSC-GATV can further lower the RRMSE by 10.93%, 19.65% and 33.13% respectively, compared to the measurement point of TV at 200 projections and a SNR of 2236. From previous publications we know that a 72 times dose reduction can be achieved for a TV regularized iterative reconstruction compared to FBP, see [165].
Combining this information with the dose reduction potential of the proposed methods, ATV, ATV+TV^2 and GATV, reveals the potential to decrease the dose and acquisition time in CT by a factor of approximately $72 \cdot 15.81 = \mathbf{1138.32}$, compared to conventional FBP.
The results of OSC-ATV+TV^2 are 3.42% more homogeneous than the results of OSC-ATV and the results of OSC-GATV are 3.52% more homogeneous than OSC-ATV+TV^2. Both methods, OSC-ATV+TV^2 and OSC-GATV, can suppress the stair-casing artifacts of TV. Among the three proposed regularization methods, OSC-ATV+TV^2 can produce results with the best contrast. It is up to 29.38 times higher than the contrast of OSC-TV.
It is well known that Total Variation transforms the image into a very sparse domain, since it keeps only the most important image features like the edges. As a result, acceptable reconstructions can be obtained for piece-wise constant objects from only 40 projections. All proposed methods in this thesis are very well suited as a sparsity transform for the Compressed Sensing paradigm. ATV, presented in chapter 3, can be understood as a generalization of TV, since for $\sigma = 1$ in equation 3.8, ATV transforms into TV. Furthermore, the weighting function in ATV acts like a threshold of the noise. It can produce accurate images from 40 projections (see figure 6.5). ATV+TV^2 presented in chapter 4 can produce images which are sparser compared to TV and ATV since the second order term, TV^2, in ATV+TV^2 penalizes edges at a higher extend compared to first

order derivatives used in TV and ATV. Consequently, images from 30 noise-free projections can be accurately reconstructed (see figure 6.5). GATV presented in chapter 5 can differentiate between edges related to noise and true, prominent edges. By penalizing only those undesired edges related to noise, the sparsity of the transformed image can further be increased and therefore, GATV can accurately reconstruct noise-free objects from only 20 projections (see figure 6.1).
Approximating the derivative of AwTV in equation 2.37 leads to worse reconstruction results compared to a mathematical correct expression of the derivative of ATV in equation 3.9. This fact is underlined by the RRMSE values of OSC-AwTV in figure 5.12 and OSC-ATV in figure 6.11 in case of the engine phantom evaluation, 40 projection views and a SNR of 316, 223 or 158: The RRMSE of OSC-ATV is up to 1.5 times lower than the RRMSE of OSC-AwTV for this example.
Judging the reconstruction results of FBP in figure 2.12, it becomes clear that this method cannot be used in an under-sampled scenario. FBP needs at least 200 projection views to obtain an artifact-free result. Furthermore, FBP cannot remove noise during the reconstruction and therefore, the images in figure 2.13 are heavily corrupted by noise, even for a SNR of 1000. The artifacts and noise corruption further intensifies when a low-dose measurement is reconstructed from few projections, see for example the FBP results in figure 5.4.
For OSC-ATV and OSC-ATV+TV^2, suitable parameters have to be found for each phantom individually so as to achieve the best result possible. In other words: Applying these parameters to other phantoms could be problematic. Since the parameters of these methods have been optimized for the Forbild phantom, the best possible RRMSE can be achieved solely for that phantom. In case of other data, e.g. the engine or the lung phantom, the methods produce some outlying RRMSE values for example in figure 6.11, 10 to 40 views, or figure 6.12, 10 to 30 views. These outlying RRMSE values can also be seen in the overall evaluation in figures 6.8 and 6.9. For OSC-GATV the situation is different. The parameters found for this method are applicable to all examined phantoms, projection views and noise levels and therefore no outlying values appear in the quality measurements.
All quality measures presented in this dissertation are very well suited to quantify the reconstruction results. However, there are some limitations to these measures: The homogeneity is very inaccurate for extreme small deviations, e.g. found in the background of the Forbild phantom: Although the result of ATV+TV^2 in figure 6.1 is obviously not that homogeneous as GATV, for a SNR = 223 and 40 views, (especially not in the background of the phantom) the homogeneity of both methods in figure 6.21 is equal. A reason could be that the homogeneity of the whole object was computed instead of a specific ROI. Furthermore, the homogeneity is an extremely non-linear measure. Even a small deviation of less than 1% can lead to a much more homogeneous result, as the results indicate.
The method to examine the spatial resolution in section 4.3.4 does not directly measure the spatial resolution, but the contrast resolution. The spatial resolution can only be measured by analyzing the Modulation Transfer Function and this function is only valid for linear systems. For non-linear systems, we need a different measure to rate the spatial resolution. However, since the spatial resolution depends on the contrast, the method presented in section 4.3.4 is a suitable alternative to rate the spatial resolution.
The execution time of FBP (performed on the CPU) is approximately 100 times faster than our iterative algorithm (performed on the GPU). However, recent publications have shown that clinically-reasonable patient images can be reconstructed in approximately 78 seconds [270] using efficiently implemented iterative algorithms. This can be achieved by a reconstruction algorithm that yields fast convergence rates. A topic of future research could be to incorporate the regularization functions presented in this dissertation into one of these efficiently implemented reconstruction algorithms and then perform experiments on a large clinical dataset. We concluded that in case of piece-wise phantoms which meet the criteria described in section 5.3.1, the dose and the acquisition time in CT can be reduced by approximately 3 orders of magnitudes. Whether this conclusion does apply to the clinical patient data case is to be examined in future.

Bibliography

[1] A matlab implementation of the siddon method by munir ahmad. `http://www.mathworks.com/matlabcentral/fileexchange/24479-pet-reconstruction-system-matrix`. Accessed: 2015-08-03.

[2] The volume library. `http://www9.informatik.uni-erlangen.de/External/vollib/`. Accessed: 2015-08-03.

[3] Mónica Abella, Jeffrey Fessler, et al. A new statistical image reconstruction algorithm for polyenergetic x-ray ct. In *Biomedical Imaging: From Nano to Macro, 2009. ISBI'09. IEEE International Symposium on*, pages 165–168. IEEE, 2009.

[4] Adam M Alessio, Paul E Kinahan, and Thomas K Lewellen. Modeling and incorporation of system response functions in 3-d whole body pet. *Medical Imaging, IEEE Transactions on*, 25(7):828–837, 2006.

[5] AH Andersen and Avinash C Kak. Simultaneous algebraic reconstruction technique (sart): a superior implementation of the art algorithm. *Ultrasonic imaging*, 6(1):81–94, 1984.

[6] John MM Anderson, Bernard Anthony Mair, Murali Rao, and C-H Wu. Weighted least-squares reconstruction methods for positron emission tomography. *Medical Imaging, IEEE Transactions on*, 16(2):159–165, 1997.

[7] Chuanyong Bai, Ling Shao, Angela J Da Silva, and Zuo Zhao. A generalized model for the conversion from ct numbers to linear attenuation coefficients. *Nuclear Science, IEEE Transactions on*, 50(5):1510–1515, 2003.

[8] Harrison H Barrett and Kyle J Myers. Foundations of image science. *Foundations of Image Science, by Harrison H. Barrett, Kyle J. Myers, pp. 1584. ISBN 0-471-15300-1. Wiley-VCH, October 2003.*, 1, 2003.

[9] HH Barrett and Howard Gifford. Cone-beam tomography with discrete data sets. *Physics in medicine and biology*, 39(3):451, 1994.

[10] Samit Basu and Bruno De Man. Branchless distance driven projection and backprojection. In *Electronic Imaging 2006*, pages 60650Y–60650Y. International Society for Optics and Photonics, 2006.

[11] Kees Joost Batenburg and Jan Sijbers. Dart: a practical reconstruction algorithm for discrete tomography. *Image Processing, IEEE Transactions on*, 20(9):2542–2553, 2011.

[12] Amir Beck and Marc Teboulle. Fast gradient-based algorithms for constrained total variation image denoising and deblurring problems. *Image Processing, IEEE Transactions on*, 18(11):2419–2434, 2009.

[13] Freek J Beekman, Hugo WAM de Jong, and Sander van Geloven. Efficient fully 3-d iterative spect reconstruction with monte carlo-based scatter compensation. *Medical Imaging, IEEE Transactions on*, 21(8):867–877, 2002.

[14] Freek J Beekman, C Kamphuis, and MA Viergever. Improved spect quantitation using fully three-dimensional iterative spatially variant scatter response compensation. *Medical Imaging, IEEE Transactions on*, 15(4):491–499, 1996.

[15] Freek J Beekman and Chris Kamphuis. Ordered subset reconstruction for x-ray ct. *Physics in medicine and biology*, 46(7):1835, 2001.

[16] Freek J Beekman, Eddy TP Slijpen, and Wiro J Niessen. Selection of task-dependent diffusion filters for the post-processing of spect images. *Physics in medicine and biology*, 43(6):1713, 1998.

[17] Marcel Beister, Daniel Kolditz, and Willi A Kalender. Iterative reconstruction methods in x-ray ct. *Physica medica*, 28(2):94–108, 2012.

[18] Giovanni Bellettini, Vicent Caselles, and Matteo Novaga. The total variation flow in r n. *Journal of Differential Equations*, 184(2):475–525, 2002.

[19] Thomas M Benson, Bruno KB De Man, Lin Fu, and J-B Thibault. Block-based iterative coordinate descent. In *Nuclear Science Symposium Conference Record (NSS/MIC), 2010 IEEE*, pages 2856–2859. IEEE, 2010.

[20] Dimitri P Bertsekas. A new class of incremental gradient methods for least squares problems. *SIAM Journal on Optimization*, 7(4):913–926, 1997.

[21] Jacob Beutel, Harold L Kundel, and Richard L Van Metter. Handbook of medical imaging, volume 1: Physics and psychophysics. 2000.

[22] Junguo Bian, Jeffrey H Siewerdsen, Xiao Han, Emil Y Sidky, Jerry L Prince, Charles A Pelizzari, and Xiaochuan Pan. Evaluation of sparse-view reconstruction from flat-panel-detector cone-beam ct. *Physics in medicine and biology*, 55(22):6575, 2010.

[23] Junguo Bian, Jiong Wang, Xiao Han, Emil Y Sidky, Lingxiong Shao, and Xiaochuan Pan. Optimization-based image reconstruction from sparse-view data in offset-detector cbct. *Physics in medicine and biology*, 58(2):205, 2013.

[24] Wolfgang Birkfellner, Rudolf Seemann, Michael Figl, Johann Hummel, Christopher Ede, Peter Homolka, Xinhui Yang, Peter Niederer, and Helmar Bergmann. Wobbled splattinga fast perspective volume rendering method for simulation of x-ray images from ct. *Physics in medicine and biology*, 50(9):N73, 2005.

[25] Harald Birkholz. A unifying approach to isotropic and anisotropic total variation denoising models. *Journal of computational and applied mathematics*, 235(8):2502–2514, 2011.

[26] VAINSHTE. BK. Finding structure of objects from projections. *SOVIET PHYSICS CRYSTALLOGRAPHY, USSR*, 15(5):781, 1971.

[27] P Boccacci, P Bonetto, P Calvini, and AR Formiconi. A simple model for the efficient correction of collimator blur in 3d spect imaging. *Inverse Problems*, 15(4):907, 1999.

[28] Charles Bouman and Ken Sauer. A generalized gaussian image model for edge-preserving map estimation. *Image Processing, IEEE Transactions on*, 2(3):296–310, 1993.

[29] Charles Bouman, Ken Sauer, et al. A unified approach to statistical tomography using coordinate descent optimization. *Image Processing, IEEE Transactions on*, 5(3):480–492, 1996.

[30] Ronald N Bracewell. Strip integration in radio astronomy. *Australian Journal of Physics*, 9(2):198–217, 1956.

[31] Kristian Bredies, Karl Kunisch, and Thomas Pock. Total generalized variation. *SIAM Journal on Imaging Sciences*, 3(3):492–526, 2010.

[32] David J Brenner and Eric J Hall. Computed tomographyan increasing source of radiation exposure. *New England Journal of Medicine*, 357(22):2277–2284, 2007.

[33] Rodney A Brooks and Giovanni DiChiro. Principles of computer assisted tomography (cat) in radiographic and radioisotopic imaging. *Physical medical biology*, 21(5):689–732, 1976.

[34] Rodney A Brooks, Gary H Glover, Alan J Talbert, Robert L Eisner, and Frank A DiBianca. Aliasing: A source of streaks in computed tomograms. *Journal of computer assisted tomography*, 3(4):511–518, 1979.

[35] Antonio Brunetti and Bruno Golosio. A new algorithm for computer tomographic reconstruction from partial view projections. *Medical physics*, 28(4):462–468, 2001.

[36] Michael H Buonocore, William R Brody, and Albert Macovski. A natural pixel decomposition for two-dimensional image reconstruction. *Journal of Computer Assisted Tomography*, 5(6):950, 1981.

[37] Jerrold T Bushberg and John M Boone. *The essential physics of medical imaging*. Lippincott Williams & Wilkins, 2011.

[38] Thorsten M Buzug. *Computed tomography: from photon statistics to modern cone-beam CT*. Springer Science & Business Media, 2008.

[39] Charles L Byrne. Block-iterative methods for image reconstruction from projections. *IEEE transactions on image processing: a publication of the IEEE Signal Processing Society*, 5(5):792–794, 1995.

[40] Emmanuel Candes and Justin Romberg. Sparsity and incoherence in compressive sampling. *Inverse problems*, 23(3):969, 2007.

[41] Emmanuel J Candès. The restricted isometry property and its implications for compressed sensing. *Comptes Rendus Mathematique*, 346(9):589–592, 2008.

[42] TD Capricelli and PL Combettes. A convex programming algorithm for noisy discrete tomography. In *Advances in Discrete Tomography and Its Applications*, pages 207–226. Springer, 2007.

[43] Richard E Carson. A maximum likelihood method for region-of-interest evaluation in emission tomography. *Journal of computer assisted tomography*, 10(4):654–663, 1986.

[44] Richard E Carson and Kenneth Lange. Comment: the em parametric image reconstruction algorithm. *Journal of the American Statistical Association*, 80(389):20–22, 1985.

[45] Yair Censor, Tommy Elfving, Gabor T Herman, and Touraj Nikazad. On diagonally relaxed orthogonal projection methods. *SIAM Journal on Scientific Computing*, 30(1):473–504, 2008.

[46] Antonin Chambolle and Pierre-Louis Lions. Image recovery via total variation minimization and related problems. *Numerische Mathematik*, 76(2):167–188, 1997.

[47] Tony Chan, Selim Esedoglu, Frederick Park, and A Yip. Recent developments in total variation image restoration. *Mathematical Models of Computer Vision*, 17, 2005.

[48] Tony Chan, Antonio Marquina, and Pep Mulet. High-order total variation-based image restoration. *SIAM Journal on Scientific Computing*, 22(2):503–516, 2000.

[49] Pierre Charbonnier, Laure Blanc-Féraud, Gilles Aubert, and Michel Barlaud. Deterministic edge-preserving regularization in computed imaging. *Image Processing, IEEE Transactions on*, 6(2):298–311, 1997.

[50] Guang-Hong Chen, Jie Tang, Shuai Leng, et al. Prior image constrained compressed sensing (piccs). In *Proc Soc Photo Opt Instrum Eng*, volume 6856, page 685618, 2008.

[51] Ping-Chun Chiao, W Leslie Rogers, Neal H Clinthorne, Jeffrey Fessler, Alfred O Hero, et al. Model-based estimation for dynamic cardiac studies using ect. *Medical Imaging, IEEE Transactions on*, 13(2):217–226, 1994.

[52] Kihwan Choi, Jing Wang, Lei Zhu, Tae-Suk Suh, Stephen Boyd, and Lei Xing. Compressed sensing based cone-beam computed tomography reconstruction with a first-order method. *Medical physics*, 37:5113, 2010.

[53] David Colton and Rainer Kress. *Inverse acoustic and electromagnetic scattering theory*, volume 93. Springer Science & Business Media, 2012.

[54] Laurent Condat. A direct algorithm for 1d total variation denoising. *IEEE Signal Processing Letters*, 20(11):1054–1057, 2013.

[55] Allan Macleod Cormack. Representation of a function by its line integrals, with some radiological applications. ii. *Journal of Applied Physics*, 35(10):2908–2913, 1964.

[56] M Courdurier, F Noo, M Defrise, and H Kudo. Solving the interior problem of computed tomography using a priori knowledge. *Inverse problems*, 24(6):065001, 2008.

[57] CR Crawford and AC Kak. Aliasing artifacts in computerized tomography. *Applied Optics*, 18(21):3704–3711, 1979.

[58] Imre Csiszar. Why least squares and maximum entropy? an axiomatic approach to inference for linear inverse problems. *The annals of statistics*, pages 2032–2066, 1991.

[59] MJ Daly, JH Siewerdsen, DJ Moseley, DA Jaffray, and JC Irish. Intraoperative cone-beam ct for guidance of head and neck surgery: Assessment of dose and image quality using a c-arm prototype. *Medical physics*, 33:3767, 2006.

[60] Ingrid Daubechies, Bin Han, Amos Ron, and Zuowei Shen. Framelets: Mra-based constructions of wavelet frames. *Applied and computational harmonic analysis*, 14(1):1–46, 2003.

[61] Robert De Levie. An improved numerical approximation for the first derivative. *Journal of Chemical Sciences*, 121(5):935–950, 2009.

[62] Bruno De Man. Iterative reconstruction for reduction of metal artifacts in computed tomography. *status: published*, 2001.

[63] Bruno De Man and Samit Basu. Distance-driven projection and backprojection in three dimensions. *Physics in medicine and biology*, 49(11):2463, 2004.

[64] Bruno De Man, Johan Nuyts, Patrick Dupont, Guy Marchal, and Paul Suetens. Reduction of metal streak artifacts in x-ray computed tomography using a transmission maximum a posteriori algorithm. *IEEE transactions on nuclear science*, 47(3):977–981, 2000.

[65] Bruno De Man, Johan Nuyts, Patrick Dupont, Guy Marchal, and Paul Suetens. An iterative maximum-likelihood polychromatic algorithm for ct. *Medical Imaging, IEEE Transactions on*, 20(10):999–1008, 2001.

[66] Alvaro R De Pierro. A modified expectation maximization algorithm for penalized likelihood estimation in emission tomography. *IEEE Transactions on Medical Imaging*, 14(1):132–137, 1994.

[67] Zsuzsanna Deák, Jochen M Grimm, Marcus Treitl, Lucas L Geyer, Ulrich Linsenmaier, Markus Körner, Maximilian F Reiser, and Stefan Wirth. Filtered back projection, adaptive statistical iterative reconstruction, and a model-based iterative reconstruction in abdominal ct: an experimental clinical study. *Radiology*, 266(1):197–206, 2013.

[68] Maurice Debatin. Gpu-accelerated iterative stochastic limited-angle tomography with non-linear regularization and a priori information. *Diploma Thesis University of Mannheim*, pages 1–179, 2011.

[69] Maurice Debatin and Jürgen Hesser. Accurate low-dose iterative ct reconstruction from few projections by generalized anisotropic total variation minimization for industrial ct. *Journal of X-Ray Science and Technology*, 23(6):701–726, 2015.

[70] Maurice Debatin, Dzmitry Stsepankou, and Jürgen Hesser. Ct reconstruction from few-views by higher order adaptive weighted total variation minimization. *Fully 3D*, pages 134–137, 2013.

[71] Maurice Debatin, Piotr Zygmanski, Dzmitry Stsepankou, and Jürgen Hesser. Ct reconstruction from few-views by anisotropic total variation minimization. In *Nuclear Science Symposium and Medical Imaging Conference (NSS/MIC), 2012 IEEE*, pages 2295–2296. IEEE, 2012.

[72] Michel Defrise and Grant T Gullberg. Image reconstruction. *Physics in medicine and biology*, 51(13):R139–54, 2006.

[73] Michel Defrise, Frédéric Noo, Rolf Clackdoyle, and Hiroyuki Kudo. Truncated hilbert transform and image reconstruction from limited tomographic data. *Inverse problems*, 22(3):1037, 2006.

[74] Michel Defrise, Christian Vanhove, and Xuan Liu. An algorithm for total variation regularization in high-dimensional linear problems. *Inverse Problems*, 27(6):065002, 2011.

[75] Alexander H Delaney and Yoram Bresler. A fast and accurate fourier algorithm for iterative parallel-beam tomography. *Image Processing, IEEE Transactions on*, 5(5):740–753, 1996.

[76] Omer Demirkaya. Reduction of noise and image artifacts in computed tomography by nonlinear filtration of projection images. In *Medical Imaging 2001*, pages 917–923. International Society for Optics and Photonics, 2001.

[77] Arthur P Dempster, Nan M Laird, and Donald B Rubin. Maximum likelihood from incomplete data via the em algorithm. *Journal of the Royal Statistical Society. Series B (Methodological)*, pages 1–38, 1977.

[78] George X Ding and Charles W Coffey. Radiation dose from kilovoltage cone beam computed tomography in an image-guided radiotherapy procedure. *International Journal of Radiation Oncology* Biology* Physics*, 73(2):610–617, 2009.

[79] Synho Do, W Clem Karl, Mannudeep K Kalra, Thomas J Brady, and Homer Pien. A variational approach for reconstructing low dose images in clinical helical ct. In *Biomedical Imaging: From Nano to Macro, 2010 IEEE International Symposium on*, pages 784–787. IEEE, 2010.

[80] David C Dobson and Fadil Santosa. Recovery of blocky images from noisy and blurred data. *SIAM Journal on Applied Mathematics*, 56(4):1181–1198, 1996.

[81] David L Donoho. Superresolution via sparsity constraints. *SIAM Journal on Mathematical Analysis*, 23(5):1309–1331, 1992.

[82] David L Donoho. Compressed sensing. *Information Theory, IEEE Transactions on*, 52(4):1289–1306, 2006.

[83] David L Donoho, Michael Elad, and Vladimir N Temlyakov. Stable recovery of sparse overcomplete representations in the presence of noise. *Information Theory, IEEE Transactions on*, 52(1):6–18, 2006.

[84] Paulus Petrus Bernardus Eggermont, Gabor T Herman, and Arnold Lent. Iterative algorithms for large partitioned linear systems, with applications to image reconstruction. *Linear algebra and its applications*, 40:37–67, 1981.

[85] Andrew J Einstein, Milena J Henzlova, and Sanjay Rajagopalan. Estimating risk of cancer associated with radiation exposure from 64-slice computed tomography coronary angiography. *Jama*, 298(3):317–323, 2007.

[86] Idris Elbakri, Jeffrey Fessler, et al. Statistical image reconstruction for polyenergetic x-ray computed tomography. *Medical Imaging, IEEE Transactions on*, 21(2):89–99, 2002.

[87] Idris A Elbakri and Jeffrey A Fessler. Segmentation-free statistical image reconstruction for polyenergetic x-ray computed tomography. 2002.

[88] Idris A Elbakri and Jeffrey A Fessler. Efficient and accurate likelihood for iterative image reconstruction in x-ray computed tomography. In *Medical Imaging 2003*, pages 1839–1850. International Society for Optics and Photonics, 2003.

[89] Idris A Elbakri and Jeffrey A Fessler. Segmentation-free statistical image reconstruction for polyenergetic x-ray computed tomography with experimental validation. *Physics in medicine and biology*, 48(15):2453, 2003.

[90] Alaa Eleyan and Hasan Demirel. Co-occurrence matrix and its statistical features as a new approach for face recognition. *Turk J Elec Eng & Comp Sci*, 19(1):97–107, 2011.

[91] Hakan Erdogan and Jeffrey A Fessler. Ordered subsets algorithms for transmission tomography. *Physics in medicine and biology*, 44(11):2835, 1999.

[92] Hakan Erdogan and Jeffrey A Fessler. Monotonic algorithms for transmission tomography. In *Biomedical Imaging, 2002. 5th IEEE EMBS International Summer School on*, pages 14–pp. IEEE, 2002.

[93] LA Feldkamp, LC Davis, and JW Kress. Practical cone-beam algorithm. *JOSA A*, 1(6):612–619, 1984.

[94] Bing Feng, Jeffrey A Fessler, and Michael A King. Incorporation of system resolution compensation (rc) in the ordered-subset transmission (ostr) algorithm for transmission imaging in spect. *Medical Imaging, IEEE Transactions on*, 25(7):941–949, 2006.

[95] Jeffrey Fessler, Neal H Clinthorne, W Leslie Rogers, et al. Regularized emission image reconstruction using imperfect side information. *Nuclear Science, IEEE Transactions on*, 39(5):1464–1471, 1992.

[96] Jeffrey A Fessler. Penalized weighted least-squares image reconstruction for positron emission tomography. *Medical Imaging, IEEE Transactions on*, 13(2):290–300, 1994.

[97] Jeffrey A Fessler. Statistical image reconstruction methods for transmission tomography. *Handbook of Medical Imaging*, 2:1–70, 2000.

[98] Jeffrey A Fessler, Edward P Ficaro, Neal H Clinthorne, and Kenneth Lange. Grouped-coordinate ascent algorithms for penalized-likelihood transmission image reconstruction. *Medical Imaging, IEEE Transactions on*, 16(2):166–175, 1997.

[99] Jeffrey A Fessler and Donghwan Kim. Axial block coordinate descent (abcd) algorithm for x-ray ct image reconstruction. In *Proc. Intl. Mtg. on Fully 3D Image Recon. in Rad. and Nuc. Med*, pages 262–5, 2011.

[100] Carey E Floyd Jr, Ronald J Jaszczak, Kim L Greer, and R Edward Coleman. Inverse monte carlo as a unified reconstruction algorithm for ect. *Journal of nuclear medicine: official publication, Society of Nuclear Medicine*, 27(10):1577–1585, 1986.

[101] Andreas Robert Formiconi. Least squares algorithm for region-of-interest evaluation in emission tomography. *Medical Imaging, IEEE Transactions on*, 12(1):90–100, 1993.

[102] P Forthmann, T Köhler, PGC Begemann, and M Defrise. Penalized maximum-likelihood sinogram restoration for dual focal spot computed tomography. *Physics in medicine and biology*, 52(15):4513, 2007.

[103] TG Freeman. The mathematics of medical imaging. *Springer Undergraduate Texts in Mathematics and Technology, Springer Science and Business Media, LLC, Springer, NY, doi*, 10:978–0, 2010.

[104] B Roy Frieden. Restoring with maximum likelihood and maximum entropy. *JOSA*, 62(4):511–518, 1972.

[105] Ramesh R Galigekere, Karl Wiesent, and David W Holdsworth. Cone-beam reprojection using projection-matrices. *Medical Imaging, IEEE Transactions on*, 22(10):1202–1214, 2003.

[106] RR Galigekere, K Wiesent, and DW Holdsworth. Techniques to alleviate the effects of view aliasing artifacts in computed tomography. *Medical physics*, 26(6):896–904, 1999.

[107] Donald Geman and George Reynolds. Constrained restoration and the recovery of discontinuities. *IEEE Transactions on pattern analysis and machine intelligence*, 14(3):367–383, 1992.

[108] Stuart Geman and Donald Geman. Stochastic relaxation, gibbs distributions, and the bayesian restoration of images. *Pattern Analysis and Machine Intelligence, IEEE Transactions on*, (6):721–741, 1984.

[109] RW Gerchberg. Super-resolution through error energy reduction. *Journal of Modern Optics*, 21(9):709–720, 1974.

[110] Alban Gervaise, Benoît Osemont, Sophie Lecocq, Alain Noel, Emilien Micard, Jacques Felblinger, and Alain Blum. Ct image quality improvement using adaptive iterative dose reduction with wide-volume acquisition on 320-detector ct. *European radiology*, 22(2):295–301, 2012.

[111] Pascal Getreuer. Rudin-osher-fatemi total variation denoising using split bregman. *Image Processing On Line*, 10, 2012.

[112] Peter Gilbert. Iterative methods for the three-dimensional reconstruction of an object from projections. *Journal of theoretical biology*, 36(1):105–117, 1972.

[113] Michael Goitein. Three-dimensional density reconstruction from a series of two-dimensional projections. *Nuclear Instruments and Methods*, 101(3):509–518, 1972.

[114] Tom Goldstein and Stanley Osher. The split bregman method for l1-regularized problems. *SIAM Journal on Imaging Sciences*, 2(2):323–343, 2009.

[115] Varun P Gopi, Zangen Zhu, P Palanisamy, Khan Wahid, Paul Babyn, et al. Iterative method for ct image reconstruction from reduced number of projection views. In *Electrical and Computer Engineering (CCECE), 2013 26th Annual IEEE Canadian Conference on*, pages 1–4. IEEE, 2013.

[116] Richard Gordon, Robert Bender, and Gabor T Herman. Algebraic reconstruction techniques (art) for three-dimensional electron microscopy and x-ray photography. *Journal of theoretical Biology*, 29(3):471–481, 1970.

[117] Yann Gousseau and Jean-Michel Morel. Are natural images of bounded variation? *SIAM Journal on Mathematical Analysis*, 33(3):634–648, 2001.

[118] Markus Grasmair and Frank Lenzen. Anisotropic total variation filtering. *Applied Mathematics & Optimization*, 62(3):323–339, 2010.

[119] Peter J Green. Iteratively reweighted least squares for maximum likelihood estimation, and some robust and resistant alternatives. *Journal of the Royal Statistical Society. Series B (Methodological)*, pages 149–192, 1984.

[120] Peter J Green. Bayesian reconstructions from emission tomography data using a modified em algorithm. *Medical Imaging, IEEE Transactions on*, 9(1):84–93, 1990.

[121] Peter J Green. On use of the em for penalized likelihood estimation. *Journal of the Royal Statistical Society. Series B (Methodological)*, pages 443–452, 1990.

[122] Xuejun Gu, Dongju Choi, Chunhua Men, Hubert Pan, Amitava Majumdar, and Steve B Jiang. Gpu-based ultra-fast dose calculation using a finite size pencil beam model. *Physics in medicine and biology*, 54(20):6287, 2009.

[123] Huaiqun Guan and Richard Gordon. Computed tomography using algebraic reconstruction techniques (arts) with different projection access schemes: a comparison study under practical situations. *Physics in medicine and biology*, 41(9):1727, 1996.

[124] Weihong Guo and Wotao Yin. Edgecs: Edge guided compressive sensing reconstruction. In *Visual Communications and Image Processing 2010*, pages 77440L–77440L. International Society for Optics and Photonics, 2010.

[125] James Hamill and Thomas Bruckbauer. Iterative reconstruction methods for high-throughput pet tomographs. *Physics in medicine and biology*, 47(15):2627, 2002.

[126] Weimin Han, Hengyong Yu, and Ge Wang. A general total variation minimization theorem for compressed sensing based interior tomography. *Journal of Biomedical Imaging*, 2009:21, 2009.

[127] Eric W Hansen. Theory of circular harmonic image reconstruction. *JOSA*, 71(3):304–308, 1981.

[128] Eberhard Hansis, D Schafer, O Dossel, and Michael Grass. Evaluation of iterative sparse object reconstruction from few projections for 3-d rotational coronary angiography. *Medical Imaging, IEEE Transactions on*, 27(11):1548–1555, 2008.

[129] KENNETH M Hanson. Method to evaluate image-recovery algorithms based on task performance. In *Medical Imaging II*, pages 336–343. International Society for Optics and Photonics, 1988.

[130] Kenneth M Hanson and George W Wecksung. Bayesian approach to limited-angle reconstruction in computed tomography. *JOSA*, 73(11):1501–1509, 1983.

[131] Kenneth M Hanson and George W Wecksung. Local basis-function approach to computed tomography. *Applied Optics*, 24(23):4028–4039, 1985.

[132] Kenneth M Hanson and George W Wecksung. Local basis-function approach to computed tomography. *Applied Optics*, 24(23):4028–4039, 1985.

[133] Amy K Hara, Robert G Paden, Alvin C Silva, Jennifer L Kujak, Holly J Lawder, and William Pavlicek. Iterative reconstruction technique for reducing body radiation dose at ct: feasibility study. *American Journal of Roentgenology*, 193(3):764–771, 2009.

[134] Robert M Haralick, Karthikeyan Shanmugam, and Its' Hak Dinstein. Textural features for image classification. *Systems, Man and Cybernetics, IEEE Transactions on*, (6):610–621, 1973.

[135] Chris Harris and Mike Stephens. A combined corner and edge detector. In *Alvey vision conference*, volume 15, page 50. Citeseer, 1988.

[136] Joan Hatton, Boyd McCurdy, and Peter B Greer. Cone beam computerized tomography: the effect of calibration of the hounsfield unit number to electron density on dose calculation accuracy for adaptive radiation therapy. *Physics in medicine and biology*, 54(15):N329, 2009.

[137] Tom Hebert and Richard Leahy. A generalized em algorithm for 3-d bayesian reconstruction from poisson data using gibbs priors. *Medical Imaging, IEEE Transactions on*, 8(2):194–202, 1989.

[138] Tom Hebert, Richard Leahy, and Manbir Singh. Fast mle for spect using an intermediate polar representation and a stopping criterion. *Nuclear Science, IEEE Transactions on*, 35(1):615–619, 1988.

[139] Gabor T Herman. Image reconstruction from projections. *Real-Time Imaging*, 1(1):3–18, 1995.

[140] Gabor T Herman and Ran Davidi. Image reconstruction from a small number of projections. *Inverse problems*, 24(4):045011, 2008.

[141] Gabor T Herman and Lorraine B Meyer. Algebraic reconstruction techniques can be made computationally efficient [positron emission tomography application]. *Medical Imaging, IEEE Transactions on*, 12(3):600–609, 1993.

[142] Sami Hissoiny, Benoît Ozell, and Philippe Després. Fast convolution-superposition dose calculation on graphics hardware. *Medical physics*, 36(6):1998–2005, 2009.

[143] IK Hong, ST Chung, HK Kim, YB Kim, YD Son, and ZH Cho. Ultra fast symmetry and simd-based projection-backprojection (ssp) algorithm for 3-d pet image reconstruction. *Medical Imaging, IEEE Transactions on*, 26(6):789–803, 2007.

[144] Stefan Horbelt, Michael Liebling, and Michael Unser. Discretization of the radon transform and of its inverse by spline convolutions. *Medical Imaging, IEEE Transactions on*, 21(4):363–376, 2002.

[145] Godfrey N Hounsfield. Computerized transverse axial scanning (tomography): Part 1. description of system. *The British journal of radiology*, 46(552):1016–1022, 1973.

[146] Godfrey Newbold Hounsfield. Method of and apparatus for examining a body by radiation such as x or gamma radiation, November 11 1975. US Patent 3,919,552.

[147] JM Hoxworth, D Lal, GP Fletcher, AC Patel, M He, RG Paden, and AK Hara. Radiation dose reduction in paranasal sinus ct using model-based iterative reconstruction. *American Journal of Neuroradiology*, 35(4):644–649, 2014.

[148] Jiang Hsieh. Adaptive streak artifact reduction in computed tomography resulting from excessive x-ray photon noise. *Medical Physics*, 25(11):2139–2147, 1998.

[149] Jiang Hsieh. Computed tomography: principles, design, artifacts, and recent advances. SPIE Bellingham, WA, 2009.

[150] Yu-Lung Hsieh, Gengsheng L Zeng, and Grant T Gullberg. Projection space image reconstruction using strip functions to calculate pixels more" natural" for modeling the geometric response of the spect collimator. *Medical Imaging, IEEE Transactions on*, 17(1):24–44, 1998.

[151] Jicun Hu, Kwok Tam, and Jinyi Qi. An approximate short scan helical fdk cone beam algorithm based on nutating curved surfaces satisfying the tuys condition. *Medical physics*, 32(6):1529–1536, 2005.

[152] John H Hubbell and Stephen M Seltzer. Tables of x-ray mass attenuation coefficients and mass energy-absorption coefficients. *National Institute of Standards and Technology*, 1996.

[153] H Malcolm Hudson and Richard S Larkin. Accelerated image reconstruction using ordered subsets of projection data. *Medical Imaging, IEEE Transactions on*, 13(4):601–609, 1994.

[154] RH Huesman. The effects of a finite number of projection angles and finite lateral sampling of projections on the propagation of statistical errors in transverse section reconstruction. *Physics in medicine and biology*, 22(3):511, 1977.

[155] Mohammad K Islam, Thomas G Purdie, Bernhard D Norrlinger, Hamideh Alasti, Douglas J Moseley, Michael B Sharpe, Jeffrey H Siewerdsen, and David A Jaffray. Patient dose from kilovoltage cone beam computed tomography imaging in radiation therapy. *Medical physics*, 33(6):1573–1582, 2006.

[156] Shigeru Izumi, S Kamata, K Satoh, and H Miyai. High energy x-ray computed tomography for industrial applications. *Nuclear Science, IEEE Transactions on*, 40(2):158–161, 1993.

[157] Filip Jacobs, Erik Sundermann, Bjorn De Sutter, Mark Christiaens, and Ignace Lemahieu. A fast algorithm to calculate the exact radiological path through a pixel or voxel space. *Journal of computing and information technology*, 6(1):89–94, 1998.

[158] Robert Jacques, Russell Taylor, John Wong, and Todd McNutt. Towards real-time radiation therapy: Gpu accelerated superposition/convolution. *Computer methods and programs in biomedicine*, 98(3):285–292, 2010.

[159] David A Jaffray. Emergent technologies for 3-dimensional image-guided radiation delivery. In *Seminars in radiation oncology*, volume 15, pages 208–216. Elsevier, 2005.

[160] David A Jaffray, Jeffrey H Siewerdsen, John W Wong, and Alvaro A Martinez. Flat-panel cone-beam computed tomography for image-guided radiation therapy. *International Journal of Radiation Oncology* Biology* Physics*, 53(5):1337–1349, 2002.

[161] Tobias Lindstrøm Jensen, Jakob Heide Jørgensen, Per Christian Hansen, and Søren Holdt Jensen. Implementation of an optimal first-order method for strongly convex total variation regularization. *BIT Numerical Mathematics*, 52(2):329–356, 2012.

[162] Abdul J Jerri. The shannon sampling theoremits various extensions and applications: A tutorial review. *Proceedings of the IEEE*, 65(11):1565–1596, 1977.

[163] Xun Jia, Bin Dong, Yifei Lou, and Steve B Jiang. Gpu-based iterative cone-beam ct reconstruction using tight frame regularization. *Physics in medicine and biology*, 56(13):3787, 2011.

[164] Xun Jia, Xuejun Gu, Josep Sempau, Dongju Choi, Amitava Majumdar, and Steve B Jiang. Development of a gpu-based monte carlo dose calculation code for coupled electron–photon transport. *Physics in medicine and biology*, 55(11):3077, 2010.

[165] Xun Jia, Yifei Lou, Ruijiang Li, William Y Song, and Steve B Jiang. Gpu-based fast cone beam ct reconstruction from undersampled and noisy projection data via total variation. *Medical physics*, 37:1757, 2010.

[166] Xun Jia, Peter Ziegenhein, and Steve B Jiang. Gpu-based high-performance computing for radiation therapy. *Physics in medicine and biology*, 59(4):R151, 2014.

[167] Jian-Yue Jin, Lei Ren, Qiang Liu, Jinkoo Kim, Ning Wen, Huaiqun Guan, Benjamin Movsas, and Indrin J Chetty. Combining scatter reduction and correction to improve image quality in cone-beam computed tomography (cbct). *Medical physics*, 37(11):5634–5644, 2010.

[168] Xin Jin, Liang Li, Zhiqiang Chen, Li Zhang, and Yuxiang Xing. Anisotropic total variation for limited-angle ct reconstruction. In *Nuclear Science Symposium Conference Record (NSS/MIC), 2010 IEEE*, pages 2232–2238. IEEE, 2010.

[169] Don H Johnson and Sinan Sinanovic. Symmetrizing the kullback-leibler distance. 2003.

[170] Peter M Joseph. An improved algorithm for reprojecting rays through pixel images. *Medical Imaging, IEEE Transactions on*, 1(3):192–196, 1982.

[171] Peter M Joseph and Raymond A Schulz. View sampling requirements in fan beam computed tomography. *Medical physics*, 7(6):692–702, 1980.

[172] Marc Kachelrieß, Timo Berkus, and Will Kalender. Quality of statistical reconstruction in medical ct. In *Nuclear Science Symposium Conference Record, 2003 IEEE*, volume 4, pages 2748–2752. IEEE, 2003.

[173] Marc Kachelriess, Stefan Schaller, and Willi A Kalender. Advanced single-slice rebinning in cone-beam spiral ct: Theoretical considerations and medical applications. In *Medical Imaging 2000*, pages 494–505. International Society for Optics and Photonics, 2000.

[174] Marc Kachelriess, Oliver Watzke, and Willi A Kalender. Generalized multi-dimensional adaptive filtering for conventional and spiral single-slice, multi-slice, and cone-beam ct. *Medical physics*, 28(4):475–490, 2001.

[175] Stefan Kaczmarz. Angenäherte auflösung von systemen linearer gleichungen. *Bulletin International de lAcademie Polonaise des Sciences et des Lettres*, 35:355–357, 1937.

[176] Jari Kaipio and Erkki Somersalo. *Statistical and computational inverse problems*, volume 160. Springer Science & Business Media, 2006.

[177] Jari Kaipio and Erkki Somersalo. Statistical inverse problems: Discretization, model reduction and inverse crimes. *Journal of Computational and Applied Mathematics*, 198(2):493–504, 2007.

[178] Willi A Kalender. X-ray computed tomography. *Physics in medicine and biology*, 51(13):R29, 2006.

[179] Mannudeep K Kalra, Michael M Maher, Thomas L Toth, Bernhard Schmidt, Bryan L Westerman, Hugh T Morgan, and Sanjay Saini. Techniques and applications of automatic tube current modulation for ct 1. *Radiology*, 233(3):649–657, 2004.

[180] Mannudeep K Kalra, Conrad Wittram, Michael M Maher, Amita Sharma, Gopal B Avinash, Kelly Karau, Thomas L Toth, Elkan Halpern, Sanjay Saini, and Jo-Anne Shepard. Can noise reduction filters improve low-radiation-dose chest ct images? pilot study 1. *Radiology*, 228(1):257–264, 2003.

[181] Mannudeep K Kalra, Mischa Woisetschläger, Nils Dahlström, Sarabjeet Singh, Subbarao Digumarthy, Synho Do, Homer Pien, Petter Quick, Bernhard Schmidt, Martin Sedlmair, et al. Sinogram-affirmed iterative reconstruction of low-dose chest ct: effect on image quality and radiation dose. *American Journal of Roentgenology*, 201(2):W235–W244, 2013.

[182] Chris Kamphuis and Freek J Beekman. Accelerated iterative transmission ct reconstruction using an ordered subsets convex algorithm. *Medical Imaging, IEEE Transactions on*, 17(6):1101–1105, 1998.

[183] Alexander Katsevich. Analysis of an exact inversion algorithm for spiral cone-beam ct. *Physics in medicine and biology*, 47(15):2583, 2002.

[184] Alexander Katsevich. Theoretically exact filtered backprojection-type inversion algorithm for spiral ct. *SIAM Journal on Applied Mathematics*, 62(6):2012–2026, 2002.

[185] Alexander Katsevich. An improved exact filtered backprojection algorithm for spiral computed tomography. *Advances in Applied Mathematics*, 32(4):681–697, 2004.

[186] Alexander I Katsevich, Guenter Lauritsch, Herbert Bruder, Thomas Flohr, and Karl Stierstorfer. Evaluation and empirical analysis of an exact fbp algorithm for spiral cone-beam ct. In *Medical Imaging 2003*, pages 663–674. International Society for Optics and Photonics, 2003.

[187] Richard A Ketcham and William D Carlson. Acquisition, optimization and interpretation of x-ray computed tomographic imagery: applications to the geosciences. *Computers & Geosciences*, 27(4):381–400, 2001.

[188] Dae-Hong Kim, Hee-Joung Kim, Chang-Lae Lee, Pil-Hyun Jeon, Su-Jin Park, and Ye-Seul Kim. Evaluation of reconstructed images on the micro-ct system using total variation minimization. In *Nuclear Science Symposium and Medical Imaging Conference (NSS/MIC), 2012 IEEE*, pages 2386–2389. IEEE, 2012.

[189] Sangroh Kim, Terry T Yoshizumi, Donald P Frush, Greta Toncheva, and Fang-Fang Yin. Radiation dose from cone beam ct in a pediatric phantom: risk estimation of cancer incidence. *American Journal of Roentgenology*, 194(1):186–190, 2010.

[190] David B Kirk and W Hwu Wen-mei. *Programming massively parallel processors: a hands-on approach*. Newnes, 2012.

[191] Pavel Kisilev, Michael Zibulevsky, and Yehoshua Y Zeevi. Wavelet representation and total variation regularization in emission tomography. In *Image Processing, 2001. Proceedings. 2001 International Conference on*, volume 1, pages 702–705. IEEE, 2001.

[192] JS Kole. Statistical image reconstruction for transmission tomography using relaxed ordered subset algorithms. *Physics in medicine and biology*, 50(7):1533, 2005.

[193] Hiroyuki Kudo, Matias Courdurier, Frédéric Noo, and Michel Defrise. Tiny a priori knowledge solves the interior problem in computed tomography. *Physics in medicine and biology*, 53(9):2207, 2008.

[194] David E Kuhl and Roy Q Edwards. Image separation radioisotope scanning 1. *Radiology*, 80(4):653–662, 1963.

[195] Yiannis Kyriakou, Thomas Riedel, and Willi A Kalender. Combining deterministic and monte carlo calculations for fast estimation of scatter intensities in ct. *Physics in medicine and biology*, 51(18):4567, 2006.

[196] Patrick J La Riviere. Penalized-likelihood sinogram smoothing for low-dose ct. *Medical physics*, 32(6):1676–1683, 2005.

[197] Patrick J La Rivière, Junguo Bian, Phillip Vargas, et al. Penalized-likelihood sinogram restoration for computed tomography. *Medical Imaging, IEEE Transactions on*, 25(8):1022–1036, 2006.

[198] Patrick J La Rivière and David Matthew Billmire. Reduction of noise-induced streak artifacts in x-ray computed tomography through spline-based penalized-likelihood sinogram smoothing. *Medical Imaging, IEEE Transactions on*, 24(1):105–111, 2005.

[199] Patrick J La Rivière and Xiaochuan Pan. Nonparametric regression sinogram smoothing using a roughness-penalized poisson likelihood objective function. *Medical Imaging, IEEE Transactions on*, 19(8):773–786, 2000.

[200] Kenneth Lange. Convergence of em image reconstruction algorithms with gibbs smoothing. *Medical Imaging, IEEE Transactions on*, 9(4):439–446, 1990.

[201] Kenneth Lange, Mark Bahn, and Roderick Little. A theoretical study of some maximum likelihood algorithms for emission and transmission tomography. *Medical Imaging, IEEE Transactions on*, 6(2):106–114, 1987.

[202] Kenneth Lange and Richard Carson. Em reconstruction algorithms for emission and transmission tomography. *Journal of computer assisted tomography*, 8(2):306–316, 1984.

[203] Samuel J LaRoque, Emil Y Sidky, and Xiaochuan Pan. Accurate image reconstruction from few-view and limited-angle data in diffraction tomography. *JOSA A*, 25(7):1772–1782, 2008.

[204] Giovanni M Lasio, Bruce R Whiting, and Jeffrey F Williamson. Statistical reconstruction for x-ray computed tomography using energy-integrating detectors. *Physics in medicine and biology*, 52(8):2247, 2007.

[205] Pascal Thériault Lauzier and Guang-Hong Chen. Characterization of statistical prior image constrained compressed sensing (piccs): Ii. application to dose reduction. *Medical physics*, 40(2):021902, 2013.

[206] Ho Lee, Lei Xing, Ran Davidi, Ruijiang Li, Jianguo Qian, and Rena Lee. Improved compressed sensing-based cone-beam ct reconstruction using adaptive prior image constraints. *Physics in medicine and biology*, 57(8):2287, 2012.

[207] Soo-Jin Lee. Accelerated coordinate descent methods for bayesian reconstruction using ordered subsets of projection data. In *International Symposium on Optical Science and Technology*, pages 170–181. International Society for Optics and Photonics, 2000.

[208] Jonathon Leipsic, Troy M LaBounty, Brett Heilbron, James K Min, GB John Mancini, Fay Y Lin, Carolyn Taylor, Allison Dunning, and James P Earls. Adaptive statistical iterative reconstruction: assessment of image noise and image quality in coronary ct angiography. *American Journal of Roentgenology*, 195(3):649–654, 2010.

[209] Shuai Leng, Jie Tang, Joseph Zambelli, Brian Nett, Ranjini Tolakanahalli, and Guang-Hong Chen. High temporal resolution and streak-free four-dimensional cone-beam computed tomography. *Physics in medicine and biology*, 53(20):5653, 2008.

[210] Robert M Lewitt. Multidimensional digital image representations using generalized kaiser–bessel window functions. *JOSA A*, 7(10):1834–1846, 1990.

[211] Robert M Lewitt and Samuel Matej. Overview of methods for image reconstruction from projections in emission computed tomography. *Proceedings of the IEEE*, 91(10):1588–1611, 2003.

[212] Meihua Li, Hiroyuki Kudo, Jicun Hu, and Roger H Johnson. Improved iterative algorithm for sparse object reconstruction and its performance evaluation with micro-ct data. *Nuclear Science, IEEE Transactions on*, 51(3):659–666, 2004.

[213] Tianfang Li, Xiang Li, Jing Wang, Junhai Wen, Hongbing Lu, Jiang Hsieh, and Zhengrong Liang. Nonlinear sinogram smoothing for low-dose x-ray ct. *Nuclear Science, IEEE Transactions on*, 51(5):2505–2513, 2004.

[214] Zhengrong Liang. Compensation for attenuation, scatter, and detector response in spect reconstruction via iterative fbp methods. *Medical physics*, 20(4):1097–1106, 1993.

[215] Zhengrong Liang, Ronald Jaszczak, and Kim Greer. On bayesian image reconstruction from projections: uniform and nonuniform a priori source information. *Medical Imaging, IEEE Transactions on*, 8(3):227–235, 1989.

[216] Kevin J Little and Patrick J La Riviere. An algorithm for modeling non-linear system effects in iterative ct reconstruction. In *Nuclear Science Symposium and Medical Imaging Conference (NSS/MIC), 2012 IEEE*, pages 2174–2177. IEEE, 2012.

[217] Yan Liu, Zhengrong Liang, Jianhua Ma, Hongbing Lu, Ke Wang, Hao Zhang, and William Moore. Total variation-stokes strategy for sparse-view x-ray ct image reconstruction. *Medical Imaging, IEEE Transactions on*, 33(3):749–763, 2014.

[218] Yan Liu, Jianhua Ma, Yi Fan, and Zhengrong Liang. Adaptive-weighted total variation minimization for sparse data toward low-dose x-ray computed tomography image reconstruction. *Physics in medicine and biology*, 57(23):7923, 2012.

[219] Yong Long, Jeffrey Fessler, James M Balter, et al. 3d forward and back-projection for x-ray ct using separable footprints. *Medical Imaging, IEEE Transactions on*, 29(11):1839–1850, 2010.

[220] Stephen Loose and Konrad W Leszczynski. On few-view tomographic reconstruction with megavoltage photon beams. *Medical physics*, 28(8):1679–1688, 2001.

[221] AK Louis. Approximate inverse for linear and some nonlinear problems. *Inverse problems*, 12(2):175, 1996.

[222] Alfred K Louis. Filter design in three-dimensional cone beam tomography: circular scanning geometry. *Inverse problems*, 19(6):S31, 2003.

[223] Hongbing Lu, Ing-Tsung Hsiao, Xiang Li, and Zhengrong Liang. Noise properties of low-dose ct projections and noise treatment by scale transformations. In *Nuclear Science Symposium Conference Record, 2001 IEEE*, volume 3, pages 1662–1666. IEEE, 2001.

[224] Hongbing Lu, Xiang Li, Tsung Hsiao, and Zhengrong Liang. Analytical noise treatment for low-dose ct projection data by penalized weighted least-square smoothing in the kl domain. In *Medical Imaging 2002*, pages 146–152. International Society for Optics and Photonics, 2002.

[225] Hongbing Lu, Xiang Li, Lihong Li, Dongqing Chen, Yuxiang Xing, Jiang Hsieh, and Zhengrong Liang. Adaptive noise reduction toward low-dose computed tomography. In *Medical Imaging 2003*, pages 759–766. International Society for Optics and Photonics, 2003.

[226] Leon B Lucy. An iterative technique for the rectification of observed distributions. *The astronomical journal*, 79:745, 1974.

[227] Maria Lyra and Agapi Ploussi. Filtering in spect image reconstruction. *Journal of Biomedical Imaging*, 2011:10, 2011.

[228] Marius Lysaker and Xue-Cheng Tai. Iterative image restoration combining total variation minimization and a second-order functional. *International Journal of Computer Vision*, 66(1):5–18, 2006.

[229] Jianhua Ma, Qianjin Feng, Yanqiu Feng, Jing Huang, and Wufan Chen. Generalized gibbs priors based positron emission tomography reconstruction. *Computers in biology and medicine*, 40(6):565–571, 2010.

[230] Jianhua Ma, Zhengrong Liang, Yi Fan, Yan Liu, Jing Huang, Wufan Chen, and Hongbing Lu. Variance analysis of x-ray ct sinograms in the presence of electronic noise background. *Medical Physics*, 39:4051, 2012.

[231] Jianhua Ma, Hua Zhang, Yang Gao, Jing Huang, Zhengrong Liang, Qianjing Feng, and Wufan Chen. Iterative image reconstruction for cerebral perfusion ct using a pre-contrast scan induced edge-preserving prior. *Physics in medicine and biology*, 57(22):7519, 2012.

[232] SH Manglos, GM Gagne, A Krol, FD Thomas, and R Narayanaswamy. Transmission maximum-likelihood reconstruction with ordered subsets for cone beam ct. *Physics in Medicine and Biology*, 40(7):1225, 1995.

[233] Samuel Matej and Robert M Lewitt. Practical considerations for 3-d image reconstruction using spherically symmetric volume elements. *Medical Imaging, IEEE Transactions on*, 15(1):68–78, 1996.

[234] Samuel Matej and Robert M Lewitt. 3d-frp: direct fourier reconstruction with fourier reprojection for fully 3-d pet. *Nuclear Science, IEEE Transactions on*, 48(4):1378–1385, 2001.

[235] Cynthia H McCollough, Michael R Bruesewitz, and James M Kofler Jr. Ct dose reduction and dose management tools: Overview of available options 1. *Radiographics*, 26(2):503–512, 2006.

[236] Cynthia H McCollough, Andrew N Primak, Natalie Braun, James Kofler, Lifeng Yu, and Jodie Christner. Strategies for reducing radiation dose in ct. *Radiologic Clinics of North America*, 47(1):27–40, 2009.

[237] William D McDavid, Robert G Waggener, William H Payne, and Michael J Dennis. Spectral effects on three-dimensional reconstruction from x rays. *Medical physics*, 2(6):321–324, 1975.

[238] Li Meihua, Haiquan Yang, Kazuhito Koizumi, and Hirouyuki Kudo. Fast cone-beam ct reconstruction using cuda architecture. 2007.

[239] Chunhua Men, Xuejun Gu, Dongju Choi, Amitava Majumdar, Ziyi Zheng, Klaus Mueller, and Steve B Jiang. Gpu-based ultrafast imrt plan optimization. *Physics in medicine and biology*, 54(21):6565, 2009.

[240] Chunhua Men, Xun Jia, and Steve B Jiang. Gpu-based ultra-fast direct aperture optimization for online adaptive radiation therapy. *Physics in medicine and biology*, 55(15):4309, 2010.

[241] Koen Michielsen, Katrien Van Slambrouck, Anna Jerebko, and Johan Nuyts. Patchwork reconstruction with resolution modeling for digital breast tomosynthesis. *Medical physics*, 40(3):031105, 2013.

[242] Frédéric A Miéville, Laureline Berteloot, Albane Grandjean, Paul Ayestaran, François Gudinchet, Sabine Schmidt, Francis Brunelle, François O Bochud, and Francis R Verdun. Model-based iterative reconstruction in pediatric chest ct: assessment of image quality in a prospective study of children with cystic fibrosis. *Pediatric radiology*, 43(5):558–567, 2013.

[243] Klaus Mueller. *Fast and accurate three-dimensional reconstruction from cone-beam projection data using algebraic methods*. PhD thesis, The Ohio State University, 1998.

[244] Klaus Mueller, Roni Yagel, and John J Wheller. Fast implementations of algebraic methods for three-dimensional reconstruction from cone-beam data. *Medical Imaging, IEEE Transactions on*, 18(6):538–548, 1999.

[245] Martin J Murphy, James Balter, Stephen Balter, Jose A BenComo Jr, Indra J Das, Steve B Jiang, C-M Ma, Gustavo H Olivera, Raymond F Rodebaugh, Kenneth J Ruchala, et al. The management of imaging dose during image-guided radiotherapy: report of the aapm task group 75. *Medical physics*, 34(10):4041–4063, 2007.

[246] Menahem Nassi, William R Brody, Barry P Medoff, and ALBERT Macovski. Iterative reconstruction-reprojection: an algorithm for limited data cardiac-computed tomography. *Biomedical Engineering, IEEE Transactions on*, (5):333–341, 1982.

[247] Frank Natterer. *The mathematics of computerized tomography*, volume 32. Siam, 1986.

[248] Frank Natterer et al. *Mathematical methods in image reconstruction*. Siam, 2001.

[249] Frank Natterer and KP Hadeler. Efficient implementation of optimalalgorithms in computerized tomography. *Mathematical Methods in the Applied Sciences*, 2(4):545–555, 1980.

[250] Shanzhou Niu, Yang Gao, Zhaoying Bian, Jing Huang, Wufan Chen, Gaohang Yu, Zhengrong Liang, and Jianhua Ma. Sparse-view x-ray ct reconstruction via total generalized variation regularization. *Physics in medicine and biology*, 59(12):2997, 2014.

[251] Tianye Niu, Xiaojing Ye, Quentin Fruhauf, Michael Petrongolo, and Lei Zhu. Accelerated barrier optimization compressed sensing (abocs) for ct reconstruction with improved convergence. *Physics in medicine and biology*, 59(7):1801, 2014.

[252] Tianye Niu and Lei Zhu. Accelerated barrier optimization compressed sensing (abocs) reconstruction for cone-beam ct: phantom studies. *Medical physics*, 39(7):4588–4598, 2012.

[253] Frederic Noo, Rolf Clackdoyle, and Jed D Pack. A two-step hilbert transform method for 2d image reconstruction. *Physics in Medicine and Biology*, 49(17):3903, 2004.

[254] Frederic Noo, Michel Defrise, Rolf Clackdoyle, and Hiroyuki Kudo. Image reconstruction from fan-beam projections on less than a short scan. *Physics in Medicine and Biology*, 47(14):2525, 2002.

[255] Frederic Noo, K Schmitt, K Stierstorfer, and H Schondube. Image representation using mollified pixels for iterative reconstruction in x-ray ct. In *Nuclear Science Symposium and Medical Imaging Conference (NSS/MIC), 2012 IEEE*, pages 3453–3455. IEEE, 2012.

[256] Johan Nuyts, Bruno De Man, Jeffrey A Fessler, Wojciech Zbijewski, and Freek J Beekman. Modelling the physics in the iterative reconstruction for transmission computed tomography. *Physics in medicine and biology*, 58(12):R63, 2013.

[257] Johan Nuyts, Christian Michel, and Patrick Dupont. Maximum-likelihood expectation-maximization reconstruction of sinograms with arbitrary noise distribution using nec-transformations. *Medical Imaging, IEEE Transactions on*, 20(5):365–375, 2001.

[258] John Nuyts, Bruno De Man, Patrick Dupont, Michel Defrise, Paul Suetens, and Luc Mortelmans. Iterative reconstruction for helical ct: a simulation study. *Physics in medicine and biology*, 43(4):729, 1998.

[259] João P Oliveira, José M Bioucas-Dias, and Mário AT Figueiredo. Adaptive total variation image deblurring: a majorization–minimization approach. *Signal Processing*, 89(9):1683–1693, 2009.

[260] John M Ollinger. Maximum-likelihood reconstruction of transmission images in emission computed tomography via the em algorithm. *Medical Imaging, IEEE Transactions on*, 13(1):89–101, 1994.

[261] Joseph A O'Sullivan and Jasenka Benac. Alternating minimization algorithms for transmission tomography. *Medical Imaging, IEEE Transactions on*, 26(3):283–297, 2007.

[262] Jed D Pack, Frédéric Noo, and Rolf Clackdoyle. Cone-beam reconstruction using the backprojection of locally filtered projections. *Medical Imaging, IEEE Transactions on*, 24(1):70–85, 2005.

[263] X Pan et al. Few-view tomography using roughness-penalized nonparametric regression and periodic spline interpolation. *Nuclear Science, IEEE Transactions on*, 46(4):1121–1128, 1999.

[264] Xiaochuan Pan, Emil Y Sidky, and Michael Vannier. Why do commercial ct scanners still employ traditional, filtered back-projection for image reconstruction? *Inverse problems*, 25(12):123009, 2009.

[265] Xiaochuan Pan, Jeffrey Siewerdsen, Patrick J La Riviere, and Willi A Kalender. Anniversary paper: Development of x-ray computed tomography: The role of medical physics and aapm from the 1970s to present. *Medical physics*, 35(8):3728–3739, 2008.

[266] VY Panin, F Kehren, H Rothfuss, D Hu, C Michel, and ME Casey. Pet reconstruction with system matrix derived from point source measurements. *Nuclear Science, IEEE Transactions on*, 53(1):152–159, 2006.

[267] VY Panin, GL Zeng, and GT Gullberg. Total variation regulated em algorithm. In *Nuclear Science Symposium, 1998. Conference Record. 1998 IEEE*, volume 3, pages 1562–1566. IEEE, 1998.

[268] Justin C Park, Sung Ho Park, Jin Sung Kim, Youngyih Han, Min Kook Cho, Ho Kyung Kim, Zhaowei Liu, Steve B Jiang, Bongyong Song, and William Y Song. Ultra-fast digital tomosynthesis reconstruction using general-purpose gpu programming for image-guided radiation therapy. *Technology in cancer research & treatment*, 10(4):295–306, 2011.

[269] Justin C Park, Sung Ho Park, Jong Hoon Kim, Sang Min Yoon, Su Ssan Kim, Jin Sung Kim, Zhaowei Liu, Tyler Watkins, and William Y Song. Four-dimensional cone-beam computed tomography and digital tomosynthesis reconstructions using respiratory signals extracted from transcutaneously inserted metal markers for liver sbrta). *Medical physics*, 38(2):1028–1036, 2011.

[270] Justin C Park, Bongyong Song, Jin Sung Kim, Sung Ho Park, Ho Kyung Kim, Zhaowei Liu, Tae Suk Suh, and William Y Song. Fast compressed sensing-based cbct reconstruction using barzilai-borwein formulation for application to on-line igrt. *Medical physics*, 39(3):1207–1217, 2012.

[271] Dennis L Parker. Optimal short scan convolution reconstruction for fan beam ct. *Medical Physics*, 9(2):254–257, 1982.

[272] Upendra Parvathaneni, George E Laramore, and Jay J Liao. Technical advances and pitfalls in head and neck radiotherapy. *Journal of oncology*, 2012, 2012.

[273] Etienne P Payot, Francoise J Preteux, Yves L Trousset, and Regis Guillemaud. Generalized support constraint for three-dimensional reconstruction from incomplete fourier spectra. *Journal of Electronic Imaging*, 6(4):426–438, 1997.

[274] SN Penfold, Reinhard W Schulte, Yair Censor, and Anatoly B Rosenfeld. Total variation superiorization schemes in proton computed tomography image reconstruction. *Medical physics*, 37(11):5887–5895, 2010.

[275] Hui Peng and Henry Stark. Image recovery in computer tomography from partial fan-beam data by convex projections. *Medical Imaging, IEEE Transactions on*, 11(4):470–478, 1992.

[276] Roger Penrose. A generalized inverse for matrices. In *Mathematical proceedings of the Cambridge philosophical society*, volume 51, pages 406–413. Cambridge Univ Press, 1955.

[277] M Persson, D Bone, and Håkan Elmqvist. Total variation norm for three-dimensional iterative reconstruction in limited view angle tomography. *Physics in Medicine and Biology*, 46(3):853, 2001.

[278] François Pontana, Alain Duhamel, Julien Pagniez, Thomas Flohr, Jean-Baptiste Faivre, Anne-Lise Hachulla, Jacques Remy, and Martine Remy-Jardin. Chest computed tomography using iterative reconstruction vs filtered back projection (part 2): image quality of low-dose ct examinations in 80 patients. *European radiology*, 21(3):636–643, 2011.

[279] William H Press, Saul A Teukolsky, William T Vetterling, and Brain P Flannery. Minimization or maximization of functions. *Chapter*, 10:394–455, 1992.

[280] Jinyi Qi, Richard M Leahy, Simon R Cherry, Arion Chatziioannou, and Thomas H Farquhar. High-resolution 3d bayesian image reconstruction using the micropet small-animal scanner. *Physics in medicine and biology*, 43(4):1001, 1998.

[281] Johann Radon. 1.1 über die bestimmung von funktionen durch ihre integralwerte längs gewisser mannigfaltigkeiten. *Classic papers in modern diagnostic radiology*, 5, 2005.

[282] Magdalena Rafecas, Guido Böning, Bernd J Pichler, Eckhart Lorenz, Markus Schwaiger, Sibylle Ziegler, et al. Effect of noise in the probability matrix used for statistical reconstruction of pet data. *Nuclear Science, IEEE Transactions on*, 51(1):149–156, 2004.

[283] GN Ramachandran and AV Lakshminarayanan. Three-dimensional reconstruction from radiographs and electron micrographs: application of convolutions instead of fourier transforms. *PNAS*, 68(9):2236–2240, 1971.

[284] JC Ramirez-Giraldo, J Trzasko, S Leng, L Yu, A Manduca, and CH McCollough. Nonconvex prior image constrained compressed sensing (ncpiccs): Theory and simulations on perfusion ct. *Medical physics*, 38(4):2157–2167, 2011.

[285] Rangaraj Rangayyan, Atam Prakash Dhawan, and Richard Gordon. Algorithms for limited-view computed tomography: an annotated bibliography and a challenge. *Applied optics*, 24(23):4000–4012, 1985.

[286] Essam A Rashed and Hiroyuki Kudo. Statistical image reconstruction from limited projection data with intensity priors. *Physics in medicine and biology*, 57(7):2039, 2012.

[287] Wesley Jacob Rich. Examining the accuracy of the normal approximation to the poisson random variable. *Masters Theses and Doctoral Dissertations*, page 262, 2009.

[288] William Hadley Richardson. Bayesian-based iterative method of image restoration. *JOSA*, 62(1):55–59, 1972.

[289] Cyril Riddell and Yves Trousset. Rectification for cone-beam projection and backprojection. *Medical Imaging, IEEE Transactions on*, 25(7):950–962, 2006.

[290] Ludwig Ritschl, Frank Bergner, Christof Fleischmann, and Marc Kachelrieß. Improved total variation-based ct image reconstruction applied to clinical data. *Physics in medicine and biology*, 56(6):1545, 2011.

[291] Anthony Joseph Rockmore and Albert Macovski. A maximum likelihood approach to emission image reconstruction from projections. *Nuclear Science, IEEE Transactions on*, 23(4):1428–1432, 1976.

[292] Junyan Rong, Qimei Liao, Wenlei Liu, Peng Gao, Chun Jiao, and Hongbing Lu. Ct reconstruction from few-views by edge guided tv minimization. In *Nuclear Science Symposium and Medical Imaging Conference (NSS/MIC), 2013 IEEE*, pages 1–3. IEEE, 2013.

[293] Wilhelm Conrad Röntgen. On a new kind of rays. *Science*, pages 227–231, 1896.

[294] Leonid I Rudin, Stanley Osher, and Emad Fatemi. Nonlinear total variation based noise removal algorithms. *Physica D: Nonlinear Phenomena*, 60(1):259–268, 1992.

[295] Georg-Friedemann Rust, Volker Aurich, and Maximilian Reiser. Noise/dose reduction and image improvements in screening virtual colonoscopy with tube currents of 20 mas with nonlinear gaussian filter chains. In *Medical Imaging 2002*, pages 186–197. International Society for Optics and Photonics, 2002.

[296] Berkman Sahiner and Andrew E Yagle. Region-of-interest tomography using exponential radial sampling. *Image Processing, IEEE Transactions on*, 4(8):1120–1127, 1995.

[297] Jason Sanders and Edward Kandrot. *CUDA by example: an introduction to general-purpose GPU programming*. Addison-Wesley Professional, 2010.

[298] Ken Sauer and Charles Bouman. A local update strategy for iterative reconstruction from projections. *Signal Processing, IEEE Transactions on*, 41(2):534–548, 1993.

[299] Ken Sauer and Bede Liu. Nonstationary filtering of transmission tomograms in high photon counting noise. *Medical Imaging, IEEE Transactions on*, 10(3):445–452, 1991.

[300] Jürgen J Scheins, Fritz Boschen, and Hans Herzog. Analytical calculation of volumes-of-intersection for iterative, fully 3-d pet reconstruction. *Medical Imaging, IEEE Transactions on*, 25(10):1363–1369, 2006.

[301] Otmar Scherzer. *Handbook of Mathematical Methods in Imaging: Vol. 1*. Springer Science & Business Media, 2011.

[302] Colas Schretter. A fast tube of response ray-tracer. *Medical physics*, 33(12):4744–4748, 2006.

[303] JA Seibert and JM Boone. X-ray scatter removal by deconvolution. *Medical physics*, 15(4):567–575, 1988.

[304] M. I. Sezan and H. Stark. Image restoration by the method of convex projections: part 2 applications and numerical results. *IEEE Trans Med Imaging*, 1(2):95–101, 1982.

[305] GC Sharp, N Kandasamy, H Singh, and Michael Folkert. Gpu-based streaming architectures for fast cone-beam ct image reconstruction and demons deformable registration. *Physics in medicine and biology*, 52(19):5771, 2007.

[306] Lawrence A Shepp and Benjamin F Logan. The fourier reconstruction of a head section. *Nuclear Science, IEEE Transactions on*, 21(3):21–43, 1974.

[307] Lawrence A Shepp and Yehuda Vardi. Maximum likelihood reconstruction for emission tomography. *Medical Imaging, IEEE Transactions on*, 1(2):113–122, 1982.

[308] Daxin Shi. A simplified implementation of total variation iterative reconstruction algorithm suitable for parallel computation. In *2009 IEEE Nuclear Science Symposium Conference Record (NSS/MIC)*, pages 4130–4133, 2009.

[309] Yuying Shi and Qianshun Chang. Efficient algorithm for isotropic and anisotropic total variation deblurring and denoising. *Journal of Applied Mathematics*, 2013, 2013.

[310] Robert L Siddon. Fast calculation of the exact radiological path for a three-dimensional ct array. *Medical physics*, 12:252, 1985.

[311] Emil Y Sidky, Yuval Duchin, Xiaochuan Pan, and Christer Ullberg. A constrained, total-variation minimization algorithm for low-intensity x-ray ct. *Medical physics*, 38(S1):S117–S125, 2011.

[312] Emil Y Sidky, Jakob H Jørgensen, and Xiaochuan Pan. Convex optimization problem prototyping for image reconstruction in computed tomography with the chambolle–pock algorithm. *Physics in medicine and biology*, 57(10):3065, 2012.

[313] Emil Y Sidky, Chien-Min Kao, and Xiaochuan Pan. Accurate image reconstruction from few-views and limited-angle data in divergent-beam ct. *Journal of X-ray Science and Technology*, 14(2):119–139, 2006.

[314] Emil Y Sidky and Xiaochuan Pan. Image reconstruction in circular cone-beam computed tomography by constrained, total-variation minimization. *Physics in medicine and biology*, 53(17):4777, 2008.

[315] Jeffrey H Siewerdsen and David A Jaffray. Cone-beam computed tomography with a flat-panel imager: magnitude and effects of x-ray scatter. *Medical physics*, 28(2):220–231, 2001.

[316] Alvin C Silva, Holly J Lawder, Amy Hara, Jennifer Kujak, and William Pavlicek. Innovations in ct dose reduction strategy: application of the adaptive statistical iterative reconstruction algorithm. *American Journal of Roentgenology*, 194(1):191–199, 2010.

[317] BW Silverman, MC Jones, JD Wilson, and DW Nychka. A smoothed em approach to indirect estimation problems, with particular, reference to stereology and emission tomography. *Journal of the Royal Statistical Society. Series B (Methodological)*, pages 271–324, 1990.

[318] Sarabjeet Singh, Mannudeep K Kalra, Matthew D Gilman, Jiang Hsieh, Homer H Pien, Subba R Digumarthy, and Jo-Anne O Shepard. Adaptive statistical iterative reconstruction technique for radiation dose reduction in chest ct: a pilot study. *Radiology*, 259(2):565–573, 2011.

[319] Sarabjeet Singh, Mannudeep K Kalra, Jiang Hsieh, Paul E Licato, Synho Do, Homer H Pien, and Michael A Blake. Abdominal ct: Comparison of adaptive statistical iterative and filtered back projection reconstruction techniques 1. *Radiology*, 257(2):373–383, 2010.

[320] Arkadiusz Sitek, Ronald H Huesman, and Grant T Gullberg. Tomographic reconstruction using an adaptive tetrahedral mesh defined by a point cloud. *Medical Imaging, IEEE Transactions on*, 25(9):1172–1179, 2006.

[321] AB Smith, WP Dillon, R Gould, and M Wintermark. Radiation dose-reduction strategies for neuroradiology ct protocols. *American Journal of Neuroradiology*, 28(9):1628–1632, 2007.

[322] Rebecca Smith-Bindman, Jafi Lipson, Ralph Marcus, Kwang-Pyo Kim, Mahadevappa Mahesh, Robert Gould, Amy Berrington de González, and Diana L Miglioretti. Radiation dose associated with common computed tomography examinations and the associated lifetime attributable risk of cancer. *Archives of internal medicine*, 169(22):2078–2086, 2009.

[323] Donald L Snyder. Utilizing side information in emission tomography. *Nuclear Science, IEEE Transactions on*, 31(1):533–537, 1984.

[324] Donald L Snyder, Abed M Hammoud, and Richard L White. Image recovery from data acquired with a charge-coupled-device camera. *JOSA A*, 10(5):1014–1023, 1993.

[325] Donald L Snyder, Carl W Helstrom, Aaron D Lanterman, Mohammad Faisal, and Richard L White. Compensation for readout noise in ccd images. *JOSA A*, 12(2):272–283, 1995.

[326] Donald L Snyder, Michael Miller, et al. The use of sieves to stabilize images produced with the em algorithm for emission tomography. *Nuclear Science, IEEE Transactions on*, 32(5):3864–3872, 1985.

[327] William Song, Bryan Schaly, Glenn Bauman, Jerry Battista, and Jake Van Dyk. Image-guided adaptive radiation therapy (igart): Radiobiological and dose escalation considerations for localized carcinoma of the prostate. *Medical physics*, 32(7):2193–2203, 2005.

[328] William Y Song, Srijit Kamath, Shuichi Ozawa, Shlomi Al Ani, Alexei Chvetsov, Niranjan Bhandare, Jatinder R Palta, Chihray Liu, and Jonathan G Li. A dose comparison study between xvi® and obi® cbct systems. *Medical physics*, 35(2):480–486, 2008.

[329] J Webster Stayman, Hao Dang, Yifu Ding, and Jeffrey H Siewerdsen. Pirple: a penalized-likelihood framework for incorporation of prior images in ct reconstruction. *Physics in medicine and biology*, 58(21):7563, 2013.

[330] JW Stayman, W Zbijewski, Y Otake, A Uneri, S Schafer, J Lee, JL Prince, and JH Siewerdsen. Penalized-likelihood reconstruction for sparse data acquisitions with unregistered prior images and compressed sensing penalties. In *SPIE Medical Imaging*, pages 79611L–79611L. International Society for Optics and Photonics, 2011.

[331] David Strong and Tony Chan. Edge-preserving and scale-dependent properties of total variation regularization. *Inverse problems*, 19(6):S165, 2003.

[332] D Stsepankou, A Arns, SK Ng, P Zygmanski, and J Hesser. Evaluation of robustness of maximum likelihood cone-beam ct reconstruction with total variation regularization. *Physics in medicine and biology*, 57(19):5955, 2012.

[333] Predrag Sukovic and Neal H Clinthorne. Penalized weighted least-squares image reconstruction for dual energy x-ray transmission tomography. *Medical Imaging, IEEE Transactions on*, 19(11):1075–1081, 2000.

[334] Timothy P Szczykutowicz and Guang-Hong Chen. Dual energy ct using slow kvp switching acquisition and prior image constrained compressed sensing. *Physics in medicine and biology*, 55(21):6411, 2010.

[335] Eiichi Tanaka. Improved iterative image reconstruction with automatic noise artifact suppression. *Medical Imaging, IEEE Transactions on*, 11(1):21–27, 1992.

[336] Jie Tang, Brian E Nett, and Guang-Hong Chen. Performance comparison between total variation (tv)-based compressed sensing and statistical iterative reconstruction algorithms. *Physics in medicine and biology*, 54(19):5781, 2009.

[337] Xiangyang Tang, Jiang Hsieh, Roy A Nilsen, Sandeep Dutta, Dmitry Samsonov, and Akira Hagiwara. A three-dimensional-weighted cone beam filtered backprojection (cb-fbp) algorithm for image reconstruction in volumetric cthelical scanning. *Physics in Medicine and Biology*, 51(4):855, 2006.

[338] Jean-Baptiste Thibault, Charles A Bouman, Ken D Sauer, and Jiang Hsieh. A recursive filter for noise reduction in statistical iterative tomographic imaging. In *Electronic Imaging 2006*, pages 60650X–60650X. International Society for Optics and Photonics, 2006.

[339] Jean-Baptiste Thibault, Ken D Sauer, Charles A Bouman, and Jiang Hsieh. A three-dimensional statistical approach to improved image quality for multislice helical ct. *Medical physics*, 34(11):4526–4544, 2007.

[340] Christoph Thilmann, Simeon Nill, Thomas Tucking, Angelika Hoss, Bernd Hesse, Lars Dietrich, Rolf Bendl, Bernhard Rhein, P Haring, Christian Thieke, et al. Correction of patient positioning errors based on in-line cone beam cts: clinical implementation and first experiences. *Radiat Oncol*, 1(1):16, 2006.

[341] Zhen Tian, Xun Jia, Kehong Yuan, Tinsu Pan, and Steve B Jiang. Low-dose ct reconstruction via edge-preserving total variation regularization. *Physics in medicine and biology*, 56(18):5949, 2011.

[342] Zhen Tian, Xun Jia, Kehong Yuan, Tinsu Pan, and Steve B Jiang. Low-dose ct reconstruction via edge-preserving total variation regularization. *Physics in medicine and biology*, 56(18):5949, 2011.

[343] Andreĭ Tikhonov. *Numerical methods for the solution of ill-posed problems*.

[344] Robert D Timmerman and Lei Xing. *Image-guided and adaptive radiation therapy*. Lippincott Williams & Wilkins, 2012.

[345] Michel S Tohme and Jinyi Qi. Iterative image reconstruction for positron emission tomography based on a detector response function estimated from point source measurements. *Physics in medicine and biology*, 54(12):3709, 2009.

[346] Thomas L Toth, Erdogan Cesmeli, Aziz Ikhlef, and Tetsuya Horiuchi. Image quality and dose optimization using novel x-ray source filters tailored to patient size. In *Medical imaging*, pages 283–291. International Society for Optics and Photonics, 2005.

[347] Heang K Tuy. An inversion formula for cone-beam reconstruction. *SIAM Journal on Applied Mathematics*, 43(3):546–552, 1983.

[348] Bert Vandeghinste, Bart Goossens, Jan De Beenhouwer, Aleksandra Pizurica, Wilfried Philips, Stefaan Vandenberghe, and Steven Staelens. Split-bregman-based sparse-view ct reconstruction. In *11th International meeting on Fully Three-Dimensional Image Reconstruction in Radiology and Nuclear Medicine (Fully 3D 11)*, pages 431–434, 2011.

[349] Eugene Veklerov, J Llacer, and Edward J Hoffman. Mle reconstruction of a brain phantom using a monte carlo transition matrix and a statistical stopping rule. *Nuclear Science, IEEE Transactions on*, 35(1):603–607, 1988.

[350] Julia Velikina, Shuai Leng, and Guang-Hong Chen. Limited view angle tomographic image reconstruction via total variation minimization. In *Medical Imaging*, pages 651020–651020. International Society for Optics and Photonics, 2007.

[351] Curtis R Vogel and Mary E Oman. Iterative methods for total variation denoising. *SIAM Journal on Scientific Computing*, 17(1):227–238, 1996.

[352] Rameez Wajid, A Bin Mansoor, and Marius Pedersen. A study of human perception similarity for image quality assessment. In *Colour and Visual Computing Symposium (CVCS), 2013*, pages 1–6. IEEE, 2013.

[353] Ge Wang and Ming Jiang. Ordered-subset simultaneous algebraic reconstruction techniques (os-sart). *Journal of X-ray Science and Technology*, 12(3):169–178, 2004.

[354] Han Wang, Laurent Desbat, and Samuel Legoupil. Image representation by blob and ct reconstruction from few projections. In *Nuclear Science Symposium and Medical Imaging Conference (NSS/MIC), 2011 IEEE*, pages 3971–3976. IEEE, 2011.

[355] Jing Wang, Tianfang Li, Hongbing Lu, and Zhengrong Liang. Penalized weighted least-squares approach to sinogram noise reduction and image reconstruction for low-dose x-ray computed tomography. *Medical Imaging, IEEE Transactions on*, 25(10):1272–1283, 2006.

[356] Jing Wang, Tianfang Li, and Lei Xing. Iterative image reconstruction for cbct using edge-preserving prior. *Medical physics*, 36:252, 2009.

[357] Jing Wang, Zhengrong Liang, Hongbing Lu, and Lei Xing. Recent development of low-dose x-ray cone-beam computed tomography. *Current Medical Imaging Reviews*, 6(2):72–81, 2010.

[358] Jing Wang, Hongbing Lu, Zhengrong Liang, Daria Eremina, Guangxiang Zhang, Su Wang, John Chen, and James Manzione. An experimental study on the noise properties of x-ray ct sinogram data in radon space. *Physics in medicine and biology*, 53(12):3327, 2008.

[359] Jing Wang, Weihua Mao, and Timothy Solberg. Scatter correction for cone-beam computed tomography using moving blocker strips: a preliminary study. *Medical physics*, 37(11):5792–5800, 2010.

[360] Steve Webb. From the watching of shadows. 1990.

[361] Ning Wen, Huaiqun Guan, Rabih Hammoud, Deepak Pradhan, T Nurushev, Shidong Li, and Benjamin Movsas. Dose delivered from varian's cbct to patients receiving imrt for prostate cancer. *Physics in medicine and biology*, 52(8):2267, 2007.

[362] Bruce R Whiting. Signal statistics in x-ray computed tomography. In *Medical Imaging 2002*, pages 53–60. International Society for Optics and Photonics, 2002.

[363] Paul A Wolf, Jakob S Jørgensen, Taly G Schmidt, and Emil Y Sidky. Few-view single photon emission computed tomography (spect) reconstruction based on a blurred piecewise constant object model. *Physics in medicine and biology*, 58(16):5629, 2013.

[364] Fang Xu and Klaus Mueller. Accelerating popular tomographic reconstruction algorithms on commodity pc graphics hardware. *Nuclear Science, IEEE Transactions on*, 52(3):654–663, 2005.

[365] Fang Xu and Klaus Mueller. Real-time 3d computed tomographic reconstruction using commodity graphics hardware. *Physics in medicine and biology*, 52(12):3405, 2007.

[366] Jinchao Xu. Iterative methods by space decomposition and subspace correction. *SIAM review*, 34(4):581–613, 1992.

[367] Jingyan Xu and Benjamin MW Tsui. Electronic noise modeling in statistical iterative reconstruction. *Image Processing, IEEE Transactions on*, 18(6):1228–1238, 2009.

[368] Qiong Xu, Xuanqin Mou, Shaojie Tang, and Yanbo Zhang. Ct reconstruction based on improved total variation minimization. In *Nuclear Science Symposium Conference Record (NSS/MIC), 2010 IEEE*, pages 3241–3244. IEEE, 2010.

[369] Qiong Xu, Hengyong Yu, Xuanqin Mou, and Ge Wang. Dictionary learning based low-dose x-ray ct reconstruction. In *11th International Meeting on Fully Three-Dimensional Image Reconstruction in Radiology and Nuclear Medicine*, pages 259–63. World Scientific, 2011.

[370] Qiong Xu, Hengyong Yu, Xuanqin Mou, Lei Zhang, Jiang Hsieh, and Ge Wang. Low-dose x-ray ct reconstruction via dictionary learning. *Medical Imaging, IEEE Transactions on*, 31(9):1682–1697, 2012.

[371] Wei Xu and Klaus Mueller. A performance-driven study of regularization methods for gpu-accelerated iterative ct. In *Workshop on High Performance Image Reconstruction (HPIR)*. Citeseer, 2009.

[372] Wei Xu and Klaus Mueller. Evaluating popular non-linear image processing filters for their use in regularized iterative ct. In *Nuclear Science Symposium Conference Record (NSS/MIC), 2010 IEEE*, pages 2864–2865. IEEE, 2010.

[373] Guorui Yan, Jie Tian, Shouping Zhu, Yakang Dai, and Chenghu Qin. Fast cone-beam ct image reconstruction using gpu hardware. *Journal of X-ray Science and Technology*, 16(4):225–234, 2008.

[374] Ming Yan, Jianwen Chen, Luminita A Vese, John Villasenor, Alex Bui, and Jason Cong. Em+ tv based reconstruction for cone-beam ct with reduced radiation. In *Advances in Visual Computing*, pages 1–10. Springer, 2011.

[375] Ming Yan and Luminita A Vese. Expectation maximization and total variation-based model for computed tomography reconstruction from undersampled data. In *SPIE Medical Imaging*, pages 79612X–79612X. International Society for Optics and Photonics, 2011.

[376] Jiansheng Yang, Hengyong Yu, Ming Jiang, and Ge Wang. High-order total variation minimization for interior tomography. *Inverse problems*, 26(3):035013, 2010.

[377] Kai Yang, Shih-Ying Huang, Nathan J Packard, and John M Boone. Noise variance analysis using a flat panel x-ray detector: A method for additive noise assessment with application to breast ct applications. *Medical physics*, 37:3527, 2010.

[378] Yangbo Ye, Hengyong Yu, and Ge Wang. Exact interior reconstruction with cone-beam ct. *International journal of biomedical imaging*, 2007, 2008.

[379] Sua Yoo and Fang-Fang Yin. Dosimetric feasibility of cone-beam ct-based treatment planning compared to ct-based treatment planning. *International Journal of Radiation Oncology* Biology* Physics*, 66(5):1553–1561, 2006.

[380] Dan C Youla and Heywood Webb. Image restoration by the method of convex projections: Part 1?theory. *Medical Imaging, IEEE Transactions on*, 1(2):81–94, 1982.

[381] Daniel F. Yu and Jeffrey A Fessler. Edge-preserving tomographic reconstruction with nonlocal regularization. *Medical Imaging, IEEE Transactions on*, 21(2):159–173, 2002.

[382] Hengyong Yu and Ge Wang. Compressed sensing based interior tomography. *Physics in medicine and biology*, 54(9):2791, 2009.

[383] Hengyong Yu, Yangbo Ye, and Ge Wang. Interior reconstruction using the truncated hilbert transform via singular value decomposition. *Journal of X-ray science and technology*, 16(4):243, 2008.

[384] Lifeng Yu, Michael R Bruesewitz, Kristen B Thomas, Joel G Fletcher, James M Kofler, and Cynthia H McCollough. Optimal tube potential for radiation dose reduction in pediatric ct: principles, clinical implementations, and pitfalls. *Radiographics*, 31(3):835–848, 2011.

[385] Lifeng Yu, Shuai Leng, Lingyun Chen, James M Kofler, Rickey E Carter, and Cynthia H McCollough. Prediction of human observer performance in a 2-alternative forced choice low-contrast detection task using channelized hotelling observer: Impact of radiation dose and reconstruction algorithms. *Medical physics*, 40(4):041908, 2013.

[386] Lifeng Yu, Xiaochuan Pan, and Charles A Pelizzari. Image reconstruction with a shift-variant filtration in circular cone-beam ct. *International Journal of Imaging Systems and Technology*, 14(5):213–221, 2004.

[387] Zhicong Yu, Frédéric Noo, Frank Dennerlein, Adam Wunderlich, Günter Lauritsch, and Joachim Hornegger. Simulation tools for two-dimensional experiments in x-ray computed tomography using the forbild head phantom. *Physics in Medicine and Biology*, 57(13):N237, 2012.

[388] Zhou Yu, Jean-Baptiste Thibault, Charles Bouman, Ken D Sauer, Jiang Hsieh, et al. Fast model-based x-ray ct reconstruction using spatially nonhomogeneous icd optimization. *Image Processing, IEEE Transactions on*, 20(1):161–175, 2011.

[389] Joseph Zambelli, Brian E Nett, Shuai Leng, Cyril Riddell, Barry Belanger, and Guang-Hong Chen. Novel c-arm based cone-beam ct using a source trajectory of two concentric arcs. In *Medical Imaging*, pages 65101Q–65101Q. International Society for Optics and Photonics, 2007.

[390] W Zbijewski, AP Colijn, and FJ Beekman. Monte carlo based scatter correction for cone-beam micro-ct. In *Proceedings of The 7th International Conference on Fully 3D Reconstruction In Radiology and Nuclear Medicine. Saint Malo, France*, 2003.

[391] Wojciech Zbijewski and Freek J Beekman. Characterization and suppression of edge and aliasing artefacts in iterative x-ray ct reconstruction. *Physics in medicine and biology*, 49(1):145, 2004.

[392] Wojciech Zbijewski and Freek J Beekman. Comparison of methods for suppressing edge and aliasing artefacts in iterative x-ray ct reconstruction. *Physics in medicine and biology*, 51(7):1877, 2006.

[393] Wojciech Zbijewski and Freek J Beekman. Efficient monte carlo based scatter artifact reduction in cone-beam micro-ct. *Medical Imaging, IEEE Transactions on*, 25(7):817–827, 2006.

[394] Gengsheng L Zeng, Ya Li, and Alex Zamyatin. Iterative total-variation reconstruction versus weighted filtered-backprojection reconstruction with edge-preserving filtering. *Physics in medicine and biology*, 58(10):3413, 2013.

[395] GL Zeng. Image reconstructiona tutorial. *Computerized Medical Imaging and Graphics*, 25(2):97–103, 2001.

[396] Kai Zeng, Bruno De Man, Jean-Baptiste Thibault, Zhou Yu, Charles Bouman, and Ken Sauer. Spatial resolution enhancement in ct iterative reconstruction. In *Nuclear Science Symposium Conference Record (NSS/MIC), 2009 IEEE*, pages 3748–3751. IEEE, 2009.

[397] Yi Zhang, Wei-Hua Zhang, Hu Chen, Meng-Long Yang, Tai-Yong Li, and Ji-Liu Zhou. Few-view image reconstruction combining total variation and a high-order norm. *International Journal of Imaging Systems and Technology*, 23(3):249–255, 2013.

[398] Jian Zhou and Jinyi Qi. Fast and efficient fully 3d pet image reconstruction using sparse system matrix factorization with gpu acceleration. *Physics in medicine and biology*, 56(20):6739, 2011.

[399] Hongqing Zhu, Huazhong Shu, Jian Zhou, and Limin Luo. A weighted least squares pet image reconstruction method using iterative coordinate descent algorithms. In *Nuclear Science Symposium Conference Record, 2004 IEEE*, volume 6, pages 3380–3384. IEEE, 2004.

[400] Lei Zhu, N Robert Bennett, and Rebecca Fahrig. Scatter correction method for x-ray ct using primary modulation: Theory and preliminary results. *Medical Imaging, IEEE Transactions on*, 25(12):1573–1587, 2006.

[401] Mingqiang Zhu, Stephen J Wright, and Tony F Chan. Duality-based algorithms for total-variation-regularized image restoration. *Computational Optimization and Applications*, 47(3):377–400, 2010.

[402] Zangen Zhu, Khan Wahid, Paul Babyn, David Cooper, Isaac Pratt, and Yasmin Carter. Improved compressed sensing-based algorithm for sparse-view ct image reconstruction. *Computational and mathematical methods in medicine*, 2013, 2013.

[403] Tingliang Zhuang, Joseph Zambelli, Brian Nett, Shuai Leng, and Guang-Hong Chen. Exact and approximate cone-beam reconstruction algorithms for c-arm based cone-beam ct using a two-concentric-arc source trajectory. In *Medical Imaging*, pages 691321–691321. International Society for Optics and Photonics, 2008.

[404] Andy Ziegler, Thomas Köhler, Tim Nielsen, and Roland Proksa. Efficient projection and backprojection scheme for spherically symmetric basis functions in divergent beam geometry. *Medical physics*, 33(12):4653–4663, 2006.

[405] Yu Zou and Xiaochuan Pan. Exact image reconstruction on pi-lines from minimum data in helical cone-beam ct. *Physics in Medicine and Biology*, 49(6):941, 2004.